Modeling and Controlling Topographical Nonuniformity in Thermoplastic Micro- and Nano-Embossing

by

Hayden Kingsley Taylor

B.A., University of Cambridge (2004)
M.Eng., University of Cambridge (2004)

Submitted to the Department of Electrical Engineering and Computer Science
in partial fulfillment of the requirements for the degree of

Doctor of Philosophy
in Electrical Engineering and Computer Science

at the

Massachusetts Institute of Technology

September 2009

Signature of Author: .....

Department of Electrical Engineering and Computer Science
June 29, 2009

Certified by: .....

Duane S. Boning
Professor of Electrical Engineering and Computer Science
Thesis Supervisor

Accepted by: .....

Professor Terry P. Orlando
Chair, Department Committee on Graduate Students

Modeling and Controlling Topographical Nonuniformity in Thermoplastic Micro- and Nano-Embossing

by

Hayden Kingsley Taylor

B.A., University of Cambridge (2004)
M.Eng., University of Cambridge (2004)

Submitted to the Department of Electrical Engineering and Computer Science
on June 29, 2009 in partial fulfillment of the
requirements for the degree of Doctor of Philosophy
in Electrical Engineering and Computer Science

Abstract

The embossing of thermoplastic polymeric plates is valuable for manufacturing micro- and nano-fluidic devices and diffractive optics. Meanwhile, the imprinting of sub-micrometer-thickness thermoplastic layers has emerged as a lithographic technique with exceptional resolution. Yet neither hot micro-embossing nor thermal nanoimprint lithography will be fully adopted without efficient numerical techniques for simulating these processes. This thesis contributes a computationally inexpensive approach to simulating the embossing of feature-rich patterns into thermoplastic polymeric materials.

The simulation method employs a linear viscoelastic model for the embossed layer, and computes the distribution of contact pressure between the polymeric surface and an embossing stamp. An approximation to the embossed topography of the polymeric layer is thereby generated as a function of the material being embossed, the stamp's design, and the embossing process's temperature, duration, and applied load. For a stamp design described with an 800 × 800 matrix of topographical heights, simulation can be completed within 30–100 s using a computer with an Intel Pentium 4 processor and 2 GB RAM. This method is sufficiently fast for it to be employed iteratively when designing a pattern to be embossed or when selecting processing parameters. The method is able to build abstracted representations of feature-rich patterns, increasing the simulation speed still further. The viscoelastic properties of three materials — polymethylmethacrylate, polycarbonate, and Zeonor 1060R, a cyclic olefin polymer — have been experimentally calibrated as functions of temperature. For a test-pattern having features with diameters 5 μm to 90 μm, simulated and experimental topographies agree with r.m.s. errors of less than 2 μm across all processing conditions tested, with absolute topographical heights ranging up to 30 μm.

In thermal nanoimprint lithography, the key challenge is to minimize spatial variation of the polymeric layer's residual thickness where stamp protrusions press down into the layer. The simulation method is therefore extended to incorporate elastic stamp deflections and their influence on residual layer thickness. Some design-rules are proposed that could help to minimize residual layer thickness variation. A way is also proposed for representing any shear-thinning of the imprinted layer.

Thesis supervisor: Duane S. Boning
Title: Professor of Electrical Engineering and Computer Science

Acknowledgements

The last five years have brought a cornucopia of opportunities and rewards. For many of them I must thank my advisor, Duane Boning: his inspired guidance and his unswerving confidence in me have made it possible to explore so many avenues of research while still remembering the location of the main Ph.D. highway. I have certainly found that having an idea a day keeps the doctorate away, but the great warmth and the spirit of curiosity that pervade the Boning Group have made it easy to sustain enthusiasm while seeking progress.

I am also grateful to the other members of my thesis committee: Jay Han, Yee Cheong Lam, and Todd Thorsen. They have all helped with perceptive questions and timely suggestions of new areas for investigation. Professor Lam, in particular, has spent hours poring over paper drafts and helping me to set my research priorities. I am grateful for constructive discussions with many others, particularly Lallit Anand, Brian Anthony, George Barbastathis, David Hardt, Martin Schmidt, and Kamal Youcef-Toumi.

The Kennedy Memorial Trust put a great deal of faith in me when it funded my first year here. I thank its MIT Trustee, Richard Lester, for his helpful advice, and its former Secretary, Anna Mason, for her tireless work, especially in helping all the Kennedy Scholars to adjust to life in Boston. I also thank the Singapore–MIT Alliance for its support throughout the last five years. The Cambridge–MIT Institute has provided additional funding.

The dedication and energy of my collaborators is remarkable. Ciprian Iliescu and Bangtao Chen at the Institute of Engineering and Biotechnology in Singapore have given support and inspiration in several directions, and provided the polysulfone films used in Chapter 6. Ivan Reading and Li Shiguang of the Singapore Institute of Manufacturing Technology have shared their insights, providing help in conceiving a bond toughness measurement technique that exploits the modeling work of this thesis.

My fellow students in the Boning Research Group have been a delight to work with. Outside the group, I particularly appreciate the fruitful interactions that I have had with other participants in the Singapore–MIT Alliance's Manufacturing Systems and Technology Flagship Research Programme. Matt Dirckx has given me extensive access to the embossing apparatus that he built, and my discussions with him have been a source of great inspiration. Melinda Hale has also frequently helped with embossing experiments. Nici Ames helped me to begin to understand polymer mechanics. Discussions with Aaron Mazzeo, Eehern Wong, Shawn Chester, David Henann, Vijay Shilpiekandula, Dan Burns, Vikas Srivastava, and Zhiguang Xu have provided multifarious insights. These colleagues have all given exhaustively of their time to help me, and I hope that I have been able to reciprocate in ways that have helped them. Working with these fantastic individuals in such a collegial atmosphere has made for a very happy five years.

My visits to Singapore have been productive and enjoyable largely because of the hospitality, friendship, and assistance of the staff and students at Nanyang Technological University and SIMTech: in particular, Lip Pin Yeo, Chin Hock Kua, Tran Duc Vi, Mei Ling Ang, and Jason Chong.

The staff of the Microsystems Technology Laboratories at MIT is truly outstanding, and their dedication and patience have made much of this research possible. I am particularly grateful to Kurt Broderick and Dennis Ward for their extensive help and advice. Others richly deserving of thanks are Sharlene Blake, Mira Whiting, James Freedman of the Technology Licensing Office, Debb Hodges-Pabon, and Chadwick Collins.

Finally I thank my family and friends for their support, particularly my parents, Brenda and Graham, my grandparents Beatrice and Arthur, and Keely Sayers. Both my father and grandfather saw me start but have not lived to see me finish this degree and, having been thousands of miles away from home at times when I should have been closer, I am perhaps most in debt to them.

Biography

Hayden Taylor was born in Bristol, United Kingdom, in 1981. He attended Bristol Grammar School and Trinity College, Cambridge, receiving the B.A. and M.Eng. degrees in Electrical and Electronic Engineering in 2004. He was sponsored as an undergraduate by STMicroelectronics. He is a Senior Scholar of Trinity College, Cambridge, and received the Cambridge University Engineering Department's Baker Prize in 2004. He is a member of the IEEE, the Institution of Engineering and Technology, SPIE, the Institute of Physics, and the Sigma Xi honor society. He was an Institution of Electrical Engineers Jubilee Scholar 2000–4, and was a Kennedy Scholar for the academic year 2004–5. Hayden's research interests include simulation methods for micro- and nano-fabrication processes, materials testing techniques for microsystems, and the uses of polymeric materials in microsystems.

Contents

1. Introduction

This thesis describes a set of numerical simulation techniques that could enhance the benefits of using two promising micro- and nano-fabrication processes: (*i*) the micro-embossing of thermoplastic polymers, and (*ii*) nanoimprint lithography. The work provides a computationally inexpensive way to predict the topography of a thermoplastic polymeric layer after it has been patterned using a stamp of a given design. The simulation methods are intended to help their users to refine stamp designs and select optimal processing parameters.

1.1. Contributions of this thesis

1.1.1. Computationally inexpensive modeling of bulk micro-embossing

The micron-scale embossing of thermoplastic sheets having millimeter-scale thickness is of particular value for the fabrication of biomedical microfluidic devices and diffractive optics. We propose an approximate and highly computationally inexpensive viscoelastic model for the hot-embossing of complex patterns. We show that the embossing of a linear viscoelastic material can be simulated just as simply as that of a purely elastic one, and we experimentally calibrate our model for three thermoplastics commonly used in hot-embossing: polymethylmethacrylate, polycarbonate, and a cyclic olefin polymer, Zeonor 1060R.

1.1.2. A simple material characterization method

Any simulation method naturally needs knowledge of the mechanical properties of the material(s) being embossed or imprinted. Scores of different materials have already been used for embossing/imprinting, and we anticipate that new and useful polymers will be developed in the future. The process of calibrating the simulation approach for additional materials should therefore be as fast and inexpensive as possible. To this end, we have designed (*i*) standard embossing test patterns, (*ii*) a small set of characterization experiments to be performed on any new material, and (*iii*) a procedure for extracting property information from the resulting topographies.

1.1.3. 'Hierarchical' modeling approach for embossing feature-rich patterns

Even when using the simplified model described above, many realistic patterns will contain too many features for their embossing to be simulated within a reasonable time. We therefore describe a method for abstracting the layout representation of feature-rich patterns so that their embossing can be simulated in a far shorter time than if each individual feature were represented separately.

1.1.4. Study of the impact of trapped air in micro-embossing

While some hot micro-embossing systems place the polymer/stamp environment under vacuum before embossing, others do not. There has not until now been a quantitative understanding of the influence of trapped air upon the embossing process. We extend our modeling technique to represent the effects of trapped air, and show that as the areal density of stamp protrusions becomes small, the relative importance of the presence of air becomes greater. We are able to specify how processing parameters should be adjusted to compensate for the presence of trapped air inside stamp cavities.

1.1.5. Computationally inexpensive modeling of nanoimprint

In thermal nanoimprint lithography, a thin layer of thermoplastic polymer is spun on to a comparatively hard substrate and then imprinted with a stamp. It is important not only to ensure that the cavities of the stamp are filled with polymer, but also to achieve a thin and uniform *residual* layer of polymer in the regions where stamp protrusions have pressed down into the layer. It therefore becomes necessary to model nanometer-scale elastic deflections of the stamp and the substrate, in addition to deformation of the polymer layer. We describe a way of carrying out this modeling for linear viscoelastic resist materials. The modeling method can be used both at the scale of individual features, and in a 'hierarchical' manner, where complex patterns are described in an abstracted form. We also suggest a computationally inexpensive way of accounting for any effects of shear-thinning.

1.1.6. A flexible simulation/calibration framework

All of these modeling techniques are implemented in Matlab, using object-oriented code that is designed to be readily extended if further physical phenomena need to be captured. Definitions of stamps, material properties, and sets of processing conditions have a standard format that is independent of whether bulk micro-embossing or nanoimprint is being simulated. There is also a set of methods that automates the extraction of material properties from metrology data. This simulation framework can be made directly available to the research community, and is ready to be developed further into a design-for-manufacture product for companies using nanoimprint lithography.

With the guidance provided by our methods, manufacturers of hot-embossed and nanoimprinted devices could expect to enjoy reduced product development costs, increased manufacturing speed, a reduced rate of production of defective parts, and a reduced time-to-market for new products.

1.2. Thermoplastic micro-embossing: background

The hot embossing of thermoplastic polymers has in recent years attracted attention as a promising microfabrication process. In hot embossing, a polymeric substrate is heated until it softens, and a hard, reusable, patterned stamp is then pressed into the substrate before both the stamp and the substrate are cooled and then separated (Figure 1.1). Hot embossing has certain advantages over other polymer microfabrication processes. The micro-casting of curable liquid resins — a process which, when used with elastomers such as polydimethylsiloxane (PDMS), is widely known as 'soft lithography' [1] — is ideal for prototyping a few tens of a particular device, although considerable manual skill is required to handle the highly flexible components produced. Ways of automating soft lithography have so far proved largely elusive. Injection molding, meanwhile, can form microscopic features [2] and is easily automated, but tooling and equipment costs are relatively high. Hot embossing, in contrast, combines moderate cost with ease of automation, and can therefore help to bridge the gap between the invention and the commercialization of a number of micro- and nano-fluidic devices. Substrates processed by hot-embossing can range in size from a single chip to a continuous roll of material [3–5], making the process both amenable to prototyping and potentially even more cost-efficient than injection molding for very high-volume manufacturing.

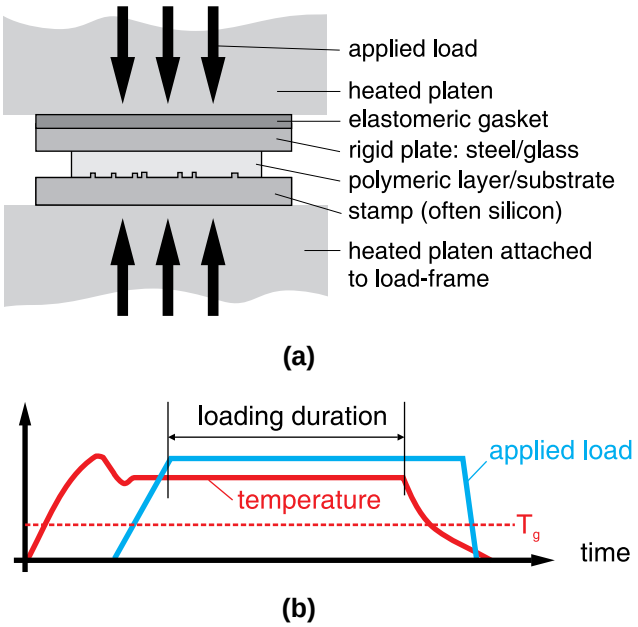

Figure 1.1: Thermoplastic micro-embossing process: (a) experimental set-up (not to scale); (b) typical temperature and load courses, showing unloading below the glass-transition temperature, T_g, of the polymer.

1.2.1. Considerations in using thermoplastic embossing

When thermoplastic embossing is used to produce micro-/nano-fluidic devices, the embossed layer is typically many times as thick as the channels are deep — although one can envisage cases in which the substrate thickness would be comparable to the feature depth, for example in portable 'smart-card'-format diagnostic devices or multi-layer designs. The use of polymeric structural materials (instead of, say, silicon or glass) is attractive because they offer scope for very low costs per unit area, and thus the production of disposable biomedical devices. Some polymeric materials transmit ultraviolet light, which is useful for the stimulation and analysis of samples placed inside the fluidic devices [6]. Moreover, the

mechanical toughness of polymeric materials makes them more suitable than silicon or glass for use at the point of care. Spatial uniformity is important in the embossing of microfluidic channels, and even more so in the production of *nano*-fluidic channels, whose performance is often crucially dependent upon their smallest dimension [7]. The surface properties of embossed micro- and nano-fluidic devices — especially their roughness [8–12], trapped electrical charge density [13–15] and related hydrophobicity [16–18] — also influence their performance, and the nature of the hot embossing process itself, in conjunction with any subsequent treatments [19–24] can strongly affect these properties. Successful embossing also demands a stamp that can deform the polymeric layer into the desired shape and then be withdrawn without fracturing, and without damaging the embossed layer. The lifetime of the stamp needs to be sufficiently long for the embossing process to be economically attractive, and a wide range of stamp materials and surface treatments is being investigated in an attempt to attain suitable lifetimes [25–28].

1.2.2. Alternatives to thermoplastic embossing

Soft Lithography. The casting of curing elastomeric resins such as polydimethylsiloxane (PDMS) is widely used in the prototyping of micro- and nano-fluidic devices [1] because it does not require specialist equipment to carry out, and because of the material's attractive surface chemistry, its UV transparency, and its low autofluorescence. There has, however, been little progress in developing PDMS processing equipment suitable for the medium-to-large-scale production of micro- and nano-fluidic devices. Moreover, even the stiffest formulations of PDMS have an elastic modulus of no more than ~10 MPa, making it hard to use the material to fabricate collapse-free channels with sub-micron depths [29]. Stiffer polymers such as thermoplastics and UV-curable acrylates therefore appear to be preferable for nanofluidic fabrication.

UV-curing polymers have been found to shrink by a few percent during polymerization [30], which, depending on the substrate size and the embossed pattern may either aid or hinder removal of the stamp, but must certainly be carefully compensated for in dimension-critical applications. UV-curing polymers are, nevertheless, being investigated in earnest for use in microelectromechanical systems (MEMS) fabrication [31, 32].

Micron-scale injection molding promises higher throughput than hot embossing, but injection pressures are at least ten times higher than typical embossing pressures and as a result would introduce larger residual stresses and hence birefringence into the material, a potentially serious defect for biomedical microsystems relying on optical inspection through the formed polymeric part. The high mold and equipment costs compared with those of hot embossing mean that injection molding could only be appropriate for runs of at least tens of thousands of parts; we, meanwhile, are interested in technology for medium-scale prototyping and custom runs as well as for high-volume production. Moreover, flexible planar microfluidic substrates may in fact prove more economical to produce by embossing than by injection molding, even in large volumes, since an embossing process can be adapted to a continuous, reel-to-reel configuration, while injection molding cannot.

Indeed, **reel-to-reel embossing** has received attention from industry, especially from Avery [33] and 3M [4], Several other researchers have demonstrated reel-to-reel technology: Larsen *et al.* have used a combination of gravure and nanoimprint to pattern conducting polyaniline [3], Seo *et al*. have proposed continuous nano-scale imprinting with elastomeric roller stamps [34], and Tan, Chou *et al.* have demonstrated a roller imprint system with a nickel roller [5].

Several other technologies may be worth investigating. **Stereolithography** — localized photopolymerization within a bath of liquid, forming arbitrarily shaped components — is constantly improving in speed and spatial resolution, and could become useful for highly customized microfabrication [35]. **Two-photon polymerization**, a sophisticated form of stereolithography, allows the production of arbitrarily shaped 3-D components, and offers superior spatial resolutions of 100 nm or

better [36]. We also believe that the **blow-molding** of microfluidic channels from thermoplastic polymeric films would be a worthwhile avenue of research.

These alternative technologies are all promising, but the straightforward embossing of thermoplastic plates combines the potential for impressive throughput and unbeaten lateral resolution. As a result, hot embossing has seen extensive industrial investment, although modeling and simulation approaches have not kept pace with the fabrication technology itself.

1.3. Thermoplastic micro-embossing: challenges and possible solutions

There are several pitfalls to be avoided in thermoplastic micro-embossing; some of the more common ones are discussed below and illustrated in Figure 1.2.

1.3.1. Temperature, pressure or hold-time too low

An inappropriate choice of processing parameters can cause the incomplete filling of stamp cavities (Figure 1.2a–d). Depending on the properties of the material and the capabilities of the embossing apparatus, a solution may be to increase the embossing pressure, extend the loading duration, or increase the temperature of embossing. Introducing any of these changes, though, might result in one or more of the problems listed below.

1.3.2. Substrate cooled too much before demolding

The larger the temperature swing between embossing and demolding, the greater the differential thermal contraction of the substrate and stamp. For a temperature swing of 60 K from embossing to demolding and a substrate diameter of 100 mm, we would expect a contraction of the substrate relative to the stamp of up to 10^{-4} K^{-1} × 50 mm × 60 K = 300 μm at the substrate edge, which would cause features on the stamp to be dragged through the substrate over distances at least comparable in size with the diameters of the features themselves. We have observed the ‘smearing’ and piling up of material in the regions adjacent to embossed features where the substrate experiences lateral compression during cooling [37]. These regions are always located on the side of the feature closer to the edge of the substrate (Figure 1.2e). The heights of these asymmetrical ridges have been observed to exceed 10 μm in some cases; whether the ridges develop before or after unloading is not yet known. As the substrate contracts globally after unloading it does appear to push itself away from the stamp, and we hypothesize that the hard, sharp edges of features on the stamp can sometimes *slice* through material in the sidewalls of embossed features, leaving the fronds of polymer that we have observed on the substrate surface (Figure 1.2f).

Worgull *et al.* suggest a way of reducing damage to the stamp and embossed part during demolding [38]. They propose including robust protrusions on the stamp, surrounding the functional features; these edge rings would carry most of the lateral stamp–polymer forces that arise during thermal contraction. Guo *et al*. describe simulations of a similar idea [39, 40]. Since the greatest relative motion of stamp and substrate during cooling occurs at the edge of the substrate [41], it makes sense for stress barriers to be at the edge of the stamp and to enclose all fragile features.

Thermal contraction-induced damage may also be reduced by demolding as close as possible to the embossing temperature, so that as little differential thermal contraction as possible takes place before demolding. We have ourselves already investigated the fidelity of pattern replication that is possible with hot demolding [37], as have Ro *et al.* [42] and Leveder *et al*. [43, 44]. In addition to considering the

temperature of demolding, the *rate* of cooling prior to demolding could be important: rapid thermal cycling is being pursued extensively as a way of reducing cycle times (*e.g.* by Yao *et al.* [45]) but reduces the opportunity for radial creep of the polymer layer during cooling and is therefore likely to trap more residual stresses and lead to higher demolding forces.

1.3.3. Substrate cooled too little before demolding

If demolding is done at or above the glass transition temperature, parts of the embossed pattern may become distorted as the polymer subsequently cools. In particular, the bottom surfaces of features that are hot-demolded tend to 'spring back' and become bowed (Figure 1.2g), as we have observed [37]. The longer after demolding that the polymer takes to cool to below its glass transition temperature, the more severe the shape distortion (Figure 1.2h). Embossing and demolding temperatures must therefore be chosen carefully if thermal contraction damage and parasitic shape recovery are both to be avoided.

1.3.4. Poor substrate-scale temperature uniformity

The arguments above, when taken to their logical conclusion, might suggest that both embossing *and* demolding should be done within the polymer's glass-transition region, where behavior is typically elastic-plastic. This approach, however, brings another difficulty. The temperature uniformity of an embossing machine's heated platens is usually no better than about ± 1°C over a 100 mm square region [46]. A thermoplastic polymer's mechanical properties are highly sensitive to temperature when the material is in its glass-transition region. Embossing in the glass-transition region could therefore introduce substantial substrate-scale nonuniformity. In contrast, if embossing is done several tens of degrees above the glass-transition, a few degrees' temperature variation will not influence substrate-scale embossing uniformity.

1.3.5. Particles trapped between substrate and stamp

The presence of trapped particles can result in point-defects in the embossed pattern. If they are large enough and hard enough, particles also risk damaging the stamp.

1.3.6. Platens non-parallel

If the embossing machine applies pressure using two solid platens that are not perfectly parallel, we expect that at the substrate scale a wedge-shaped pressure distribution will develop, and equivalent features at different positions on the substrate will therefore be filled to differing heights (Figure 1.2i).

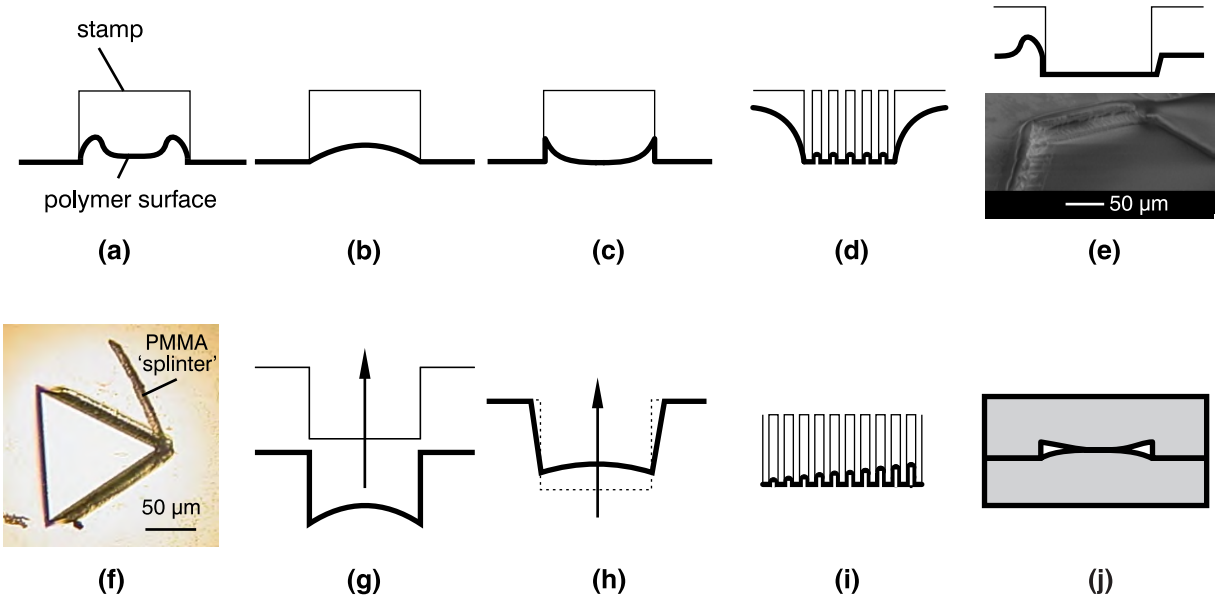

Figure 1.2: Defect types observed in hot micro- and nano-embossing. (a) two-peak incomplete stamp filling; (b) one-peak incomplete filling; (c) sidewall filling/wetting; (d) array of features acting as one incompletely formed feature; (e) asymmetric piling up of material caused during substrate cooling and demolding; (f) shearing off of piled-up material during demolding; (g) elastic shape recovery at bases of features after demolding; (h) overall shape recovery of embossed feature if allowed to stand, unloaded, above the glass transition; (i) pressure variation across a stamp produces non-uniform cavity filling; (j) shallow encapsulated voids collapse during fabrication or filling with fluid. See Section 1.8.1 for a discussion of modes (a)–(c).

1.3.7. Summary

The main current challenges in MEMS hot embossing development are therefore (*i*) the control of embossed surfaces' physical and chemical properties, (*ii*) the minimization of processing cycle time while maintaining the fidelity of patterns across the whole embossed area, and (*iii*) the fabrication of embossing stamps with acceptable demolding performance and lifetime. In this thesis we focus on the second of these challenges, by aiming to model the mechanics of embossing in a way that assists the design of patterns and the selection of process parameters.

1.4. Bonding of thermoplastics: requirements and challenges

To produce a complete micro- or nano-fluidic device, the embossed layer usually needs to be bonded to a second layer, enclosing fluidic channels. The bond formed must be tough enough to prevent delamination in use, with special consideration given to the stresses induced by any hydrodynamic pressures within the fluidic channels. The bonding method used should avoid excessive distortion of the shapes of the channels, and ideally will not introduce foreign materials, such as adhesives, that might clog the channels or change the chemical properties of the channel walls.

One of the simplest and most promising methods for bonding thermoplastics involves heating both layers to a precisely chosen temperature within their glass transition regions, and pressing the layers together for a certain time. It is thought that polymer chains at the interface interdiffuse to form the bond.

When thermal bonding is done, the price paid is a certain amount of distortion of the channels (Figure 1.2j): the bulk of the polymer material is able to flow under the applied bonding load. If the temperature, pressure or loading duration is even slightly too high, this distortion can become unacceptably large and even cause the channels to collapse. The wider a channel in proportion to its depth, the more likely collapsing is to occur. Because of the valuable simplicity of the thermal bonding method, though, it would be worth modeling this distortion process so that it could be controlled by a prudent selection of bonding parameters.

1.5. Nanoimprint lithography: background

1.5.1. The need for a replacement for photolithography

As the feature sizes required in semiconductor manufacturing shrink, it is being widely argued that photolithography will struggle to deliver them. All of the options that are being considered to extend the resolution of photolithography — including double patterning, the use of new immersion fluids and lens materials, and extreme-ultraviolet (EUV) photolithography — add considerable expense. Even if the engineering challenges of EUV can be resolved, estimates of the capital costs of these tools are in the range of $60M–$100M. As a result, some radically different approaches to lithography are being developed. Maskless lithography — such as zone-plate array lithography and multiple-electron-beam systems — are receiving attention, as is nanoimprint lithography (NIL), which is now well established on the International Technology Roadmap for Semiconductors (ITRS) as an option for the 32 nm node and beyond [47]. Typical capital costs of NIL tools are in the range $1M–$10M. The quest to develop NIL technology has led to the creation of the NIL Consortium [48], with industrial and academic partners, and to the funding by the European Commission of a major collaborative project, Emerging Nanopatterning Methods (NaPa) [49].

1.5.2. Variants and capabilities of nanoimprint lithography

Nanoimprint has been advocated for a very broad range of patterning applications — many of them quite separate from semiconductor manufacturing — and several variants of the process have emerged. Each has its own strengths and weaknesses. There have been several good recent review articles comparing the different variants of nanoimprint and assessing their capabilities [50–55]. In all types of nanoimprint, the objective is to mechanically pattern a deformable layer on the surface of a comparatively hard substrate. Sub-100 nm lateral resolutions are usually sought, and the deformed material is usually polymeric. An important requirement is to make as thin and uniform as possible the *residual* parts of the deformed layer that sit beneath stamp protrusions. The main variants of nanoimprint are illustrated in Figure 1.3 and summarized below.

1.5.3. Droplet-dispensed, step-and-flash nanoimprint

Step-and-flash imprint lithography (SFIL) [56] patterns a wafer die-by-die, by pressing a transparent stamp into a region of ultraviolet-curable resist and illuminating the resist through the stamp. In some SFIL tools the resist is dispensed as an array of droplets whose locations and volumes are tailored to the distribution of cavities on the stamp; in this way, imprinting time and residual layer thickness variation can both be reduced compared to the use of a single, larger, dispensed volume.

Since the die-sized imprinting tool is much smaller than the whole wafer, wafer-scale uniformity of the residual layer may be optimized through die-by-die positioning of the stamp relative to the substrate.

In SFIL, the viscosity of the uncured resist is sufficiently low that capillary forces play a crucial role in causing the resist to fill cavities of the stamp. The pressure mechanically applied to the stamp is typically less than 100 kPa.

An extension of SFIL replaces the die-sized stamp with a highly flexible substrate-sized one; a low-viscosity liquid resist is applied as droplets or by pipetting, and capillary forces are still crucial in filling the stamp. Uses of substrate-sized UV-curing imprint are the fabrication of patterned-media hard disk drives and photonic-crystal LEDs.

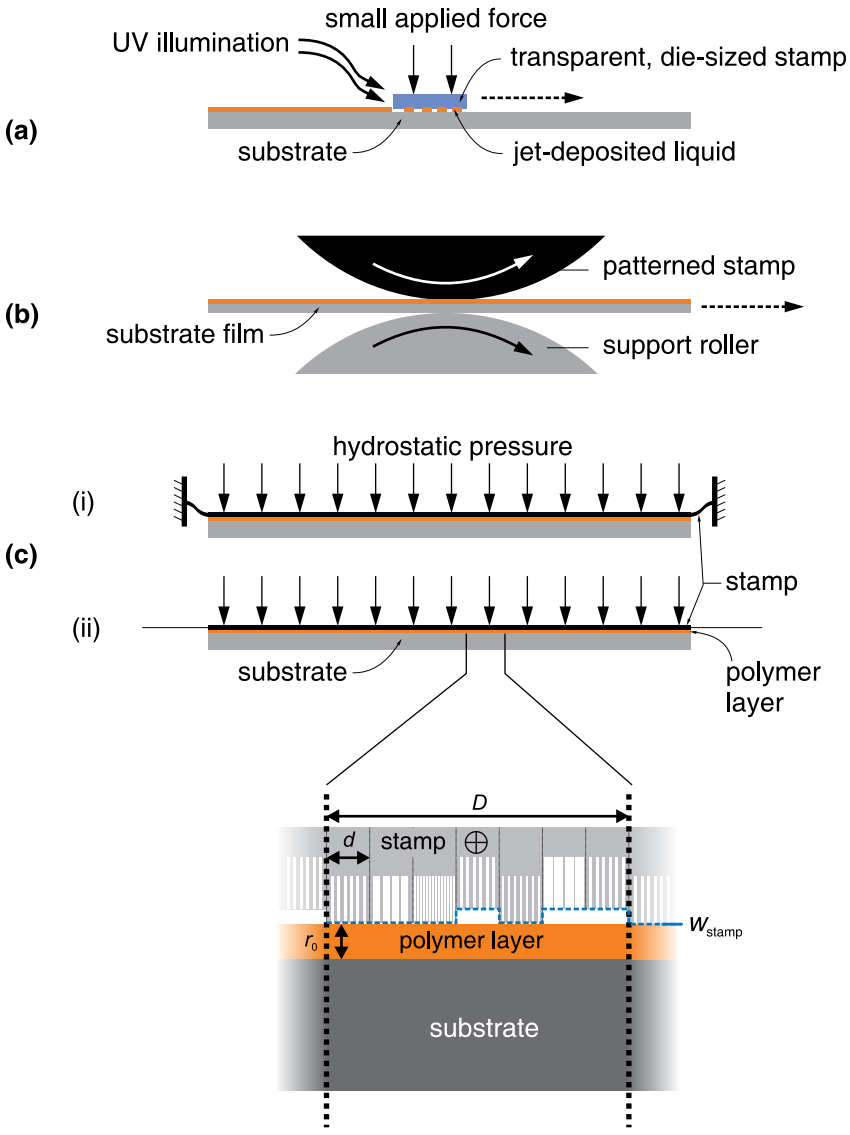

Figure 1.3: Types of nanoimprint lithography. (a) Step-and-flash; (b) reel-to-reel, which may be thermal or UV-curing; (c) wafer-scale, which may use thermoplastic, UV-curing or hybrid resists. Two variants of (c) are shown: where the edge of the stamp is (i) clamped and (ii) free.

1.5.4. Spun-on resist layers

In this variant of NIL, a resist layer, usually polymeric and typically ~100 nm thick, is spun on to a wafer. The layer is subsequently imprinted with a stamp that is typically the size of the whole wafer.

Thermal NIL. If the resist is thermoplastic it can be softened by heating and then imprinted. The pattern is 'frozen' in place by cooling before the stamp is removed. Thermal nanoimprint (T-NIL) has been demonstrated in a research setting to produce features as small as ~6 nm in diameter [57, 58].

UV or heat-curing NIL. Just as certain droplet-dispensed resists can be UV-cured, so can some spun-on layers of resist. Obducat, for example, offers the option of using UV-curing resists in its machines, as well as resists that cure by exposure to heat. The use of heat to cure the resist removes the need for the stamp to be UV-transparent.

Room-temperature NIL. It has been demonstrated that certain spun-on resist materials may be nano-imprinted without the need of *either* thermoplastic softening *or* a curing step. Materials investigated include very low molecular-weight polymers [59] and 'spun-on glass' (organosilica dissolved in alcohol) [60]. Such 'room-temperature NIL' (RT-NIL) or 'cold forging' schemes are suitable for step-and-repeat implementations, with the possible advantage of eliminating any heating/cooling or curing time [61–64].

Imprinting partially UV-cured resists. Many useful, imprintable materials require UV-curing; yet the use of a UV-transparent stamp is not always affordable or desirable. To circumvent this difficulty, processes have been demonstrated whereby the spun-on resist is partially cross-linked with a brief UV-exposure, then imprinted (usually at room temperature), and fully cured *after* removal of the stamp. This approach has been shown to work with SU-8 [65] and certain semiconducting polymers [66].

1.5.5. Roll-to-roll imprint

For particularly large substrates, the use of roll-to-roll imprint is appealing. There have been laboratory-scale demonstrations of heat- and UV-curing roll-to-roll nanoimprint [67], and there is an extensive EU Framework 7 project, 'Lab on Foil', making use of roll-to-roll imprint to prototype integrated diagnostic devices [68]. There do not, however, yet appear to be established companies focusing on the production of roll-to-roll imprint equipment capable of producing features at the sub-micron scale.

1.5.6. Characteristics of the nanoimprint equipment market

There are around six suppliers of nanoimprint machines today. Süss MicroTec [69] and EV Group [70] are suppliers of laboratory-scale photolithography equipment that have adapted their products for nanoimprint. Molecular Imprints is a company specializing in UV-curing imprint tools: they sell what they claim are slot-in replacements for photolithography in semiconductor manufacturing. These machines use the step-and-flash variant of imprint with droplet-based resist dispensing, quartz stamps, and sophisticated mechanical stamp alignment systems. Molecular Imprints also sell tools for substrate-sized imprint, using flexible stamps to pattern photonic crystal LED wafers and hard disk platters. Obducat sells both research- and manufacturing-scale tools that imprint an entire wafer or disk platter in one step using a flexible polymeric stamp. The resists used in Obducat machines are generally spun on and may be thermoplastic or UV- or heat-curing. Nanonex takes a similar approach to Obducat, as apparently does NanoLithoSolution.

1.5.7. Alternatives to nanoimprint

The possibilities discussed by the International Technology Roadmap for Semiconductors for the 32 nm node include, in addition to nanoimprint, the use of EUV lithography, innovative immersion materials, double patterning, and maskless lithography.

Double patterning is already being demonstrated; its extra cost arises because there are two exposure steps per layer instead of one. There are also complex CAD challenges in distributing features appropriately among the two masks [71] and in doing optical proximity correction to account for the phase shifts that occur in partially exposed resist layers.

Several other patterning techniques may also merit consideration. **Interference lithography** has been demonstrated for the creation of highly regular patterns with feature-sizes of a few tens of nanometers, and may be of use for some of the simpler pattern applications discussed in Section 1.7.

Self-assembly has received extensive research interest and is likely to see its first applications in the production of patterns with a high degree of regularity. For example, Ladenburger *et al.* have produced dichroic filters by causing the self-assembly of silica particles within a polymer layer, curing the polymer, etching the silica away and depositing metal into the cavities left [72]. Self-assembly on its own can produce only very regular patterns, and defects are common. Structuring or directing the assembly still requires a lithographic process of some kind. Directed self-assembly is, nevertheless, included on the ITRS as a possibility at the 18 nm node, for which options are expected to be narrowed down in around 2014.

Finally, **electrostatically induced pattern formation** has been proposed and demonstrated for the creation of some simple, regular structures [73, 74]. In this process a patterned electrode is held a small distance above a liquid resist layer and an electric field is applied across the resist. Feature-scale inhomogeneities are produced in the electric field intensity, pulling the resist surface into the desired topography. The process avoids mechanical contact between the patterned electrode and the resist, which brings an advantage in terms of electrode lifetime. The shapes of topographies that can be transferred to the resist using this process are, however, somewhat limited.

Each of these emerging lithographic methods is likely to find uses, but nanoimprint does appear to offer an at-present unmatched combination of reasonable capital equipment costs and the flexibility to produce a wide range of patterns which need not be highly regular. For nanoimprint to win wider adoption, though, more thorough modeling and simulation approaches must be made available.

1.6. Nanoimprint lithography: challenges and possible solutions

Although nanoimprint processes of several kinds have been in development for around 15 years, there remain several unsolved, or partially solved, engineering challenges. Most of them stem from the fact that mechanical contact is made between the stamp and the resist.

1.6.1. Multi-layer alignment/registration

The use of flexible stamps to conform to bowed or wavy substrates brings with it the possibility of lateral stretching of the stamp and distortion of the pattern transferred [75]. This distortion can be compounded in thermal nanoimprint, since the stamp and/or substrate may contract during cooling. In-plane pattern distortions may mean that layer-to-layer registration is rendered impossible. In the step-and-

flash variant of nanoimprint, where a smaller and much more rigid quartz stamp is typically used, lateral pattern distortion is less of a challenge, but, as with any nanopatterning process, suitable techniques are needed for aligning multiple pattern levels precisely. Nanoimprint is not necessarily any more difficult than photolithography to equip with alignment systems of a given accuracy [76] — several promising alignment techniques involving the moiré principle and diffraction have been put forward [77–81] — and indeed the layer of uncured, liquid resist between stamp and substrate can *ease* the alignment procedure by lubricating the interface.

1.6.2. Pattern dependencies: stamp bending; cavity volume density variations

It is widely recognized that in the nanoimprinting of spun-on resist layers, spatial variation of the local density of features on the stamp (or 'pattern density') leads to deflections of the stamp during imprinting and hence to unwanted residual layer thickness nonuniformity [82–88]. Non-uniform residual layer thickness is problematic in practice because it imposes a need for 'over-etching' during the subsequent step that transfers the pattern to the material beneath the resist. Material underlying regions of a pattern with thinner residual layers will be exposed to etchant for longer: it will etch more deeply and possibly experience greater parasitic lateral etching.

Broadly, regions of a stamp with few cavities or small cavities experience higher average stamp–resist contact pressures during imprinting, and thicker resulting residual layers are observed [89]. Attempts to avoid these pattern dependencies have included introducing dummy features to a stamp to homogenize pattern density, although it is recognized that in many devices there is limited freedom to vary the layout [90].

Hybrids of photolithography and mechanical imprinting have been proposed, in order to eliminate the residual layer [53, 91] or to circumvent the problems of non-uniform pattern distribution by forming fine features with imprinting and large features with photolithography, so that extensive lateral displacement of material via squeezing is not needed [92, 93]. 'Hybrid' processes, of course, require more fabrication steps and presumably therefore involve greater cost than a simple, single imprint step.

1.6.3. Incomplete cavity filling

One consequence of pattern density nonuniformity is that it may be impossible to select an initial layer thickness for spun-on resist that is suitable for every region of the stamp. Regions with few cavities will end up with a local surplus of material and large residual layers; meanwhile regions with few protrusions and large cavities will be incompletely filled [94]. Incomplete filling could be problematic in two ways. Firstly, if the imprinted pattern is to form part of a functional structure, incomplete filling is likely to be unacceptable. If, however, the aim of imprinting is to produce an etch-mask, incomplete filling might not in itself be disastrous. The only requirement is that the resist in non-residual regions be thick enough to withstand the whole etching process. The danger here, though, is that if the viscosity of the resist is too low during imprinting then 'capillary bridges' of resist can be formed between the wafer and the top of the unfilled cavity [95–97]. The action of the resist's surface tension can 'suck' resist away from the wafer such that parts of the resist that are supposed to be thick and to mask the wafer become too thin to be effective as an etch mask [98].

1.6.4. Droplet coalescence and gas trapping

The use of inkjet-dispensed UV-curing resist in patterns that are tailored to the cavity density of the stamp can help to reduce stamp deflections and residual layer nonuniformity. There are, however, drawbacks to this method. It is generally held that UV-curing imprint cannot be performed under vacuum because the liquid resist would evaporate. When droplets meet underneath the stamp, then, gas is trapped and takes time to dissolve in the resist. Opinion is divided as to whether this dissolving time is

throughput-limiting [99, 100]. Gas can also become trapped inside stamp cavities as the interface between gas and uncured resist moves laterally across them. Several researchers have used numerical simulations to investigate the relationship between a cavity's geometry and the propensity of gas to become trapped in it [101–104].

1.6.5. Elastic residual-layer recovery

In both thermoplastic and room-temperature imprint lithography of spun-on layers, post-unloading 'spring-back', or thickness recovery, of the residual layer has been widely observed [105–107]. The conditions governing whether recovery occurs include the temperature and pressure of imprinting: elastic recovery generally seems to become less severe when imprinting is done further above the glass-transition of the polymer. Elastic recovery has been studied at the feature-scale: springback generally occurs in the centers of large imprinted features, leaving a band of plastically deformed material — that does not spring back — near the edges of the feature. There have also been attempts to explain this phenomenon's dependence upon local pattern density [108].

1.6.6. Stamp removal

There is a challenging trade-off to be made in selecting the material or surface-coating of a nanoimprint stamp. It would, on the one hand, ideally be highly hydrophilic so that capillary forces assist as far as possible with the filling of cavities. On the other hand, if the stamp surface has too great an affinity for the resist material there can be a risk of the resist adhering to the stamp [109–111], causing so-called 'pull-out' defects upon removal of the stamp, and creating a need for the stamp to be cleaned. As a result there have in fact been efforts to formulate UV-curing resist material with a surfactant that migrates to the resist–stamp interface and whose molecules are broken upon exposure to the UV light [112].

Whatever stamp material or surface-coating is selected [113], it must be compatible with the stringent requirements on stamp lifetime that are discussed below in Section 1.6.7. Covalently-bonded fluorinated silane stamp coatings have been explored [114], as well as chemical vapor-deposited fluorinated polymer layers. Bulk fluorinated polymers have also been investigated as a mold material [115]. Ion-beam bombardment of a spun-on resist [116] and additional anti-stiction coatings spun on to the resist before imprinting have been investigated as ways of aiding mold release.

1.6.7. Template/stamp fabrication, inspection, and lifetime

Aside from the choice of stamp materials, fabrication of the stamp is challenging because of the need to create nano-scale features on its surface. Stamps are predominantly made using e-beam lithography followed by reactive ion etching. The choice of resist for e-beam exposure is important: a balance needs to be struck between writing time, resolution, and line roughness, and it is crucial to get this balance correct in order to make affordable stamps [117]. Moreover, great attention must be paid to the specifics of the etching process. Stamps having rough sidewalls or sidewalls with a re-entrant taper present an increased likelihood of pull-out defects [118], so the choice of etching process must pay close attention to sidewall angle and roughness.

If the stamps are particularly stiff, as in step-and-flash imprint, they must be produced without waviness [119]: the starting stamp material needs to be carefully prepared.

An analysis published by Canon, a photolithography equipment manufacturer that appears also to be working on a nanoimprint tool, suggests that for a stamp cost of $150K — comparable to that of an extreme-UV mask — the stamp would need to have a lifetime of ~10^6 imprints in order for the cost of ownership of NIL to compete with that of EUV, assuming the throughput of an NIL tool to be 25 wafers per hour [76].

Because of the imperfections inherent in e-beam stamp manufacture and the possibility of stamp–resist adhesion in use, stamp inspection techniques are needed so that excessively defective stamps are not used in production. These tools need a sufficiently high resolution to measure sub-30 nm features as well as adequate throughput to keep the cost of stamp production affordable. The development of such tools is an active area of research. Atomic force microscopy, scanning electron microscopy and scatterometry are all being pursued [120, 121].

The dual needs to prolong stamp lifetime and contain inspection costs present a possible dilemma. An approach advocated by at least one imprint equipment manufacturer, Obducat, is to make polymeric 'daughter' stamps from the e-beam-fabricated master, and to use these daughter stamps to imprint the actual products. This approach both increases throughput, by allowing the product to be produced on multiple imprint machines simultaneously, and prolongs the life of the expensive e-beam-produced master by limiting the rate at which impressions are made from it. It is possible, however, that the use of daughter stamps can increase the *measurement* burden, because each new daughter stamp may need to be inspected before use. If the daughter stamps are re-used many times, there may also be a need to inspect the multiple stamps periodically for new defects.

1.6.8. 'Defectivity'

The four main types of defects addressed in the nanoimprint literature are (*i*) those occurring during template fabrication, (*ii*) delamination of resist from the wafer, or 'pull-out', (*iii*) incomplete filling, and (*iv*) particle-related [122–125]. The combined occurrences of these four types of defects need to be reduced in order to make nanoimprint attractive for CMOS applications. Current reports on the defect rate of SFIL are in the region of 5 cm^{-2} after ~1000 stamp imprints [125].

1.6.9. Summary

Of these challenges, it is primarily the challenge of pattern dependencies that this thesis aims to address. Essentially, the more heterogeneous the pattern — in areal density or in feature-size distribution — the harder nanoimprint is to use successfully. The other challenges can, and probably will, eventually be dealt with through improved materials science or machine design, but pattern dependencies are inherent in the physics of imprint and need to be modeled so that engineers can control them.

In the next section, we enumerate some specific applications that have been proposed for nanoimprint. For each application we give an impression of the level of regularity, or otherwise, of the patterns that need to be imprinted, and the relative defect-tolerance of the application.

1.7. Nanoimprint lithography: applications

What is exciting about nanoimprint lithography is that because it can be performed in one step on substrates many inches in diameter, it is affordable for certain manufacturing applications where photolithography has *never* been affordable. For example, nanoimprint enables the large-area patterning of photonic crystal LEDs or of bit-patterned hard-disk drives, which have simple designs and no requirement for multi-level alignment. At the other end of the complexity scale, nanoimprint is promising — but not yet accepted — for the production of complex integrated circuits with feature sizes that photolithography is struggling to provide. Broadly, the more stringent an application's requirements for a low density of defects, for multi-level registration, and for critical dimension uniformity, the longer it will be before nanoimprint is ready for adoption in that application. In this section we discuss the various

applications that have been proposed for nanoimprint, in the approximate chronological order in which we expect them to come to fruition.

1.7.1. Photonic crystal LEDs

There is today a $250M business in high-brightness LEDs that incorporate a photonic lattice on the surface of their semiconductor components. These LEDs are used in flat-panel displays and pico-projectors; because of their greatly superior efficiency to conventional LEDs, they are a strong contender to replace incandescent and fluorescent lighting in buildings everywhere.

Fabricating the photonic crystal lattice is perhaps the ideal application for the flavor of nanoimprint in which the resist is spun on as a uniform layer [126, 127]. Firstly, the pattern is a completely regular array of circular holes, so the thickness of a spun-on resist layer can be tailored precisely to the areal density of the pattern that will be imprinted, allowing a thin and uniform residual layer to be obtained. Secondly, the products are highly defect-tolerant: a few missing holes in the lattice do not substantially reduce the brightness of the light produced. The InGaN-based substrates that are currently used are known to exhibit tens of microns of bow, but nanoimprint is largely able to cope with this challenge because stamps can be made sufficiently flexible to conform to the bowed wafer. As LED manufacturers scale up production they are likely to try to move from the 75–100 mm-diameter wafers that they appear to use today to larger wafer sizes. Obducat, one of the main suppliers of wafer-scale nanoimprint machines, has successfully sold multiple tools to LED manufacturers such as Luminus Devices. Droplet-dispensed UV-curing imprint has also been demonstrated for the fabrication of photonic crystals [128].

There is also interest in using nanoimprint to produce photonic structures, such as waveguides, with greater geometrical complexity than that of a regular lattice [129, 130]. Many of these structures, in spite of their sophistication, have little variation of feature size or pattern density, and therefore appear relatively straightforward to reproduce via NIL. There is a growing family of applications in which these photonic structures are designed to interact with fluids [131], and may, for example, be functionalized to sense the presence of certain biological molecules in the fluid [132]. In such cases, the choice of material for the photonic structure must be compatible with the biochemical surroundings in which it will be used.

1.7.2. Metamaterials: mechanical and electromagnetic

The structuring of materials, usually at the sub-micron scale, to give them new and useful mechanical or electromagnetic properties has received burgeoning interest in recent years. Examples are the creation of superhydrophobic or superoleophobic surfaces by way of a designed surface roughness [133], and the creation of negative-refractive-index materials in the form of sub-wavelength periodic structures incorporating a conductor and an insulator [134]. Sub-wavelength optics exhibiting form birefringence [135], and beamsplitting, polarizing [67, 136], filtering [137], and lens behavior have also been demonstrated [138]. The patterns usually involved in metamaterials are highly regular and therefore ideally suited to the use of nanoimprint.

Some metamaterials may require three-dimensional structures to be fabricated, and there has been work to develop multi-layer nanoimprint processes, which involve the transferring of patterns from a sacrificial layer to the structure being built [91, 139].

1.7.3. Tissue/membrane engineering

Thermoplastic embossing at the nano-scale has been used to create scaffolds designed to direct cellular placement and alignment [140, 141], and to make nanoporous membranes with a variety of filtering/sieving applications [142]. Engineered tissue scaffolds or porous membranes are biological ‘metamaterials’ in the sense that a material is given completely new overall property by being patterned. Again, these materials’ highly regular structures make them amenable to nanoimprinting.

1.7.4. Discrete-track and bit-patterned hard disk drives

As demand grows for higher data-storage densities, it is proving necessary to *pattern* the magnetic film that stores information in hard disk drives. Patterned media allow bits of data to be stored in closer physical proximity than in a continuous film. One approach is to pattern a series of concentric magnetic tracks; another is to produce arrays of discrete posts of magnetic material, with one bit being stored per post. The current target diameter for these bits is ~20 nm. Nanoimprint is ideally suited to transferring these patterns because it is possible to pattern a whole disk platter in one imprint step [143]. Whereas in the production of LEDs, the imprinting of spun-on resist layers seems to be the favored approach, in hard-disk production the use of low-viscosity, droplet-dispensed UV-curing resists is currently winning out, with Molecular Imprints being the predominant supplier of imprint tools for hard-disk manufacturing. Several disk manufacturers are known to be developing bit-patterned hard disk drives.

Much of the surface area of a patterned-media hard disk contains a uniform pattern of tracks or posts, but there are also so-called ‘servo’ regions which allow the data-reading head to locate itself as it moves across the disk. These servo patterns have feature sizes as large as a few microns and their presence could perturb the residual layer thickness in surrounding data regions. Residual layer thickness variation propagates to variation of the diameters of the final magnetic data bits, and these dimensions can have a powerful effect on the ability of the bit to retain its data. There is certainly a role here for modeling of any pattern-dependent residual layer nonuniformity.

Many disk drive platters are double-sided and there has been work to achieve side-to-side alignment of bit patterns when imprinting them simultaneously. For example, the photolithography equipment manufacturer ASML has recently patented a method whereby two elastic imprint stamps, each having an initial curvature, make contact and interlock through the hole located at the center of the platen to be patterned. The stamps are then curled down to make contact with the resist and the platen.

1.7.5. Organic solar cell production

There appear to be several ways in which large-area organic solar cells can be enhanced by micro- or nano-patterning. Firstly is the creation of grooved or randomly patterned diffractive back-planes that cause light not immediately absorbed in the semiconducting region to propagate laterally through the cell via total internal reflection [144]. Secondly is the nano-patterning of the interface between the two differently-doped semiconducting polymer regions that constitute the organic cell: increasing the area of the interface has been shown to enhance efficiency [145–147]. Thirdly is the nano-patterning of the surface of the cell to enhance its optical absorbance [148]. Fourthly, contact printing with nano-patterned elastomeric stamps has been used to transfer metal electrode patterns to the front surfaces of polymeric solar cells: these metal layers are reported to be only a few tens of nm thick and to offer an impressive combination of low sheet-resistance and high optical transmissivity [149].

All components of an organic solar cell could be produced from conducting or semiconducting polymers, and nanoimprint would be an attractive way to pattern them. Given the sizes of solar cells — more than a meter in diameter in some cases — reel-to-reel imprinting seems the most likely variant of nanoimprint to succeed here.

1.7.6. Planarization

There has been interest in the use of flowable materials for planarization. The idea is to ‘imprint’ the flowable material with a flat ‘stamp’ so that it forms a planarizing, and usually insulating, layer. For planarization to be successful, the compliance of the stamp, the volume of flowable material and the planarizing load applied need to be chosen appropriately so that the underlying topography does not propagate excessively to the planarized surface.

1.7.7. Flat-panel displays

There are several steps in the manufacture of thin-film transistor-based flat-panel displays that could benefit from the use of nanoimprint. These include the formation of highly regular patterns — as found in diffusers and in liquid-crystal alignment materials [150, 151]. There has also been at least one report of the successful use of UV-curing nanoimprint to produce the lens arrays that cover the reflective portions of the pixels of transflective displays [152]. Moreover, the formation of the pixel-controlling transistors could itself be done via nanoimprint instead of photolithography.

For newer displays based on field-emission, the use of nanoimprint has been proposed as a way of forming the emitter tips: in the work of Baba *et al*., a polyimide layer was imprinted and then converted by argon ion irradiation to produce carbon-based emitters [153].

The possible applications of NIL in display manufacturing include, then, patterning steps with highly regular arrays of a single feature size and shape, as well as steps in which the pattern is still periodic but with a greater variety of feature shape and size within each period of the pattern. In any case, likely feature sizes are a few microns or larger, and substrate sizes can be several hundreds of millimeters. Roll-to-roll imprinting seems likely to be the most attractive method for display manufacturing.

1.7.8. Biomedical micro- and nano-devices

The boundaries between micro-embossing and nanoimprint are at their most blurred when it comes to biomedical devices. Lateral feature sizes in these chips can span five or more orders of magnitude: from 20 nm-wide DNA-sieving channels to mm-scale fluid reservoirs and ports [7]. Biomedical micro- and nano-devices have been widely demonstrated, both embossed into mm-thick plates of polymer and imprinted into spun-on or UV-curing polymeric layers [3, 154, 155]. It is not surprising that nanoimprint equipment manufacturers are keen to exploit this small but potentially explosive market. The use of nanoimprint for biological applications brings material selection challenges that are not seen in any of the other applications: the polymers used must often satisfy certain criteria for their permeability to air and water, their UV transparency, and the propensity for certain molecules or cells to adhere to them.

Nanoimprint and contact printing have also been discussed for some time as a potential method of fabricating DNA and protein microarrays at lower cost and higher density than is possible with the current photolithographic or inkjet-spotting methods [141]. There is growing interest in nanowire-based field-effect sensors, in which lithography is usually needed to pattern the nanowires on to the sensor [156].

1.7.9. Surface acoustic wave (SAW) filters

There is an increasing need to reduce below 100 nm the feature sizes of the interdigital transducers that form the cores of these devices. Nanoimprint has been demonstrated for this task [157]. The interdigital array itself is usually a highly regular set of parallel lines, but this array is typically surrounded by electrode regions of substantially different feature sizes and densities. Because of these pattern density variations and the fact that the pattern must be placed on a piezoelectric substrate such as the highly brittle $LiNbO_3$, we would expect the patterning of these devices to present their own distinct challenges.

1.7.10. Solid-state memory: Flash, and newer alternatives

The arrival of nanoimprint has coincided with an acceleration of efforts to devise denser, lower-power and less expensive alternatives to Flash as a non-volatile solid-state memory. Nanoimprint is being used, for example, in the prototyping of resistance RAM [158], and is being proven for use in Flash memory itself [159]. Some radical nanoimprint-based fabrication approaches have been proposed, including

‘Topolithography’ in which a single imprint step would be followed by a stack of thin-film depositions and a polish-back step to create memory arrays [160].

A particularly appealing property of NIL is that multi-level stamps can be used to combine the work of two or more traditional lithographic steps into one imprinting step. This capability could be of enormous benefit in dual damascene processes, whereby a single nanoimprint step could transfer both a via pattern and an interconnect layer to a device. The process could involve the imprinting of a resist followed by timed etching to transfer the multi-level topography to the oxide below [161–163]. Alternatively, a multi-level pattern could be imprinted into a spun-on insulator material that would remain permanently on the chip. Multilevel molds have also been proposed for the fabrication of self-aligned gate–source–drain structures [164].

1.7.11. Logic/microprocessors

Nanoimprint is being investigated vigorously for the manufacture of solid-state memories because the motivation to increase data densities and reduce manufacturing costs is particularly acute. Compared to photolithography, nanoimprint does suffer from relatively high occurrence rates of point-defects, but this is a problem that can be dealt with, to some extent, in solid-state memory manufacture: these devices incorporate a certain amount of redundancy and can be programmed after manufacture to compensate for ‘dead’ memory regions.

Logic and microprocessor manufacturing, meanwhile, is far less defect-tolerant and involves a much wider range of pattern designs than are encountered in solid-state memory. For both these reasons nanoimprint has so far attracted less interest in these applications. If and when the capabilities of nanoimprint improve, we anticipate that interest will grow in using it for logic and microprocessors.

Table 1.1: Applications of nanoimprint lithography and their characteristics.

Application	Most promising variant of NIL, or variant whose use is most widely reported	Characteristic feature size(s); pattern homogeneity	Defect tolerance	Maturity of use
Photonic crystal LEDs	Imprint spun-on layer	100–700 nm; highly uniform	High	Moderate: in production
Other photonic devices	Not yet clear	100–700 nm; more heterogeneous patterns than LEDs	Moderate to high, but critical-dimension tolerances small	In development
Metamaterials	Any (roll-to-roll attractive for large-area materials)	< 500 nm; highly regular	High	In development
Tissue/ membrane engineering	Any (roll-to-roll attractive for large-area materials)	< 1μm; highly regular	High	In development
Hard disk drives: patterned media	UV-curing of droplet-dispensed liquid	~20 nm, with servo regions having features up to a few microns	Fairly high to defects affecting individual bits, but critical dimension tolerances small	In development; preparing for production
Photovoltaics	Roll-to-roll (large area)	10–500 nm; highly homogeneous	High (but tolerance is low to *severe* defects that short electrodes)	In development
Planarization	Not yet clear	Stamp is blank	Very low	Has been tried; limited acceptance
Displays	Not yet clear	As small as several μm	Low to moderate: pixel defects reduce value of displays	In devt; preparing for production
Biomedical micro-and nano-devices	Not clear: *thermal* NIL may allow a wider range of materials to be used, satisfying biocompatibility or optical specifications	Can be highly heterogeneous: features from 10^{-8} m to 10^{-3} m	Fairly high	Still largely experimental
Surface acoustic wave devices	Not yet clear	In many cases < 100 nm	Not clear	In devt; preparing for production
Solid-state memory	Not yet clear, but extensive research data have been published using UV-curing of droplet-dispensed liquid	~50 nm, and reducing; complex patterns	Moderate, but limited according to the amount of redundancy in the circuit design	Embryonic: some results published
Logic/ microprocessors	Step-and-flash: can deliver good multi-layer registration and can cope better with heterogeneous patterns	~50 nm, and reducing; complex patterns that vary greatly from chip to chip	Very low	Not yet ready

1.8. Embossing/imprinting: length-scales of interest

The embossing/imprinting applications described above span at least five orders of magnitude in both lateral feature size and the thickness of the imprinted layer. Figure 1.4 illustrates the regions of the cavity-width/layer-thickness plane that could be occupied by each of the applications discussed. What this diagram does not indicate, however, is how broadly dispersed across the range of possible sizes the features of a particular device will be. For example, although biological micro-/nano-devices have been reported with features in the range 10 nm to several mm, one particular device will not necessarily contain features spanning this full range. As we shall see in the following chapters, what determines the difficulty of embossing or imprinting a given pattern is partly the *range* of feature sizes in the pattern.

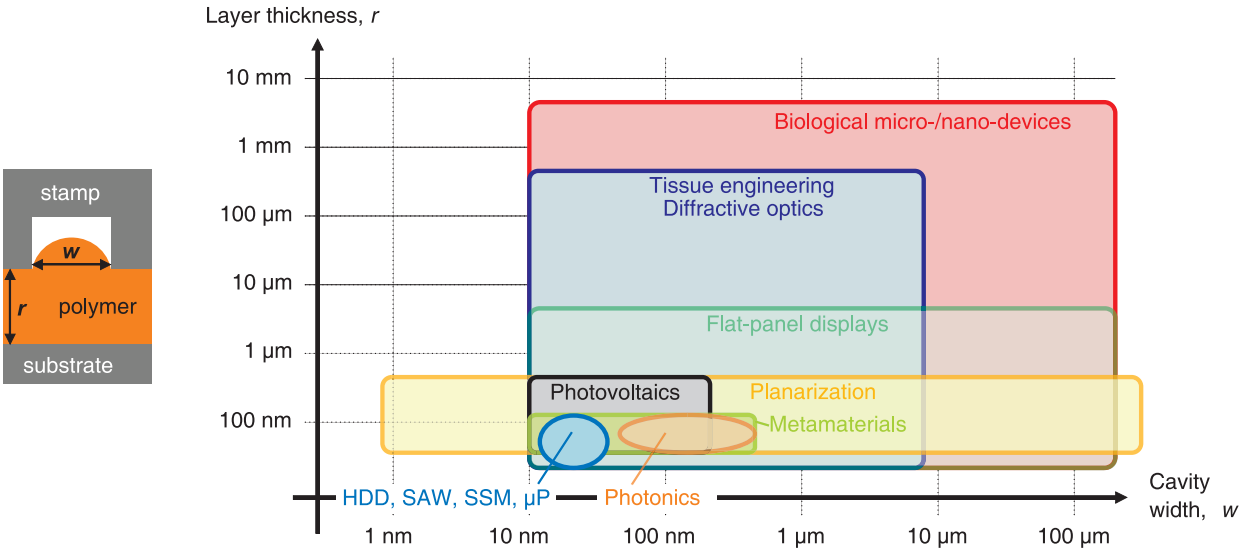

Figure 1.4: Length-scales of interest in micro- and nano-embossing and imprinting. Application areas are plotted in the cavity-width/layer-thickness plane. HDD: hard disk drive; SAW: surface acoustic wave; SSM: solid-state memory; µP: logic/microprocessors.

1.8.1. Observed feature-filling modes

Two distinct modes have been widely observed in the filling of stamp cavities during hot embossing/imprinting [87, 95, 165–169]. In general, when the cavity width w is larger than the layer thickness r, material is initially pushed up from the polymer surface near the edges of the cavity, forming two topographical peaks in the polymer surface. If, on the other hand, w is less than r, material rises with a single peak at the center of the cavity. These two modes can be mapped on the w–r plane as shown in Figure 1.5. Not a single one of the applications that we have discussed lies clearly on one side or other of the dividing line between the two modes. What is needed, therefore, is a modeling method that captures both modes in a unified way.

Topographies resembling the "$w > r$" mode have also been observed by Juang *et al.* under non-isothermal conditions [168] whereby the embossing stamp was heated but the substrate was not. Although r was large in these experiments, the depth of the *softened* layer of polymer was smaller than w. Yao *et al.* find the mode of filling in non-isothermal embossing to depend strongly on the ratio of the processing time to the time taken for heat to diffuse across the polymer beneath the cavity [170]. When the processing time is substantially less than the cross-cavity heat diffusion time, the softened polymer material rises directly up the sidewalls of the stamp protrusion. For processing times much longer than the

heat diffusion time, Yao found that material across the whole cavity was softened and the cavity thus filled much as it would have in the basic isothermal situation. Non-isothermal embossing could have useful applications and it would be valuable to model it.

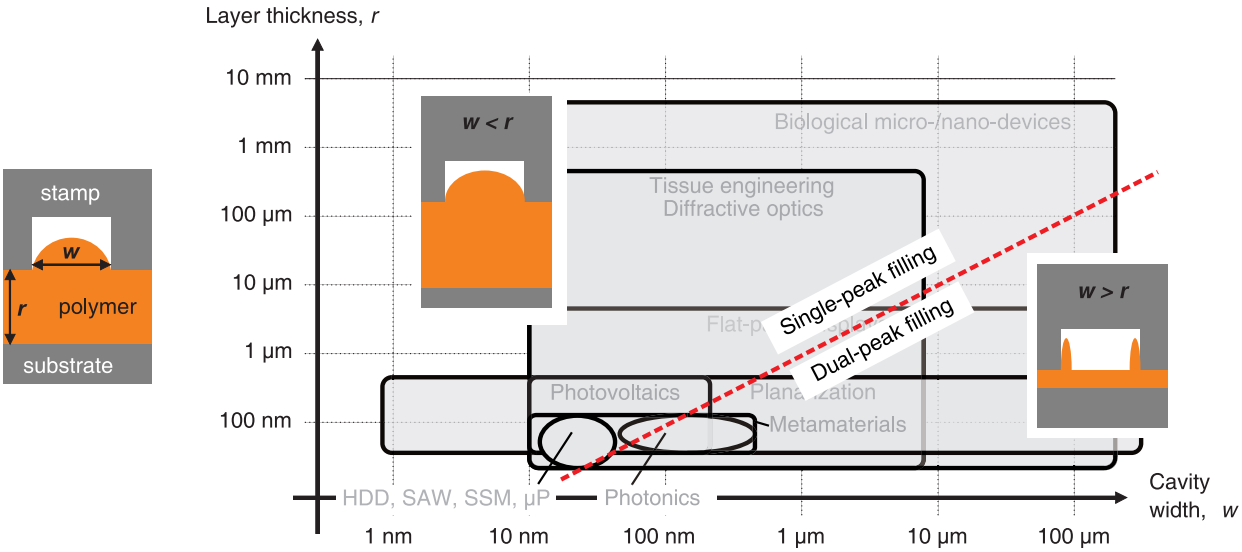

Figure 1.5: Modes of filling in embossing/imprinting.

1.9. The need for embossing/imprinting simulation

As we have seen, a pattern to be hot-embossed or nanoimprinted could contain thousands of features ranging in diameter from a few nanometers to several millimeters. Both in hot micro-embossing and in every variant of nanoimprint, an embossing load–time profile must be selected, usually such that every cavity on the stamp is filled with polymer as required. In thermoplastic processes and those that rely on thermal curing, a temperature–time profile must also be selected. In processes relying on UV-curing, the intensity–time profile of illumination must similarly be chosen.

There are, however, usually constraints on the maximum load, temperature, or illumination intensity that can be applied: these limitations may stem, for example, from the design of the embossing apparatus, the desire to restrict differential thermal contraction of stamp and substrate [37, 39], or the possibility of polymer or substrate degradation at very high temperatures. Moreover, the loading duration is usually constrained by a desire to maximize throughput.

One way to select processing parameters would be through ‘trial-and-error’ experimentation. This approach, though, is prone to being slow and expensive in materials and labor. Moreover, without at least some prior knowledge of the properties of the stamp and layer materials, there can be an increased risk of fracturing the stamp during early experimentation, delaying process-development severely. Lastly, trial-and-error does not guarantee that *optimal* processing parameters will be found: opportunities to reduce processing cycle-time or energy usage might be missed.

Another approach, feasible for simple patterns, would be to derive a set of ‘rules of thumb’ that would recommend processing parameters based on a characteristic size and density of features on the stamp and on the properties of the material being embossed/imprinted. In this way, physical experimentation need not be carried out afresh for each new product design. As the complexity of the pattern to be

embossed/imprinted increases, though, simple ‘rules of thumb’ are less able to provide guidance and may fail to predict locations of incomplete cavity filling.

What appears to be needed, therefore, is a way of simulating the embossing/imprinting of feature-rich patterns. Apart from verifying the extent of cavity filling, there are several other outputs that embossing/imprinting simulations would ideally be able to provide.

- In nanoimprint, engineers need to know that the processing parameters they have chosen will not result in an unacceptably thick or non-uniform residual layer.
- In thermoplastic micro-embossing, lateral stamp–polymer contact forces arise from the differential thermal contraction of stamp and substrate during cooling. These stresses can lead to fracture of the stamp and/or permanent distortion of the embossed features. It would be useful to be able to simulate whether fracture or distortion is likely to occur for a given stamp design and processing parameters. Such simulations could aid ‘demolding-friendly’ design of the stamp and the selection of appropriate stamp materials and processing parameters.
- In nanoimprint, the challenge of stamp removal lies not in the risk of stamp fracture but in the possibility of delaminating certain resist features from the substrate. It would be useful to be able to identify the likely locations of any such ‘pull-out’ defects, so that patterns could be redesigned to reduce the probability of these defects.

Not only can simulation be used to guide process parameter selection; it can be used to help refine the design itself. In Section 1.12 we will discuss these different possibilities. Since the arguments for simulation grow stronger as embossed/imprinted patterns become more complex, we expect the contributions of this thesis to be most valuable in the design of biomedical micro-/nano-devices, solid-state memories, logic, and microprocessors.

1.10. Modeling priorities

Figure 1.6 summarizes the factors known to influence the topographies of embossed patterns. A huge amount of experimentation has been reported addressing each of the factors, but it is recognized that there is not yet a unified approach to characterizing and modeling all of these sources of nonuniformity together. Cross [54] says that ‘an understanding of global printing mechanics’ is needed, and believes that ‘coupling between local flow uniformity, die roughness and die compliance over many decades will require approximate or statistical methods’. Meanwhile, Mendels [171] discusses the need for a unified model of wafer-, cavity- and surface-scale effects in NIL.

We believe that the most urgent need lies in modeling feature-scale and pattern-density effects: there is not yet a practical and accurate way of simulating the embossing of feature-rich patterns into a viscoelastic substrate. Such a capability would provide process engineers with a way of choosing an appropriate embossing temperature, pressure and loading duration for a given stamp design. It could also allow device designers to optimize their stamp designs, improving embossing fidelity or even reducing the required embossing pressure, temperature or loading time. We envisage helping designers to decide how uniformly features should be distributed across a stamp, and whether very large or very small embossed features should be redesigned in order to improve embossing fidelity. Non-uniformity at the substrate scale is also important and we would ideally provide a way of integrating it with pattern-level modeling.

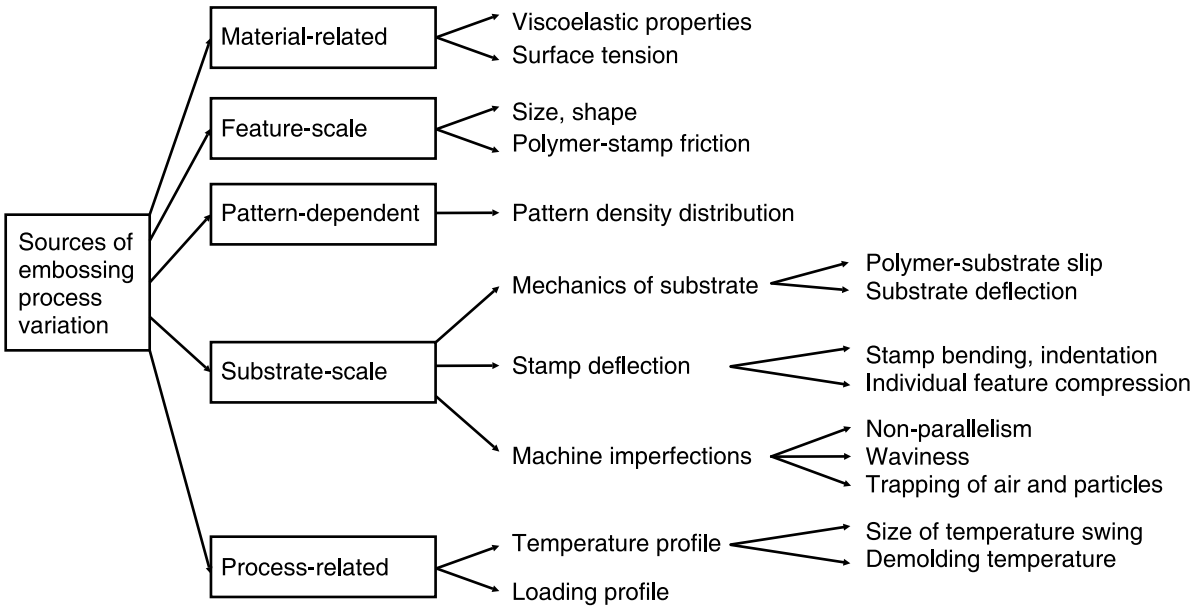

Figure 1.6: Factors contributing to topographical variation in thermoplastic micro- and nano-embossing.

1.11. Existing simulation approaches

There is a large body of experimental work in the literature that describes pattern dependencies in thermoplastic micro-embossing and in nanoimprint. Much of this work makes an attempt to explain the observed phenomena through numerical simulation. The simulations reported are generally for a single feature and assume plane-strain geometry. There have been far fewer attempts to simulate the embossing of feature-rich patterns.

1.11.1. Spun-on resist layers: finite-element approaches

There have been several attempts to describe thermoplastic micro-embossing and nanoimprint through the finite-element modeling of very simple geometries [165, 167, 172–182]. The embossed material layer has variously been described as a Newtonian liquid [165, 169, 172, 177], as a shear-thinning liquid [165, 167], as linear-elastic [176], with a Mooney-Rivlin rubber-elastic model [174, 178], with a Johnson-Cook strain-hardening model [61], and with linear [173, 175] and non-linear [179, 180] viscoelastic models. More comprehensive, thermomechanically-coupled, finite-deformation material models have also been developed (*e.g.* [181, 182]) and applied to simulate the microembossing of bulk polymeric substrates [182].

Surface tension effects have generally been regarded as negligible in the simulation of thermoplastic NIL and micro-embossing, where the polymer's viscosity during imprinting is usually at least 10^3 Pa.s and bulk forces are considered to dominate over surface forces. Indeed, of the feature-scale, thermal NIL simulation work surveyed, only the work of Jeong accounts for capillary force effects [169].

1.11.2. SFIL: solution of Navier-Stokes equations

For step-and-flash imprint, meanwhile, the viscosity of the uncured resist is typically much lower (~ 1 mPa.s) than in thermal NIL, and capillary effects are of crucial importance. There has been extensive work to model the merging and pinning of liquid resist droplets as they are squeezed beneath the imprint stamp [99, 101, 102]. These simulations solve the Navier-Stokes equations under an assumption that fluid motion is constrained to be parallel to the plane of the substrate.

There have been efforts to model the relationships between geometry and resist–stamp contact angle under which gas becomes parasitically trapped in a stamp cavity during the spreading of resist. Both Daisuke [103] and Reddy [104] found independently, through simulation, that gas became more likely to be trapped in part of a cavity as a fluid front advanced across it when any of the following increased: (*i*) the ratio of cavity height to residual layer thickness; (*ii*) the ratio of cavity width to residual layer thickness; (*iii*) the stamp–resist contact angle. Droplet-merging and cavity-filling simulations at the die-scale are still prohibitively slow, however, and there certainly appears to be a need for a faster simulation capability in this area.

There has also been work to model the dissolution of trapped gas pockets: some work suggests that in typical imprint processes air bubbles can take over ten seconds to dissolve [99], potentially limiting the throughput of the process, while others believe that it is possible to engineer an imprint system in which dissolution is so quick as to be unimportant [100].

Finite-element approaches and detailed solutions of the Navier-Stokes equations certainly capture many of the physical phenomena observed in micro-embossing and in nanoimprint. They are currently too computationally costly, though, to extend to the feature-rich patterns of complete devices.

1.11.3. 'Coarse-grain' approaches

For the simulation of thermal nanoimprint lithography, Zaitsev *et al.* have proposed a simplified 'coarse-grain' approach in which the imprinted polymeric layer is modeled as a Newtonian fluid and the pattern of the stamp is represented by a matrix of cells, each assumed to contain features of a single size and packing density [89, 183–186]. The solution procedure assumes an elastic model for the deflections of the stamp and the substrate and confines motion of the Newtonian resist to being parallel to the plane of the substrate. Simplified Navier-Stokes equations are solved assuming a constant stamp velocity. Simulation durations are reported to be in the region of 20 minutes for a 128-square grid of cells [187]. To produce a simulation tool that could be used iteratively in the design process — with simulations perhaps needing to be run by an engineer several times each day — a further substantial increase in simulation speed would be beneficial.

1.11.4. Contact mechanics-based approaches

Efficient numerical simulations of the deformations of elastic [188, 189] and elastic-plastic [190–192] bodies — which are sometimes rough and/or multi-layered [188, 191, 192] — have been widely used by researchers in tribology. These simulations rely on a description of the deformation of the material's surface in response to a point-load, together with, in the elastic-plastic cases, a criterion for yielding of the material. The overall topography of the material's surface is calculated by spatially convolving an iteratively-found contact pressure distribution with the point-load response. Sub-surface stresses can similarly be estimated by convolving contact pressures with the appropriate kernel functions [189]. The convolution itself may be effected using fast Fourier transforms [188, 190, 191] or other summation methods [193, 194]. The solution for the contact-pressure distribution has successfully been performed with iterative conjugate-gradient methods combined with kinematic constraints on the surface deformation [188, 190, 193], or with methods that seek a minimum of elastic potential energy in the layer [191].

The validity of these contact mechanics-based approaches is limited to cases where surface curvatures remain small and all deflections are a small proportion of any layer's thickness. These linear methods have nevertheless proved to be of great value because of their fast computation. Lei *et al*. suggest using such an approach to represent the micro-embossing of thick, rubbery polymeric layers [195]. They develop an approximate analytical expression for the shape of the deformed surface of such a layer when embossed with a simple trench, and show rough agreement between their expression and the measured topography of polymethylmethacrylate layers embossed under a small set of processing conditions.

1.12. How simulation could fit into the design flow

It is important to be clear how we envisage an embossing/imprinting simulation capability being used to design products: the intended frequency of use of any simulation method determines how quickly it will need to run. We consider two cases: the use of nanoimprint in semiconductor manufacturing, and the use of bulk microembossing for making labs-on-chip.

1.12.1. Nanoimprint for semiconductor manufacturing

We draw inspiration from existing design-for-manufacture practices in the semiconductor industry. Integrated circuit layout designers regularly use software to check that the mask designs they have produced are amenable to manufacturing. Because semiconductor manufacturing process parameters are generally fixed for a given fabrication facility, it is the chip design that must conform to certain requirements in order to ensure manufacturability. It is usual for these requirements to be encoded in a set of geometrical *design rules*. Common rules include maximum and minimum feature sizes and separations, pattern-density bounds, and the prohibition of non-orthogonal lines. These rules are motivated, for example, by the resolution limitations of photolithography, the properties of dielectric and metal polishing apparatus, and a need to limit the rate of electromigration of interconnect metal. The rules are enforced by design-rule checking software, which takes a layout and identifies any parts of it that do not conform to the specified rules. The layout designer is then required to correct the design and re-run the check.

Most chip designs are built in a highly hierarchical way, with simple layout 'cells' being re-used many times in the synthesis of 'blocks', which are then assembled to form a chip. Design rule checks are run at each level of the hierarchy; while checks at the cell level might take only a few seconds to run and could be performed many times while refining the design of new cells, a design-rule check at the chip level could reasonably be expected to take more than a day, and is usually done when the design is complete and before the chip is sent to be manufactured. Since design-rule violations are sometimes introduced when cells or blocks are brought together to construct whole chips, it is not uncommon for cell-, block-, and chip-level design-rule checks all to identify errors.

Some makers of design-for-manufacture software are arguing that, with reducing feature sizes, rule-based design checking is reaching the end of its useful life, and will need to be augmented or replaced by *model-based* checking which incorporates an element of physical simulation into the checking procedure. Naturally the speed of execution of these models needs to be great enough that they can be used conveniently, and without extending development times.

Another important part of the current design-for-manufacture flow is *optical proximity correction* (OPC), in which a mask design is systematically modified by automatic software to pre-correct for the diffraction that will occur during the image-projection step of photolithography. This correction step is highly computationally intensive and requires dedicated processor farms. Increasingly, the makers of optical proximity correction tools are trying to find ways to integrate their computational methods with

the layout design process. The aim of integration is to help designers produce designs that are as area-efficient as possible in spite of the limitations imposed by diffraction.

The above description of the status quo suggests several stages at which *nanoimprint* simulation might be used in a semiconductor design process. Simulation could be used:

- At the very end of the design process, when the layout has been fixed, to select appropriate nanoimprint process parameters. It is likely, though, that the process parameters will be fixed for a given fabrication facility, so that the *design* will need to conform to certain specifications;
- Between stamp design and fabrication, as part of an automatic software tool that would systematically modify the shapes of individual stamp features. Any modifications would aim to make the design more amenable to replication with NIL. This procedure would be equivalent to OPC for photolithography;
- At the chip-level, at the very end of the design process, to provide model-based checking of manufacturability. The software would highlight any locations on the chip that would be defect-prone during imprinting. At this stage, if problems were found, manual layout changes by engineers would still be possible;
- At the cell- or block-level, to provide model-based design checking as an integral part of the design process. It would be normal for the design check to be run several times — even, perhaps, five or ten times in a day — as a designer refined their layout;
- To create a set of nanoimprint-aware 'design-rules' that would be incorporated into existing design-rule checks.

These possible modes of use suggest that there may well be a need to run cell- or block-level design checks (containing hundreds to millions of features) within a fraction of a working day. Engineers working on a specific layout block cannot necessarily command the use of a processor farm to make these frequent design checks, and might well need to be able to run the checks using their own workstations.

1.12.2. Bulk microembossing for biomedical micro-/nano-devices

The business of designing and producing biomedical micro-/nano-devices is far less mature than the semiconductor industry, and there is no existing infrastructure of design-for-manufacture software in this field. Any embossing simulation capability for biomedical devices would therefore need to stand alone. The key inputs to an embossing simulation are likely to be (*i*) an electronic drawing of the device layout (*e.g.* in DXF format), (*ii*) a mechanical model of the material being embossed, and (*iii*) a set of processing parameters (*e.g.* temperature–time and pressure–time profiles).

Biomedical device designs are *not* necessarily constructed from a series of re-usable standard 'cell' designs, as semiconductors are. A simulation tool might therefore need to interpret mask designs containing many thousands of features at a single level of layout hierarchy.

Our approach aims to enable engineers to refine their selection of processing parameters based upon successive simulations of the embossing process. It could also help device designers to improve the *designs* of embossed patterns — for example, by enlarging some of the smallest cavities on a stamp to ensure their complete penetration by the polymeric material.

Since process simulation is not widely used today in developing biomedical microdevices, there is no clear benchmark for the speed at which a simulation should run. Our ultimate measures of success are whether the simulation approach offers a faster or less expensive way than practical experimentation for selecting effective embossing parameters and refining the pattern design.

1.13. Structure of thesis

The remainder of this thesis has the following structure. Chapter 2 presents a computationally inexpensive way of simulating the thermoplastic embossing of relatively thick layers, at the scale of multiple individual features. Chapter 4 extends this method to represent the embossing of very feature-rich patterns in a simplified way. Chapter 5 investigates the impact of the presence of trapped air inside stamp cavities during bulk thermoplastic embossing. Chapter 6 develops the feature-scale modeling approach for the micron-scale embossing of *finite*-thickness thermoplastic layers, and Chapter 7 proposes a complete approach to simulating the nanoimprinting of complex patterns into spun-on thermoplastic layers.

2. Modeling bulk micro-embossing

In this chapter, we are concerned with polymeric layers that are substantially thicker than the dimensions of the features being embossed and whose average molecular weight is high enough that at typical embossing temperatures the material is ‘rubbery’ in behavior [196].

2.1. Theory and modeling method

2.1.1. Defining the material’s point load–time response

We begin by adopting a Kelvin-Voigt linear viscoelastic model (Figure 2.1a) for the embossed polymeric layer. This model encapsulates the idea that, upon loading, the polymer network of the material deforms over time, approaching a limiting configuration that is imposed by physical entanglements of the polymer chains. This limiting configuration is described by an elastic modulus, E, while a viscosity, η, represents intermolecular resistance to flow. Both the viscosity and the elastic modulus of this model are decreasing functions of temperature, T, with the viscosity falling by several orders of magnitude in the vicinity of the glass-transition temperature, T_g. The use of this model is inspired by the observation that at typical hot-embossing temperatures, amorphous polymers such as PMMA may be ‘rubbery’ in consistency [182]. In reality, there is a possibility for slipping of the polymer chain entanglements, but this possibility is neglected in the present model.

It is known that in reality bulk amorphous polymers exhibit a highly *non*-linear strain-rate dependence. What makes our present approximation of linearity workable is that in hot embossing the average strain rate of the polymer is very low — on the order of 10^{-4}/s to 10^{-3}/s for a 1 mm-thick sheet compressed by several tens of microns over the course of a few minutes. In this strain-rate range, the sensitivity of an amorphous polymer’s behavior to strain rate is usually much smaller than at larger strain rates.

There will certainly be substantially faster strain rates than 10^{-3}/s near the edges of each microscopic feature being embossed, but we suppose these high rates to exist in only a very small proportion of the volume of the material, meaning that a linear model built assuming strain rates in the 10^{-4}/s to 10^{-3}/s range should enable a reasonable approximation to the overall topographies produced by hot embossing.

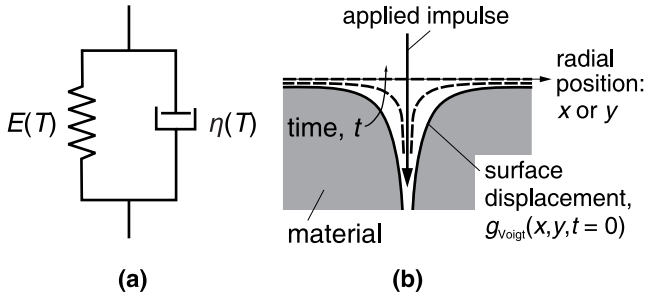

Figure 2.1: (a) Kelvin-Voigt model. (b) Response of such a material to an impulse applied normally to the surface at ($x = 0, y = 0$) and at time $t = 0$.

We consider a polymeric layer whose surface initially lies in the x–y plane ($z = 0$) and whose thickness in comparison with the dimensions of the pattern being embossed is sufficiently large that the layer may be regarded as infinitely thick. We consider the application, from time $t = 0$ to ∞, of a constant unit compressive load normal to the surface of the material at the point ($x = 0$, $y = 0$). Supposing that the material is linear viscoelastic, assuming that curvatures of the material's surface remain small, and neglecting inertial effects in the material, the stress distribution in the material remains essentially unchanged with time and does not depend on the relative magnitudes of elasticity and viscosity. The shape of the deformed surface therefore simply scales over time, beginning as a flat surface at $t = 0$, and approaching, for $t = \infty$, a topography determined only by the material's elasticity. Adapting a standard result for a point-loaded linear-*elastic* half-space [189], the response of the surface positions of a Kelvin-Voigt layer is therefore:

$$s_{Voigt}(x, y, t) = \frac{-(1-\nu^2)\left[1-\exp\left(\frac{-Et}{\eta}\right)\right]}{\pi E\sqrt{x^2+y^2}} \tag{2.1}$$

where ν is Poisson's ratio, and displacements are defined as negative downwards into the layer. Embossing is assumed to occur at a constant temperature, so that E, ν and η are fixed while the topography is evolving. Via differentiation of (2.1) with respect to time, it follows that the impulse, or 'point-load–time', response of the material layer (Figure 2.1b) is:

$$g_{Voigt}(x, y, t) = \frac{-(1-\nu^2)\exp\left(\frac{-Et}{\eta}\right)}{\pi\eta\sqrt{x^2+y^2}}. \tag{2.2}$$

This analysis assumes deflections of the surface to be small in comparison with the thickness of the layer, and neglects any tractions applied parallel to the layer. Any capillary forces at the stamp-polymer interface are also neglected, because stresses in the bulk of the material are considered to dominate strongly.

We can now describe the topography, $w(x, y, t)$, of an embossed viscoelastic layer as the convolution of the evolving contact pressure distribution $p(x, y, t)$ with the point-load–time response, as follows:

$$w(x, y, t) = \frac{-(1-\nu^2)}{\pi\eta}\int_0^t\int_{-\infty}^{\infty}\int_{-\infty}^{\infty}\frac{p(x', y', t')\exp\left(\frac{-E}{\eta}(t-t')\right)}{\sqrt{(x-x')^2+(y-y')^2}}\,\mathrm{d}x'\mathrm{d}y'\mathrm{d}t'. \tag{2.3}$$

The topography, w, is defined as negative down into the material, and the contact pressures, p, as positive compressive. In hot-embossing, we assume the topography to be 'frozen' in place by subsequent cooling of the material while still under load. Since the material remains solid throughout the embossing cycle, any surface-tension forces between the stamp and the embossed layer are neglected. The thermal expansivities of the stamp and embossed layer are also neglected: for typical temperature swings encountered during embossing, a polymer's thermal expansion and contraction are on the order of only 1%. The stamp, meanwhile, is assumed to be rigid. Common stamp materials are silicon or nickel, with Young's moduli above 100 GPa. In comparison with even the room-temperature elastic moduli of thermoplastic polymers — a few GPa — stamp materials are well modeled as rigid.

The description of the material's response to a point load, and the use of superposition to build a simulation of an embossed topography, assume that material deflections are 'small'. While deflections are indeed small compared with the thicknesses of the embossed substrates (10–50 μm embossed depths are typical, while substrates are usually ~ 1 mm in thickness), the local *curvatures* of hot-embossed surfaces are rarely small at all, with sharp edges often being introduced. The assumption of small deflections is

therefore imperfect; it is made to enable fast computation and its validity needs to be checked, as we do in this chapter by comparison with experimental results.

Various methods might be used to calculate the stamp–polymer contact pressure distribution and thereby evaluate the embossed topography. Since the complex designs of embossing stamps are likely to be difficult to describe using continuous functions, we expect discrete, numerical solution approaches to be the more appropriate. The embossing process might be broken into a series of time-slices, and the evolving pressure distribution and topography found for each slice. In this way, as cavities in an embossing stamp begin to be filled with the polymer, the portion of the stamp in contact with the polymer could be tracked. Next, however, we show that a correct evaluation of the final embossed topography can in fact be made *without* resorting to time-slicing.

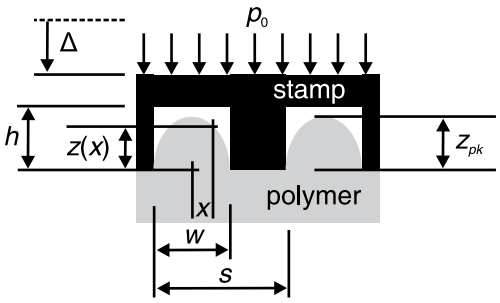

Figure 2.2: Cavity nomenclature, including stamp displacement Δ and peak cavity penetration z_{pk}.

2.1.2. The use of a scaled contact-pressure spatial-average

We now define a new pressure variable, $p_s(x, y, t_h)$, which is an exponentially-weighted average of the true pressure distributions over the whole loading duration, the time period 0 to t_h:

$$p_s(x,y,t_h) = \frac{E}{\eta}\int_0^{t_h} p(x,y,t')\exp\left(\frac{-E}{\eta}(t_h - t')\right)\mathrm{d}t' \cdot \tag{2.4}$$

Suppose that the spatial average of the applied pressure $p(x, y, t)$ is known, as a function $p_0(t)$, and that the pattern being embossed is spatially periodic with period D in both x and y. By integrating (2.4) over a whole spatial period in x and y, we see that the spatial average, $p_{s,0}(t_h)$, of $p_s(x, y, t_h)$ is

$$p_{s,0}(t_h) = \frac{E}{\eta}\int_0^{t_h}\frac{1}{D^2}\int_0^D\int_0^D p(x,y,t')\mathrm{d}x\mathrm{d}y\exp\left(\frac{-E}{\eta}(t_h - t')\right)\mathrm{d}t' = \frac{E}{\eta}\int_0^{t_h} p_0(t')\exp\left(\frac{-E}{\eta}(t_h - t')\right)\mathrm{d}t' \cdot \tag{2.5}$$

Re-writing (2.3) in terms of $p_s(x, y, t_h)$, we have:

$$w(x,y,t_h) = \frac{-(1-\nu^2)}{\pi E}\int_{-\infty}^{\infty}\int_{-\infty}^{\infty}\frac{p_s(x,y,t_h)}{\sqrt{(x-x')^2+(y-y')^2}}\mathrm{d}x'\mathrm{d}y' \cdot \tag{2.6}$$

We note that (2.6) also describes the topography of a simple linear-*elastic* layer with a Young's modulus E and exposed *instantaneously* to the pressure distribution $p_s(x, y, t_h)$ having the spatial average defined in (2.5). We can therefore very quickly simulate the topography of the viscoelastic layer at time t_h by performing a simulation for an *elastic* layer subjected to an appropriately scaled spatial pressure average $p_{s,0}(t_h)$. This equivalence is illustrated in Figure 2.3.

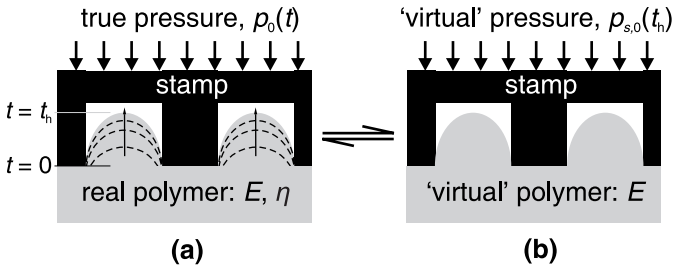

Figure 2.3: Equivalence between the 'real' viscoelastic case (a) and a 'virtual' equivalent simulation performed for a modified stamp-average pressure $p_{s,0}$ and a purely elastic substrate (b). The final substrate topographies in each case are the same.

In many embossing processes the applied spatial pressure average p_0 is constant for the duration, t_h, of the embossing period. In these cases we can simplify (2.5) to

$$p_{s,0}(t_h) = p_0\left[1-\exp\left(\frac{-t_h E}{\eta}\right)\right]. \tag{2.7}$$

In such a situation, we can perform the equivalent simulation by assuming the elastic layer to have an elastic modulus E and the pressure distribution to have a spatial average of $p_0[1-\exp(-t_h E/\eta)]$, where t_h is the loading duration. Equally, we could perform a simulation with an elastic modulus of $E/[1-\exp(-t_h E/\eta)]$ and an applied pressure distribution with spatial average p_0.

It is perhaps intuitively obvious that the use of a scaled Young's modulus or pressure average can provide a correct solution for topography when the contact pressure distribution does not change over time. What we have demonstrated above is that the use of this scaling procedure is valid even when the pressure distribution *does* change over time — as, for example, happens when a stamp cavity begins to be filled with polymer. A similar argument is presented by Lee and Radok for the simple case of a smooth rigid sphere indenting a viscoelastic half-space [197].

2.1.3. Computational approach

To enable a numerical solution for embossed topographies, we now discretize our spatial representation of the embossing stamp and embossed substrate. We discretize the stamp and substrate surfaces on a square grid having pitch d in the x and y directions. We model stamp–substrate contact pressures as being uniform within each element of this square grid, and take the displacement at the center of each element of the grid to represent that throughout the element. In this work we use 'element' to mean a region represented by a single number in a discretized map of pressure or topography; the word does not have the meaning that is usually understood when describing the finite element method.

We adopt the simulation scheme described in the previous section, in which the topography at time t_h is computed by simulating a 'virtual', purely elastic layer of Young's modulus E, statically loaded with a virtual pressure distribution $p_s[m, n]$ (compressive positive) having an appropriate spatial average that is a function of the material properties, the loading time and the true spatial average of the contact pressure.

The 'point-load' response of the purely elastic, virtual substrate adopted for the simulation is defined as the surface's response to unit pressure applied uniformly over the element [0, 0]. The displacement (negative into the substrate) at the center of each element of the surface [m, n], where $x = md$ and $y = nd$, is then:

$$g[m,n] = -\frac{1-\nu^2}{\pi E}\left[f(x_2,y_2) - f(x_1,y_2) - f(x_2,y_1) + f(x_1,y_1)\right]$$

where

$$f(x,y) = y\ln\left(x+\sqrt{x^2+y^2}\right) + x\ln\left(y+\sqrt{x^2+y^2}\right) \qquad (2.8)$$

and

$$x_1 = md - d/2;\ \ x_2 = md + d/2;\ \ y_1 = nd - d/2;\ \ y_2 = nd + d/2.$$

Equations (2.8) above provide a way to make approximate simulations of the embossing of three-dimensional substrates by representing surface deflections in a 2-D matrix (Figure 2.4a). There may also be situations in which we wish to represent the embossing of a prismatic pattern. In such cases a plane-strain representation of the embossed substrate is more efficient, and we would represent surface deflections with a 1-D vector (Figure 2.4b). The response of the viscoelastic surface to unit pressure, applied over the infinitely long, *d*-wide strip of substrate at $m = 0$, would be [189]:

$$g[m] = -\frac{1-\nu^2}{\pi E}\left[d\left(m+\frac{1}{2}\right)\ln(2m+1)^2 - d\left(m-\frac{1}{2}\right)\ln(2m-1)^2 + const.\right]\cdot \qquad (2.9)$$

It has been found experimentally that PMMA is essentially incompressible above its glass-transition temperature [182]. We therefore assume in this work that Poisson's ratio of any embossed layer equals 0.5. The values of $g[m, n]$ or $g[m]$ are therefore shifted by a constant so that each filter's mean value is zero.

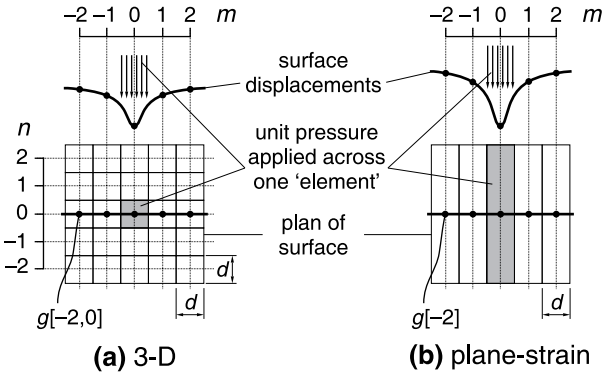

Figure 2.4: Discrete representations of the point-load responses of elastic layers. In the three-dimensional case (a), unit pressure is considered to be applied in the central $d \times d$ region of the surface, and values of surface deformation $g[m, n]$ are defined at the center of each region. In the plane-strain case (b), unit pressure is considered to be applied to a *d*-wide strip of infinite out-of-plane extent.

We assume that the pressure distribution applied to the substrate is periodic in space: in both *x* and *y* (*m* and *n*) if we are modeling 3-D embossing, and in *x* (*m*) if modeling plane-strain embossing. We also assume that the embossed substrate is infinite in lateral extent. These are realistic approximations for the many embossing processes in which a wafer-sized substrate is embossed using a stamp that is 'tiled' with many copies of a device to be manufactured. If the true stamp pattern is not spatially periodic, we can 'pad' our representation of the stamp with zero-contact-pressure regions at the edges, such that our assumption of periodicity does not affect simulation results.

Our assumption of periodicity makes it simple to evaluate the convolution of pressure with the impulse response using discrete Fourier transforms. We assume a period of M elements in the m direction and, in the case of a 3-D representation, N elements in the n direction. The following equations may be written to describe the discrete convolution:

$$\left.\begin{aligned} G[m',n'] &= \sum_{m=0}^{M-1}\exp\left(\frac{-2\pi j m m'}{M}\right)\sum_{n=0}^{N-1}\exp\left(\frac{-2\pi j n n'}{N}\right)g[m,n] \\ P[m',n'] &= \sum_{m=0}^{M-1}\exp\left(\frac{-2\pi j m m'}{M}\right)\sum_{n=0}^{N-1}\exp\left(\frac{-2\pi j n n'}{N}\right)p_s[m,n] \\ w[m,n] &= \frac{1}{MN}\sum_{m'=0}^{M-1}\exp\left(\frac{2\pi j m m'}{M}\right)\sum_{n'=0}^{N-1}\exp\left(\frac{2\pi j n n'}{N}\right)P_s[m',n']\,G[m',n'] \end{aligned}\right\} \quad (2.10)$$

where m' and n' are coordinates in the spatial frequency plane, $p_s[m, n]$ is the 'virtual' applied pressure distribution whose spatial average is as described in (2.5), and $w[m, n]$ is the true resulting topography.

This convolution procedure is implemented using fast Fourier transforms (FFTs) and is used in an algorithm to find the values of $p_s[m, n]$ and $w[m, n]$ that are consistent with the substrate's viscoelastic properties and the application of a known spatial-average pressure to the back of the rigid stamp having topography $w_{\text{stamp}}[m, n]$. The algorithm is based on that of Xie [198], and is described below.

1. An initial guess is made for the set of stamp elements, C, in contact with the substrate. Usually the portion of the stamp in which $w_{\text{stamp}}[m, n]$ takes its minimum value is considered to be initially in contact with the substrate.

2. Next, a contact pressure distribution $p_s[m, n]$ is found that satisfies equilibrium with the known applied average pressure, $p_{s,0}(t_h)$, and that is consistent with the stamp remaining rigid while the polymer deforms. $p_s[m, n]$ is taken to be zero for all $[m, n]$ outside the assumed stamp–substrate contact region C. To find $p_s[m, n]$, steps (a) to (c) below are used:

   (a) A set of pressures $p_f[m, n]$ is found that would be required to deform the substrate into the shape $w_{\text{stamp}}[m, n]$ *within* the contact region. The shape adopted by the substrate outside the contact region is constrained only by the mechanical response of the substrate. A stabilized biconjugate gradient method [199] is used, together with the convolution procedure (denoted by *) of (2.10):

$$\left.\begin{aligned} w_f[m,n] &= p_f[m,n] * g[m,n] \\ p_f[m,n] &= 0 \quad \forall \quad (m,n) \notin C \\ w_f[m,n] &= w_{stamp}[m,n] \quad \forall \quad (m,n) \in C \end{aligned}\right\} \quad (2.11)$$

   (b) A set of pressures $p_e[m, n]$ is found that is consistent with *unit* displacement of every element of C:

$$\left.\begin{aligned} w_e[m,n] &= p_e[m,n] * g[m,n] \\ p_e[m,n] &= 0 \quad \forall \quad (m,n) \notin C \\ w_e[m,n] &= 1 \quad \forall \quad (m,n) \in C \end{aligned}\right\} \quad (2.12)$$

(c) The estimate of $p_s[m, n]$ is then found as the superposition of $p_f[m, n]$ and whatever multiple, Δ, of $-p_e[m, n]$ makes the spatial average of $p_s[m, n]$ equal that calculated in (2.5):

$$\left.\begin{aligned} p_s[m,n] &= p_f[m,n] - \Delta p_e[m,n] \\ \frac{1}{MN}\sum_{m=1}^{M}\sum_{n=1}^{N} p_s[m,n] &= p_{s,0}(t_h) \end{aligned}\right\} \qquad (2.13)$$

The estimate of $w[m, n]$ is then $p_s[m, n] * g[m, n]$. Δ is the rigid-body displacement of the stamp, defined positive-downwards into the material.

3. A refined estimate is made of the parts of the stamp in contact with the polymer. Cells are added to the contact set C where $w[m, n] > w_{stamp}[m, n] - \Delta$: substrate material cannot penetrate stamp material. Cells are removed from C where $p_s[m, n] < 0$: the stamp is assumed not to stick to the substrate. It is further assumed that embossing is performed in a vacuum, or, alternatively, that any air trapped in stamp cavities during embossing readily diffuses into the polymer and so does not impede filling of the cavity by the polymer. Regions of the substrate that do not belong to C, therefore, are assumed to experience no pressure at their surface.
4. Step 2 is then repeated with the refined estimate of the contents of set C, until either the contact set estimate is unchanged with a new iteration, or a pre-defined maximum number of iterations is reached.

The key to the method's speed is that Step 2 above involves solving sets of *linear* equations; the non-linearity involved in establishing the true contents of the contact set C is kept within Step 3, which does not involve the solution of any sets of equations, but rather the straightforward addition and removal of elements of C. The method is implemented in the Matlab language (The Mathworks, Natick, MA) [199].

2.1.4. Time-stepped numerical verification of the 'virtual'-pressure simulation approach

The method described above relies on the observation that the embossing of a viscoelastic layer can be represented using a 'static', or 'virtual', simulation in which the polymeric layer is modeled as purely elastic and the spatial average of the applied pressure is a function (2.5) of the true spatial-average pressure applied, the true elasticity and viscosity of the material, and the loading duration. The derivation given in Section 2.1.2 indicates that the topography predicted by such a static simulation is exactly equivalent to that implied by the full viscoelastic model, even when the portion of the stamp in contact with the substrate evolves over time. This equivalence is now verified by comparing the output of a series of 'static' simulations, each representing a different loading duration, with that of a time-stepped simulation that explicitly describes the developing surface profile of the polymer. The geometry simulated in this verification is a rectangular trench in plane-strain.

For the time-stepped approach, the simulation proceeds as follows:

1. Initially, the polymer's surface is flat, and the region of the stamp in contact with the substrate is that for which the topography of the stamp takes its minimum value.
2. A contact pressure distribution is found that is consistent with deforming just the *elastic* part of the Kelvin-Voigt model into the current topography of the polymer surface within the contact region.
3. The spatial-average of the pressure distribution found in 2 is subtracted from the spatial-average of the total embossing pressure applied to the stamp: the difference is the average pressure available for driving viscous flow of the polymer.

4. A contact pressure distribution is found that is consistent with moving the stamp down into the polymeric layer at unit velocity. (Since the stamp is rigid and cannot rotate, every part of it must move at the same velocity.) The point-load-time response function used here represents the behavior of the viscous part of the material only, and is equal to the point-load response of the elastic part scaled by E/η.
5. The actual stamp velocity is calculated by dividing the average pressure available for flow, found in 3, by the average pressure needed for unit stamp velocity, found in 4.
6. For the current time-step, of length Δt, the distance moved by the stamp is the velocity found in step 5 multiplied by Δt.
7. The topography is updated by adding the time-step's incremental change of topography to the current topography. The incremental change of topography is the pressure distribution found in 4, convolved with the point-load-time response of the viscous part of the polymer, and multiplied by the ratio calculated in 5.
8. If the updated topography intersects with the stamp, the elements of intersection are added to the stamp–substrate contact region.
9. Step 2 is returned to, unless the specified duration of the simulation has been reached, in which case the simulation ends.

The results of the time-stepped and equivalent 'static' simulations are compared in Figure 2.5: the two approaches yield indistinguishable results both for topography and for rigid-body stamp displacement, and the relationship between $p(x, y, t)$ and $p_s(x, y, t)$ is shown to be as defined in (2.4).

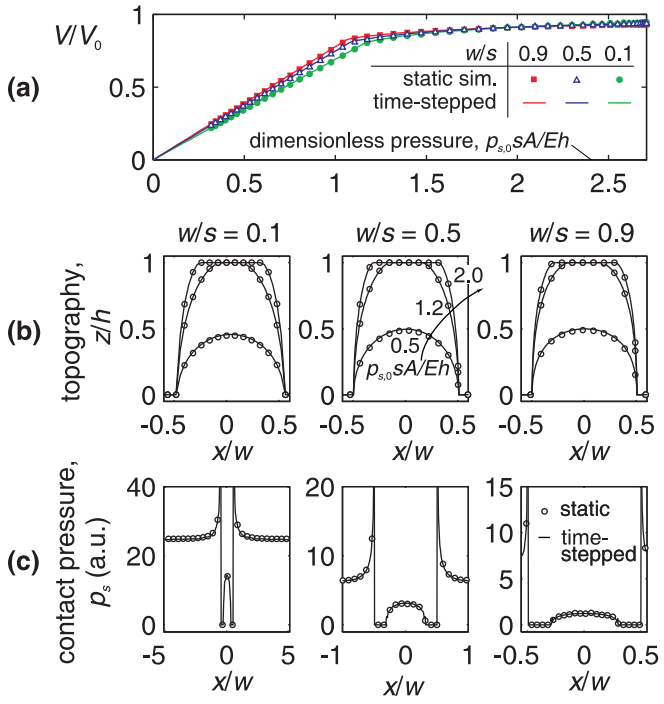

Figure 2.5: Numerical verification of the validity of a static simulation using an elastic 'virtual' substrate in a case where the true stamp–substrate contact-set changes over time. A single-step static simulation of the filling of an array of long trenches is compared with a time-stepped viscoelastic simulation, as described in the text. Equivalence of these two simulation schemes is demonstrated. (a) Rigid-body stamp displacements as a function of time; (b) comparison of simulated topographies; (c) the contact pressure distribution found in the one-step simulation using an elastic 'virtual' substrate is plotted together with an exponentially-weighted time-average, $p_s(x, y, t)$, of the evolving pressure distribution $p(x, y, t)$ found in the time-stepped simulation. Here, $p_{s,0}sA/Eh = 2$. A is a non-dimensional, pattern-dependent constant described in Chapter 4. V and V_0 are also defined in Chapter 4.

2.1.5. Fineness of discretization required for a realistic solution

Simulations are now demonstrated to establish how finely discretized the representation of a stamp should be in order to secure meaningful results. These test simulations represent the partial penetration by an elastic deformable layer into an array of long, narrow cavities with width *w* and pitch *s*. Predicted topographies are compared for a range of width-to-space ratios, *w/s*, and for several levels of coarseness of discretization of the stamp. Cross-sections of the simulated topographies are plotted in Figure 2.6. In the simulation case where the stamp pitch *s* is represented by only eight spatial elements and *w/s* = 0.125, the cavity itself occupies only one spatial element. As illustrated in Figure 2.6a, the peak penetration distance predicted is, in this case, approximately 20% larger than predictions made at finer levels of discretization. As soon as the cavity is represented by four or more spatial elements, further refinement of the discretization affects the predicted peak penetration distance by only a few percent.

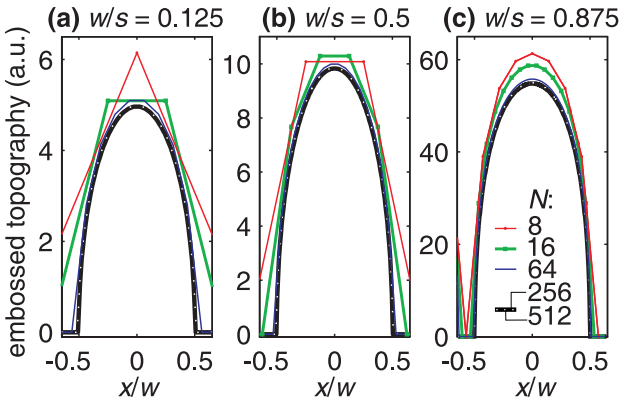

Figure 2.6: Simulated topographies of material penetrating one of an infinite array of long, parallel trenches. Simulations were performed at a range of levels of discretization for each geometry, where *N*, the number of elements spanning *s* in the discretized reperesentation of the stamp, ranged from 8 to 512. In general, simulated topographies are consistent with one another to within approximately 5%, provided that each feature on the stamp — whether a cavity or ridge — is represented by at least four elements.

For *w/s* = 0.875, discretizing the stamp pitch *s* with eight elements means that the ridge on the stamp separating cavities is represented by only one spatial element; in that case the predicted cavity penetration is ~15% higher than that predicted for much finer levels of discretization. When each stamp ridge is represented by *two* spatial elements, the predicted penetration is still ~10% higher than for finer discretization.

Clearly, comparison with experimental data or carefully calibrated finite-element simulations is needed to confirm the *physical* correctness of any simulation results; what is indicated by these simple simulations is that, provided each stamp cavity or ridge is represented by at least four spatial elements, further refinement of the level of discretization makes no more than a few percent difference to the amplitudes of the predicted topographies.

The discrepancies observed at the coarsest levels of discretization might, in the future, be overcome through the use of ‘singular’ pressure elements to represent the edges of contact regions, or by the representation of contact pressure using overlapping elements having a pyramidal pressure distribution; both these approaches are suggested by Johnson [189].

2.1.6. Temperature dependence of viscosity and elasticity

We adopt the following phenomenological functions for the temperature-dependence of η and E. The model for Young's modulus, E, is a simplified version of that used by Arruda and Boyce [181], while that for viscosity represents a straightforward Williams-Landel-Ferry temperature-dependence [200].

$$E(T) = 0.5(E_g + E_r) - 0.5(E_g - E_r)\tanh\left(\frac{T - T_g}{\Delta T}\right) \tag{2.14}$$

$$\eta(T) = \eta_0 \exp\left(\frac{-c_1(T - T_g)}{c_2 + T - T_g}\right) \tag{2.15}$$

E_g is the 'glassy' value of the elastic modulus, exhibited by the material at temperatures well below the glass transition temperature, T_g. E_r is the 'rubbery' value of the modulus, exhibited well above the glass transition, and c_1, c_2, η_0 and ΔT are material constants. It is assumed that strain rates in the material during embossing are, on average, small enough that the conversion of mechanical work to heat does not cause a substantial temperature increase of the polymer bulk: we assume that T may be modeled as constant during embossing.

2.2. Experimental method

Experiments were performed to check the validity of the linear Kelvin-Voigt model described above. Samples were obtained of three polymers commonly used in hot micro-embossing: polymethylmethacrylate (PMMA) from McMaster Carr (Princeton, NJ), polycarbonate (PC) from McMaster Carr, and Zeonor 1060R, a cyclic olefin polymer (as a gift from Zeon Chemicals L.P., Louisville, KY). Since the simulation approach implicitly assumes that the embossed pattern is spatially periodic, a quasi-periodic test-stamp pattern was designed. This pattern is illustrated in Figure 2.7: each stamp carries a 3-by-3 array of identical patterned regions, each patterned region containing an 8-by-8 'patchwork' of features where each patch is uniformly patterned with rectangular trenches or square holes of a particular diameter and pitch. The pitches used are 25, 50 and 100 μm, and cavity diameters range from 5 to 90 μm. For each pitch/width combination there are two sets of trenches patterned at different locations on the stamp, with one set oriented perpendicularly to the other. The arrangement of the 64 patches was randomly chosen. Test stamps were fabricated in silicon using deep reactive ion etching. The etch-depth of the stamps used to emboss PC and Zeonor 1060R was 20 μm, as was that of the stamp used to emboss PMMA at 110 °C. For the PMMA samples embossed at other temperatures, a stamp with an identical pattern but with an etch-depth of 30 μm was used. This difference in etch-depths was not for any particular experimental reason, and was accounted for in fitting the model to the data. The etch-mask was a 1 μm-thick layer of OCG 825 photoresist, which was removed, after etching, by a 30-minute oxygen plasma exposure followed by immersion in a 'piranha' mixture of hydrogen peroxide and sulfuric acid solutions.

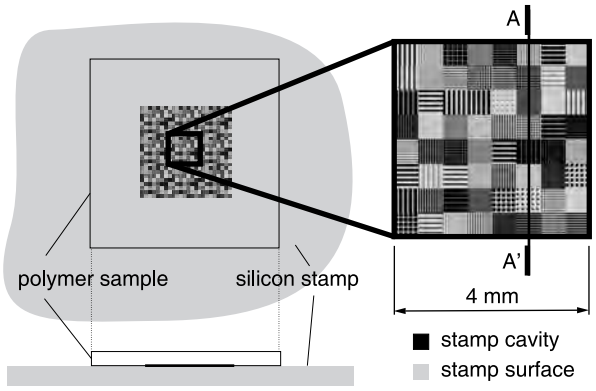

Figure 2.7: Test pattern and experimental configuration; results along section A–A' are plotted in Figure 2.8.

Samples of each of the polymers were then embossed using the apparatus illustrated in Figure 1.1a. An Instron (Norwood, MA) 5869 testing machine was fitted with custom platens through which Paratherm (West Conshohocken, PA) type MR heat-transfer fluid was pumped to create the temperature–time profile of Figure 1.1b [201]. Platen temperatures were monitored using thermocouples embedded approximately 1 mm beneath the platen surfaces, and temperatures were successfully maintained within approximately ±1 °C of their specified values throughout each embossing period of duration t_h.

The processing parameters used and the sequence of experiments are given in Table 2.1. Applied sample-average pressures were chosen to be low enough that not all features on a stamp were filled with polymer, allowing material properties to be extracted from the resulting sample topographies. In each experiment the embossing load was ramped up over a period of 10 s. After embossing, the samples were cooled and then unloaded. PMMA samples were unloaded at 90 °C, PC samples at 115 °C and Zeonor 1060R samples at 70 °C.

The values of the experimental parameters for each material included a range of loading durations at each of four or more temperatures. These experiments made it possible to fit elasticity and viscosity as functions of temperature from around the glass-transition temperature up to 20–30 °C above it. In addition, sets of samples were processed in which the temperature and loading duration were kept constant but the sample-average pressure was varied from sample to sample. The purpose of those experiments was to test the validity of a linear material model: if the assumption of linearity is valid, doubling the pressure should approximately double the cavity penetration depths in those cases where material has not touched the tops of the cavities.

For the embossing of PMMA above 110 °C, two samples were processed at each set of experimental conditions, thus providing a measure of variability of the experimental procedure.

The embossed polymer samples were 25 mm square and ~1.5 mm thick, and therefore extended beyond the patterned region of the stamp. Outside the patterned region, the flat surface of the silicon stamp pressed against the polymer. An initial simulation was constructed to represent the full size of the embossed sample, including the central patterned region and a featureless border. It was established from this simulation that the average contact pressure *within* the central patterned region of the stamp was less than 0.5% lower than the global average pressure applied across the sample. It is therefore reasonable to perform further simulations for only the central 4 mm square patterned region of the stamp, assuming the average pressure across this smaller region to equal the sample-average pressure.

The topographies of the embossed samples were measured with a Zygo (Middlefield, CT) NewView white-light interferometer. The interferometer was programmed to assemble a map of the central 4 mm-square patterned region of each sample. These topographical maps were then processed using custom-

written Matlab routines that extracted the peak height, z_{pk}, of material penetrating a representative feature near the center of each of the 64 differently patterned regions.

Table 2.1: Experimental parameters and randomized sequences of experiments for each material characterized. Positions in the experimental sequence are shown in parentheses and defined separately for each material. p_0 is the nominal sample-average pressure, in MPa, that was applied for the nominal loading duration. For each of the sets of conditions marked with asterisks, one further sample was subsequently embossed and then 'soaked' without an applied load, as described in Section 2.3.8.

	Temp (°C)	p_0 (MPa)	Nominal loading durations, t_h (min) (position(s) in experimental sequence)
PMMA	110	2	2 (42); 4 (40); 4 (43); 5* (41); 30* (44)
		4	0 (1); 5 (2)
		8	0 (38); 1 (35); 2 (36); 3 (33); 4 (37); 5* (34); 30* (39)
	115	1	0 (10); 2 (28, 31); 5 (13, 23); 30 (7, 11)
	117	0.5	2 (4, 20); 5 (19, 22); 30 (14, 29)
	130	0.5	0 (17); 2* (9, 32); 5* (8, 24)
		0.75	2 (12, 25)
		1.0	2 (3, 15)
		1.5	2 (16, 18)
	140	0.5	0 (6, 26); 2 (27, 30); 5 (5, 21)
PC	140	2	2 (12); 5 (11); 30 (20)
		4	2 (6)
		8	2 (13)
		10	2 (14)
	145	0.5	5 (5); 20 (2)
		1	2 (15)
		2	2 (16)
		2.5	2 (17)
	150	0.5	2 (1); 5 (9); 30 (19)
	155	0.5	2 (7); 5 (3); 30 (18)
		1.0	2 (8)
		2.0	2 (10)
		2.5	2 (4)
Zeonor 1060R	100	1	2 (5); 5 (13); 30 (16)
		2	2 (1); 5 (4)
		4	2 (8)
		5	2 (10)
	105	0.14	2 (6); 5 (14)
		0.5	30 (19)
	110	0.14	2 (15); 5 (12); 30 (17)
	120	0.14	2 (2); 5 (3); 30 (18)
		0.30	2 (7)
		0.54	2 (9)
		0.70	2 (11)

2.3. Results and discussion

2.3.1. Model fitting and fidelity

The results of fitting the linear viscoelastic model to experimental data are illustrated in Figure 2.8–Figure 2.15. Meanwhile Appendix A contains additional plots showing data from a wider range of features on the test pattern. The fitting procedure for each material involved three steps. The first step was to consider only the peak penetration data, z_{pk}, for the longest loading duration at each temperature tested. It was temporarily assumed that at these long loading durations the topography had reached the limiting shape set by the elastic modulus of the material. Estimates were thus made for the parameters governing $E(T)$ by comparing the measured values of z_{pk} with those obtained in a single simulation employing specified 'dummy' values for E and p_0.

The second step was to examine the experimental results for two-minute nominal loading durations. These data, in combination with the estimates for $E(T)$ from the first step, allowed the parameters governing $\eta(T)$ to be estimated. Thirdly, all parameter estimates were refined simultaneously using a residual least-squares minimization routine that considered all experimental data.

In the experiments, the ramp-up time of the load was 10 s and the cooling time at the end of each test was several tens of seconds, such that the nominal loading duration, t_h, understates the actual length of time for which each sample experienced a load while above its glass transition temperature. (Indeed, even samples with a nominal loading duration of zero exhibited a measurable topography.) A further fitting parameter, t_{delay}, was therefore introduced: it is a delay term approximately representing this additional time under load and above T_g. The full nominal embossing load was modeled as being applied for $t_h + t_{delay}$.

Using the model thus obtained, forward simulations were performed adopting each set of experimental parameters in turn, and those simulation results are plotted in the graphs that follow. All refined parameter estimates are shown in Table 2.2, along with the fitting r.m.s. errors obtained, which are modest in comparison with the stamps' cavity heights of 20–30 μm.

Table 2.2: Viscoelastic parameters fit for three common hot-embossing materials, and rms fitting errors across all experimental measurements per material.

Parameter	PMMA	PC	Zeonor 1060R
E_g (MPa)	4.1	9.0	2.5
E_r (MPa)	1.9	0.0	0.0
ΔT (K)	8.5	13.9	12.0
η_0 (Pa.s)	$9.9 \cdot 10^{11}$	$1.5 \cdot 10^{10}$	$5.9 \cdot 10^{12}$
c_1	12.5	6.5	6.0
c_2 (K)	4.4	11.2	30.0
T_g (K)	380	414	377
t_{delay} (s)	15	30	30
r.m.s. fitting error (μm)	1.34	1.20	1.73

2.3.2. Analysis of PMMA results

Figure 2.8 compares measured and simulated topographies for PMMA embossed under three illustrative sets of processing conditions. Each pane of the graph corresponds to the 4 mm-long section A–A' defined in Figure 2.7. Comparing Figure 2.8a with Figure 2.8b, we see that the simulation method is able to track the topography that evolves as the wider cavities in a pattern become filled while the narrower cavities remain unfilled. Comparing Figure 2.8a with Figure 2.8c, meanwhile, shows that the nature of the pattern dependencies observed is essentially the same at 140 °C as at 110 °C: in other words, our delayed-elasticity model is appropriate across the full range of temperatures explored experimentally. Feature-size and -shape dependencies of the cavity penetration depth are well represented by the simulations, as are cases in which the cavity penetration varies across an array of equally-sized cavities in response to the cavity sizes in adjacent regions. Broadly, regions of small and/or sparse cavities suppress the cavity penetration depths in surrounding regions.

Figure 2.9 shows peak cavity penetrations for the two PMMA samples embossed at 130 °C under 0.5 MPa for 2 minutes. For each feature geometry, the average peak penetration measured from the two samples is plotted together with the output of the fitted simulation model. The data indicate that the peak penetration depth increases rapidly with increasing width-to-pitch ratio, or 'cavity density'. In addition, and as expected, the peak penetration depth appears to be proportional to the feature pitch for a given feature shape and width-to-pitch ratio. Arrays of long rectangular cavities of a particular width and pitch experience about 50% deeper material penetration for a given applied pressure than do arrays of square cavities with the same width and pitch. All of these effects are well represented by our simulation model.

The experimental data for parallel rectangular trenches ('parallel lines') having a relative rotation of zero follow the same trend as those for lines with a relative rotation of 90°. The same is true for the experimental data from the PC and Zeonor 1060R samples investigated. These observations lend support to our use of an isotropic material model throughout the work.

Figure 2.10, meanwhile, shows measured and modeled cavity penetration depths for 50 μm-pitch rectangular cavities embossed into PMMA at temperatures of 110 °C, 115 °C, and 140 °C. The strong dependence of cavity penetration depth upon local width-to-pitch (w/s) ratio is maintained throughout this range of temperatures. The nature of the evolution of cavity filling with time changes markedly, meanwhile, as the temperature of embossing increases. At 110 °C, which is barely above the material's glass-transition temperature, the topography appears to evolve fairly steadily throughout the full 30-minute range of loading durations that was explored. At 115 °C, an initial rapid evolution of the topography within the first five minutes of loading gives way to slower evolution for longer loading durations. At 140 °C, however, the topography appears to obtain a limiting shape within the first two minutes of loading, and applying a load for a longer period does not make a substantial difference to the final topography. Very similar behavior to that at 140 °C was observed in the PMMA experiments carried out at 130 °C.

This temperature-dependence of the temporal response of PMMA has been well captured with the Kelvin-Voigt model of delayed elasticity that we have adopted and fitted.

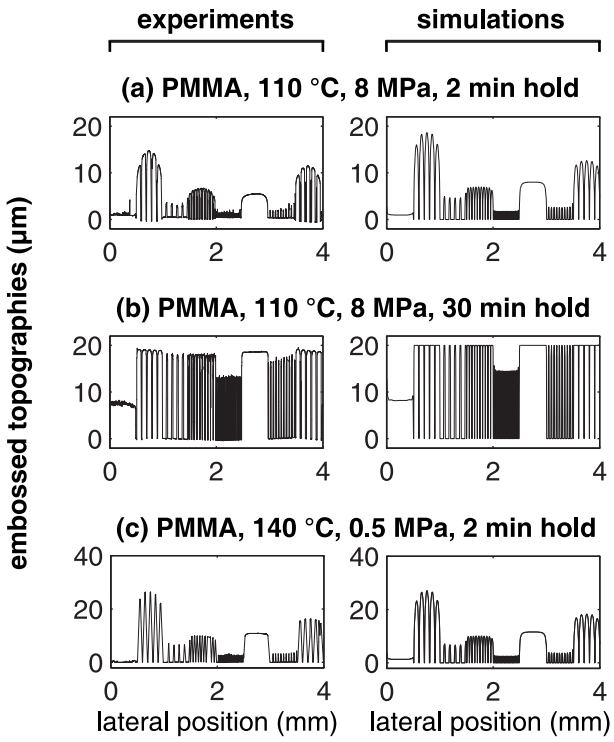

Figure 2.8: Examples of measured *vs.* simulated topographies for PMMA. A comparison of (a) and (b) shows that the simulation model is effective in tracking the progressive filling of cavities as the polymer compliance increases. A comparison of (a) and (c) shows that pattern dependencies are essentially the same in nature across the range of temperatures explored experimentally: 110 °C to 140 °C.

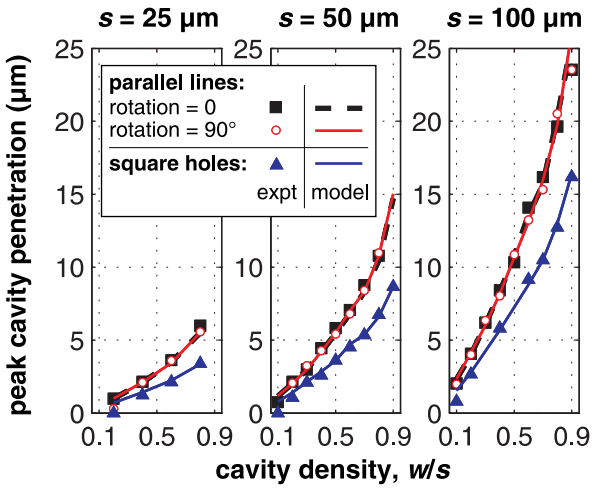

Figure 2.9: Measured and simulated cavity peak penetration depths, z_{pk}, for PMMA embossed at 130 °C under 0.5 MPa for 2 minutes.

The error bars in Figure 2.10b and Figure 2.10c indicate of the amount of sample-to-sample variation encountered in the experimental procedures used. The sample-to-sample variation observed is usually on the order of 10%, but is occasionally much larger. This variation could have arisen because the embossing machine's platens were not perfectly parallel and the orientation of each sample with respect to the platens was not controlled. The occasional presence of trapped particles between the stamp and a polymeric sample could also have contributed to sample-to-sample variation.

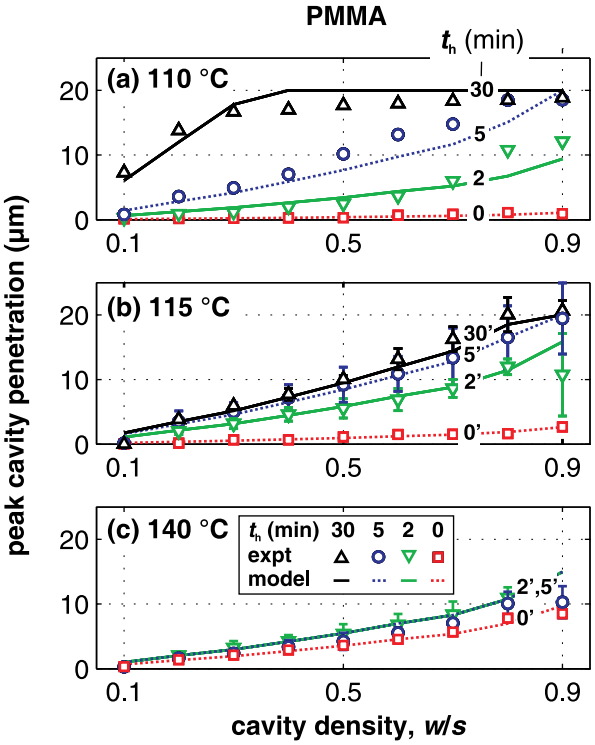

Figure 2.10: Evolution of cavity penetration depths, z_{pk}, for PMMA as a function of the cavity opening density, *w/s*, of 50-μm-pitch rectangular cavities, at three temperatures and for varying loading durations. (a) 110 °C, 8 MPa; (b) 115 °C, 1 MPa; (c) 140 °C, 0.5 MPa. In (b) and (c), symbols indicate the mean experimental value of z_{pk} for two samples processed nominally identically, and error bars represent the ranges of the measured results.

Results from the embossing of PMMA are presented in a summarized form in Figure 2.11. We define a characteristic parameter, the 'pattern-specific compliance', which equals the mean value of the peak penetration depths z_{pk} across all 64 regions of the test pattern, divided by the average applied embossing pressure p_0. In Figure 2.11a, the pattern-specific compliance is plotted as a function of loading duration for three of the temperatures tested. At 110 °C we see that the time-constant for evolution of PMMA's compliance is several hundred seconds; at 115 °C the quicker evolution is clearly seen and at 140 °C the time-constant of the material's mechanical response is well under a minute.

Figure 2.11b and Figure 2.11c explore the pressure-sensitivity of cavity penetration rate. The sample-average of z_{pk} is plotted against the applied sample-average pressure for two of the temperatures explored: 110 °C (Figure 2.11b) and 130 °C (Figure 2.11c). At 110 °C there is modest agreement, and at 130 °C close agreement, between the experimental values of average cavity penetration and those simulated under the assumption of a linear viscoelastic material model. The relationship between average peak cavity penetration and sample-average pressure is not necessarily a straight line — even though the

material model is linear — because, under the larger embossing pressures considered, some of the cavities had begun to fill with polymeric material.

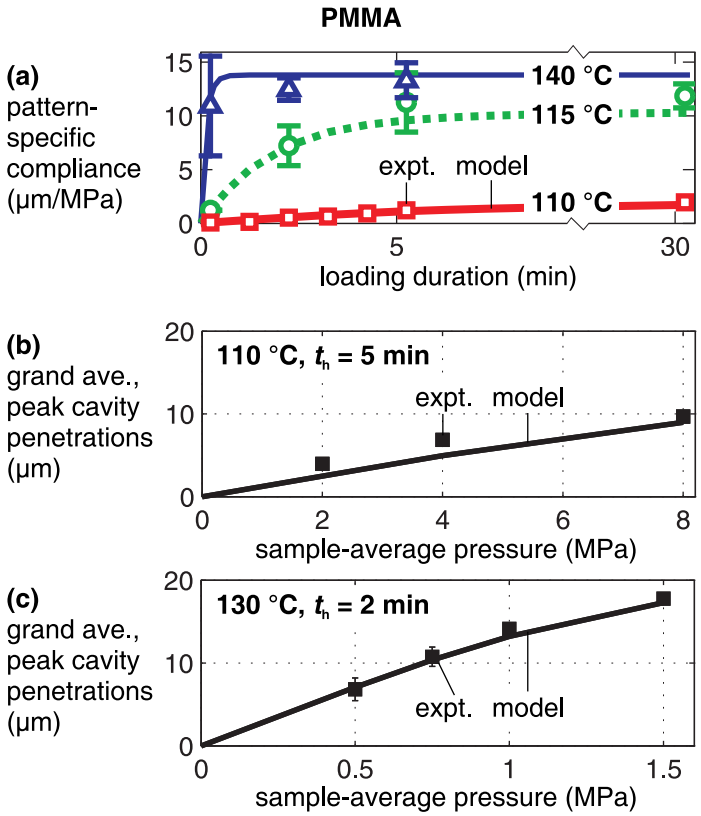

Figure 2.11: Summary of PMMA embossing and modeling results. (a) Pattern-specific compliance as a function of embossing temperature and loading duration. (b) Average cavity penetration depths as a function of average embossing pressure, at 110 °C and for a five-minute loading duration. (c) Average cavity penetration depths as a function of average embossing pressure, at 130 °C and for a two-minute loading duration.

2.3.3. PC and Zeonor 1060R results

The pattern dependencies that are observed in the embossing of PC (Figure 2.12) and Zeonor 1060R (Figure 2.14) are, as expected, very similar to those seen with PMMA. The relationships between topography, temperature, and time, however, are rather different from the case of PMMA, although the relationships are still readily described with an appropriately calibrated Kelvin-Voigt model. In the cases of both PC (Figure 2.13) and Zeonor 1060R (Figure 2.15), topographies continue to evolve 30 minutes after loading, even at temperatures ~20 °C above their nominal glass-transitions. In contrast, PMMA embossed at 130 °C — 20 °C above *its* glass-transition — had attained a virtually final topography within two minutes of load application.

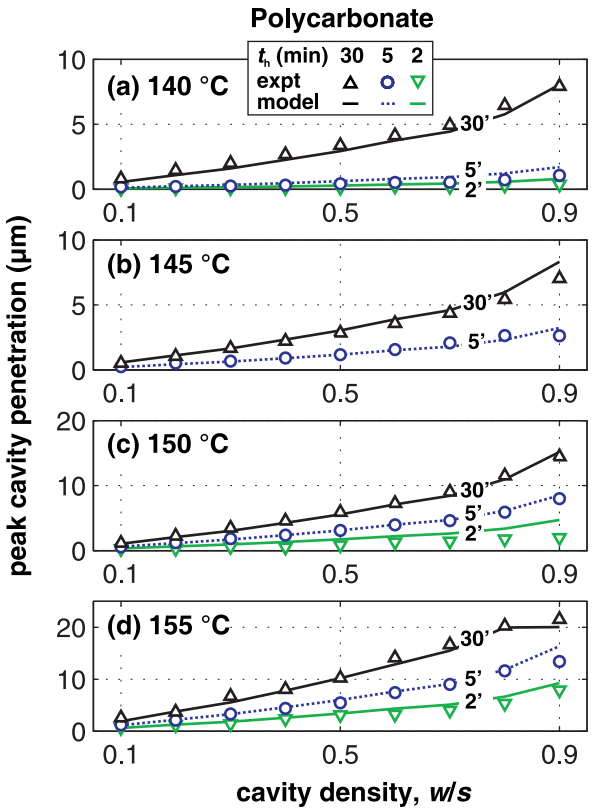

Figure 2.12: Evolution of cavity penetration depths, z_{pk}, for PC as a function of the cavity opening density, *w/s*, of 50-μm-pitch rectangular cavities, at four temperatures and for varying loading durations. (a) 140 °C, 2 MPa; (b) 145 °C, 0.5 MPa; (c) 150 °C, 0.5 MPa; (d) 155 °C, 0.5 MPa.

For PC two minutes after load application at 155 °C (~20 °C above T_g) its pattern-specific compliance is similar in magnitude to that of PMMA under comparable conditions (130 °C). As time proceeds, however, PC's compliance continues to grow, whereas that of PMMA remains relatively constant. Meanwhile, Zeonor 1060R at 120 °C (~20 °C above T_g) exhibits about four times as much compliance after 2 minutes' loading as does PMMA, and about eight times as much compliance after 30 minutes' loading. What these observations imply for engineers making a selection from among PMMA, PC, and Zeonor 1060R is that for a given average embossing pressure and a typical embossing temperature of 20 °C above T_g, it is easier to fill the cavities of a pattern when using Zeonor 1060R, or, to some extent, PC, than it is when using PMMA.

Figure 2.13c provides further support for the use of a linear material model to describe PC under the embossing conditions investigated. Figure 2.13b, which summarizes the pressure-dependence of cavity penetration for PC embossed at 140 °C, shows rather poorer agreement between experiment and simulation, although it should be noted that here the absolute cavity penetrations are less than 2 μm and thus particularly susceptible to the sample-to-sample variation that might be caused by particles trapped between a sample and the stamp. Figure 2.15b and Figure 2.15c, meanwhile, indicate that a linear material model is appropriate for Zeonor 1060R under the range of conditions explored.

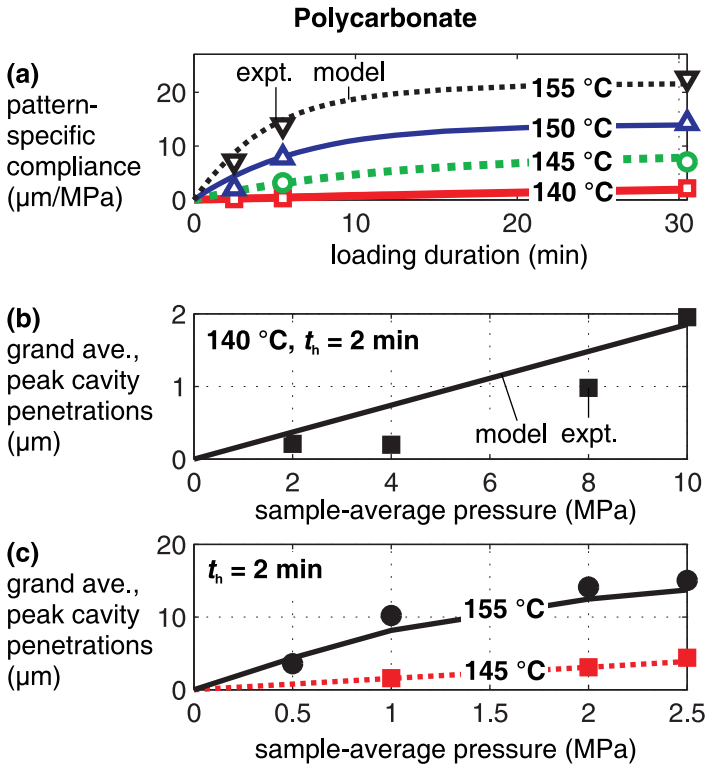

Figure 2.13: Summary of PC embossing and modeling results. (a) Pattern-specific compliance as a function of embossing temperature and loading duration. (b) Average cavity penetration depths as a function of average embossing pressure, at 140 °C and for a two-minute loading duration. (c) Average cavity penetration depths as a function of average embossing pressure, at both 145 °C and 155 °C, for a two-minute loading duration.

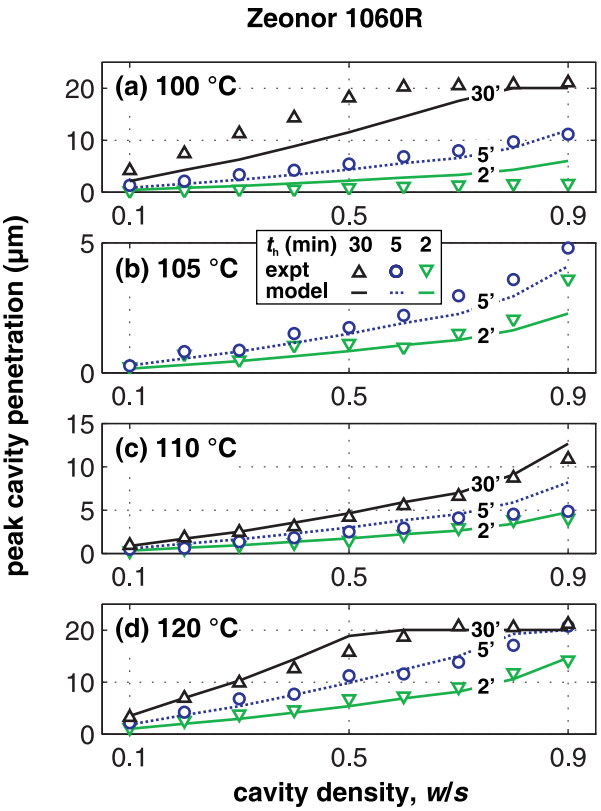

Figure 2.14: Evolution of cavity penetration depths, z_{pk}, for Zeonor 1060R as a function of the cavity opening density, *w/s*, of 50-μm-pitch rectangular cavities, at four temperatures and for varying loading durations. (a) 100 °C, 1 MPa; (b) 105 °C, 0.14 MPa; (c) 110 °C, 0.14 MPa; (d) 120 °C, 0.14 MPa.

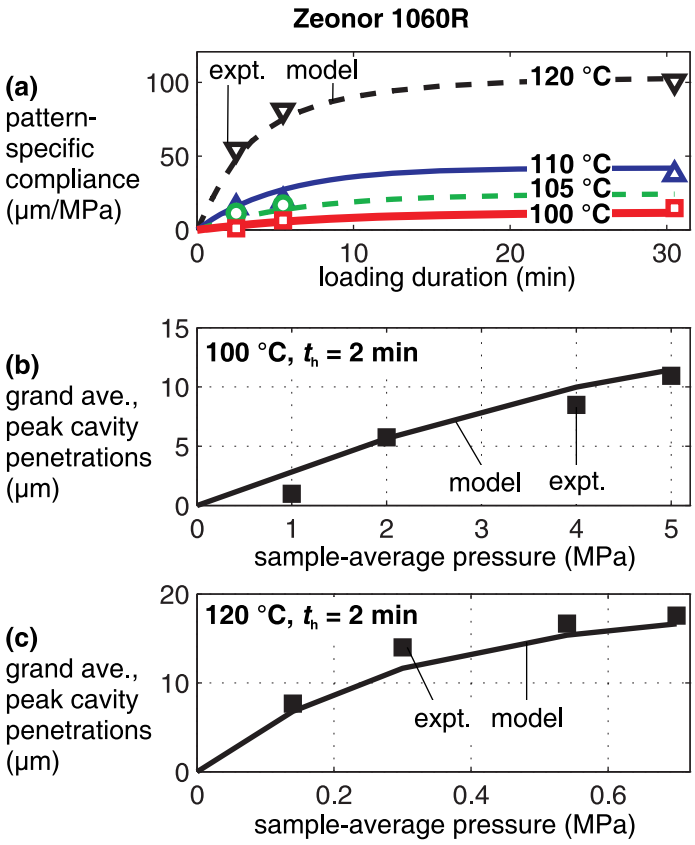

Figure 2.15: Summary of Zeonor 1060R embossing and modeling results. (a) Pattern-specific compliance as a function of embossing temperature and loading duration. (b) Average cavity penetration depths as a function of average embossing pressure, at 100 °C and for a two-minute loading duration. (c) Average cavity penetration depths as a function of average embossing pressure, at 120 °C and for a two-minute loading duration.

2.3.4. Comparison of fitted model with bulk stress–strain data

It was argued in Section 2.1.1 that a linear Kelvin-Voigt model would offer a good approximation for simulating micro-embossing because the strain-rate in virtually the whole of the embossed polymer sheet would be less than 10^{-3}/s. The linear model does appear to represent our micro-embossing experimental data well. Here we illustrate the limits of validity of the model that we have fitted, by comparing its predictions with experimental data from the bulk compression of PMMA and PC at a range of strain rates. The bulk compression data are courtesy of Nici Ames and Shawn Chester [202].

Figure 2.16 illustrates this comparison for PMMA. Experimental data and the prediction of our model are both plotted for compressive strains increasing from zero to 1.0 followed by a complete unloading. Evidently our model does not represent the measured behavior particularly closely, but it does go some way to representing two important features. Firstly, for strain rates up to 10^{-2}/s, the transition of material behavior from elastic-plastic to rubbery with increasing temperature is roughly described by the Kelvin-Voigt model fitted. The model reflects the possibility of permanent deformation when the viscous component of material behavior is substantial. Secondly, the softening of the material with increasing temperature is captured. For 110 °C, however, our model becomes completely unrealistic above about 10^{-3}/s because it does not capture the marked reduction of yield stress that occurs with increasing strain

rate. Neither can the linear model represent the strain-stiffening that occurs — for all temperatures and strain-rates — at compressive strains above around 0.8. Moreover, at 120 °C, the viscous component of the fitted model appears too small.

Figure 2.17 shows a similar comparison between bulk compression data and the fitted Kelvin-Voigt model in the case of PC. Here, the model does reflect the transition from elastic-plastic to somewhat rubbery behavior that occurs between 140 °C and 150 °C at a strain rate of 10^{-3}/s. At higher strain rates, however, the fitted model does a poor job of representing reality.

These comparisons have provided a picture of the limitations of our model, and suggest that great care would need to be taken if trying to apply the simulation method for much faster imprinting processes than currently envisioned.

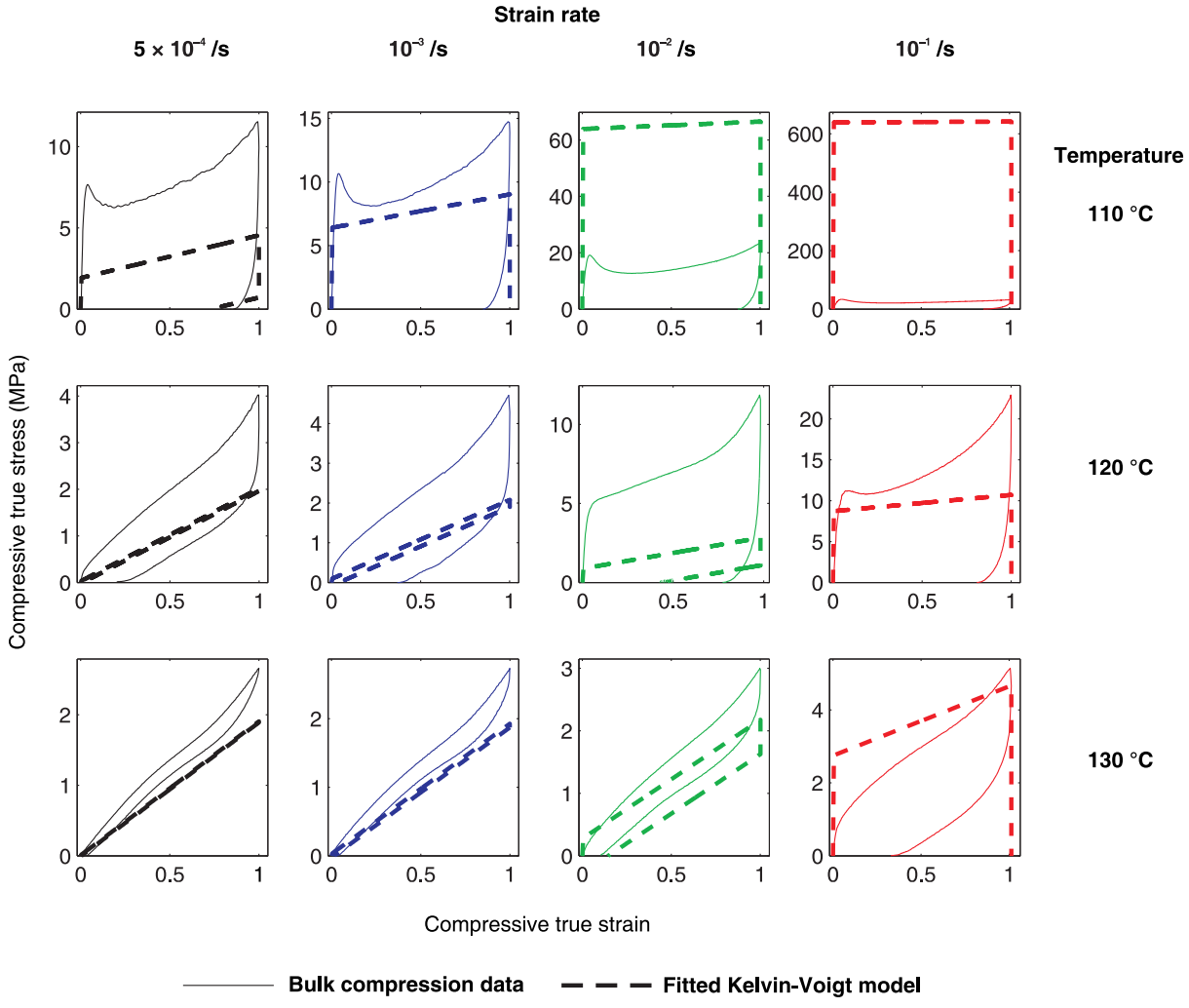

Figure 2.16: Comparison of experimental bulk compression data for PMMA with the predictions of the linear Kelvin-Voigt model fit to the microembossing experiments of this thesis. Comparisons are made for temperatures of 110, 120 and 130 °C and for strain rates of 5×10^{-4}, 10^{-3}, 10^{-2}, and 10^{-1} /s.

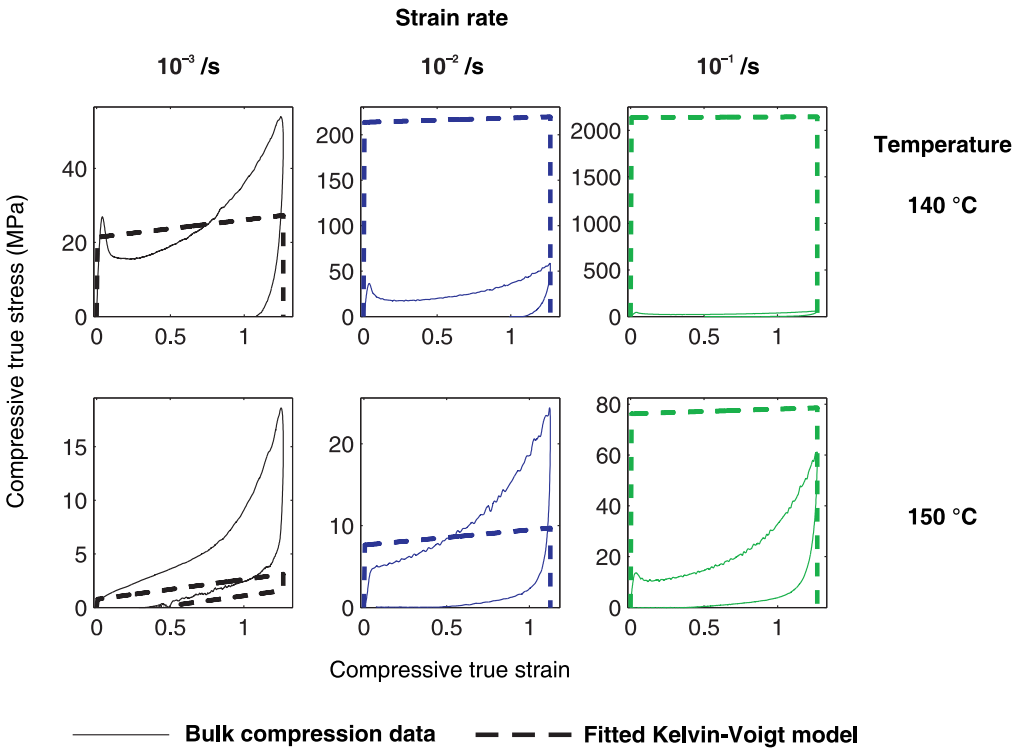

Figure 2.17: Comparison of experimental bulk compression data for polycarbonate with the predictions of the linear Kelvin-Voigt model fit to the microembossing experiments of this thesis. Comparisons are made for temperatures of 140 and 150 °C and for strain rates of 10^{-3}, 10^{-2}, and 10^{-1} /s.

2.3.5. Verification of the isothermal embossing assumption

In Section 2.1, the assumption was introduced that the conversion of mechanical work to heat does not cause a substantial temperature increase of the polymer bulk. To support this assumption, we model the generation of heat in the polymer using an extremely simple representation of the embossing set-up. The majority of the polymeric sheet is assumed to be compressed at a rate of 5×10^{-4}/s (corresponding to a 30 µm compression of a 1 mm-thick layer during one minute). A 100 µm-thick layer of the polymer adjacent to the stamp, however, is assumed to be embossed with microscopic features and to experience a volume-average strain rate of 10^{-1}/s: even this is undoubtedly an overestimate. The rate P at which energy is dissipated in a volume of material V with Newtonian viscosity η being strained at a rate $\mathrm{d}\gamma/\mathrm{d}t$ is:

$$P = 0.5V\eta\left(\frac{\mathrm{d}\gamma}{\mathrm{d}t}\right)^2. \tag{2.16}$$

For the purposes of this estimation we assume the embossed material to be PMMA and its nominal temperature to be 110 °C, at which, according to the linear viscoelastic model we have fit, its dissipative component has a viscosity of 6×10^9 Pa.s.

The polymer sheet is assumed to be in contact with a silicon stamp of thickness 0.5 mm whose other face is in perfect thermal contact with a heatsink. We suppose all heat to be generated at the bottom of the quickly-straining 100 µm-thick layer of PMMA, so that heat has to flow through 100 µm of polymer and

then through the silicon towards the heatsink. The steady-state temperature rise ΔT in the vicinity of the embossed features due to the dissipation of mechanical energy is therefore given by:

$$\Delta T = \Phi\left(\frac{h_w}{\sigma_{Si}} + \frac{h_e}{\sigma_{PMMA}}\right) \tag{2.17}$$

where Φ is the rate of generation of heat near the surface of the polymer, h_w is the wafer thickness of 0.5 mm, h_e is the 100 µm polymer layer being embossed, and σ_{Si} = 100 W/m-K and σ_{PMMA} = 0.19 W/m-K are the thermal conductivities of silicon and PMMA respectively.

Assuming that 100% of dissipative power P is converted to heat, the rate of heat generation per unit area in the fast-straining region of the polymer is:

$$\Phi = 0.5 h_e \eta \left(\frac{\mathrm{d}\gamma}{\mathrm{d}t}\right)^2 = 0.5 \times 0.1\,\mathrm{mm} \times 6 \times 10^9\,\mathrm{Pa\,s} \times (0.1/\mathrm{s})^2 = 30\,\mathrm{W/m^2}\,. \tag{2.18}$$

Meanwhile the rate of heat generation in the slow-straining bulk of the polymer is only

$$\Phi = 0.5 h_e \eta \left(\frac{\mathrm{d}\gamma}{\mathrm{d}t}\right)^2 = 0.5 \times 0.9\,\mathrm{mm} \times 6 \times 10^9\,\mathrm{Pa\,s} \times (5 \times 10^{-4}/\mathrm{s})^2 = 0.7\,\mathrm{W/m^2} \tag{2.19}$$

and we therefore neglect this second component of heat generation. We evaluate the temperature drop across the fast-straining polymer layer and the silicon stamp as:

$$\Delta T = \Phi\left(\frac{h_w}{\sigma_{Si}} + \frac{h_e}{\sigma_{PMMA}}\right) = 30\,\mathrm{W/m^2} \times \left(\frac{0.5\,\mathrm{mm}}{100\,\mathrm{W/mK}} + \frac{0.1\,\mathrm{mm}}{0.19\,\mathrm{W/mK}}\right) = 0.016\,\mathrm{K}. \tag{2.20}$$

We see that compared to the nominal embossing temperature of 383 K, the temperature drop is negligible. At higher embossing temperatures, the material's value of η will be lower, the rate of doing mechanical work on the polymer will be lower, and the temperature rise ΔT will be even smaller. The assumption of isothermal embossing therefore seems justified for ordinary processing conditions.

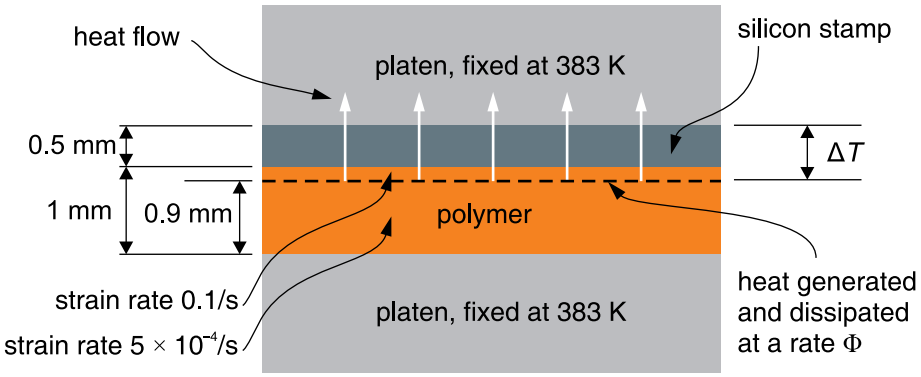

Figure 2.18: A greatly simplified model of a microembossing arrangement, showing the dissipation of mechanical energy as heat.

2.3.6. Aspect ratios of embossed features

It is known that rubbery polymers exhibit strain-stiffening [203]; we therefore anticipate that the linear viscoelastic model we use will make increasingly erroneous predictions as the absolute strains in an embossed pattern increase. The larger the ratio of an embossed feature's height to its width, the larger the strains in it will be. In the experiments conducted here, almost none of the embossed features had peak heights larger than their widths: the 5 μm-wide features penetrated their cavities by no more than about 5 μm, and so on. We therefore have evidence that our modeling approach is reasonably faithful for feature height-to-width aspect ratios of at least one.

2.3.7. Effectiveness of a continuum model

For all experiments performed, the smallest cavity diameter on the stamp was 5 μm and the model fits the data as closely at this cavity size as it does for cavities of width 90 μm. It therefore appears appropriate, at these dimensions, to model the investigated materials as solid continua. Since 5 μm is several hundreds of times larger than the diameter of any one of the polymeric molecules composing the materials, the use of a continuum model is rational.

There is little in the literature addressing the possibility of non-continuum effects in polymer micro-embossing or injection molding, but simulations performed by Yao and Kim for polystyrene indicate that, assuming a gyration radius of 26 nm for the polymer molecules, non-bulk effects only become significant when the cavity width falls below around 1 μm [204].

2.3.8. Effects of 'soaking' samples at high temperature after embossing

Implicit in the linear Kelvin-Voigt model presented is that when an embossed sample is cooled under a load, residual stresses are trapped in the component. If, instead, the embossing load were to be removed while the specimen was held at a relatively high temperature, we would expect these internal stresses to drive a shape recovery that would eventually cause the polymeric surface to return to its flat, pre-embossing state. If the time-course of the sample temperature and sample-average applied pressure were to be as illustrated in Figure 2.19a — with an embossing step of duration t_0 immediately followed by a 'soaking', or annealing, period of t_0 with no applied load but unchanged temperature — the expression for the sample-average 'virtual' pressure given in (2.5) reduces to:

$$\left.\begin{aligned} p_{s,0}(t_0) &= p_0\left[1-\exp\left(-\frac{Et_0}{\eta}\right)\right] \\ &\text{and} \\ p_{s,0}(2t_0) &= p_0\left[\exp\left(-\frac{Et_0}{\eta}\right)-\exp\left(-\frac{2Et_0}{\eta}\right)\right]. \end{aligned}\right\} \tag{2.21}$$

We note that as Et_0/η increases, the ratio $p_{s,0}(2t_0)/p_{s,0}(t_0)$ decreases, and there is a corresponding increase in the proportion of the embossed topographical height expected to disappear during the soaking period.

To test this implication of the model, six further PMMA samples were embossed under the range of conditions illustrated in Figure 2.19b–g. After cooling and removal of the stamp, each of these further samples was re-heated to its embossing temperature and soaked at that temperature, without an applied load, for a time equal to the sample's original embossing duration. At 130 °C the material is in a rubbery state, Et_0/η is much larger than 1, and the embossed topography does indeed revert almost to a flat surface after either 2 or 5 minutes' soaking (Figure 2.19f and g). In both 130 °C cases there is just ~1 μm of

residual topography, with all surface height changes located near the *edges* of regions where stamp protrusions had contacted the PMMA.

In the case of embossing and soaking at 110 °C, however, the predictions of a linear Kelvin-Voigt model are not borne out. Whereas the chosen model predicts that as t_0 increases a greater proportion of the embossed topography should disappear during the soaking step, we do in fact see markedly *less* decay of the topography for t_0 = 30 minutes than for t_0 = 5 minutes (Figure 2.19b–e). These observations give the impression that at 110 °C a portion of the material's deformation is effectively permanent. It might therefore be imagined that a better approximation to PMMA's behavior at 110 °C would be obtained by combining the present Voigt material model with the Maxwell model of our earlier work [205].

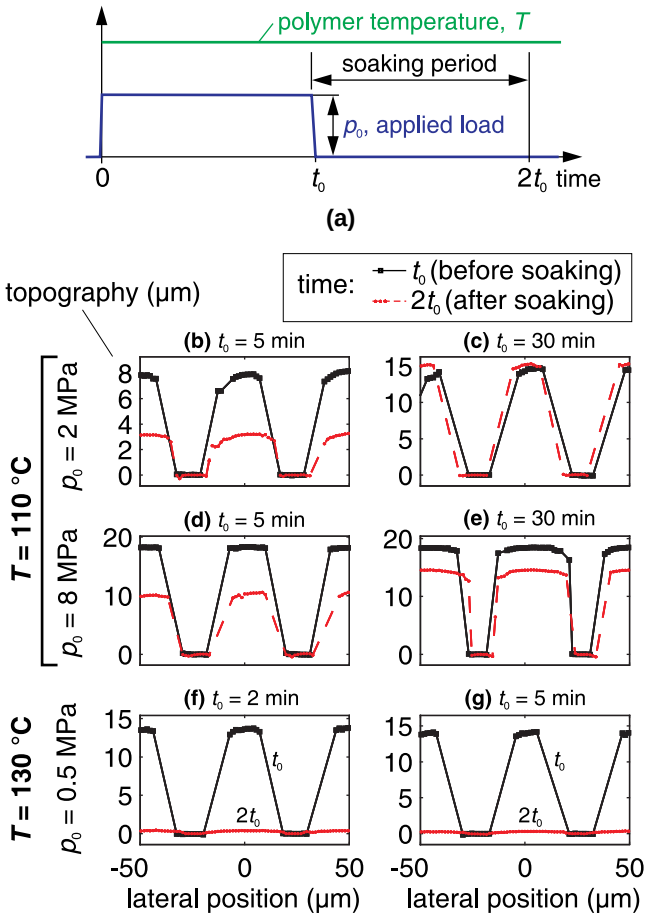

Figure 2.19: The effects of soaking previously embossed PMMA components at the embossing temperature but with no applied load. Effective temperature and pressure time-courses are defined in (a). Each pane shows the measured cross-sectional topographies of embossed ridges (*s* = 50 μm; *w*/*s* = 0.8) on two samples: one that was embossed but not subsequently soaked, and one that was soaked after embossing and separation from the stamp.

A hypothesis of permanent material deformation at 110 °C was probed by processing two additional samples (not noted in Table 2.1). These new samples were embossed at 110 °C for five minutes under 2 MPa and 8 MPa, and were subsequently soaked for five minutes at the higher temperature of 130 °C. Measured topographies from these samples, both before and after soaking, are illustrated in Figure 2.20: they indicate that the PMMA samples have returned to having virtually flat surfaces after soaking at 130 °C. What this result suggests is that the deformation of PMMA that we observed at 110 °C is not truly permanent: it can be recovered by increasing the temperature of soaking. A more plausible explanation, then, for the behavior shown in Figure 2.19b–e is that the stress–strain-rate relationship of PMMA is substantially non-linear at 110 °C. The shape-recovery seen during soaking, then, would not necessarily be expected to follow the trends predicted by a linear Kelvin–Voigt model.

These experiments lend further support to the use of a Kelvin–Voigt model throughout the temperature range explored for PMMA, with the caveat that we are not modeling potentially important material non-linearities near T_g.

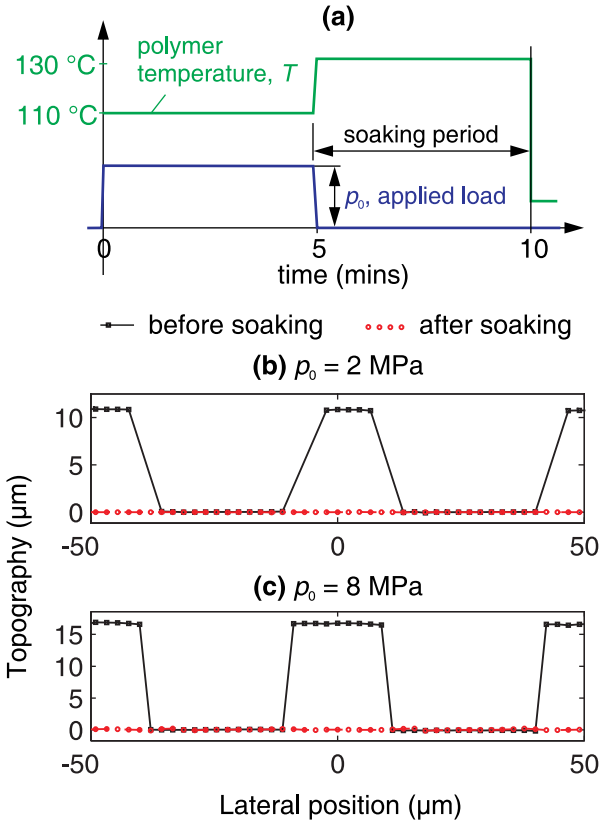

Figure 2.20: Topographies of PMMA samples embossed at 110 °C, measured both before (black symbols) and after (red symbols) annealing for five minutes at 130 °C with no externally applied load. In (a) are shown the temperature and load profiles effectively applied to the sample. In (b) and (c) are shown the measured cross-sectional topographies in a region of embossed ridges (s = 50 μm; w/s = 0.5), for two different values of average embossing pressure.

We have also examined the soaking behavior of PC and Zeonor 1060R. Two samples of each material were embossed and subsequently soaked. The experimental conditions are reported in Table 2.3 and measured topographies are plotted in Figure 2.21. The measured embossing temperatures were determined using a thermocouple buried in one of the embossing platens, and they differ by up to 2 °C from the nominal temperatures. The temperature set-points for the soaking periods were the same as for the embossing periods, although the actual platen temperatures were not recorded during soaking. The 'measured' average embossing pressures are based on the applied loads reported by the load-cell of the embossing apparatus.

Table 2.3: Embossing temperatures and average pressures for two additional samples of PC and two of Zeonor 1060R. The embossing and annealing times were both five minutes for each sample. The target embossing temperature and pressure, and also the actual values measured during *embossing*, are shown in the table. Measured peak topographical heights are reported for a region of embossed ridges (*s* = 50 μm; *w*/*s* = 0.5), as are the corresponding peak heights obtained in simulations using the models fit in this chapter.

Material	Nominal parameters		Measured parameters during embossing		Measured cavity penetration heights (μm)		Simulated cavity penetration heights (μm)	
	Temp. (°C)	p_0 (MPa)	Temp. (°C)	p_0 (MPa)	Before soak	After soak	Before soak	After soak
Zeonor 1060R	105	2.0	103	2.1	6.0	1.3	17.0	10.4
	120	0.14	118	0.22	17.0	11.5	14.4	7.0
PC	145	4.0	143	4.1	7.0	5.0	6.2	4.9
	155	0.5	153	0.55	17.0	3.5	6.1	2.3

There was substantial shape recovery in each of the four samples during soaking. We have used our fitted material models together with the expressions of (2.21) in an attempt to simulate the shape recovery that was observed during soaking. The temperatures and embossing pressures assumed for the simulations are those measured from the experiments. Each of the simulations shows a reduction of cavity penetration heights, during soaking, to a fraction of their post-embossing values (Table 2.3). The correspondence between experimentation and simulation goes little further, however. We attribute this poor quantitative correspondence to uncontrolled variations of the temperatures of each sample during embossing and annealing. During embossing, both faces of the polymer sample were in contact with the heated stamp or with a platen; during annealing, one of the faces was exposed to air, and the polymer temperature could therefore have been slightly lower during annealing than during embossing. Moreover, and as discussed above, temperature varies by several degrees Celsius across the platens used, and the position of each sample relative to the platens was not carefully controlled. The compliances of PC and Zeonor 1060R can vary by several tens of percent with only a 1 °C change of polymer temperature, so it is plausible that poor temperature control is to blame for these discrepancies.

In spite of these difficulties, the observation that topographies embossed into PC and Zeonor 1060R decay when annealed further supports our use of a Kelvin–Voigt model for these materials.

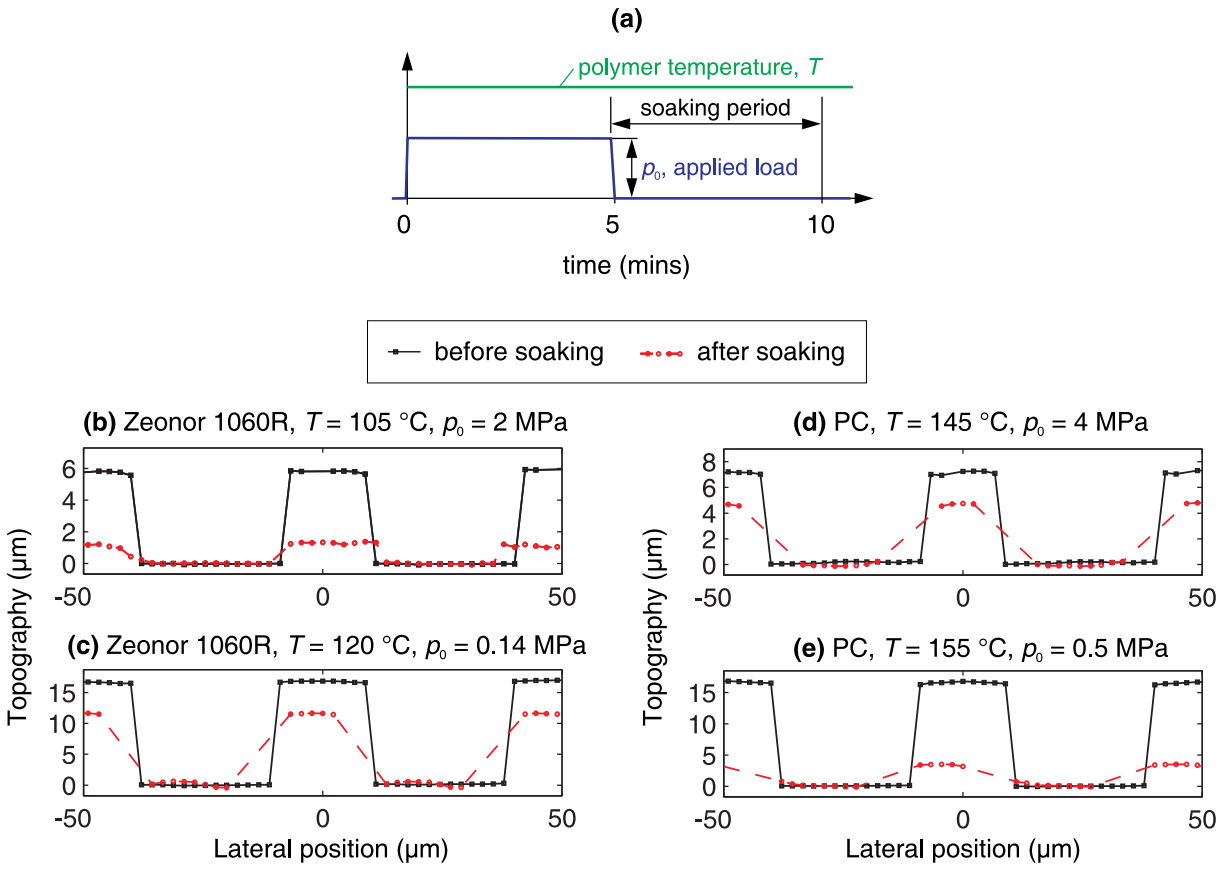

Figure 2.21: Measured topographies of Zeonor 1060R and PC samples that were embossed and subsequently soaked. The embossing and soaking durations were each five minutes for all samples. In (a) are shown the temperature and load profiles effectively applied to the sample. In (b)–(e) are shown the measured cross-sectional topographies in a region of embossed ridges (s = 50 µm; w/s = 0.5).

2.3.9. Computational speed

The principal advantage of the proposed simulation approach is its high computational speed. To quantify this speed, we ran a series of simulations and recorded their durations. These simulations were run using Matlab on a desktop computer with Windows XP, two 3.2 GHz Intel Pentium 4 processors, and 2 GB of RAM.

Firstly, plane-strain simulations were run in which one period of the pattern of the stamp (in this case, an array of parallel trenches) was represented by a vector of topographical heights. The length of the vector, N, was varied from 128 to 1024. For each value of N, simulations were run in which the width-to-pitch ratio of the cavities was varied from 1.5% to 98.5%. The execution times of these simulations are plotted in Figure 2.22a: they are all less than about two seconds.

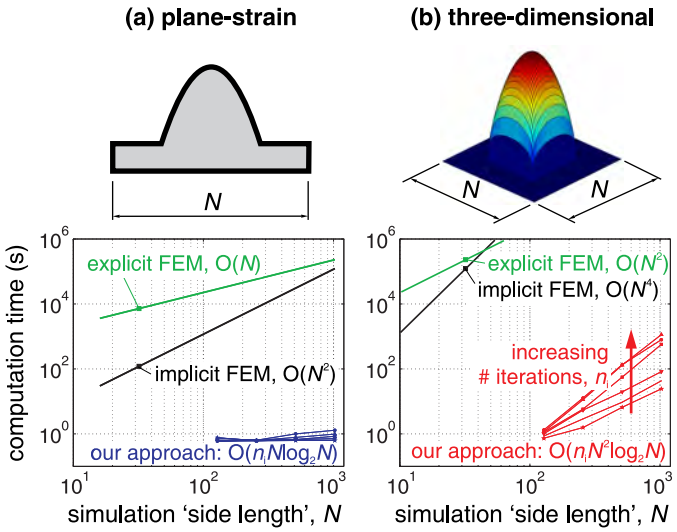

Figure 2.22: Comparison of computation times (a) plane-strain; (b) 3-D model.

Secondly, three-dimensional simulations were conducted, in which one period of the stamp design — again an array of parallel trenches — was represented by an N-by-N matrix of topographical heights. Although the computation times (Figure 2.22b) scale predominantly as N^2, the number of iterations, n_i, required by the biconjugate gradient algorithm to obtain a contact-pressure solution is a function both of N and of p_c, the proportion of the stamp area in contact with the polymer. As the cavity width-to-pitch ratio decreases, and p_c consequently increases, there is an increase in the total number of iterations required by the algorithm to find a satisfactory solution. This relationship is illustrated in Figure 2.23, and, for the case in which the contact-pressure distribution is to be found with a relative residual of 10^{-3}, may be approximated as:

$$n_i \approx 2.5[(p_c + 0.66)\log_2 N - 3] \tag{2.22}$$

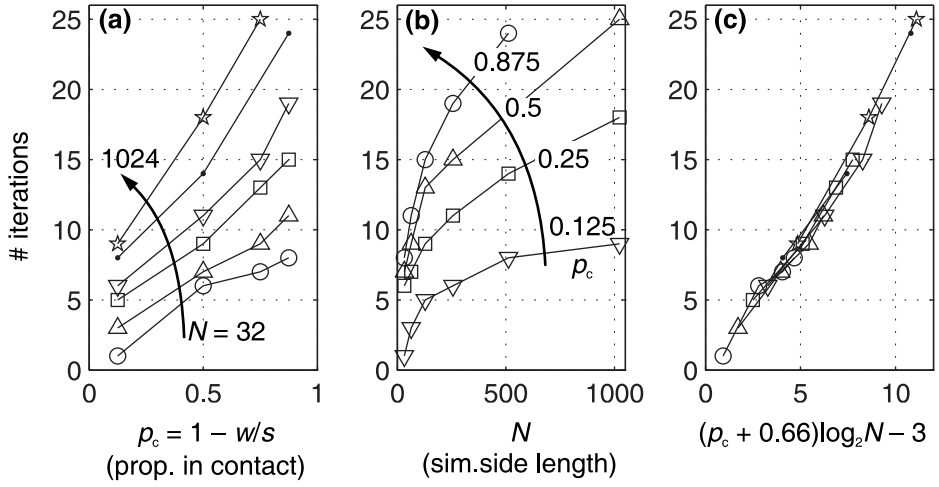

Figure 2.23: The relationship between n_i, the number of required iterations on the contact pressure distribution to obtain a relative residual of 10^{-3}, and (a) the proportion of the stamp area in contact with the polymer; (b) the side-length of the simulation. (c) represents the relationship between n_i, p_c and N in a compact way.

The time *per* iteration, meanwhile, is composed not merely of the time for the FFT computation — which is confirmed to scale approximately as $N^2\log_2 N$ [206] — but also of the time taken to compute the residuals and, if necessary, a new trial pressure distribution. It makes sense that the time for this latter component should be proportional to the number of stamp elements in contact with the polymer surface: $p_c N^2$. We therefore have the following expression for the total simulation time:

$$t_{sim} \approx 4n_c\,(n_i + 1)\,(k_{conv}N^2\log_2 N + k_{iter}N^2 p_c). \tag{2.23}$$

For our implementation, k_{conv} was found to be 4×10^{-8} s, and k_{iter} to be $\sim 10^{-7}$ s. In (2.23), n_c is the number of guesses made for the contents of the stamp–polymer contact set C, as defined in Section 2.1.3. For all of our simulations plotted in Figure 2.22, n_c is 1: no material touched the tops of the stamp cavities in these simulations, and the initial contact set guess was therefore correct. For simulations involving cavity filling, however, the computation time would be n_c times as long as that illustrated in Figure 2.22; satisfactory simulation results are usually obtained with $n_c < 10$. The true situation is a little more complicated than that illustrated, because p_c will in fact change as the contact set estimate changes, but $n_c = 10$ and $p_c = 1$ will yield a good upper-bound estimate for simulation time.

2.3.10. Comparison with finite element modeling

It is difficult to draw a fair comparison of the speed of our method with that of the most obvious alternative, finite-element (FE) modeling. Our method is approximate and aims to serve as a design aid, while not currently capturing the geometrical and material nonlinearities and the thermo-mechanical effects that are readily modeled with the FE method. Nevertheless, we do illustrate in Figure 2.22 expected trends in the computation time of finite-element embossing simulations.

We consider two widely-used approaches to constructing finite-element simulations. First is the 'implicit' method in which the deformation of the material is found through an iterative solution process and the computation time scales as the square of the number of material elements present in the problem's representation. Second is the 'explicit' method, in which the material's deformation is computed without iteration, by marching the problem forwards through time; here, computation time is proportional to the number of elements present, and inversely proportional to the smallest element's size [207].

A plane-strain, fully thermo-mechanically coupled explicit simulation of the embossing of a single trench in PMMA — containing on the order of 1000 elements — has been reported to take in excess of an hour using a desktop computer with four Intel Itanium processors [182], and is represented by the green symbol in Figure 2.22a. An implicit simulation of the embossing of a comparable geometry — albeit in a different material, a metallic glass — has been found to take only a few minutes running on similar equipment [208]; this is indicated by the black symbol in Figure 2.22a. Both these cases are plotted at $N = 32$ for comparison, because 32 is approximately the minimum length of vector needed in our method to simulate reliably the embossing of a single trench. The trend lines of finite-element computational time assume that the number of elements required would be proportional to N.

In the plane-strain case, our method provides a solution — albeit one with the limitations we have discussed — at least three orders of magnitude more quickly than either of the full finite-element approaches.

We adapt our comparison to the three-dimensional case by assuming that the number of finite elements required in a 3-D simulation would be proportional to N^2 (the average number of mesh elements *through the thickness* of the embossed layer would not change with N). Under these assumptions, the projected finite-element simulation times would be at least five orders of magnitude longer than those of our method (Figure 2.22b). Moreover, the comparison is based on a Matlab implementation of our approach; a compiled implementation could provide even more impressive performance.

It should be noted that the computation time of our approach — as modeled by (2.23) — increases *slightly* faster with N than that of the explicit FE method. However, by extrapolation, we predict that our method remains faster for values of N at least as large as 2^{500}, and in any case such a large simulation would demand amounts of memory and simulation time far beyond those currently practicable.

2.4. Conclusion

We have demonstrated a contact mechanics-based approach to simulating the hot micro-embossing of bulk thermoplastic polymers. A linear viscoelastic material model has been calibrated experimentally, as a function of temperature, for three materials: PMMA, PC and Zeonor 1060R. For each material, our continuum model of the embossed layer captures reasonably well the shapes of embossed topographies having features with diameters from 5 to 90 μm. The r.m.s. differences between the simulated topographical heights and the experimentally measured ones are less than 2 μm for each material, with absolute topographical heights ranging up to 30 μm. Experimental verification has been limited to embossed topographies with features whose peak heights do not exceed their widths; such aspect ratios will be sufficient for many manufactured devices.

In the next chapter we will address some further considerations to be made in designing a bulk thermoplastic embossing process. In Chapter 4 we will demonstrate a method of simulating the embossing of extremely feature-rich patterns without needing to represent those patterns at the scale of individual features.

3. Additional modeling considerations for bulk embossing

In the previous chapter, an approach was detailed for simulating the embossing of thick polymeric layers. The model was calibrated for three commonly used thermoplastic materials. We now probe some aspects of the model in more detail. Firstly, we use the model to consider how sensitive a hot-embossing process is likely to be to variation of the true processing parameters of temperature and loading duration. Secondly, we suggest a simple way to select nominal processing parameters when it is desired to fill the cavities of a stamp as completely as possible. We then use images of the birefringence of micro-embossed samples to re-examine the validity of our assumed Kelvin-Voigt material model. We also briefly investigate the long-term room-temperature shape stability of micro-embossed components. In the final parts of this chapter, we discuss the possible relaxation of several model assumptions. Specifically, we show how material compressibility can be accounted for, we suggest a way of modeling material isotropy, and we show how material models other than a Kelvin-Voigt delayed elasticity could be employed.

3.1. Sensitivity of material behavior to processing parameters

When selecting processing parameters it is important to have an understanding of how sensitive the outcome of embossing will be to unwanted deviation of those parameters from their intended values. In Section 2.3, a material model is introduced whose viscous component is a decreasing exponential function of temperature. Meanwhile, in the Voigt model adopted, the material's effective compliance increases rapidly with time near the start of the loading period, and asymptotically approaches the inverse of the model's elasticity. We would expect, therefore, that the effective compliance of a material sample at the end of an embossing cycle could, in certain circumstances, be highly sensitive to variations of temperature or loading duration. We now investigate these sensitivities for a process in which a constant sample-average pressure is applied at a single temperature throughout the loading duration.

3.1.1. Trends in compliance for the three materials tested

In Figure 2.4a are shown pseudo-color maps of the modeled compliances of PMMA, PC and Zeonor 1060R as functions of nominal temperature and pressure. We see that in the case of PMMA, the material compliance increases with temperature up to around 400 K, but that above this temperature the compliance is almost independent of temperature provided that the loading duration exceeds about one minute. At temperatures closer to the material's T_g of ~ 383 K, compliance is a strong function of both loading duration and temperature. Both PC and Zeonor 1060R, meanwhile, exhibit compliances that are comparatively strong functions of temperature and loading duration across the whole parameter space investigated.

3.1.2. Sensitivity of compliance to loading duration

One might expect it to be straightforward to control the loading duration tightly, and indeed we have been able in our experiments to control the loading profile with sub-second precision. What is not well characterized, however, is the time taken for the material to cool before unloading at the end of the embossing period. This time, which was fit as t_{delay} in Chapter 2, is on the order of one minute but is not necessarily accurately known. We therefore illustrate, in Figure 2.4b, the percentage increase in material compliance that results from the addition of one minute of loading duration. The sensitivity to loading duration is at its largest — up to around 40%/min — when the nominal loading duration is short.

3.1.3. Sensitivity of compliance to temperature

In the experiments of Chapter 2, we estimated that the temperature of embossing could be controlled, using our particular apparatus, to within ±1 K. With more sophisticated commercial apparatus it may well be possible to achieve tighter temperature control, but here we adopt ±1 K as a reasonable amount of temperature variation to expect. In Figure 2.4c are illustrated the percentage increases of compliance for a 1 K increase in temperature. What is striking here is that with PC and Zeonor 1060R, even when the material temperature is nominally 15 or 20 K above the glass-transition, a 1 K variation of temperature can bring about a 10–15% change in material compliance. This analysis supports our assertion in Section 2.3 that parasitic temperature variation could have been responsible for much of the sample-to-sample topography variation that is not captured by our model.

3.1.4. Sensitivity of topography to pressure

Since our material model is linear-viscoelastic, it assumes that, for a given material compliance, cavity penetration is proportional to applied pressure in circumstances where no material touches the tops of any of the stamp cavities. Meanwhile, we will show in Chapter 4 that when material begins to be pushed into the corners of stamp cavities, the proportion of cavity-volume filled with material increases sub-linearly with applied pressure for a given material compliance.

3.1.5. Implications for process design

We have seen from this simple analysis that material compliance — and hence the extent of stamp cavity penetration for a given applied load — can certainly be a strong function of both temperature and loading duration. Engineers designing embossing processes would therefore be well advised to select a high enough nominal embossing temperature and a long enough nominal loading duration that even if both parameters were lower in practice by a realistic amount (say, 1 K and 1 minute), successful pattern replication would still be achieved.

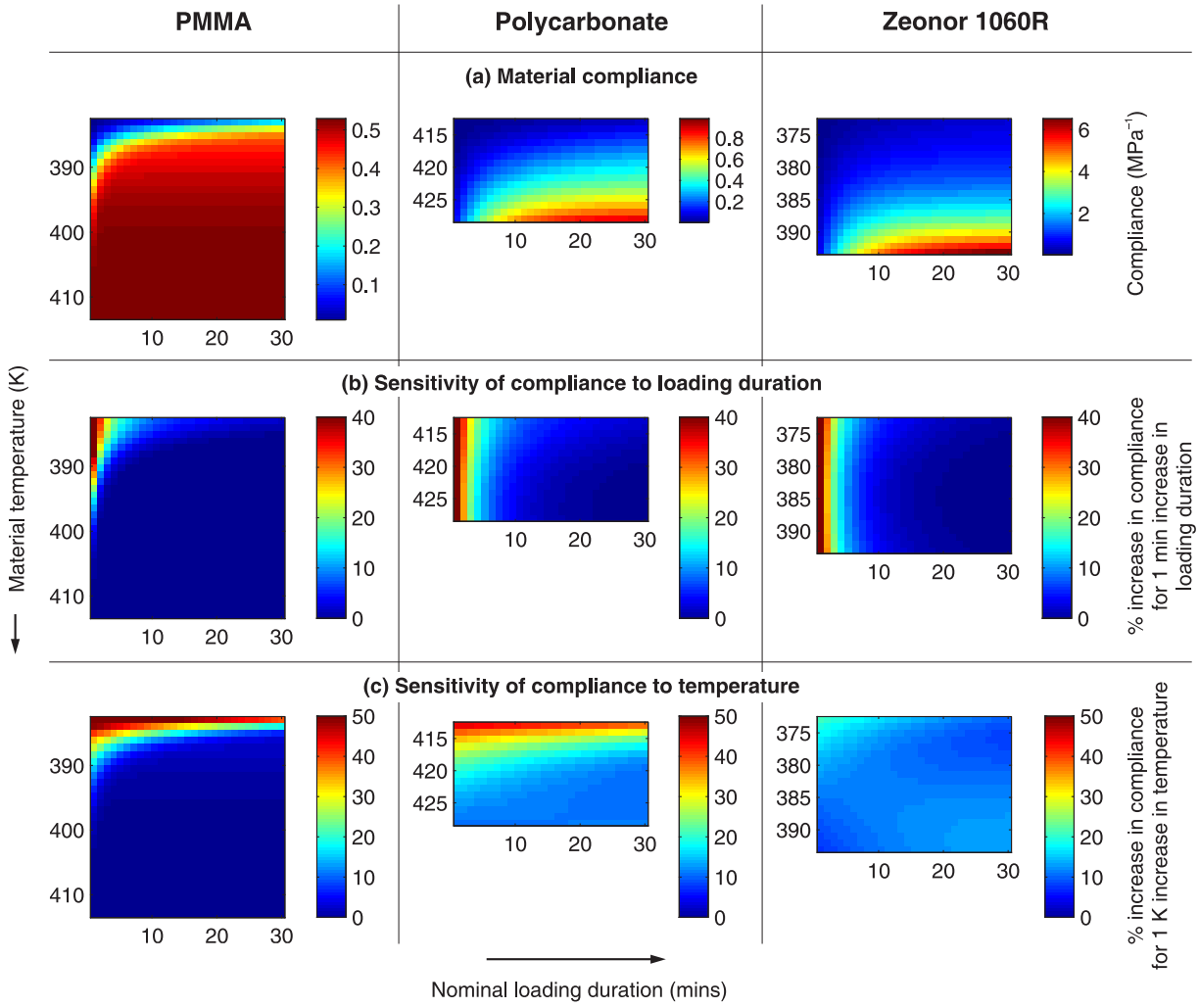

Figure 3.1: Analysis of the sensitivity of effective material compliance to perturbations of loading duration and material temperature. (a) Pseudo-color plots of the material compliances of PMMA, PC and Zeonor 1060R as functions of nominal material temperature and loading duration. (b) Percent increase in material compliance for a 1-minute increase in loading duration. (c) Percent increase in material compliance for a 1 K increase in material temperature. In all plots, the temperature scales are equal: PMMA was calibrated over a wider range of temperature than PC or Zeonor 1060R.

3.2. Selecting processing conditions efficiently when stamp-filling is obligatory

The simulation procedure described in Chapter 2 takes a pressure–time profile as an input and predicts an embossed topography as its output. In doing so, the simulation procedure must guess which portions, C, of the stamp are in contact with the polymer at the end of the embossing cycle. Often this guess needs to be refined, increasing the simulation time.

In many realistic embossing cases, however, it will be essential to fill all stamp cavities with polymer. What is then required from a simulation is a recommendation of the embossing parameters that should be used to achieve complete filling. For example, a user of the simulation method might want to know what pressure to apply at a given temperature and loading duration. The desired topography, then, becomes an *input* to the simulation, and the required embossing pressure becomes the *output*. In this situation, the simulation is actually much simpler to perform than in Chapter 2. The following procedure avoids the need to use the biconjugate gradient method to find the contact pressure distribution, and also avoids any iteration on the contact set C.

1. Assuming that the polymer is incompressible, the final topography is directly calculated from $w_{\text{stamp}}[m, n]$ by considering the conservation of polymer volume. We know that at the end of the embossing cycle every part of the stamp must be in contact with the polymer. We therefore find the value of Δ such that:

$$\sum_{n=1}^{N}\sum_{m=1}^{M}\left(w_{stamp}[m,n]-\Delta\right)=0\,. \tag{3.1}$$

   The topography of the polymer at the end of embossing is then ($w_{\text{stamp}}[m, n] - \Delta$).

2. Secondly, we simply *deconvolve* the final polymer topography ($w_{\text{stamp}}[m, n] - \Delta$) with the point load response $g[m, n]$ of the 'virtual' elastic layer of (2.6). The result of the deconvolution is a scaled pressure distribution, $p_{s,\text{deconv}}[m, n]$, that satisfies the following set of equations:

$$p_{s,deconv}[m,n]*g[m,n]=w_{stamp}[m,n]-\Delta\,. \tag{3.2}$$

   The pressure distribution $p_{s,\text{deconv}}[m, n]$ will include some negative pressures and some positive ones.

3. Since the stamp–polymer interface cannot sustain tensile stresses, every point of $p_{s,\text{deconv}}[m, n]$ is then shifted up by a constant $p_{s,0}$ to yield a new pressure distribution whose minimum value is zero:

$$\left.\begin{aligned}\left(p_{s,deconv}[m,n]+p_{s,0}\right)*g[m,n]&=w_{stamp}[m,n]-\Delta;\\ p_{s,deconv}[m,n]+p_{s,0}&\geq 0 \qquad \forall \quad m,n.\end{aligned}\right\} \tag{3.3}$$

4. The value of $p_{s,0}$ is an estimate of the spatial-average of scaled pressure that is required to fill every cavity of the stamp.

It should be noted that if the topography of the stamp contains discontinuities (*i.e.* steps), the value of $p_{s,0}$ predicted by this method will be strongly dependent on the fineness of discretization of the stamp. In the extreme case, if the stamp were infinitely finely discretized, then an infinitely large pressure $p_{s,0}$ would be predicted by this method. Indeed, according to the material model we have adopted, an infinite pressure *would* be needed to force material *perfectly* into sharp stamp corners. In practice, we are usually willing to accept a certain 'rounding off' of the profile of polymeric material forced into stamp corners. We recommend choosing a discretization pitch for the stamp representation that is equal to the maximum radius of corner 'rounding' that we are willing to accept in the finished component. We anticipate that the

method described here will then yield a value for $p_{s,0}$ that will ensure sufficiently well-formed feature corners at the end of the embossing cycle.

The most computationally expensive part of this method is deconvolving ($w_{\text{stamp}}[m, n] - \Delta$) with $g[m, n]$. This deconvolution will take only a tiny fraction of the time that the biconjugate gradient method would have taken to find a pressure solution, given a matrix $w_{\text{stamp}}[m, n]$ of the same size but where the contact set C was not full. (The biconjugate gradient method itself involves *many* forward convolutions.) If all we require of the simulation method is an estimate of the embossing pressure needed to fill cavities, the approach presented here will be greatly preferable to that of Section 2.1.

3.3. Modeling and interpreting birefringence in embossed components

Birefringence is anisotropy of the refractive index of a material. It can be made to manifest itself as a colored pattern by placing a birefringent object between two polarizing filters and illuminating the object transmissively. To first order, the birefringence of a material sample is proportional to the difference between its principal compressive stresses in a plane normal to the direction of propagation of light. The constant of proportionality (the 'stress-optic' coefficient) is a material property and is sufficiently large for many thermoplastic polymers that polymeric samples with residual stresses may exhibit easily observable birefringence.

An ability to simulate patterns of birefringence in micro-embossed structures could be valuable in three ways. Firstly, by allowing us to quantify the residual stresses in experimental samples it could help us to probe further the validity of our Voigt material model. Secondly, it could help engineers to predict the birefringence that would be associated with a candidate embossing pattern and process. Since birefringence might be parasitic in, say, microfluidic devices relying on optical inspection of their contents, a birefringence simulation could become an important design check. Thirdly, birefringence can in some circumstances be a *useful* property. Nanoimprint lithography has already been used to produce *form*-birefringent optical components [135]; the ability to simulate and therefore control *stress-induced* birefringence in micron-scale embossed patterns might offer a useful alternative way of producing optical components.

In this section, then, as a first step, we study and attempt to model the birefringence observed in a subset of the experimental samples of Chapter 2.

3.3.1. Measurement of birefringence

We have adopted the measurement configuration illustrated in Figure 3.2a–b, where an embossed polymeric sample is placed between two polarizing filters, and white light, having been polarized by one of the filters, passes through the sample and then through the second polarizing filter, the 'analyzer'. The surface of the sample that has been in contact with the embossing stamp defines the xy plane, with the x-axis being the axis of the polarizer. Light propagates in the z direction. At any given point (x, y, z) in the sample, the principal compressive stresses σ_1 and σ_2 are oriented at an angle θ to the x and y axes respectively.

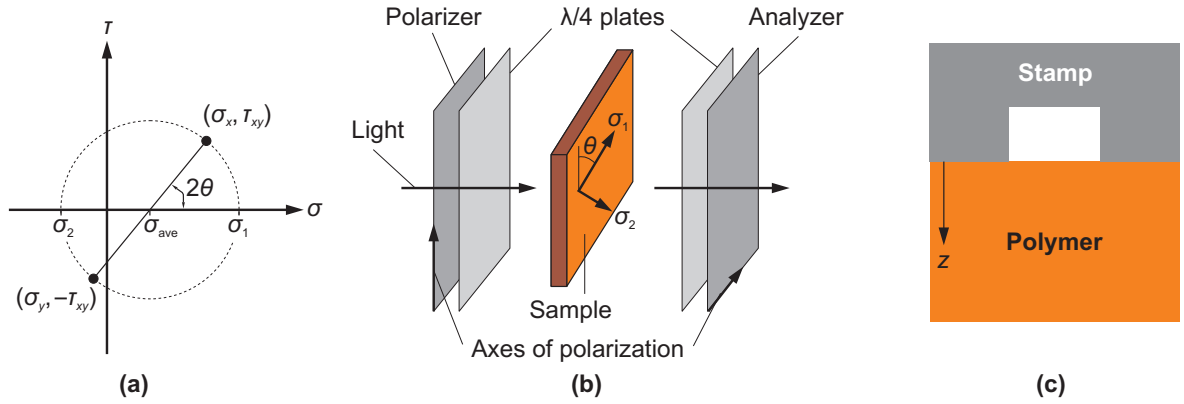

Figure 3.2: Measurement of birefringence in hot-embossed samples. (a) Mohr's circle showing definitions of the principal compressive stresses $\sigma_{1,2}$ in terms of the compressive stresses σ_x and σ_y and shear stress τ_{xy} in the frame of the sample. (b) Polariscope setup. Quarter-wave plates are present in a circular polariscope. In a plane polariscope, the quarter-wave plates are omitted. In a dark-field polariscope, the axes of polarization of polarizer and analyzer are perpendicular; in a light-field polariscope, they are parallel. The angle between the axis of principal stress σ_1 and the axis of the polarizer is θ. (c) Cross-section through embossed polymeric sample, indicating the location of the stamp during the preceding embossing step. Direction *z* is parallel to the direction of propagation of light, and the principal stress axes of interest lie in planes of constant *z*.

A polariscope that includes the quarter-wave plates illustrated in Figure 3.2b is termed a circular polariscope; one without them is a plane polariscope. In plane polariscopes, the observed birefringence pattern is strongly dependent on angle θ.

In the case of the plane polariscope, the relative orientation of the axes of polarization of the two filters is important. If they are perpendicular, the polariscope setup is referred to as 'dark-field', and regions of the sample with no birefringence would appear dark. If the filters' axes were parallel, the polariscope would, conversely, be 'light-field'. For the circular polariscope, the relative orientation of the axes of polarization does not have a strong effect; instead, the orientations of the axes of the quarter-wave plates relative to those of their adjacent polarizers determine whether the polariscope is light- or dark-field [209].

The local birefringence, $\Delta n(x, y, z)$, is the difference between the refractive indices in the 1 and 2 axes, and is proportional to the difference of principal compressive stresses. The constant of proportionality, C, is the material-dependent stress-optic coefficient:

$$\Delta n(x,y,z) = n_1(x,y,z) - n_2(x,y,z) = C\Delta\sigma(x,y,z) = C\left[\sigma_1(x,y,z) - \sigma_2(x,y,z)\right]. \tag{3.4}$$

The observed birefringence pattern is a function of the 'retardation', $\delta(x, y)$, which is the through-thickness integral of the birefringence with respect to z:

$$\delta(x,y) = \int_{z=0}^{z=t_{polymer}} C\Delta\sigma(x,y,z)\mathrm{d}z. \tag{3.5}$$

3.3.2. Simulation approach for birefringence

If we can estimate the distribution of compressive residual stresses throughout a sample, we can generate an RGB bitmap image that is a simulation of the pattern that would be observed in a polariscope. For a circular dark-field polariscope, the simulated intensity $I_{c,total}[m, n]$ in each color channel c of the RGB image can be approximated [210] by:

$$\left.\begin{aligned} I_{c,total}[m,n] &= \sum_{k_\lambda=350}^{820} I_c(\lambda)\sin^2\left(\frac{\pi\,\delta[m,n]}{\lambda}\right) \\ \text{where: } \lambda &= k_\lambda \times 1\text{ nm}; \\ x &= md;\ \ y = nd; \\ c &\in \{\text{red}, \text{green}, \text{blue}\}. \end{aligned}\right\} \tag{3.6}$$

The quantity $I_c(\lambda)$ is the normalized intensity value in color channel c arising from light of wavelength λ, and a good model for these intensity values is specified in Figure B.2 of Appendix B. The resulting total intensity values, $I_{c,total}[m, n]$, are normalized to have a maximum value of 1 in any color channel:

$$I_{c,norm}[m,n] = \frac{I_{c,total}[m,n]}{\max(I_{c,total}[m,n])} \tag{3.7}$$

where $\max(I_{c,total}[m, n])$ is the maximum value taken over all locations $[m, n]$ *and* over all three color channels c.

For a light-field polariscope, the $\sin^2(\cdot)$ term in (3.6) is replaced by a $\cos^2(\cdot)$ term having the same argument. For a plane polariscope, $I_{c,total}[m, n]$ is additionally multiplied by the attenuation term $\sin^2(2\theta[m, n])$.

We have used the simulation framework described above to plot, in Figure 3.3, the channel intensities and approximate colors that would be observed in light- and dark-field polariscopes for a range of retardations, δ.

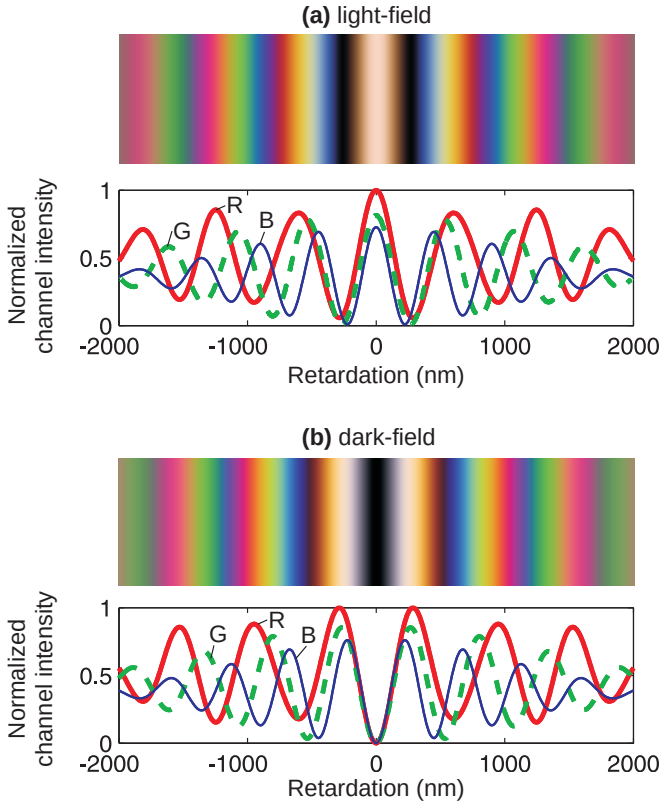

Figure 3.3: Fringe colors for (a) light-field and (b) dark-field polariscopes. Normalized RGB intensities are also plotted. Fringes are illustrated for retardations lying between ± 2000 nm.

3.3.3. Experimental observations

In Figure 3.4 are shown scanned images from a subset of the embossed samples of Chapter 2. A light-field circular polariscope was constructed by placing each sample between two photographic circular polarizing filters, and the images were obtained with an Epson Photo V100 scanner in transmissive illumination mode. Each sample is approximately 25 mm square and the central 12 mm square of each sample contains the micro-embossing test pattern.

The scan of the PMMA sample indicates that even for embossing pressures at the higher end of our experimental range, birefringence is slight. In PC, meanwhile, birefringence is much more prominent. The colored bands that extend across each of the samples indicate the residual stresses associated with their global deformation, these stresses presumably extending through the 1.5 mm thickness of the samples. At a given temperature and loading duration, increasing the embossing pressure has led to a larger number of visible birefringence fringes. At 140 °C, the sample with a loading duration of 30 minutes and p_0 = 2 MPa exhibits more closely packed fringes than the sample loaded for 2 minutes at 4 MPa, suggesting that the amount of birefringence depends not only on the pressure applied during embossing but also on the amount of material deformation achieved. In the central patterned region of each sample, we see perturbation of the birefringence patterns at the scale of individual features, and it is these perturbations that we attempt to model in the following sections.

In the case of Zeonor 1060R, we again see prominent birefringence, although the sample processed at 120 °C under 0.14 MPa for 30 minutes is an exception in that it exhibits almost no discernible birefringence.

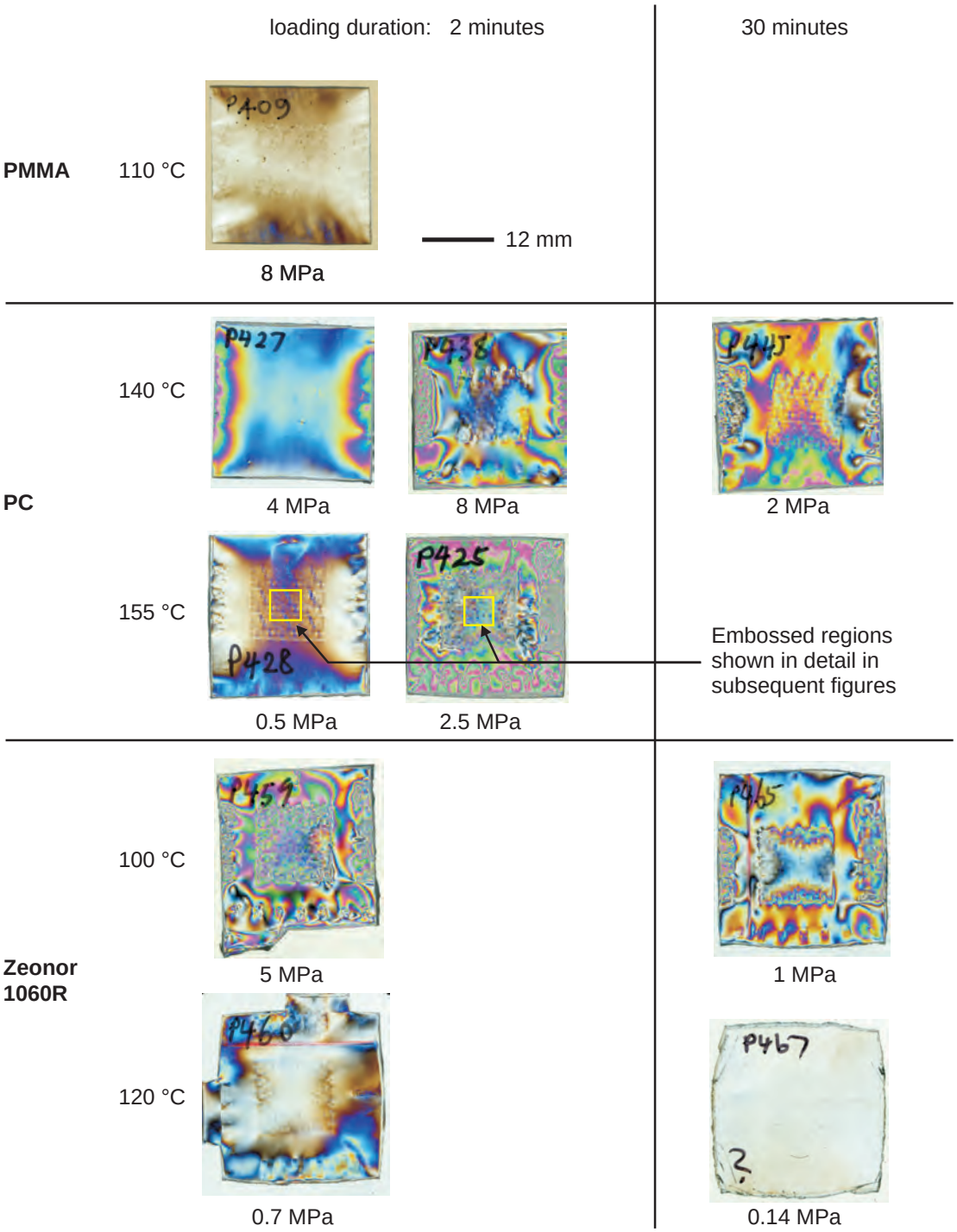

Figure 3.4: Birefringence scans in a light-field circular polariscope for several of the samples that provided the data of Chapter 2.

3.3.4. Comparing birefringence results with the residual stress predictions of a linear, Voigt model

To interpret the birefringence patterns observed, we consider the residual stresses that are implied by the linear Voigt model we have assumed. Figure 3.5 shows a one-dimensional representation of a Voigt material. During embossing, occurring at temperature T_{emboss}, the externally applied embossing load is shared between sustaining elastic deformation of the polymer network and driving further viscous flow. We denote as ε the compressive strain of this one-dimensional model at the end of the embossing period. The stress in the elastic branch just before cooling is $\varepsilon E(T_{\text{emboss}})$, where E is the temperature-dependent elasticity of the polymer network. Just after cooling and removal of the external load, meanwhile, the stresses in the two branches of the model would be in equilibrium and equal in magnitude to εE_{g}, where E_{g} is the elasticity of the material in its glassy state.

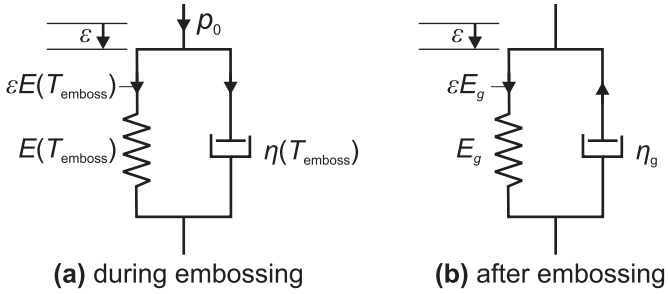

Figure 3.5: Schematic of stresses associated with the Voigt model. During embossing (a), externally applied embossing load is shared between deforming the elastic molecular network and driving viscous flow; in this 1-D representation, ε represents the strain achieved at the end of the embossing process. After embossing (b), when the material has been cooled, external loads have been removed, and viscous flow is negligibly slow, there is a residual stress in the material of εE_g.

The value of ε depends on the material's elasticity and viscosity during embossing, and on the embossing load, p_0, and duration, t_{hold}. Following the 'effective modulus' or 'virtual substrate' arguments of Section 2.1.2, we can express ε as:

$$\varepsilon = \frac{p_0\left[1-\exp\left(\frac{-t_{hold}E(T_{emboss})}{\eta(T_{emboss})}\right)\right]}{E(T_{emboss})} = \frac{p_0}{E_{effective}(T_{emboss},t_{hold})}. \tag{3.8}$$

It follows that in this uniaxial model, the residual stress is related to the embossing pressure as follows:

$$\sigma_{residual} = \varepsilon E_g = \frac{p_0 E_g}{E_{effective}(T_{emboss},t_{hold})}. \tag{3.9}$$

In a three-dimensional embossing case, we would expect the distribution of residual stresses to be equal to the distribution of total material stresses *during* embossing, multiplied by the factor $E_{\text{g}}/E_{\text{effective}}$.

To see whether this simple argument is supported by the observed birefringence patterns, we compute the quantity $p_0E_{\text{g}}/E_{\text{effective}}$ for each PC and Zeonor 1060R sample whose birefringence patterns are shown in Figure 3.4. These computed values are shown in Table 3.1. The larger the value of $p_0E_{\text{g}}/E_{\text{effective}}$, the larger, on average, we would expect residual stresses in the material, and hence birefringence, to be. The values taken for $E_{\text{effective}}$ are computed using the parameters fit in Section 2.3. Meanwhile, the value we require for E_{g} is that at room temperature, since birefringence measurements are made at room temperature. Our temperature-dependent material elasticity function is not necessarily valid this far below the glass-transition, but we do nevertheless use the value of parameter E_{g} that was fit in Section 2.3.

Table 3.1: Computed values of $p_0E_g/E_{effective}$ for the experimental samples illustrated in Figure 3.4.

Embossed material	Embossing temperature (°C)	Loading duration: 2 min		Loading duration: 30 min	
		p_0 (MPa)	$p_0E_g/E_{effective}$ (MPa)	p_0 (MPa)	$p_0E_g/E_{effective}$ (MPa)
PC	140	4	0.20	2	1.25
		8	0.40		
	155	0.5	1.21		
		2.5	6.05		
Zeonor 1060R	100	5	1.07	1	1.38
	120	0.7	2.64	0.14	2.28

Looking at the calculated values of $p_0E_g/E_{effective}$ for PC and studying the associated birefringence images, we gain some qualitative support for our continued assumption of a Voigt model. The larger $p_0E_g/E_{effective}$, the greater the sample-scale birefringence appears to be in the images. By far the largest value of $p_0E_g/E_{effective}$ occurs for the sample processed at 155 °C under 2.5 MPa, and, indeed, the associated birefringence image shows a substantially greater density of birefringence fringes than seen in the other samples.

For Zeonor 1060R, however, the birefringence images do not support the assumed Voigt model. The computed values of $p_0E_g/E_{effective}$ for the samples processed at 120 °C are substantially larger than those for the samples processed at 100 °C. Yet the amount of birefringence observed in the 120 °C samples is much *less* than in the 100 °C samples. Indeed, the sample loaded for 30 minutes at 120 °C shows almost no discernible birefringence. These results might be interpreted as indicating that a substantial portion of the deformation was *permanent* in the samples processed at 120 °C. Physically, this result could be explained in terms of slipping of the entanglements of the polymer chains, such that, when cooled, the polymer network would not sustain as much residual stress as our simple Voigt model predicts. In Section 2.3.8, meanwhile, we showed the results of annealing a Zeonor 1060R sample at 120 °C, and observed *some* shape recovery. Taking that annealing result together with the birefringence images of this section, we begin to build the impression that some, but not all, of the deformation of Zeonor 1060R at 120 °C is permanent. The amount of data that we currently have is, however, much too small to model this behavior completely.

3.3.5. Modeling birefringence patterns

The sample-scale birefringence patterns shown in Figure 3.4 are rather intricate and appear to depend both on the overall geometry of the sample and on the layout of the pattern embossed into it. In some cases, fringes appear to 'flow' around the edges of patterned regions. Simulating these patterns successfully would require a detailed model of the whole sample, and is not something that we attempt here. What we do instead is to model the comparatively small-scale birefringence variations that occur locally within the embossed test-pattern. We assume the embossed pattern to be periodic in space, and can therefore extend the discrete-space simulation procedure of Chapter 2 to model the birefringence.

The simulation relies on having computed the stamp–polymer contact distribution, $p[m, n]$, at the end of the embossing cycle, using the procedures of Chapter 2. From $p[m, n]$, we can estimate the residual compressive stresses, $\sigma_x[m, n, k_z]$ and $\sigma_y[m, n, k_z]$, and shear stresses, $\tau_{xy}[m, n, k_z]$, at a range of depths, z, beneath the embossed surface, where $z = k_z\Delta z$. Assuming a Kelvin-Voigt material model, these stresses are found by convolving $(E_g/E_{effective})\times p[m, n]$ with appropriate kernel functions, such as those defined by Nogi and Kato [188]. Nogi and Kato present analytical expressions for these kernels in the spatial frequency domain. $S_x[m, n, k_z]$ is the Fourier transform of $\sigma_x[m, n, k_z]$, describing the compressive stress in

the x-direction and at sub-surface depth $k_z\Delta z$ in response to unit pressure applied normally to the surface over the small $d \times d$ region at ($m = 0$, $n = 0$). Similarly, $S_y[m, n, k_z]$ is the Fourier transform of $\sigma_y[m, n, k_z]$, and $T_{xy}[m, n, k_z]$ is that of $\tau_{xy}[m, n, k_z]$:

$$\left.\begin{aligned} S_x[m,n,k_z] &= -\left(\frac{n\pi}{Nd}\right)^2\left(A+\tilde{A}\right)+2\nu\alpha\left(B-\tilde{B}\right)-k_z\Delta z\left(\frac{n\pi}{Nd}\right)^2\left(B+\tilde{B}\right) \\ S_y[m,n,k_z] &= -\left(\frac{m\pi}{Nd}\right)^2\left(A+\tilde{A}\right)+2\nu\alpha\left(B-\tilde{B}\right)-k_z\Delta z\left(\frac{m\pi}{Nd}\right)^2\left(B+\tilde{B}\right) \\ T_{xy}[m,n,k_z] &= -\left(\frac{n\pi}{Nd}\right)\left(\frac{m\pi}{Nd}\right)\left(A+\tilde{A}\right)-k_z\Delta z\left(\frac{n\pi}{Nd}\right)\left(\frac{m\pi}{Nd}\right)\left(B+\tilde{B}\right) \end{aligned}\right\} \tag{3.10}$$

where

$$\left.\begin{aligned} &\alpha=\sqrt{\left(\frac{m\pi}{Nd}\right)^2+\left(\frac{n\pi}{Nd}\right)^2};\quad \lambda=1-4(1-\nu);\quad \kappa=\frac{1}{4\nu-3} \\ &A=\left[-(1-2\nu)\left\{1-(1-2\alpha t_{polymer})\kappa\exp(-2\alpha t_{polymer})\right\}\right. \\ &\qquad\left.+0.5\left(\kappa-\lambda-4\kappa\alpha^2 t_{polymer}{}^2\right)\exp\left(-2\alpha t_{polymer}\right)\right]R\exp(-\alpha k_z\Delta z) \\ &\tilde{A}=\left[(1-2\nu)\kappa\left\{1+2\alpha t_{polymer}-\lambda\exp(-2\alpha t_{polymer})\right\}\right. \\ &\qquad\left.+0.5\left(\kappa-\lambda-4\kappa\alpha^2 t_{polymer}{}^2\right)\right]\exp(-2\alpha t_{polymer})R\exp(\alpha k_z\Delta z) \\ &B=\left[1-(1-2\alpha t_{polymer})\kappa\exp\left(-2\alpha t_{polymer}\right)\right]\alpha R\exp\left(-\alpha k_z\Delta z\right) \\ &\tilde{B}=\left[1+2\alpha t_{polymer}-\lambda\exp\left(-2\alpha t_{polymer}\right)\right]\kappa\exp\left(-2\alpha t_{polymer}\right)\alpha R\exp\left(\alpha k_z\Delta z\right) \\ &R=-\left[1-\left(\lambda+\kappa+4\kappa\alpha^2 t_{polymer}{}^2\right)\exp\left(-2\alpha t_{polymer}\right)+\lambda\kappa\exp\left(-4\alpha t_{polymer}\right)\right]^{-1}\alpha^{-2}. \end{aligned}\right\} \tag{3.11}$$

From these stresses, the angle θ between the 1-axis of principal stress and the axis of the polarizer can readily be computed for each location $[m, n, k_z]$. Hence the residual principal compressive stresses σ_1 and σ_2 can be found. We define the 1-direction as the axis of principal compressive stress that lies closer to the x-axis:

$$\left.\begin{aligned} \tan 2\theta &= \frac{\tau_{xy}}{\sigma_x-\sigma_{ave}} \\ \text{where}\quad \sigma_{ave} &= \frac{\sigma_x+\sigma_y}{2}. \end{aligned}\right\} \tag{3.12}$$

Figure 3.6 illustrates the distribution of simulated residual stresses after the embossing of our micron-scale test pattern. The orientations of the x and y axes are shown in the figure. The simulated region is 4 mm square and the pitch of discretization of the region is 5 μm. The simulation shown is for a case where, at the end of the embossing cycle, the quantity $(E_g/E_{\text{effective}})\times p_0$ is 0.5 MPa and no material has

touched the tops of any stamp cavities. Because the feature-edges of this pattern all run parallel to the *x* or *y* axes, the axes of principal stress are approximately parallel to the *x* and *y* axes throughout most of the material. It is only near feature corners that $\tau_{xy}[m, n, k_z]$ becomes appreciable and θ deviates substantially from zero. If the pattern were to be rotated relative to the polarizer, the principal axes of stress would of course also rotate, and θ would take on some *non*-zero value from which deviations throughout the sample would still mostly be small.

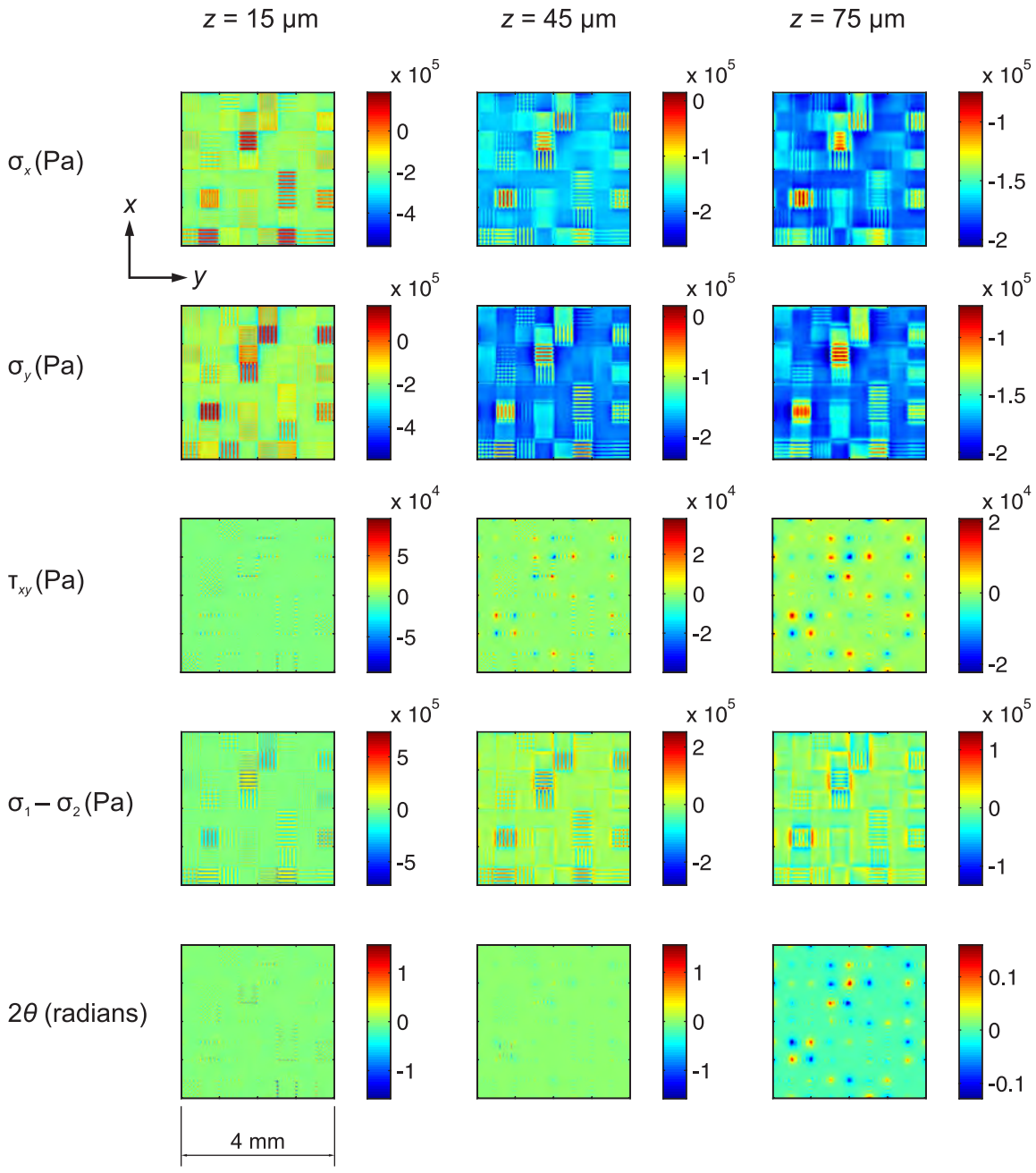

Figure 3.6: Simulated residual stresses and values of 2θ in three planes close to the embossed surface of a sample, for the case of embossing a Voigt material where $(E_g/E_{effective})\times p_0$ = 0.5 MPa.

If θ varies little with position, as in this pattern, it is relatively simple to generate an approximate simulation of the birefringence pattern for any given type of polariscope. Firstly, we evaluate the total through-sample retardation $\delta[m, n]$ as a function of position. Approximating $\sigma_1 = \sigma_x$ and $\sigma_2 = \sigma_y$, and defining $\Delta\sigma_{\text{residual}} = \sigma_1 - \sigma_2$, we have:

$$\delta[m,n] = \sum_{k_z=1}^{K_z} C\Delta\sigma_{residual}[m,n,k_z]\Delta z + \delta_0. \tag{3.13}$$

Here, C is the stress-optic coefficient, and the summation is performed over a series of K_z slices of thickness Δz, moving down into the polymer layer. The residual stresses at each layer are evaluated at a depth $k_z\Delta z$ beneath the surface of the polymer. For the specific simulations presented in this section, $K_z = 10$ and $\Delta z = 15$ µm, such that we simulate pattern-related birefringence down to a depth of 150 µm beneath the embossed surface, or 10% of the thickness of the material. Beneath this depth we assume differences of principal compressive stress arising from the presence of the microscopic pattern to be negligible.

Meanwhile, δ_0 is a 'background' retardation associated with any initial birefringence in the material and with the global distortion of the polymer plate that occurs during embossing. We assume that this sample-scale component of birefringence varies sufficiently smoothly with position that in the small region being simulated we can approximate it using the uniform value δ_0.

We also neglect any effects associated with the topography of the embossed surface, assuming that material forced up into stamp cavities experiences very small residual stresses and exhibits minimal birefringence.

The final step of the simulation is to generate the RGB image according to (3.6). If a circular polariscope is being used, the observed pattern will be essentially independent of θ. If a plane polariscope is being used, a value must be assumed for $\theta[m, n]$. In the simulations presented here, we assume a constant value of θ for the entire pattern, based purely on the orientation of the sample relative to the polarizer. In simulations of patterns having features *not* on a rectangular grid, θ would almost certainly need to be defined as a function of m and n within the pattern.

3.3.6. Calibrating birefringence simulations to experimental results

We have used the simulation procedure outlined above to try to quantify the stress-optic coefficient of two of the polycarbonate samples we examined. Considering first the sample embossed for two minutes under 0.5 MPa at 155 °C, we obtained close-up scans of the central 4 mm square region of the embossed pattern, placed between two linear polarizers. Images were obtained of the same sample in both dark- and light-field polariscope modes. These images are shown on the top row of Figure 3.7.

The captured images enable us to estimate values for C and δ_0. We continue to assume the Kelvin-Voigt material model fit in Chapter 2, and for this sample our estimate of $(E_g/E_{\text{effective}})\times p_0$ is 1.21 MPa (from Table 3.1). By iteratively varying C and δ_0 until the colors of the simulated birefringence images resembled those of the measured ones, the use of our Voigt model implies C to be 9.5×10^{-9} /Pa and δ_0, in this central 4 mm square portion of the sample, to be –230 nm.

From Figure 3.7 we see that our simulations have captured several salient features of the observed birefringence patterns. In the light-field image, a brownish color throughout much of the pattern becomes an electric blue in the vicinity of some of the patches of features, and yellowy in others: the simulation has represented these trends. Our simulation of the dark-field image also captures the coloring observed experimentally. The simulations, of course, are not perfect, and in particular it appears that the 'background' birefringence is not truly uniform across the field of view: it seems to have led to a 'patchiness' of the experimental images that cannot be represented by our simulation procedure.

What is of more concern is that our estimate for C is about three orders of magnitude larger than literature values for the stress-optic coefficient of PC (*e.g.* [211]). This discrepancy raises serious questions about the validity of our model for the evolution of residual stresses (Figure 3.5). It is possible that the value we have adopted for E_g is far too low: we used a value calibrated using data from around T_g but are trying to simulate birefringence at room temperature. It may well be, however, that a more sophisticated material model is needed to represent birefringence truly effectively.

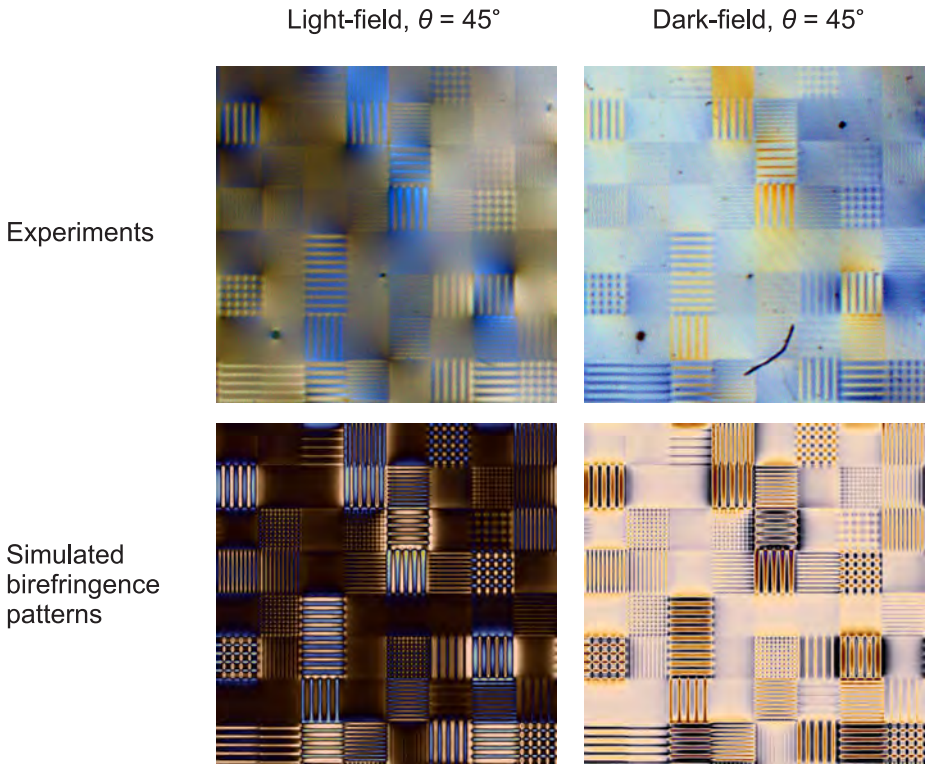

Figure 3.7: Comparison of experimental birefringence results and simulated birefringence images for a PC sample embossed at 155 °C under 0.5 MPa for two minutes. Experimental images were taken with a plane polariscope.

Figure 3.8 shows dark-field images of the pre-embossing birefringence of the three materials embossed. Considering the dark blue color of the polycarbonate image, and referring to the plot of Figure 3.3, we estimate the initial retardation of the sheet to be approximately ±650 nm. It is certainly conceivable, then, that a portion of the sample's pre-embossing birefringence remains in the polymer post-embossing and accounts for the 'background' retardation of –230 nm that was fit for the above sample.

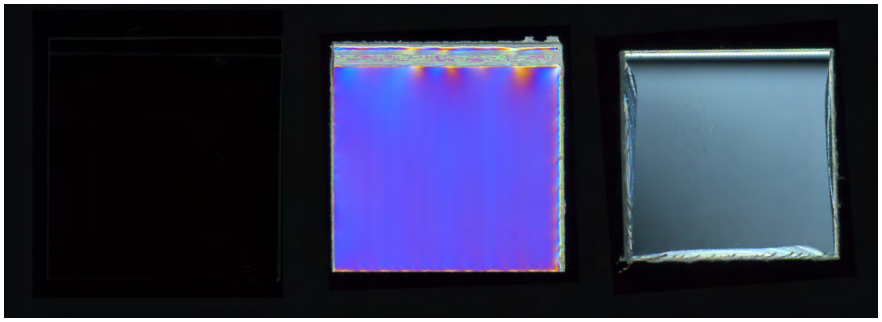

(a) **(b)** **(c)**

Figure 3.8: Dark-field plane-polariscope birefringence images for samples of (a) PMMA, (b) PC, and (c) Zeonor 1060R, after cutting but before embossing.

We have also attempted to model the birefringence in a polycarbonate sample embossed for two minutes at 155 °C under the higher pressure of 2.5 MPa. The corresponding experimental image in Figure 3.9 shows a distinct 'patchiness' of color, which presumably results from non-uniform background birefringence. It is difficult to fit values of C and δ_0 for this image, but a reasonable simulation of feature-scale birefringence variations near the center of the field of view appears to be obtained for $C = 1.9 \times 10^{-9}$/Pa and $\delta_0 = -400$ nm. If our Voigt model-based description of the evolution of residual stresses was robust, we would expect the values of C fit for the two samples to be the same; they are not. Our crude theoretical picture of how residual stresses develop after embossing does not therefore appear to be consistent with our observations. Further experiments would certainly be needed before drawing firm conclusions.

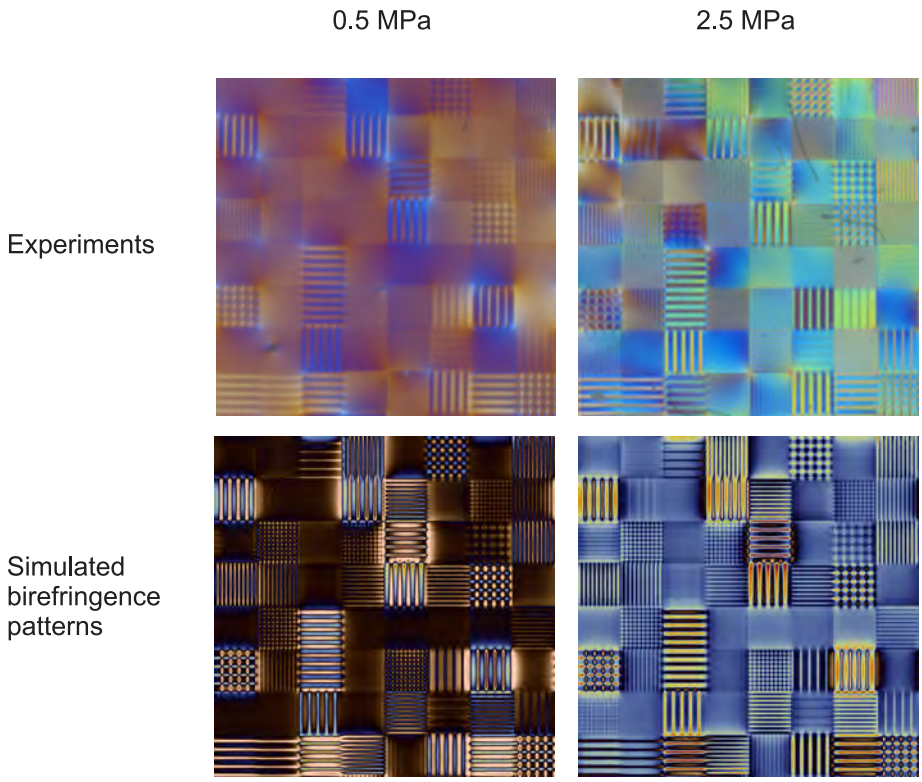

Figure 3.9: Comparison of experimental and simulated birefringence images for polycarbonate samples embossed at 155 °C for two minutes under two different pressures: 0.5 MPa and 2.5 MPa. The background retardations fit are –230 nm and –400 nm respectively; the amount of pattern-related retardation fit is identical in both cases, in spite of the fact that five times as much pressure was being applied to one of the samples as to the other.

3.3.7. Making use of birefringence

In this section we have succeeded in showing a promising way of simulating patterns of birefringence in micro-embossed components. The simulation procedure is computationally inexpensive: it merely involves generating a set of three kernel functions and performing some convolutions and multiplications. The input to a simulation is a contact pressure distribution that would presumably already have been generated during the mechanical design of the pattern.

Two key things are needed before it will be possible to harness micro-structured birefringence in the fabrication of optically useful structures. Firstly, patterns of birefringence at the scale of the polymeric sample need also to be understood and controlled: this ‘background’ birefringence can tend to dominate over pattern-dependent birefringence variations. Secondly, we need a firmer understanding of how residual stresses evolve during and after embossing in the thermoplastic materials of interest.

3.4. Room-temperature dimensional stability of micro-embossed topographies

In Section 2.3.8 we explored the substantial shape-recovery that occurs when previously embossed samples of PMMA, PC and Zeonor 1060R are ‘soaked’ above their glass-transition temperature with no externally applied loads. Below their glass-transition temperatures, meanwhile, the materials’ intermolecular resistances to flow are known to be several orders of magnitude greater than above T_g [202]. Here we confirm that at room temperature — which is well below T_g for the three materials investigated — there is no discernible change in micro-embossed topographies over a period of eight to nine months after embossing.

Three representative samples were chosen and were re-measured, between eight and nine months after embossing, using scanning white-light interferometry. Figure 3.10 shows the peak cavity penetrations of the 50 μm-pitch features on the samples, measured both before and after the 8–9 month period. There is no discernible consistent change in the peak cavity penetrations of any of the three samples measured.

These observations suggest that micro-embossed pieces of PMMA, PC or Zeonor 1060R have shelf-lives of at least eight months, provided that they are stored at room temperature. Being able to *store* microfabricated devices is not enough, however: it must also be possible to *use* the devices without unwanted shape distortions occurring. Certain types of microfluidic devices — for example polymerase chain reactors — need to operate well above room temperature. It could therefore be valuable to perform additional ageing experiments in which micro-embossed samples of various polymeric materials were held at temperatures close to, but below, the glass-transition, and any shape changes were measured over time.

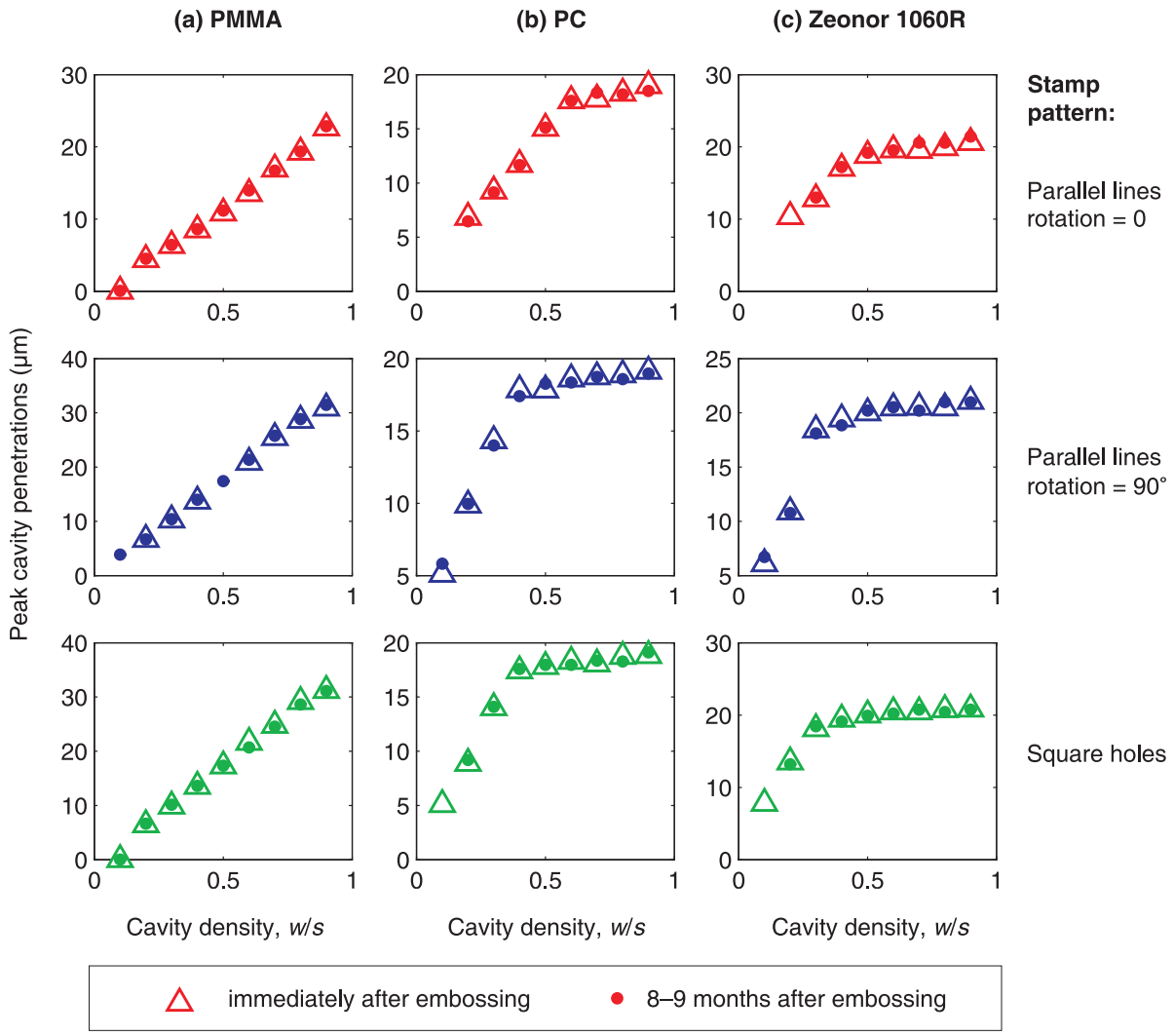

Figure 3.10: Peak cavity penetrations for one representative embossed sample of each material explored, measured (*i*) within a few days of embossing and (*ii*) 8–9 months after embossing. Feature pitch, *s*, was 50 μm. No discernible systematic shape changes have occurred in any of the materials over the time-period examined. (a) PMMA embossed at 130 °C for 2 min under 1.5 MPa; (b) PC embossed at 155 °C for 2 min under 2.5 MPa; (c) Zeonor 1060R embossed at 120 °C for 2 min under 0.7 MPa.

3.5. Compressibility of the polymeric layer

The impulse-response expressions used in Chapter 2 are derived for an infinitely thick embossed layer. Provided that layer deflections and the characteristic dimensions of the features being embossed are everywhere much smaller than the true thickness of the layer, it is reasonable to suppose that the embossed topography will be substantially insensitive to the actual layer thickness. At the bottom of such a layer, the stresses will be almost indistinguishable from those that would arise if a uniform contact pressure were applied at the top of the layer. Of course, the amount of *global* compression of the layer depends strongly on the original layer thickness and the average applied contact pressure. We can capture

this global compression in our calculated value of the stamp's rigid body displacement, Δ, by adding a constant term to every element of the filter $g[m, n]$ or $g[m]$.

Assuming that the layer is either (*i*) infinite in extent and experiences a periodic pressure distribution, or (*ii*) laterally clamped at its edges, we can represent the global compression of the layer as shown in Figure 3.11. We model the applied embossing pressure as a uniform $p_{s,0}$; the infinite extent of the layer in x and y or, equivalently, clamped layer edges are reflected by the imposition of zero strain in the x and y directions. Therefore, defining strains as positive-compressive:

$$\left.\begin{aligned} E\varepsilon_{zz} &= p_{s,0} - \nu\left(p_{xx} + p_{yy}\right) \\ E\varepsilon_{xx} &= 0 = p_{xx} - \nu\left(p_{yy} + p_{s,0}\right) \\ E\varepsilon_{yy} &= 0 = p_{yy} - \nu\left(p_{xx} + p_{s,0}\right) \\ \varepsilon_{zz} &= \frac{p_{s,0}}{E}\left(1 - \frac{2\nu^2(1+\nu)}{1-\nu^2}\right) \end{aligned}\right\} \tag{3.14}$$

The convolution of a uniform contact pressure distribution of magnitude $p_{s,0}$ with the filter $g[m, n]$ implies the following displacement, Δ, of the layer's surface:

$$\Delta = p_{s,0}\sum_{n=0}^{N-1}\sum_{m=0}^{M-1} g[m,n] \tag{3.15}$$

and Δ is proportional to the initial layer thickness, h_s:

$$\Delta = \varepsilon_{zz} h_s \tag{3.16}$$

such that:

$$\sum_{n=0}^{N-1}\sum_{m=0}^{M-1} g[m,n] = \frac{h_s}{E}\left(1 - \frac{2\nu^2(1+\nu)}{1-\nu^2}\right). \tag{3.17}$$

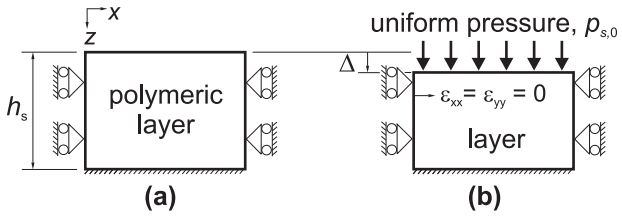

Figure 3.11: Representing global compression of finite-thickness substrates. (a) Substrate before loading; (b) substrate under *uniform* applied pressure in *z* direction.

The global compression behavior of the layer may therefore be approximated by adding a constant value to every element of $g[m, n]$ so that it satisfies (3.17) above. The same approach works in the plane-strain case. The *shape* of the simulated topography is not affected by this constant term in the filter; the only effect is a change in the rigid-body stamp displacement Δ.

It has been found experimentally that amorphous polymers are essentially incompressible above their glass-transition temperatures [202], which is why all embossing simulations in Chapter 2 assumed Poisson's ratio to equal 0.5. The values of $g[m, n]$ or $g[m]$ were therefore shifted so that the filter's mean

value was zero. We have shown here that if it is desired in the future to represent rigid-body stamp displacements for the embossing of compressible layers of finite thickness, it is possible to adjust the filter's mean value appropriately.

There will be some embossing situations in which it is inappropriate to model the substrate as infinite in lateral extent or as laterally clamped at its edges. In these cases, the global compression of the layer will be a function of the layer's specific geometry and the coefficients of friction between the layer and the surfaces with which it is in contact. As a result, care must be taken when using this modeling approach to simulate a 'displacement-controlled' embossing system in which the rigid body motion of the stamp is prescribed and the contact pressure average is allowed to vary accordingly. In displacement control, unless the global compliances of the polymeric layer and of the embossing machine are well modeled, simulation of the topography of a micro-embossed pattern is unlikely to be reliable. In force-controlled embossing, meanwhile, the fidelity of pattern filling can be well simulated without an accurate model of the overall compliance of the polymeric layer or embossing machine.

3.6. Accounting for material anisotropy

Throughout the preceding work, it has been assumed that the materials being embossed have isotropic mechanical properties. All the experimental data obtained from PMMA, PC and Zeonor 1060R have supported this assumption. There may however be cases in which an embossed polymeric sheet is strongly anisotropic. Thermoplastic sheets or plates are variously prepared by casting, extrusion, and injection molding. In the cases of extrusion and injection molding, polymer chains can become aligned in a particular direction, and strongly directional residual stresses can be introduced by the process. Here, therefore, we propose a way of capturing any material anisotropy and show the approach being used to represent observed anisotropy in a sample of Topas 5013S, a cyclic olefin polymer.

3.6.1. Modification of simulation model

To capture material anisotropy, we simply make the point-load response of the material anisotropic. A new dimensionless parameter, k_a, is introduced to represent the strength of the anisotropy. The effect of this parameter is illustrated in Figure 3.12. We define the co-ordinate system of the material using the vectors ($\mathbf{e}_1$, $\mathbf{e}_2$) and that of the stamp using (x, y) as before. The lateral extent of the point-load response is a factor of k_a greater in the material's $\mathbf{e}_1$ direction. The material's anisotropy is then related to the co-ordinate system of the stamp by redefining the point-load response of the simulation's virtual elastic layer as follows:

$$\left.\begin{aligned} g[m,n] &= -\frac{1-\nu^2}{\pi E}\left[f(x_2,y_2) - f(x_1,y_2) - f(x_2,y_1) + f(x_1,y_1)\right] \\ f(x,y) &= y\ln\left(x+\sqrt{x^2+y^2}\right) + x\ln\left(y+\sqrt{x^2+y^2}\right) \end{aligned}\right\} \qquad (3.18)$$

where

and

$x_1 = md - d/2;\ x_2 = md + d/2;\ y_1 = k_a(nd - d/2);\ y_2 = k_a(nd + d/2)$ for $x \parallel \mathbf{e}_1$;

$x_1 = k_a(md - d/2);\ x_2 = k_a(md + d/2);\ y_1 = nd - d/2;\ y_2 = nd + d/2$ for $y \parallel \mathbf{e}_1$;

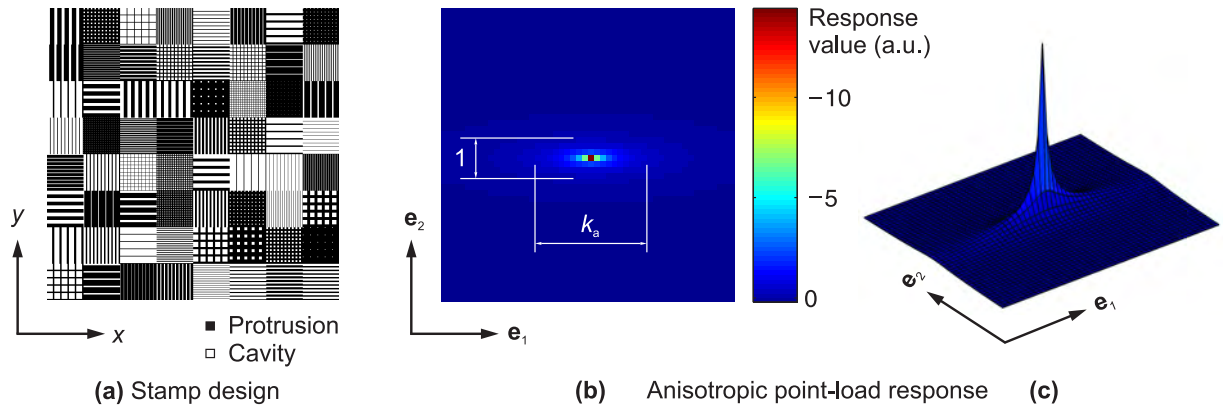

Figure 3.12: Anisotropic point-load response and its relation to the geometry of the embossed pattern. The stamp design (a) is defined in *x* and *y* co-ordinates. The anisotropic point-load response (b) is a property of the material being embossed, whose reference co-ordinates are $\mathbf{e}_1$ and $\mathbf{e}_2$. In (c) is shown a 3-D rendering of a typical anisotropic point-load response.

3.6.2. Tuning the modified model to represent anisotropy in a sample of Topas 5013S

An injection-molded, 1 mm-thick plate of the cyclic olefin polymer Topas 5013S was obtained as a gift from Topas Advanced Polymers (Florence, KY). This plate was cut into 25 mm-square pieces, and the orientation of each piece was noted relative to the framework of the supplied plate. One of the pieces was embossed with a silicon stamp carrying the test-pattern of our earlier experiments (Figure 3.12a). The relief of the test-pattern was 20 µm, and the *x* and *y* axes of the pattern were aligned to be parallel to the edges of the polymer piece. The embossing conditions were 95 °C, 800 kPa, and 4 minutes' loading duration. The material was cooled to 60 °C before unloading. A second square piece of the Topas 5013 material was then embossed under the same conditions, but with the orientation of the polymer piece relative to the stamp pattern differing by 90° from the previous experiment.

The measured peak cavity penetration heights of the two samples' patterns are plotted as symbols in Figure 3.13. In both samples, we see a strong orientation dependence of the depth of penetration of the long, slender rectangular cavities. In the case of Sample 1, those rectangular cavities whose long axis runs parallel to the *x*-axis of the stamp have filled much less deeply than the cavities running parallel to the *y*-axis. In Sample 2, this trend is reversed, with the cavities running parallel to the stamp's *x*-axis penetrating more deeply. This strong change in behavior indicates that the principal axes of the material's anisotropy run approximately parallel with the edges of the polymer squares embossed.

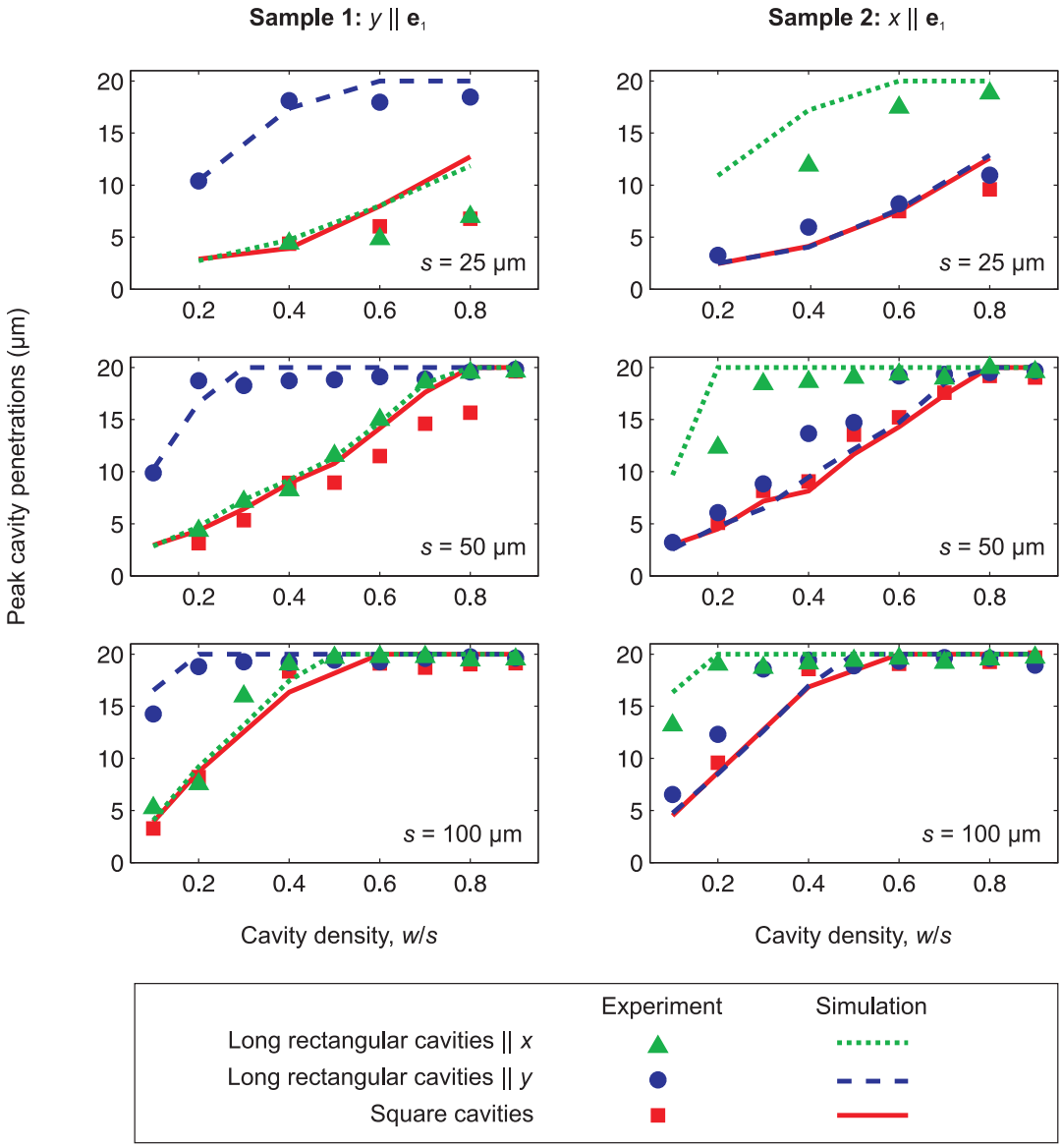

Figure 3.13: Peak cavity penetration heights for two embossed Topas 5013S samples. The orientations of Samples 1 and 2 relative to the test pattern during embossing differed by 90 °. Experimentally measured peak cavity penetrations are shown as symbols; simulation results, assuming $k_a = 4$, are shown as lines.

We have attempted to model the anisotropy of this sample of Topas 5013S, without calibrating a full viscoelastic material model. We have simply fit a value for k_a, and a value for the effective compliance of the material given the four-minute, 95 °C processing conditions used. A reasonably close approximation to experimental results is obtained by taking a value of 4 for k_a and a value of 1.6 MPa for the effective stiffness, E, of the polymeric substrate, as defined in (3.18). Poisson's ratio, ν, is assumed to be 0.5. The output of a simulation assuming these parameters is shown by the plotted lines in Figure 3.13.

3.6.3. Implications for the characterization and processing of anisotropic materials

This very preliminary attempt to model material anisotropy has provided promising results. In a sense, we are fortunate to have been able to detect the material's anisotropy with these particular experiments. Had the principal axes of the material's anisotropy instead been oriented by accident at ±45° to the *x* and *y* axes of the pattern, we would *not* expect to have seen a difference in penetration depths between the cavities parallel to *x* and those parallel to *y*. One way of making a test pattern able always to detect anisotropy would be to include slender rectangular cavities with *three* or more orientations.

The extent of material anisotropy of any given polymer plate is a strong function of its processing history. The anisotropy of one particular batch of a particular material is therefore not necessarily representative of any other batch of the same material. We envisage the use of simple embossing tests such as reported here to identify batch-to-batch variation of material anisotropy.

3.7. Generalizing the compliance function

The simulation approach developed above assumes a Voigt material model, which appears to represent well the micro-embossing behavior of the relatively high molecular-weight polymers investigated experimentally. There may, however, be good cause to use alternative representations of the polymer.

Firstly, our Voigt model does not capture all the phenomena observed. PMMA at 110 °C was seen in Section 2.3.8, for example, to exhibit an effectively permanent component to its deformation, which does not recover even when annealed. This behavior could be approximately modeled by inserting an additional dashpot in series with the Voigt model.

Secondly, we may wish to simulate the embossing of lower molecular-weight polymers, with lower entanglement densities and therefore with network slippage being dominant during embossing or imprinting. Our simulation methods may even be needed for the imprinting of *liquid* layers, as we will discuss in Chapter 6.

Fortunately, our simulation approach can readily be adapted to use any linear function of time for the compliance of the polymer. If the compliance is denoted by $J(t)$, the expression for the response of the surface of a half-space to a point load applied for all time $t > 0$ becomes:

$$s_{general}(x,y,t) = \frac{-\left(1-\nu^2\right)J(t)}{\pi\sqrt{x^2+y^2}} \tag{3.19}$$

and the corresponding impulse response becomes:

$$g_{general}(x,y,t) = \frac{-\left(1-\nu^2\right)\dfrac{\mathrm{d}J(t)}{\mathrm{d}t}}{\pi\sqrt{x^2+y^2}}. \tag{3.20}$$

The convolution integral describing the embossed topography becomes:

$$w(x,y,t) = \frac{-\left(1-\nu^2\right)}{\pi}\int_0^t\int_{-\infty}^{\infty}\int_{-\infty}^{\infty}\frac{p(x',y',t')\dfrac{\mathrm{d}J(t-t')}{\mathrm{d}t'}}{\sqrt{(x-x')^2+(y-y')^2}}\,\mathrm{d}x'\mathrm{d}y'\mathrm{d}t' \tag{3.21}$$

and we redefine our expression for the weighted time-average of applied pressure to be the dimensionless quantity:

$$p_g(x, y, t_h) = (1 - \nu^2) \int_0^{t_h} p(x, y, t') \frac{\mathrm{d}J(t - t')}{\mathrm{d}t'} \mathrm{d}t' \,. \tag{3.22}$$

Averaging spatially over one period of the embossed pattern:

$$p_{g,0}(t_h) = (1 - \nu^2) \int_0^{t_h} \frac{1}{D^2} \int_0^D \int_0^D p(x, y, t') \mathrm{d}x \mathrm{d}y \frac{\mathrm{d}J(t - t')}{\mathrm{d}t'} \mathrm{d}t' = (1 - \nu^2) \int_0^{t_h} p_0(t') \frac{\mathrm{d}J(t - t')}{\mathrm{d}t'} \mathrm{d}t' \,. \tag{3.23}$$

From here we see that (3.21) may be rewritten as:

$$w(x, y, t_h) = \frac{-1}{\pi} \int_{-\infty}^{\infty} \int_{-\infty}^{\infty} \frac{p_g(x, y, t_h)}{\sqrt{(x - x')^2 + (y - y')^2}} \mathrm{d}x' \mathrm{d}y' \,. \tag{3.24}$$

Expression (3.24) is equivalent to instantaneously embossing an elastic substrate with $E/(1–\nu^2) = 1$, with the dimensionless pressure distribution $p_g(x, y, t_h)$. From expression (3.23) we know the spatial average of $p_g(x, y, t_h)$ as a function of the spatial average of true applied pressure over time; we can therefore find $w(x, y, t_h)$ using our existing simulation procedure.

In Table 3.2 we outline some possible polymer models, although $J(t)$ could really be any linear function of time. In the table, E_i are elastic moduli, and η_i are viscosities.

Table 3.2: Comparison of possible polymer models and their corresponding compliance functions.

Type of polymer model	Possible uses	Compliance function $J(t)$ in response to step-load applied for all $t > 0$	$\frac{dJ(t)}{dt}$ (defined for $t \geq 0$)
Purely elastic	Simulating deformations of stamp and/or the substrate underlying an embossed layer of finite thickness	$\frac{1}{E}$	$\frac{\delta(t)}{E}$
Newtonian liquid	Molten polymers; very low molecular-weight polymers; nanoimprint lithography	$\frac{t}{\eta}$	$\frac{1}{\eta}$
Maxwell model	Low molecular-weight viscoelastic polymers	$\frac{t}{\eta}+\frac{1}{E}$	$\frac{1}{\eta}+\frac{\delta(t)}{E}$
Kelvin-Voigt model	Higher molecular-weight polymers whose behavior is dominated by physical entanglements of the polymer chains	$\frac{1}{E}\left[1-\exp\left(\frac{-Et}{\eta}\right)\right]$	$\frac{1}{\eta}\left[\exp\left(\frac{-Et}{\eta}\right)\right]$
Hybrid Maxwell/Voigt model (Voigt model in series with Maxwell model)	Modeling of classes of polymers with variable molecular weight; in general, representing more phenomena than the above models allow	$\frac{1}{E_1}\left[1-\exp\left(\frac{-E_1 t}{\eta_1}\right)\right]+\frac{t}{\eta_2}+\frac{1}{E_2}$	$\frac{1}{\eta_1}\left[\exp\left(\frac{-E_1 t}{\eta_1}\right)\right]+\frac{1}{\eta_2}+\frac{\delta(t)}{E_2}$

3.8. Summary

In this chapter we have probed the limits of validity of the linear viscoelastic bulk-embossing model of Chapter 2. We have also proposed several ways of extending or generalizing the approach: to simulate birefringence in embossed patterns, to capture material anisotropy, and to represent materials that are not well described by a Voigt model.

4. Hierarchical simulation of the embossing of feature-rich patterns

Many practical patterns will still be too complex to simulate within an affordable time if we use a stamp representation that is discretized at the level of individual features. We therefore now develop a way of representing stamps at far coarser levels of spatial discretization, where each spatial element of the stamp is described as containing many identical features of a certain shape, size and areal density.

4.1. Parameterizing the imprinting of certain regular patterns

The first step is to obtain the relationship between the applied pressure, the processing parameters and the resulting embossed topography for some simple, regular patterns of *infinite* extent. Here we show these relationships for stamps carrying long, parallel trenches and arrays of square holes. We use the simulation procedure developed in the previous sections to find these pressure–topography relationships. To perform the simulations we choose an appropriate 'dummy' substrate stiffness and a range of average pressures to apply to the stamp. Again, we assume the material to be incompressible, which constrains the relationship between cavity filling and stamp displacement.

We also note that since the material is assumed to behave linearly, we can non-dimensionalize the pressure–topography relationship. For initial cavity filling — before any material has touched the tops of the cavities — we describe the pattern using two non-dimensional parameters: A, the non-dimensional cavity penetration depth, and B, the non-dimensional rigid-body displacement of the stamp:

$$A = \frac{z_{pk} E}{p_{s,0} s}; \tag{4.1}$$

$$B = \frac{\Delta E}{p_{s,0} s}. \tag{4.2}$$

In (4.1) and (4.2), z_{pk} is the peak penetration of the cavity, E is the material's elastic modulus, Δ is the rigid-body displacement of the stamp, s is the pitch of the pattern, and $p_{s,0}$ is the function of average applied pressure, elasticity, viscosity, and loading duration that is given in (2.5). Figure 4.1 illustrates parameters A and B as a function of the ratio of cavity width to cavity pitch, w/s, for stamps patterned with long trenches and with square holes. By fitting polynomial functions to these simulated relationships, we obtain a model that allows us to predict the extent of cavity filling for patterns with any value of w/s.

The characterization simulations are then extended to describe what happens as material reaches the tops of the cavities. Under our assumption of material incompressibility, the proportion, V/V_0, of the total cavity volume of the stamp that is filled with material is linked to the stamp's displacement, Δ, as follows:

$$\frac{V}{V_0} = \frac{\Delta s}{wh} \text{ for long trenches; } \frac{V}{V_0} = \frac{\Delta s^2}{w^2 h} \text{ for square holes.} \tag{4.3}$$

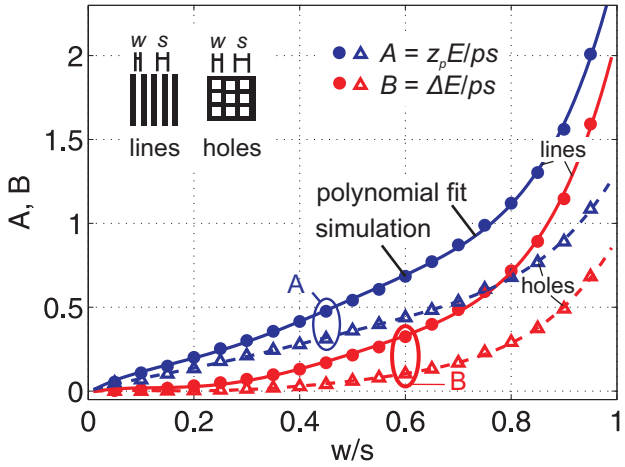

Figure 4.1: Non-dimensional parameters *A* and *B*, describing cavity penetration and stamp displacement in the embossing of an incompressible layer. Parameters are shown for stamps patterned with infinite arrays of (i) parallel trenches and (ii) square holes.

Similar relationships could easily be found for other geometries. Figure 4.2 shows the relationship between V/V_0 and non-dimensional pressure, $p_{s,0}sA/Eh$, where h is the height of the cavity. We see that V/V_0 approaches 1 for very large $p_{s,0}sA/Eh$. The shapes of the non-dimensionalised relationships have only a mild dependence on the ratio w/s (see Figure 4.3), since most of the effect of w/s is captured in the non-dimensional parameter A.

We abstract the relationship between V/V_0 and $p_{s,0}sA/Eh$ using a piecewise-linear function (Figure 4.2). A simplifying assumption is made that once a cavity volume is 95%-full, it cannot fill any further. Therefore there are three linear regions: an initial region in which V/V_0 is directly proportional to $p_{s,0}sA/Eh$ and no material has reached the top of a cavity, a second region in which V/V_0 increases more slowly with $p_{s,0}sA/Eh$ as material is pushed into the corners of the cavity, and a flat region in which no further filling is considered possible.

This characterization procedure would be performed for any 'primitive' geometries — like trenches and holes — that are likely to be deployed in stamp designs. Characterization could also be done for custom-designed 'cells' that were used repeatedly in a stamp design.

Between touching and filling, the piecewise linear approximations that we have chosen underestimate by up to ~20% the degree of filling for a given applied pressure. When filling is ~95% or more complete, however, the approximation again becomes closer to reality, so that no simulation that reports all regions of a stamp to be almost filled will be grossly inaccurate. Since we expect the simulation tool to be used to check for *completeness* of filling, we expect our approximations to be acceptable.

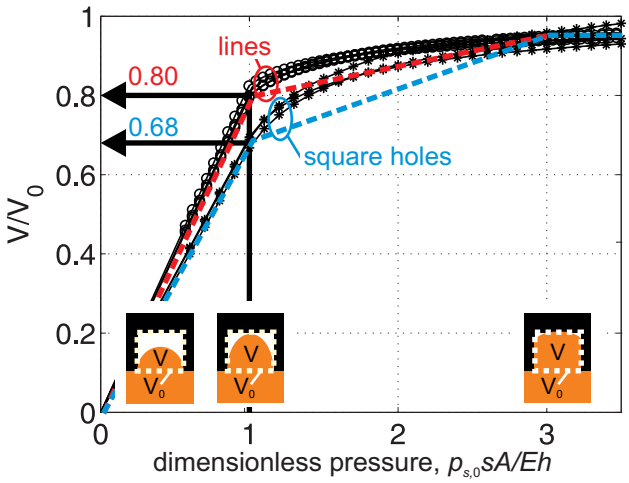

Figure 4.2: Abstraction of simple pattern simulations to non-dimensional pressure–filling relationships. Simulated relationships are shown for stamps with arrays of lines (symbols: circles) and square holes (symbols: stars). For each shape type, *w/s* ratios of 0.2, 0.5 and 0.8 are simulated and plotted. Piecewise-linear approximations to these relationships are shown.

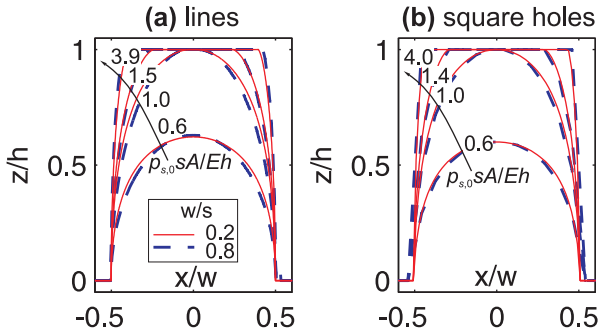

Figure 4.3: Simulated polymer topographies when embossed with stamps patterned with arrays of (a) long trenches and (b) square holes having *w/s* values of 0.2 and 0.8. Simulations are plotted on normalized axes. In these normalized representations, the shape of material penetrating the cavities is seen to be relatively insensitive to the value of *w/s*.

4.2. Modified simulation algorithm

The second stage in building a hierarchical simulation is to tie together the abstract representations of each spatial element of the heterogeneously patterned stamp, so that the pressure distribution can be found across the stamp. This stage is illustrated in Figure 4.4. We model any fine patterning within each element of the stamp as being *superimposed* upon a coarse stamp topography $w_{\text{stamp}}[m, n]$. This approach allows multi-scale stamps easily to be represented: for example, we could succinctly describe multi-micron-scale fluidic channels in conjunction with nano-structured surfaces on a stamp.

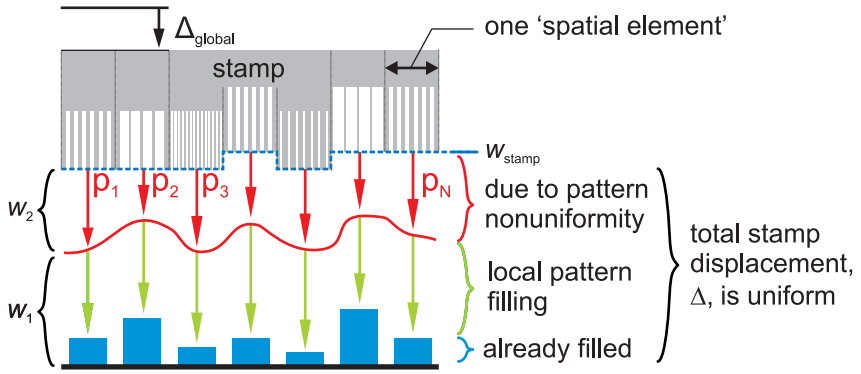

Figure 4.4: Integrating abstracted pressure–filling relationships with a model of underlying substrate deformation to perform a hierarchical simulation of the filling of rich patterns.

A single value needs to be found for the average contact-pressure, $p_s[m, n]$, in each element of the abstracted stamp, and the displacement of the stamp in each element is composed of two parts. Let $w_1[m, n]$ be the part of the stamp displacement associated with the displacement of material into any finely-patterned cavities inside stamp element $[m, n]$. Meanwhile, let $w_2[m, n]$ be the displacements associated with the *variation* of $p_s[m, n]$ from element to element of the abstracted stamp: *i.e.*, this part is computed by convolving $p_s[m, n]$ with the deflection-response of the substrate to unit pressure applied within one of the elements of the coarse stamp representation. The stamp is assumed to be rigid and not to rotate; therefore, the total displacement of the stamp is constrained by:

$$\left.\begin{aligned} w_1[m,n] + w_2[m,n] &= w_{surf}[m,n] - \Delta_{global} \quad \forall \quad (m,n) \in C \\ p_s[m,n] &= 0 \quad \forall \quad (m,n) \notin C \end{aligned}\right\} \tag{4.4}$$

where C is the set of spatial elements in which the polymeric substrate has made at least some contact with the stamp, and Δ_{global} is the rigid-body displacement of the whole stamp.

In a special case in which $w_{stamp}[m, n]$ is zero everywhere, and in which the fine pattern is identical in every part of the stamp, $w_2[m, n]$ would be zero everywhere; meanwhile, $w_1[m, n]$ is zero in any cells in which the stamp surface is flat and contains no cavities.

The solution procedure is now modified from that of Section 2.1.3. As well as iterating to find the contact set C as we did before, we now also iterate to decide in which elements of the coarse grid the finely patterned cavities are partially or fully filled. This approach means that whenever sets of simultaneous equations are solved, they are linear. The simulation proceeds as follows:

1. The non-dimensional relationships between V/V_0 and $p_s sA/Eh$ are converted into direct pressure–displacement (p_s–Δ) relationships for each element of the coarse stamp representation. As illustrated in Figure 4.5, each p_s–Δ relationship has three characteristic gradients $k_{0,\,\mathrm{I–III}}$ and three characteristic constants $k_{1,\,\mathrm{I–III}}$, defined as follows:

$$
\left.
\begin{aligned}
k_{0,I} &= \frac{sB}{E} \\
k_{0,II} &= k_{0,I}\left[\frac{V_{F0}-V_{T0}}{V_{T0}\left(p_{F0}-1\right)}\right] \\
k_{0,III} &= 0 \\
\\
k_{1,I} &= 0 \\
k_{1,II} &= \frac{Eh}{sA}\left(k_{0,I}-k_{0,II}\right) \\
k_{1,III} &= k_{1,II} + k_{0,II}\frac{p_{F0}Eh}{sA}
\end{aligned}
\right\} \qquad (4.5)
$$

Key values of these parameters for parallel trenches and square holes are given in Table 4.1.

Table 4.1: Abstraction parameters for hierarchical simulation of trenches and holes

	Lines/trenches	Square holes
V_{T0}	0.80	0.68
V_{F0}	0.95	0.95
p_{F0}	3.0	3.0

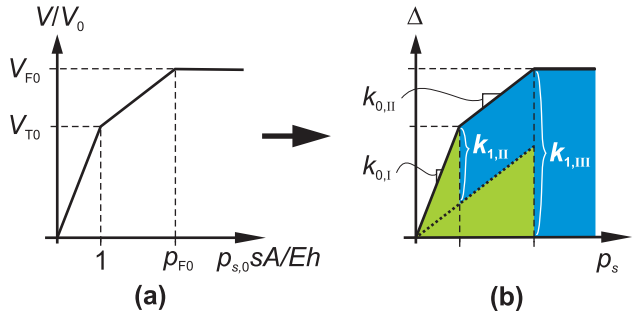

Figure 4.5: Conversion of a non-dimensional pressure–penetration relationship, (a), into a specific pressure–displacement relationship, (b), for each region of a patterned stamp. The colors of the regions of the p_s–Δ graph correspond to the colors of the components of stamp displacement illustrated in Figure 4.4.

2. We begin by assuming that every element of the stamp is in region I of its pressure–displacement graph: *i.e.* that no material has reached the tops of any cavities. An initial guess for the contact set C is also made. Usually the portion of the stamp in which $w_{\text{stamp}}[m, n]$ takes its minimum value is considered to be initially in contact with the substrate.

3. For each cell [m, n] of the stamp, we take the current estimate for the occupied region R of the pressure–displacement relationship, where R is one of {I, II, III}, and set the local compliance constants $k_0[m, n]$ and $k_1[m, n]$ according to (4.5).

4. Next, a contact pressure distribution $p_s[m, n]$ is found that satisfies equilibrium with the known applied average pressure, $p_{s,0}(t)$, and that is consistent with the stamp remaining rigid while the polymer deforms. $p_s[m, n]$ is taken to be zero for all [m, n] outside the assumed stamp–substrate contact region C. To find $p_s[m, n]$, steps (a) to (c) below are used:

   (a) A set of pressures $p_f[m, n]$ is found that would be required to deform the substrate into the shape $w_{\text{stamp}}[m, n]$ *within* the contact region. The shape adopted by the substrate outside the contact region is constrained only by the mechanical response of the substrate. A stabilized biconjugate gradient method is used, as before:

$$\left.\begin{aligned} w_f[m,n] &= p_f[m,n] * g[m,n] - k_0[m,n]p_f[m,n] - k_1[m,n] \\ p_f[m,n] &= 0 \quad \forall \quad (m,n) \notin C \\ w_f[m,n] &= w_{stamp}[m,n] \quad \forall \quad (m,n) \in C \end{aligned}\right\} \tag{4.6}$$

   (b) A set of pressures $p_e[m, n]$ is found that is consistent with *unit* displacement of every element of C. Because the $p_e[m, n]$ is an estimate of the pressures required for an *incremental* displacement of the stamp, the constants $k_1[m, n]$ do not feature in this relationship:

$$\left.\begin{aligned} w_e[m,n] &= p_e[m,n] * g[m,n] - k_0[m,n]p_e[m,n] \\ p_e[m,n] &= 0 \quad \forall \quad (m,n) \notin C \\ w_e[m,n] &= 1 \quad \forall \quad (m,n) \in C \end{aligned}\right\} \tag{4.7}$$

   (c) The estimate of $p_s[m, n]$ is then found as the superposition of $p_f[m, n]$ and whatever multiple of $-p_e[m, n]$ makes the spatial average of $p_s[m, n]$ equal that calculated according to (2.5):

$$\left.\begin{aligned} p_s[m,n] &= p_f[m,n] - \Delta_{global} p_e[m,n] \\ \frac{1}{MN}\sum_{m=1}^{M}\sum_{n=1}^{N} p_s[m,n] &= p_{s,0} \end{aligned}\right\} \tag{4.8}$$

   Δ_{global} is the rigid-body displacement of the stamp, defined positive-downwards into the material. The estimate of $w[m, n]$ is then:

$$w[m,n] = p_s[m,n] * g[m,n] - k_0[m,n]p_s[m,n] - k_1[m,n]. \tag{4.9}$$

5. Based on the newly estimated pressure-distribution $p_s[m, n]$, we revise the estimates of the region, R, of the p_s–Δ graph that is occupied by each element of the stamp. We also revise our estimate of the contents of C by adding elements for which $w[m, n] > w_{\text{stamp}}[m, n] - \Delta_{\text{global}}$ and removing elements in which $p_s[m, n] < 0$.

6. If the most recent iteration has brought about no change in the estimated value of R for any cell, or if a pre-defined maximum number of iterations have been completed, we proceed to step 7. Otherwise, we return to step 3.

7. For those elements [m, n] that are members of the contact set C, we evaluate the fill-factor V/V_0. We also evaluate the topography $w[m, n]$ for the whole area of the stamp. This completes the simulation, providing a useful estimate of the completeness of pattern filling across the stamp.

4.3. Comparison with experimental data

We begin by comparing experimental and simulated topographies at the scale of individual features. Cross-sectional topographies of representative, individual features were extracted from the white-light interferogram of one particular embossed sample: a piece of polycarbonate that had been embossed at 145 °C under 0.5 MPa for five minutes. One representative feature topography was taken from near the center of each of the 64, 0.5 mm-square regions of the test pattern illustrated in Figure 2.7.

For the sample being investigated, cavity penetrations were sufficiently small that no material had touched the tops of any of the stamp cavities. We are therefore able to model z_{pk}, the peak height of the polymer topography inside a given cavity, by using (4.1). The variables to be specified are A, which was fitted as a function of w/s and pattern shape in Section 4.1, the pattern pitch s, the material compliance E that was modeled in Chapter 2, and the local effective average pressure $p_{s,0}$, which comes from a hierarchical simulation as described in Section 4.2.

We computed the model output for z_{pk} in each of the 64 regions of the test-pattern, and divided the values of each experimentally measured feature-topography by the corresponding value of z_{pk} before plotting those topographies in Figure 4.6. Simulated feature-scale topographies are also normalized by z_{pk} and plotted as black lines in Figure 4.6: the peak values of these normalized simulations are exactly equal to 1, as expected.

In each pane of Figure 4.6 many experimental topographies are overlaid; the feature-pitch, s, is distinguished by color and the pattern density, w/s, is distinguished by symbol type. In most cases, the polynomial functions for $A(w/s)$ that we fit earlier in this chapter do appear to yield predictions for z_{pk} that are within around 20% of those measured. The *shapes* of the measured topographies are also well represented by the simulations. For the narrowest square-hole cavities, however, our approach appears to have substantially underestimated the peak penetration heights; we attribute this to imperfect fitting of the polynomial relationship between w/s and A for arrays of square holes having very low values of w/s.

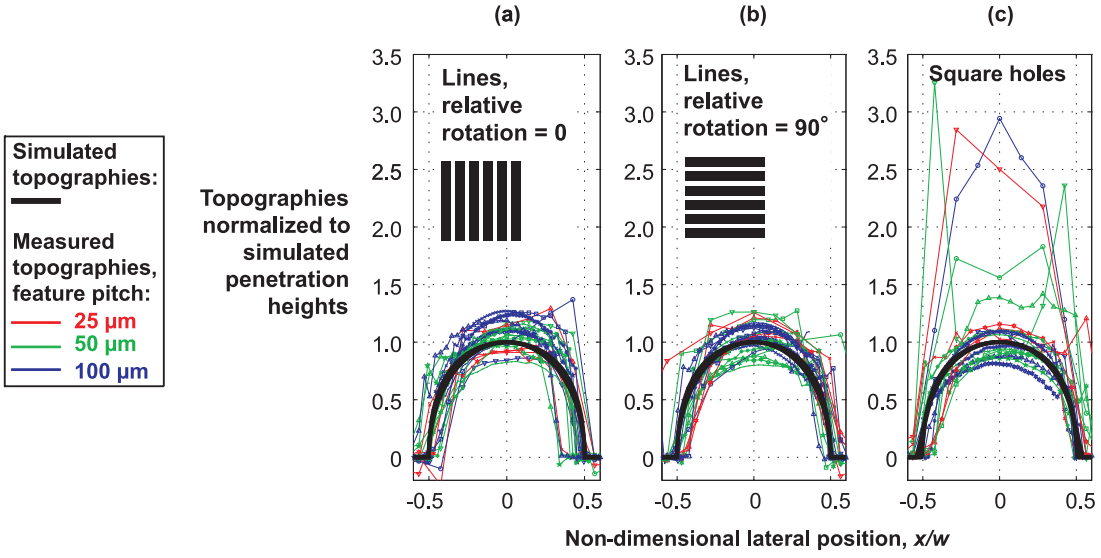

Figure 4.6: Measured cross-sectional topographies of individual features for one particular embossed sample: polycarbonate, embossed at 145 °C under 0.5 MPa for five minutes. The plotted magnitude of each topography is normalized by the peak penetration height predicted for that particular geometry using the fitted material model and parameter A, as described in Section 4.1. Lateral positions are normalized by the nominal cavity width, w. Penetration heights appear to be modeled within 20% across most cavity shapes, pitches, and densities.

We now explore the effect of varying the coarseness of discretization of a hierarchical simulation. We take an experimental topography from one particular PMMA sample, embossed at 130 °C under 0.5 MPa for two minutes. We model this particular topography using the material parameters fit in Chapter 2. Figure 4.7a shows a pseudo-color plot of the experimental data, together with a plot of the output of a 'flat' simulation in which each individual feature of the stamp is represented as part of an 800 × 800 matrix of topographical positions. We also show the outputs of two 'hierarchical' simulations, generated using the approach of Section 4.2. In the first hierarchical simulation, each 0.5 mm-square patch of features is represented by a single element of an 8 × 8 pattern matrix. In the second hierarchical simulation, each 0.5 mm-square patch of features is represented by an 8 × 8 region of a 64 × 64 pattern matrix. Representative cross-sections through the experimental and the three simulated topographies are shown in Figure 4.7b. In the case of the hierarchical simulations, what is plotted is a local prediction of z_{pk}.

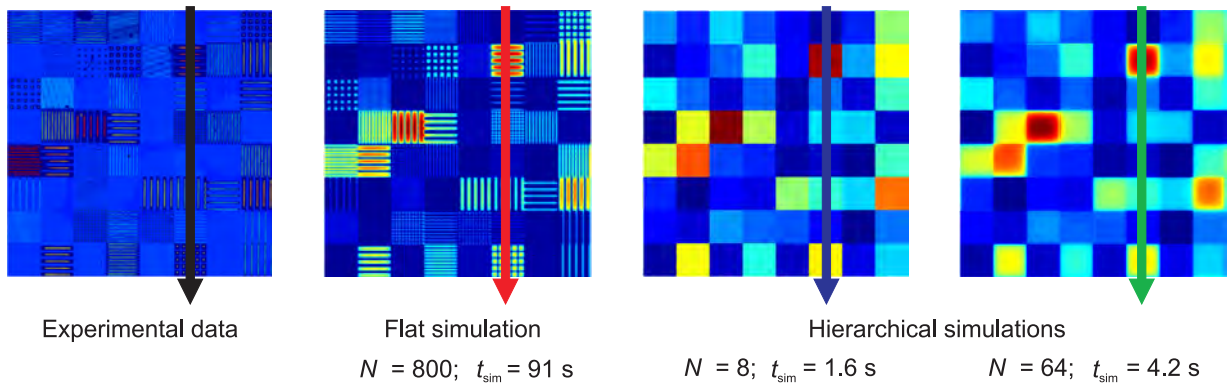

(a)

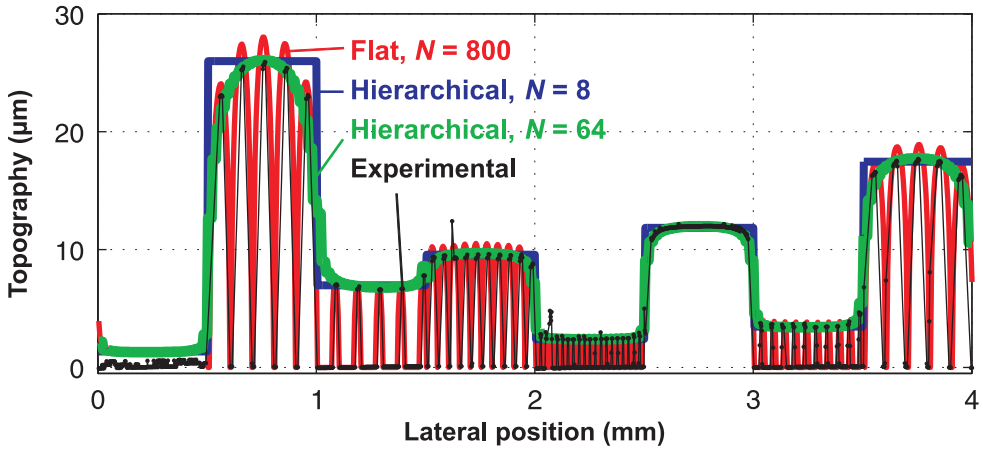

(b)

Figure 4.7: Comparison of experimental and simulated topographies at three levels of lateral discretization. The experimental results illustrated are for a PMMA sample embossed at 130 °C under 0.5 MPa for two minutes. In (a) are shown pseudo-color plots of the experimentally measured and simulated topographies; the results of a 'flat', feature-level simulation are shown as well as those of hierarchical simulations at two levels of discretization. In (b) are overlaid cross-sectional plots of experimental and simulated topographies, for the sections traced out by arrows in (a).

We see that the 'flat' simulation approach has overestimated by up to 10% the penetration depth of the widest cavities: in those cases, the stamp protrusions separating the cavities are represented in our simulation by three or fewer matrix elements, and we encounter the simulation artifact that was illustrated in Figure 2.6. In contrast, the 'hierarchical' simulation is not hindered by too coarse a representation of any individual feature, and makes a more accurate simulation of the envelope of cavity penetration depths.

Figure 4.8, meanwhile, compares measured and simulated topographies for PMMA embossed under additional illustrative sets of processing conditions. Each pane of the graph corresponds to the 4 mm-long section A–A' defined in Figure 2.7. In each case, we see that both the flat and hierarchical simulation approaches represent well the spatial variation of cavity penetration heights, even in cases where material has reached the tops of cavities and begun to fill them.

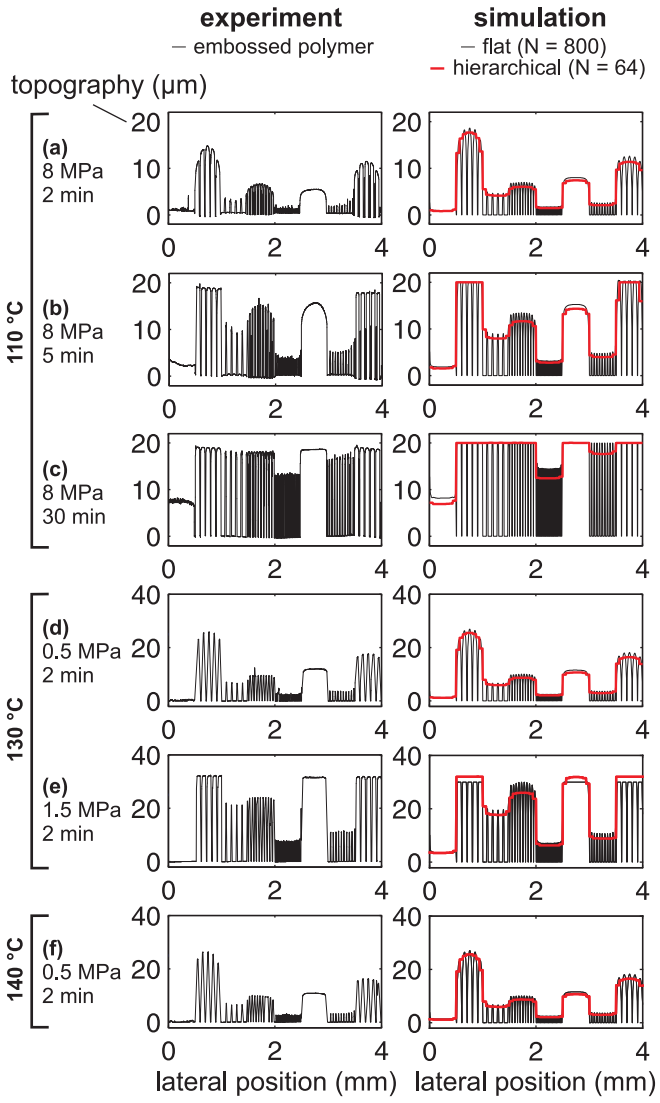

Figure 4.8: A comparison of experimental and simulated cross-sectional topographies for several embossed PMMA samples. Both 'flat' and 'hierarchical' simulated cross-sections are shown on the right-hand side of the figure. These graphs show that both the flat and hierarchical simulation modes are able to track the filling of the stamp cavities realistically.

4.4. Enhancement of computational speed

With the introduction of this hierarchical approach, the size of the simulation is no longer governed by the size of the smallest feature on the stamp, but rather by the degree of heterogeneity of the pattern on the stamp: stamps with large, regular areas containing repetitions of a certain pattern will be more succinctly described than those with little regularity.

The test pattern that has been used to calibrate our simulation methods is particularly simple, being composed of an 8 × 8 patchwork of regions each containing a homogenous array of features. For this test pattern, a great deal of computational speed is gained by switching to a hierarchical approach. Table 4.2 details the amount of simulation time saved: these times were recorded when running the simulations in Matlab on a 3 GHz Intel Pentium 4 processor with 2 GB RAM.

When cavity tops are touched by polymeric material, the simulation time grows, because multiple iterations become necessary on the stamp–polymer contact set, C, or — in the case of a hierarchical simulation — on parameters R. Reasonably faithful simulation results have been obtained with no more than 10 iterations on C or R.

Table 4.2: Summary of computation times for test pattern

Simulation approach	No cavity tops touched	Cavity tops touched
Flat N=800	79 s	750 s *
Hierarchical, N=8	4.3 s	9.2 s
Hierarchical, N=64	5.1 s	27.6 s *

*** The maximum allowed number of iterations on the contact set, 10, was reached.**

4.5. Method for characterizing unit-cells

In this chapter we have abstracted the behavior of regular arrays of parallel trenches and square holes on a stamp. Many real stamps will of course contain other types of periodic patterns. We believe that any pattern that is periodic and on a rectangular grid can readily be characterized in a way similar to that demonstrated in this chapter. The pressure–filling relationship for any given geometry, or 'unit-cell', could be reduced to a dimensionless, piecewise-linear function. The first linear section of the pressure–filling relationship would represent cavity penetration during which no material touched any part of the tops of the stamp cavities. Subsequent sections of the function would describe the increasing difficulty of forcing material into the corners of stamp cavities. This approach to abstracting the behavior of new pattern designs could readily be automated. A series of simulations would be performed with a fixed polymer compliance and a progressively increasing value of the stamp-average applied pressure $p_{s,0}$. The proportion of cavity volume filled would be recorded for each simulated value of applied pressure, and a piecewise-linear pressure–filling relationship would be fit to these results.

4.6. Bulk embossing ‘design rules’

The dimensionless parameters A and B provide a good basis for the definition of ‘design rules’ governing patterns that are to be hot-embossed. Without even running simulations, it would be possible to use the relation of (4.1) to gain an order-of-magnitude estimate of the value of $p_{s,0}$ needed to replicate patterns of a given characteristic pitch, relief, and density in a polymer of given viscoelastic properties. In general, the required magnitude of $p_{s,0}$ will be set by the region of a stamp with the *smallest* value of As/h, since that will be the most difficult region of the stamp to fill with material.

We could imagine tracing this thought process backwards, so that the temperature and pressure *capabilities* of an embossing machine and the properties of the material to be embossed would inform a *lower limit* on the allowable local As/h of a pattern. Once a design had been produced that satisfied this simple design rule, simulation could be used to verify that there were no undesirable pattern interactions introducing unforeseen defects.

4.7. Summary

This chapter has demonstrated the substantial simulation-time savings that can be enjoyed when a feature-rich pattern is abstracted on a coarse spatial grid and each region of the grid is characterized by a piecewise-linear relationship between stamp–polymer contact pressure, material properties, and the extent of cavity penetration.

5. The impact of trapped air in thermoplastic micro-embossing

In the previous chapters of this thesis, bulk micro-embossing has been modeled under the assumption that in regions where the stamp is not in contact with the polymer, no effective pressure is applied to the polymer surface. For this assumption to be realistic, one or more of three situations would need to exist. Firstly, the embossing could be performed in a chamber with a sufficiently low ambient gas pressure that any gas trapped and compressed in the cavities would exert negligible pressure on the polymer surface. Secondly, the cavities of the stamp could all be open to the atmosphere so that there is no possibility of compression of the gas in the cavities. Thirdly, any gas trapped in the cavities could permeate the polymer or the stamp or escape along the polymer–stamp interface so quickly that there is no opportunity for a substantial gas pressure build-up in the cavities.

In Chapter 2 we succeeded in fitting viscoelastic polymer models to experimental data under the assumption of no trapped gas. The simulations performed do appear to represent the measured topographies faithfully, but it is important to have an understanding of exactly how much effect the presence of trapped air has on our ability to emboss any given pattern.

In this chapter, therefore, we adapt our simulation procedure to include the presence of compressed gas in stamp cavities. The modified simulations give an impression of the impact of trapped gas for the *worst-case* situation where no gas is able to permeate the polymer or the stamp. There is little in the literature reporting the solubility and diffusivity of air in thermoplastic polymers at temperatures typical for hot-embossing, so we also perform embossing experiments to establish whether compressed gas is able to leave stamp cavities during the embossing of PMMA and Zeonor 1060R.

5.1. Modification of simulation model

The simulation procedure of Section 2.1 is modified as shown in Figure 5.1, so that regions of the polymer surface that are not in contact with the stamp can now experience a hydrostatic pressure of $p_{cav} - p_{atm}$, where p_{cav} is the absolute gas pressure in the cavities and p_{atm} is the ambient atmospheric pressure surrounding the stamp. For any pattern to be simulated, we define a matrix T whose dimensions are the same of those of the stamp representation. The value of T is 1 in any regions of the pattern where we assume stamp cavities to be sealed so that gas can be compressed inside them. T is zero in regions where cavities are assumed to be open to the surrounding atmosphere.

The stamp is in equilibrium when the pressure applied to the top of the stamp is balanced by the stamp–polymer contact pressures plus any pressures applied hydrostatically to the tops of stamp cavities by the compressed gas inside cavities. We assume that when gas is unable to escape a cavity, the absolute pressure inside that cavity is inversely proportional to the volume of the cavity that remains unfilled by polymer.

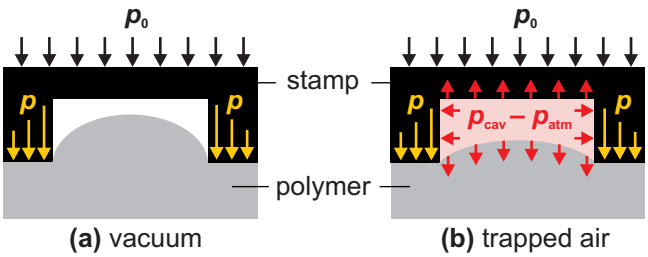

Figure 5.1: Modeling the trapping of air in cavities. For embossing in vacuum or where the cavity is open to the surrounding atmosphere (a), no net forces are exerted on material inside an unfilled cavity. If air is trapped inside the cavity (b), air of absolute pressure p_{cav} in the cavity exerts a uniform pressure on the cavity boundary. Since ambient air pressure p_{atm} is experienced by all external surfaces of the stamp and substrate, the relevant pressure to be balanced against applied embossing loads is $p_{cav} - p_{atm}$.

In this modified simulation approach we continue to exploit the equivalence between the time-dependent embossing of a viscoelastic layer and the instantaneous embossing of a 'virtual' purely elastic layer. Here, the 'virtual' layer has an 'effective' modulus that is a function of the real layer's elasticity, E, and viscosity, η, and of the loading duration, t_h. We define the effective modulus as:

$$E_{effective} = \frac{E}{\left[1 - \exp\left(-\frac{t_h E}{\eta}\right)\right]}. \tag{5.1}$$

The solution for the embossed topography is then performed for a purely elastic layer with Young's modulus $E_{\text{effective}}$ and with a pressure of p_0 applied to the back of the stamp. It should be noted that our approach is expressed slightly differently here from in Section 2.1.2, where we assumed the virtual layer to have a modulus E and we defined a *virtual* applied pressure-average $p_{s,0}$ that was a function of material parameters and loading duration. Here, we use $E_{\text{effective}}$ together with the *true* pressure average of p_0, so that it is simpler to incorporate into our solution the real values of air pressures p_{cav} inside the cavities.

The procedure therefore involves finding the pressure distribution $p[m, n]$, the embossed topography $w[m, n]$, and the cavity pressure p_{cav} at the end of the embossing cycle. We might imagine an iterative solution procedure in which an initial guess was made for the value of p_{cav}, equilibrium values for $p[m, n]$ and $w[m, n]$ were found assuming this value of p_{cav}, and the guess for p_{cav} was then refined based on $w[m, n]$ and the conservation of air mass inside the cavities. We have found, in fact, that such an approach does not guarantee convergence to a meaningful solution. Instead, we choose to increase the average applied pressure in a series of steps from zero towards its true value, p_0, re-evaluating p_{cav} at each step. The algorithm is detailed below.

1. An initial guess is made for the set of stamp elements, C, in contact with the polymer. Usually the portion of the stamp in which $w_{\text{stamp}}[m, n]$ takes its minimum value is considered to be initially in contact with the polymer. The matrix T is defined, with a value of 1 where cavities are closed and zero where they are open. A 'virtual' elastic substrate is defined with modulus $E_{\text{effective}}$ as in (5.1) and with a corresponding point load response $g[m, n]$. For the first step, $u = 1$, a spatial average of applied pressure, $p_{0,u=1}$ is defined. Usually we will have ~100 steps to ensure convergence to a meaningful solution, so $p_{0,u=1} \approx 0.01\ p_0$. Initially, we set $p_{\text{cav},u=1} = p_{\text{atm}}$ because there has so far been no polymer deformation and therefore no air compression.
2. Next, a contact pressure distribution $p_u[m, n]$ is found that satisfies equilibrium with the applied average pressure for step u, $p_{0,u}$. This solution must be consistent with the stamp remaining rigid while the polymer deforms. To find $p[m, n]$, sub-steps (a) to (d) below are used:

(a) We compute the topography $w_{\text{air},u}[m, n]$ that is produced by the hydrostatic application of a pressure $(p_{\text{cav},u} - p_{\text{atm}})$ to those regions of the polymer surface where $C = 0$ and $T = 1$. In all other portions of the surface, the applied pressure is assumed in this sub-step to be zero.

(b) A set of pressures $p_{f,u}[m, n]$ is found that would be required to deform the polymer into the shape $(w_{\text{stamp}}[m, n] - w_{\text{air},u}[m, n])$ *within* the contact region. The shape adopted by the polymer outside the contact region is constrained only by the mechanical response of the polymer. A stabilized biconjugate gradient method [199] is again used, together with the convolution procedure (denoted by *) of (2.10):

$$\left.\begin{aligned} w_{f,u}[m,n] &= p_{f,u}[m,n] * g[m,n] \\ p_{f,u}[m,n] &= 0 \quad \forall \quad (m,n) \notin C \\ w_{f,u}[m,n] &= w_{stamp}[m,n] - w_{air,u}[m,n] \quad \forall \quad (m,n) \in C \end{aligned}\right\} \tag{5.2}$$

(c) A set of pressures $p_{e,u}[m, n]$ is found that is consistent with *unit* displacement of every element of C:

$$\left.\begin{aligned} w_{e,u}[m,n] &= p_{e,u}[m,n] * g[m,n] \\ p_{e,u}[m,n] &= 0 \quad \forall \quad (m,n) \notin C \\ w_{e,u}[m,n] &= 1 \quad \forall \quad (m,n) \in C \end{aligned}\right\} \tag{5.3}$$

(d) An estimate of $p_u[m, n]$ is then found such that the stamp is in equilibrium.

$$\left.\begin{aligned} p_u[m,n] &= p_{f,u}[m,n] - \Delta_u\, p_{e,u}[m,n] + \left(p_{cav,u} - p_{atm}\right) T[m,n] \\ \frac{1}{MN}\sum_{m=1}^{M}\sum_{n=1}^{N} p_u[m,n] &= p_{0,u} \end{aligned}\right\} \tag{5.4}$$

The estimate of $w_u[m, n]$ is then $p_u[m, n] * g[m, n]$. Δ_u is the rigid-body displacement of the stamp, defined positive-downwards into the material.

3. A refined estimate is made of the parts of the stamp that are in contact with the polymer. Cells are added to the contact set C where $w_u[m, n] > (w_{\text{stamp}}[m, n] - \Delta_u)$: polymer material cannot occupy the same space as stamp material. Since $p_{0,u}$ is gradually increasing from step to step in this algorithm, we rarely see cases where $p_u[m, n] < 0$. A refined estimate of $p_{\text{cav},u+1}$ is also made, by calculating the total volumes, $V_{\text{empty},u}$, of closed cavities that remain unfilled by polymer, assuming the mass of trapped gas in the cavities to remain fixed, and imposing Boyle's Law:

$$\left.\begin{aligned} V_{empty,u} &= \sum_{m=1}^{M}\sum_{n=1}^{N}\left[\left(w_{stamp}[m,n] - w_u[m,n] - \Delta_u\right) T[m,n]\right] \\ V_{cavities} &= \sum_{m=1}^{M}\sum_{n=1}^{N}\left[w_{stamp}[m,n]\, T[m,n]\right] \\ p_{cav,u+1} &= 0.5\left[\frac{V_{cavities}}{V_{empty,u}}\, p_{atm} + p_{cav,u}\right]. \end{aligned}\right\} \tag{5.5}$$

Here, V_{cavities} is the sum of the volumes of closed stamp cavities before any polymer material has penetrated them. The value of $p_{\text{cav},u+1}$ is chosen to be the *mean* of $p_{\text{cav},u}$ and $p_{\text{atm}}(V_{\text{cavities}}/V_{\text{empty},u})$ because this has been found to ensure the smooth evolution of p_{cav}.

4. If $p_{0,u} = p_0$, the algorithm ends, and the final topography, $w_u[m, n]$, and cavity pressure, $p_{\text{cav},u}$, are reported. Otherwise, the value of $p_{0,u+1}$ is computed; usually $p_{0,u+1} = p_{0,u} + 0.01p_0$. Parts 2 and 3 of the algorithm are then executed for step u+1, using the just-calculated value of $p_{\text{cav},u+1}$ and the refined estimate of the contents of set C.

This algorithm is limited in the sense that p_{cav} is assumed to be the same in all closed cavities. This assumption would break down when a pattern contained disconnected cavities with a variety of different geometries, because they would each fill with polymer at different rates and attain different cavity pressures.

5.2. Simulations incorporating trapped air

The algorithm of Section 5.1 was used to explore the impact of trapped air upon the embossing of arrays of parallel trenches and square holes. These simulations are reported in nondimensional form, and there are three key parameters for the simulation of each pattern type. Firstly is the width-to-pitch ratio, w/s, of the pattern. Secondly is the dimensionless average pressure, p_0sA/Eh, applied to the back of the stamp; A is the pattern-dependent constant introduced in Chapter 4. Thirdly is the quantity Jp_{atm}, where $J = 1/E_{\text{effective}}$.

Jp_{atm} is a relevant dimensionless parameter for the following reason. Imagine two pieces of polymer embossed with identical stamps and taking identical surface topographies, yet with the compliance J of the first polymer sample being twice as large as that of the second. The stress fields both *inside* these polymer samples and applied at their *boundaries* must be self-similar, but stresses will be twice as large in magnitude in the case of the polymer with the lower compliance. It follows that the hydrostatic cavity pressure must be twice as large in the case of the second polymer sample. Since the volumes of the cavities are identical in the two cases, Boyle's law implies that p_{atm} must be twice as large in the second case. For geometrical similarity to be preserved between two embossing cases, then, Jp_{atm} should be constant.

Figure 5.2 shows simulation results for the embossing of an array of parallel trenches. In Figure 5.2a are shown some simulated cross-sectional topographies for three width-to-pitch ratios and three dimensionless applied pressures. We plot the topographies predicted in the case where there is no air trapping at all, together with those predicted when $Jp_{\text{atm}} = 0.2$. For normal atmospheric pressure of 100 kPa, this situation corresponds to a layer compliance of 2 MPa^{-1}. Meanwhile, in Figure 5.2b are shown graphs of the proportion of cavity-volume filled against dimensionless, stamp-average applied pressure. Three w/s values are illustrated for each of four Jp_{atm} values.

What we see from these plots is that the impact of the presence of trapped air becomes more severe as w/s increases. For $Jp_{\text{atm}} = 0.2$, $p_0sA/Eh = 1$, and $w/s = 0.9$, for example, the proportion of the cavity volume filled is only half as great in the presence of trapped air as in vacuum. Secondly, the impact of trapped air becomes more severe as Jp_{atm} increases. We understand this trend by considering that in a very stiff embossed material, where J is low, the internal stresses in the polymer dwarf the pressures that can are applied to the polymer surface by the compressed air, and the presence of the air has little impact. A very compliant substrate, conversely, is more heavily affected by the pressure that compressed air applies to the polymer surface.

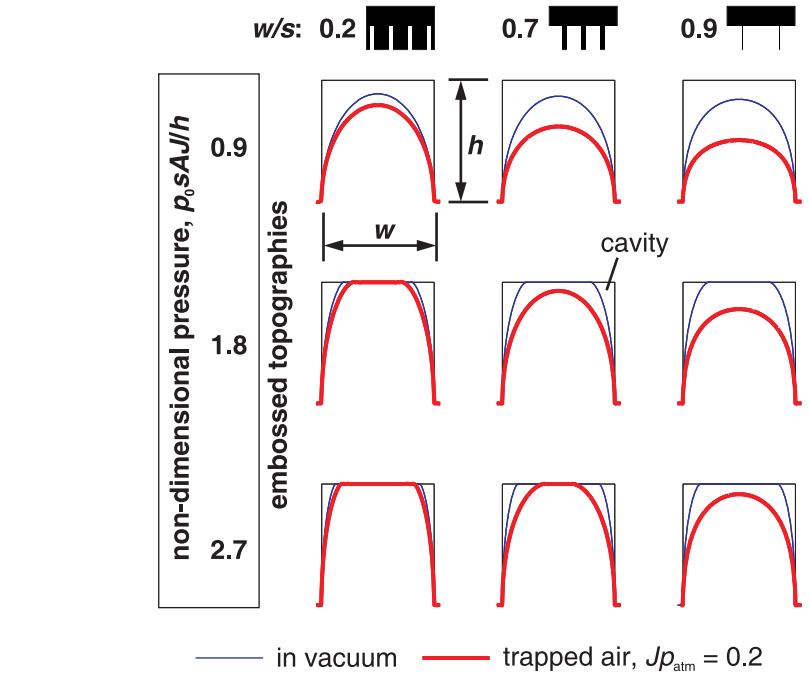

(a)

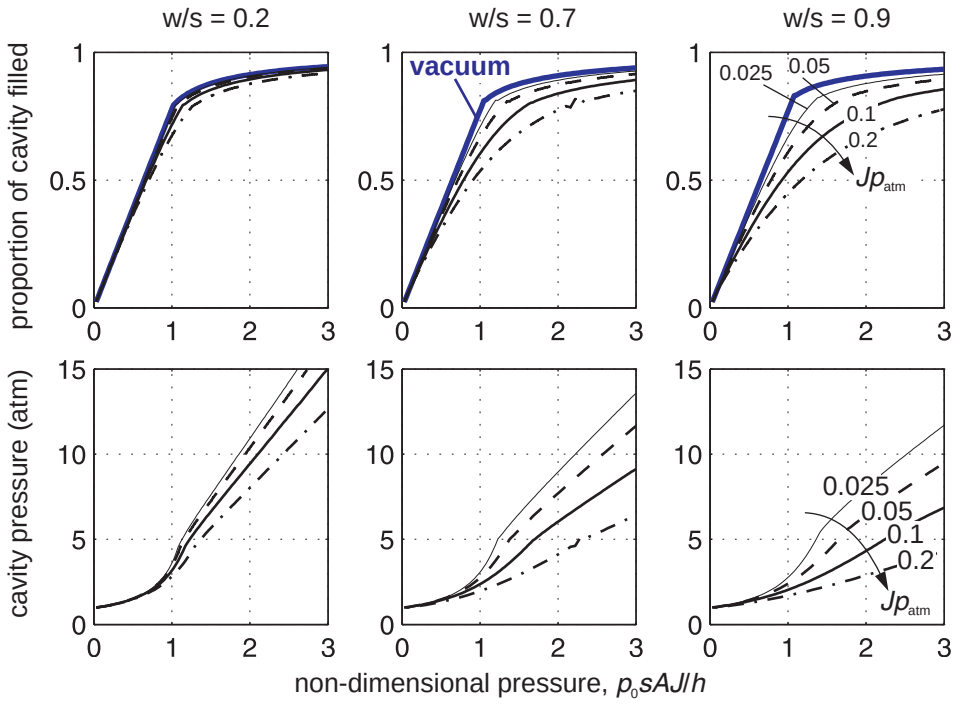

(b)

Figure 5.2: Simulated results for the embossing of long ridges with, and without, air trapped in stamp cavities. (a) Simulated cross-sections for width-to-pitch (*w/s*) ratios of stamp cavities of 0.2, 0.7 and 0.9 at non-dimensional embossing pressures up to 3. In each case, Jp_{atm} = 2. (b) Plots of the proportion of stamp cavity filled, V/V_0, against non-dimensional embossing pressure, for w/s of 0.2, 0.5 and 0.9. Simulated results are shown, both with trapped air for Jp_{atm} of 0.025, 0.05, 0.1, and 0.2, and without trapped air.

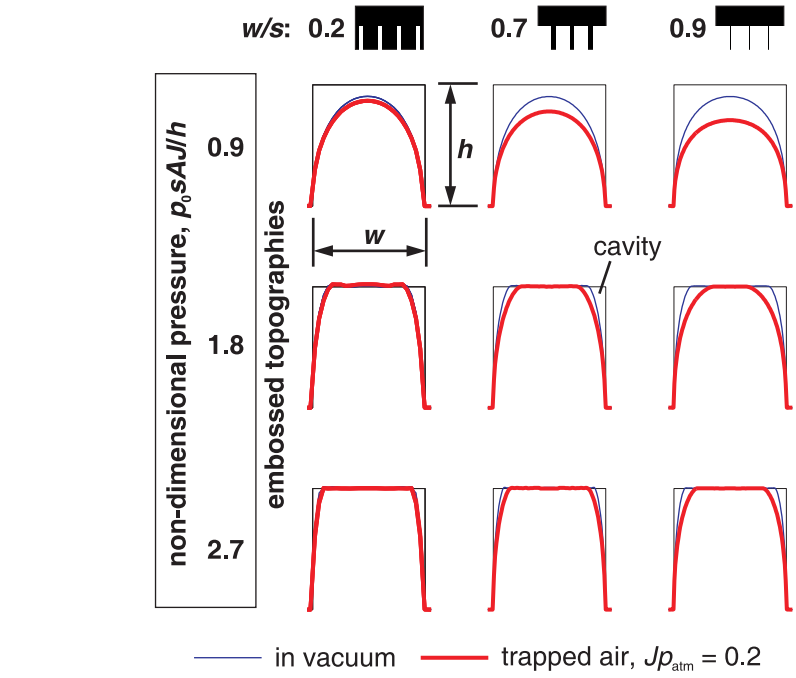

(a)

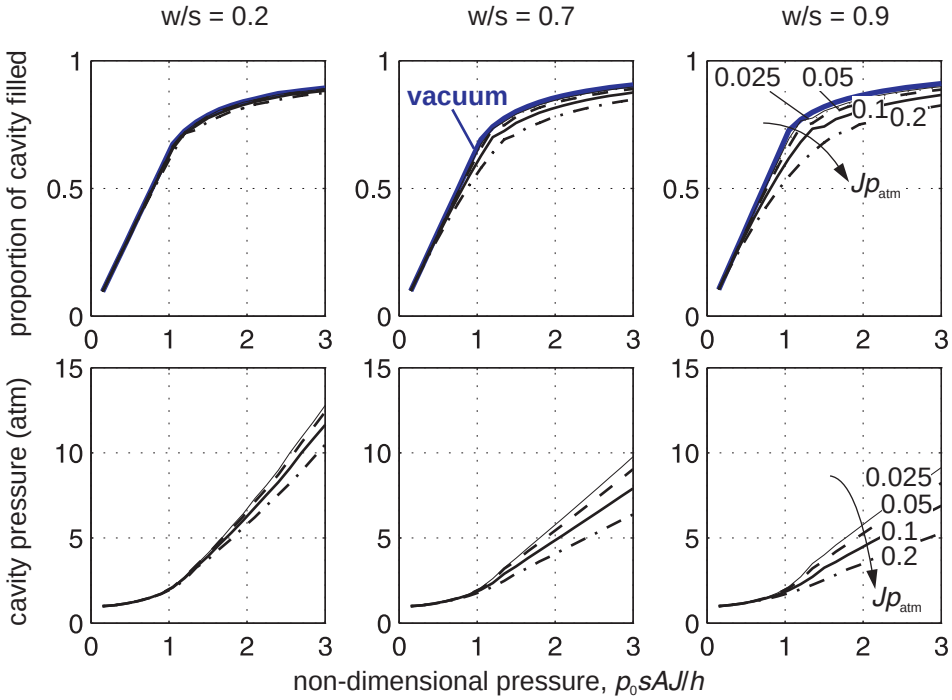

(b)

Figure 5.3: Simulated results for embossing with a stamp carrying an array of square cavities. Simulations are shown with, and without, air trapped in stamp cavities. Other than the difference in geometry, plots are as described in Figure 5.2.

Figure 5.3, meanwhile, shows the results of simulations where the stamp contains an array of square holes. The relative impact of the presence of trapped air appears much smaller for square-hole cavities than for long parallel cavities. This result can be understood by considering that for a given w/s value, the *areal* density of cavities on a stamp with square holes is only $(w/s)^2$. Meanwhile, the areal density of cavities on a stamp with parallel trenches is simply w/s. In other words, the stamp–polymer *contact* forces play a relatively larger role in setting the topography of the polymer when the stamp carries square holes, compared to when the stamp carries long parallel trenches. This comparison could readily be extended by performing simulations for any other periodic stamp pattern.

5.3. Experimental method

Experiments were conducted to establish whether or not it is reasonable to assume that air trapped inside stamp cavities remains there during embossing. The experimental set-up is illustrated in Figure 5.4. A 150 mm-diameter silicon wafer was etched to a depth of 15±2 μm with several 20 mm-square arrays of parallel trenches. Each array contained trenches of a single width and pitch, but width and pitch varied from array to array. Each polymeric sample to be embossed was 30 mm × 15 mm in size, and was drilled 10 mm from one of its shorter edges with a row of 1.6 mm-diameter holes, at a pitch of approximately 3.2 mm. The polymeric sample was then laid on top of the silicon stamp, such that its ends overlapped the edges of the chosen array of stamp trenches. The presence of the holes meant that approximately half of the trenches would be open to the atmosphere when an embossing pressure was applied, while the remaining trenches would be closed off from the atmosphere. A 1 mm-thick PTFE sheet was cut with 'fingers' and laid on top of the polymeric sample, providing routes by which the open trenches could vent to the room's atmosphere. A 1.5 mm-thick polycarbonate plate and a 1 mm-thick Neoprene gasket were placed on top of the PTFE, and the resulting stack of components was placed between the platens of the embossing apparatus described in Chapter 2.

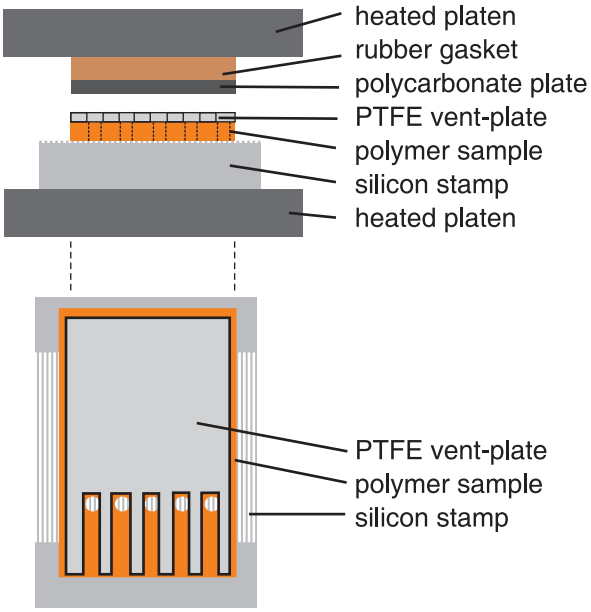

Figure 5.4: Experimental set-up, showing the thermoplastic sample (orange), the patterned silicon stamp, the PTFE 'vent-plate' and the embossing machine.

The details of experiments performed are given in Table 5.1.

Table 5.1: Experimental conditions for air-trapping experiments. Reported embossing pressures are based on actual applied loads as recorded by the embossing apparatus's load-cell, averaged over a 30 mm × 15 mm sample size.

Embossed material	Trench pitch (μm)	Width-to-pitch ratio (*w*/*s*) of trenches	Embossing temperature (°C)	Embossing pressure (MPa)	Loading duration (mins)
PMMA	50	0.8	130	0.27	2
	50	0.8	130	0.32	2
	50	0.8	130	0.32	3
	50	0.8	130	0.28	4
	50	0.8	130	0.33	5
	50	0.8	130	0.26	10
	50	0.8	130	0.34	15
Zeonor 1060R	50	0.8	110	0.16	3
	50	0.8	110	0.16	4
	50	0.8	110	0.16	5
	50	0.8	110	0.15	6.5
	50	0.8	110	0.15	10
	50	0.8	110	0.16	15
	200	0.8	110	0.16	4
	50	0.8	120	0.18	5

5.4. Comparison of experiments and simulations

5.4.1. Experiments with Zeonor 1060R

Firstly we report on the observed behavior of Zeonor 1060R. Figure 5.5 shows a comparison of experimental and simulated cross-sections for two embossed samples. The experimental data were obtained via scanning white-light interferometry. The simulations represent the embossing of an array of parallel ridges; half of the corresponding stamp cavities are modeled as being open to the atmosphere and the other half are modeled as being sealed. In these simulations, the effective compliance of the polymer at the end of the loading duration is determined using the material model that was fit in Chapter 2. Figure 5.6 indicates that for Zeonor 1060R at 110 °C, the compliance is a strong, increasing function of loading duration for at least the first 20 minutes of loading.

On the left-hand side of Figure 5.5 is shown the comparison for an array of 50 μm-pitch ridges of width 40 μm, embossed into Zeonor 1060R at 110 °C under a pressure of 165 kPa for 15 minutes. On the right of the figure is the comparison for an array of 200 μm-pitch ridges of width 160 μm, embossed for four minutes at 110 °C under a pressure of 165 kPa. Both comparisons in Figure 5.5 indicate good correspondence between the experiments and the simulations. The compliance of Zeonor 1060R is sufficiently large after 4 or 15 minutes' loading at 110 °C that the presence of trapped air has a strong influence on the depth of polymer penetration into a cavity. Cavities that were sealed off from the

surrounding atmosphere, and so contained compressed air, were penetrated only about 60% as deeply as those that were open to the surroundings.

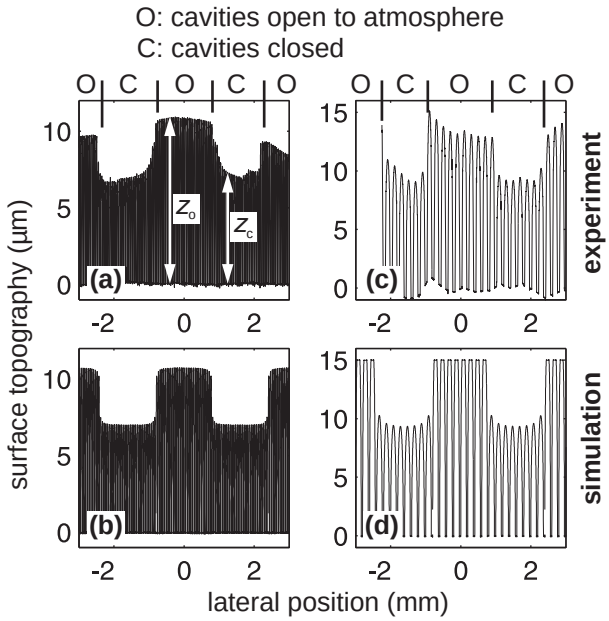

Figure 5.5: Cross-sections through embossed Zeonor 1060R topographies after embossing under a sample average pressure of 165 kPa at 110 °C. (a), (b): 50 micron-pitch ridges, *w/s* = 0.8, loading duration 15 mins; (c), (d): 200 micron-pitch ridges, *w/s* = 0.8, loading duration 4 minutes. (a) and (c) are measured, experimental topographies; (b) and (d) are corresponding simulations, assuming no permeation of air into the polymer.

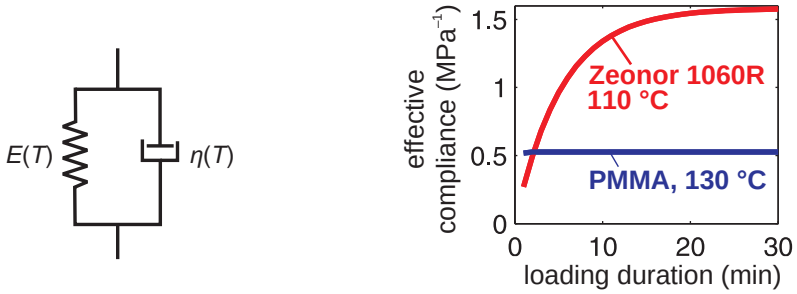

Figure 5.6: Viscoelastic material model. (a) Schematic of Kelvin-Voigt model used; (b) effective material compliances against loading duration for PMMA and Zeonor 1060R. Material parameters were experimentally fit in Chapter 2.

Meanwhile, the *evolution* of embossed Zeonor 1060R topographies over time was investigated in a series of experiments with differing loading durations. In Figure 5.7a are plotted the peak cavity penetrations against loading duration for the embossing of arrays of 50 μm-pitch, 40 μm-width ridges.

Symbols in Figure 5.7a represent experimental results, extracted from scanning white-light interferograms. Cavity penetration depths are extracted and plotted separately for the open-to-atmosphere and sealed-off regions of the stamp. The error bars represent the standard deviation of cavity penetration

depths across the width of the interferogram. This spatial variation of measured cavity penetration depth is an indication that the platens of the embossing machine were not perfectly parallel and hence that the embossing pressure applied was not uniform across the sample.

The solid lines plotted in Figure 5.7a indicate cavity penetration depths extracted from simulations of the embossing process. There is reasonable correspondence between the experimental and simulated results: cavity penetration increases with loading duration, as our Kelvin-Voigt material model predicts. If trapped air were able to permeate the Zeonor 1060R material or the stamp, or to escape in some other way, we would expect the red (sealed-cavity) symbols to move closer to the black (open-cavity) ones as the loading duration increased. There is in fact no evidence that air is leaving the cavity over the 15-minute period explored. Even if substantial amounts of air were able to leave cavities over longer periods, we anticipate that that would have little relevance for industrial hot-embossing because loading durations in excess of 15 minutes are unlikely to be acceptable in production.

The plot in Figure 5.7b is the simulated closed-cavity pressure as a function of loading duration. It indicates that the observed effects of trapped air are brought about by cavity pressures that are little more than 1.6 atmospheres in magnitude.

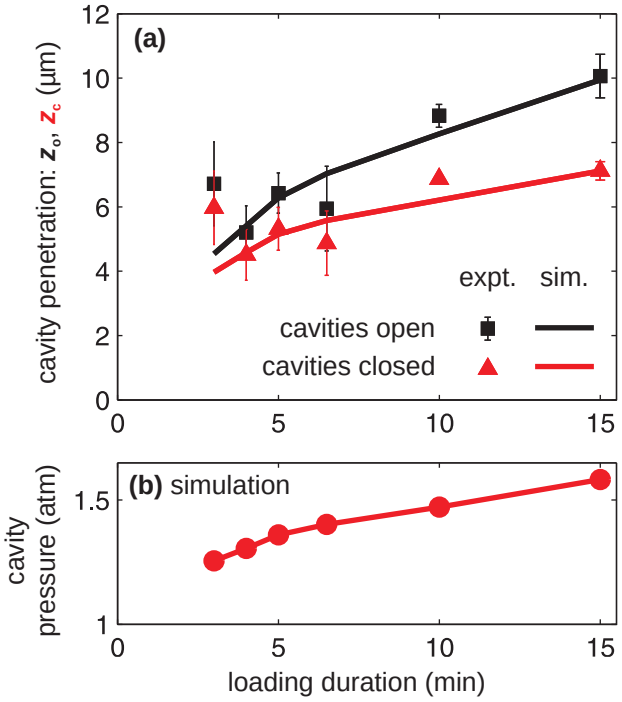

Figure 5.7: (a) Symbols: experimentally measured peak cavity penetration heights results as a function of loading duration, for Zeonor 1060R embossed at 110 °C under a sample-average pressure of approximately 165 kPa. Cavity pitches were 50 μm and their widths were 40 μm. Lines: corresponding simulated peak penetration heights, assuming no air permeation. (b) Simulated in-cavity air pressure as a function of loading duration.

5.4.2. Experiments with PMMA

We have also investigated the effect of air-trapping during the embossing of PMMA. Figure 5.8 compares measured and simulated topographies for the embossing of an array of parallel ridges with pitch 50 µm and width 40 µm. Embossing was performed at 130 °C under 270 kPa for two minutes. The correspondence between experiment and simulation is reasonably close: the cavity penetration in sealed cavities is about 10% smaller than in cavities that are open to the atmosphere.

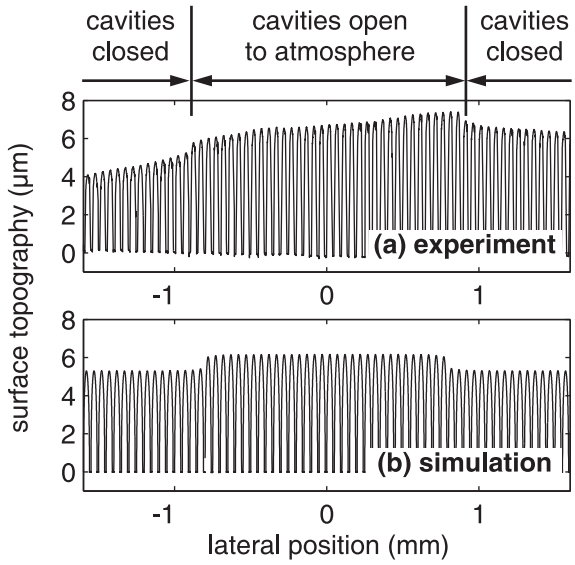

Figure 5.8: (a) Cross-section through part of measured PMMA topography after embossing at 130 °C for 2 minutes under a sample-average pressure of 270 kPa; (b) simulated cross-section assuming same processing conditions and no permeation of air. The pattern embossed is an array of parallel ridges with pitch 50 µm and width 40 µm.

The evolution of embossed PMMA topographies over time was investigated in a series of experiments with differing loading durations. In Figure 5.9a are plotted the peak cavity penetrations against loading duration for the embossing of arrays of 50 µm-pitch, 40 µm-width ridges.

The symbols in Figure 5.9a represent experimental results, extracted from scanning white-light interferograms. As in Figure 5.7a for Zeonor 1060R, cavity penetration depths are extracted and plotted separately for the open-to-atmosphere and sealed-off regions of the stamp. Although the nominal sample-average embossing pressure for each of these experiments was specified as 260 kPa, the control system of the load-frame used behaved in such a way that there was substantial sample-to-sample variation of true applied average embossing pressures, as recorded in Table 5.1. Because of these sample-to-sample pressure variations, the experimentally recorded peak cavity penetration depths do not increase monotonically with loading duration in Figure 5.9a.

The measured, sample-specific, embossing pressures were used in performing the corresponding simulations, whose results are represented as solid lines in Figure 5.9a. The simulation results track the experimentally measured cavity penetration depths results reasonably well. As we would expect for PMMA in a rubbery state at 130 °C, cavity penetration depths do not substantially increase as the loading duration progresses beyond two minutes.

If trapped air were able to permeate the PMMA material or the stamp, or to escape in some other way, we would expect the red (sealed-cavity) symbols to move closer to the black (open-cavity) ones as the loading duration increased. As we observed with Zeonor 1060R, there is no evidence that air is leaving the cavity over the 15-minute period explored.

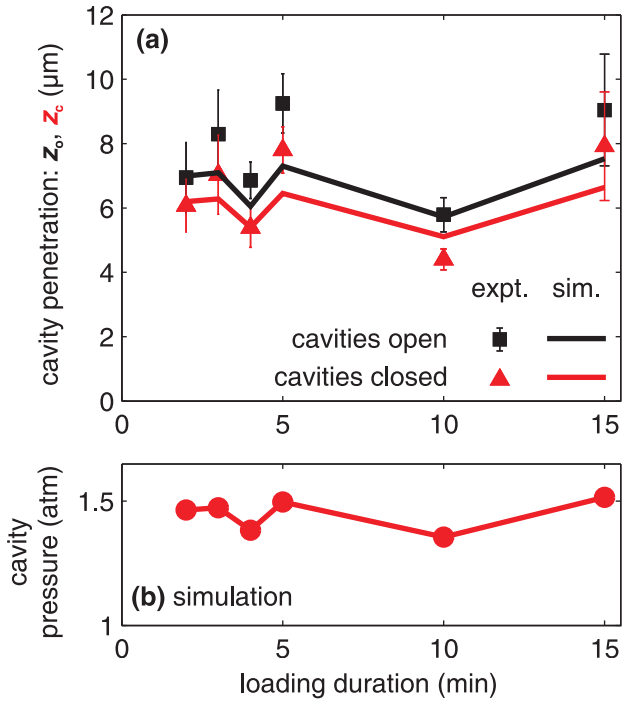

Figure 5.9: (a) Symbols: experimentally measured peak cavity penetration heights results as a function of loading duration, for PMMA embossed at 130 °C under a sample-average pressure of nominally 260 kPa. There was considerable sample-to-sample variation of the true applied pressure, with the result that the cavity penetrations recorded do not increase monotonically with loading duration. Cavity pitches were 50 μm and their widths were 40 μm. Lines: corresponding simulated peak penetration heights, assuming no air permeation. (b) Simulated in-cavity air pressure as a function of loading duration.

5.4.3. Impact of air on cavity-corner filling

Figure 5.10, meanwhile, shows a cross-sectional scanning-electron micrograph and a simulated cross-section for a Zeonor 1060R sample in which the cavities are much closer to being filled with polymer than in the previous experiments. The section of the pattern illustrated is at the interface between a region where stamp cavities were open to the atmosphere and one where stamp cavities were sealed. In the sealed-cavity region of the pattern, the 'rounding' of the edges of the embossed ridges is appreciably greater than in the open-cavity region. The simulated topography echoes this observed difference reasonably closely.

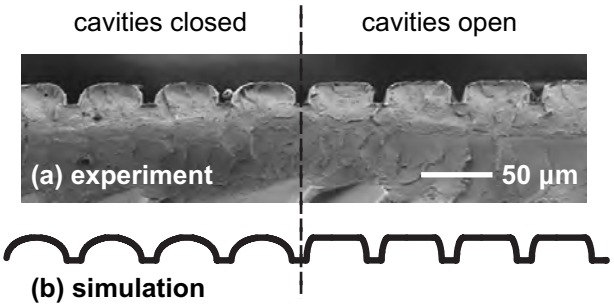

Figure 5.10: Results for the nearly-complete filling by Zeonor 1060R of long, slender stamp cavities at 120 °C. (a) Scanning electron micrographs of a cross-section through the sample. (b) A corresponding, simulated topography.

5.5. Summary

It appears that the presence of trapped air inside stamp cavities can substantially retard the filling of those cavities with polymeric material during embossing. The effect becomes more marked as the product of effective polymer compliance and atmospheric pressure increases. The effect also becomes more severe when the widths of a pattern's stamp cavities are a large proportion of the pattern's pitch. Our experiments indicate that Zeonor 1060R and PMMA — when embossed at typical temperatures and for reasonable loading durations — are not sufficiently permeable to allow much air to escape from stamp cavities during embossing.

These findings have important implications for embossing machine design, as well as for the design of patterns to be embossed and for the selection of processing parameters. The results indicate that it can certainly be advantageous to perform embossing under a reduced atmospheric pressure. A vacuum chamber is already part of certain commercial hot-embossing tools and our findings suggest that the cost of providing such a feature is likely to be warranted.

If there is no practicable or affordable way of excluding air from stamp cavities during an embossing process, one might imagine simply increasing the embossing load to compensate for the presence of air and force polymer into the cavities. Our simulation results suggest, however, that to achieve near-complete cavity-corner filling in the presence of trapped air, the embossing pressure may need to be many times greater than it would in a case where air is excluded from the cavities.

Alternatively, one could conceive of introducing special 'pressure-relief' cavity features to stamp designs. We imagine that these features would be particularly narrow cavities, connected to larger cavities on the stamp and designed not to be very deeply penetrated by polymeric material during embossing. The unfilled portions of these relief cavities would provide a 'refuge' for air that would otherwise resist the filling of the important, functional parts of the pattern. These relief cavities would of course need to be located so that they did not interfere with the function of the manufactured polymeric device.

6. Adaptation of model to the micro-embossing of finite-thickness substrates

The embossing simulation procedure described in Chapter 2 was derived for infinitely thick substrates. For micro-embossed polymeric layers on the order of 1 mm in thickness, such a model has been seen to represent experimental results well. For thinner layers, however, a more general approach is needed. We begin by confining ourselves to cases in which the thickness of the layer is reduced during embossing by only a small proportion of its original thickness.

6.1. Modification of kernel function for finite-thickness substrates

6.1.1. Definition of modified function

The key change that needs to be made to our simulation approach is in the description of how the material's surface deforms when exposed to unit pressure across a small region. The change in description is illustrated schematically in Figure 6.1: whereas for very thick layers a load applied normally to the surface causes material to be displaced predominantly downwards, for finite-thickness layers we need to account for the *lateral* displacement of material.

We use an approach described by O'Sullivan and King [212], and later employed by Peng and Bhusan [191] and by Nogi and Kato [188], in which an analytical solution is found for the Papkovich-Neuber potentials in a finite-thickness elastic layer and in the elastic half-space supporting it. The stresses and displacements in the finite-thickness layer are then found for the application of unit pressure to a central $d \times d$ region of the surface. The solution is performed in the spatial frequency domain and the inverse Fourier transform is subsequently computed numerically to give a spatial representation of the new kernel function.

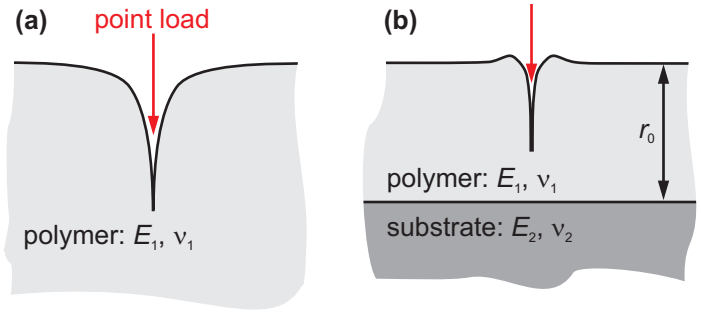

Figure 6.1: Comparison of the point-load responses of thick and thin polymeric layers. When the layer is much thicker than the characteristic lateral dimensions of the structure being imprinted (a), the layer can be well approximated as an elastic half-space. When the layer thickness is comparable with the dimensions of the pattern being imprinted (b), a different function, dependent on r_0, is required. E_i are the layers' Young's moduli; ν_i are their Poisson's ratios.

The Fourier transform of the surface deflection of layer 1 is given by:

$$C(\xi,\eta) = -\left[\frac{1-\nu_1}{\mu_1}\right]\left[1 + 4\alpha r_0 \kappa \exp(-2\alpha r_0) - \lambda\kappa \exp(-4\alpha r_0)\right]\alpha R \tag{6.1}$$

where ξ and η are spatial frequencies and

$$\left.\begin{aligned} &\alpha = k_f\sqrt{\xi^2+\eta^2}; \quad \lambda = 1 - \frac{4(1-\nu_1)}{1+(\mu_1/\mu_2)(3-4\nu_2)}; \quad \kappa = \frac{\mu_1/\mu_2 - 1}{\mu_1/\mu_2 + (3-4\nu_1)} \\ &R = -\left[1 - \left(\lambda + \kappa + 4\kappa\alpha^2 r_0^{\,2}\right)\exp(-2\alpha r_0) + \lambda\kappa\exp(-4\alpha r_0)\right]^{-1}\alpha^{-2}. \end{aligned}\right\} \tag{6.2}$$

The thickness of layer 1 (as defined in Figure 6.1) is denoted as r_0 and layer 2 is assumed infinite in thickness; μ_i are the layers' shear moduli, equal to $E_i/[2(1+\nu_i)]$. The factor k_f is introduced here as a way of 'tuning' the model to experimental results. It has no physical basis at present but has been found to be needed to model some of the results that will be presented in Section 6.4. In the absence of 'tuning', k_f is set to 1.

In this implementation, $C[\xi_m, \eta_n]$ are computed over a range of $2N$ for m and n, where $\xi_m = mk_f\pi/Nd$ and $\eta_n = nk_f\pi/Nd$. The value of $C[0, 0]$ is undefined according to (6.1); however, since most thermoplastics above their glass transition temperature are almost incompressible, we set $C[0, 0]$ to zero, with the result that the average value of the function in the spatial domain will be zero — consistent with conservation of the layer's volume. After inverse Fourier transformation of $C[\xi_m, \eta_n]$ and scaling up by the empirical factor k_f, the central $N \times N$ region of the resulting matrix is taken as the kernel function, $c[m, n]$, for use in simulation (Figure 6.2). This approach to constructing the kernel function has been found necessary in order to give accurate simulations of long-range pattern interactions. (In the subsequent simulation, $c[m, n]$ is again Fourier-transformed as part of the forward convolution with trial pressure distributions.)

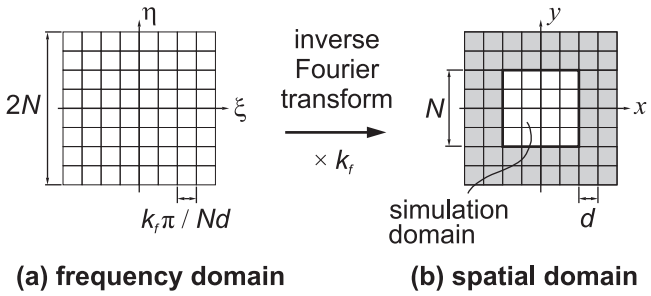

Figure 6.2: Illustration of the relationship between frequency and spatial domains in the construction of the point-load response kernel function. Coefficients in the frequency domain are calculated across a matrix with four times as many elements as are in the spatial representation of the region to be simulated. The additional empirical factor k_f is introduced to allow the characteristic length of the kernel function to be 'tuned' to experimental results if necessary. After inverse Fourier transformation and scaling by k_f, the central $N \times N$ elements of the resulting matrix are used as the kernel function. After Nogi and Kato [188].

The substrate would usually be expected to be much harder than the polymeric layer, although its stiffness and Poisson's ratio can be arbitrarily specified. The substrate is also assumed in this formulation to be bonded to the polymeric layer. If the substrate is genuinely attached to the layer — as it would be if

the polymer had been spun on to a silicon wafer prior to embossing — we would almost certainly be comfortable with this assumption. If, however, the polymer layer is self-contained (*e.g.* an extruded film), the assumption may be less valid. It would be possible to derive kernel functions for various polymer–substrate coefficients of friction.

The kernel function was evaluated and is plotted in Figure 6.3 for three values of r_0 — values that are relevant to the experiments reported later in this chapter. In the functions plotted here, the layer is assumed to have a Young's modulus of 2 MPa and a Poisson's ratio of 0.5, and each function is discretized at a 1 µm pitch and evaluated over a 512 µm × 512 µm region. For r_0 = 1 mm, the function produced by evaluating and inverse Fourier-transforming (6.1) is almost indistinguishable from the analytical function of (2.8) for an elastic half-space. For r_0 = 75 µm, the diameter of the kernel function has tightened somewhat but retains largely the same shape. For r_0 = 2.2 µm, however, the function has changed radically to a two-peak form in which material is displaced upwards around the region of application of pressure.

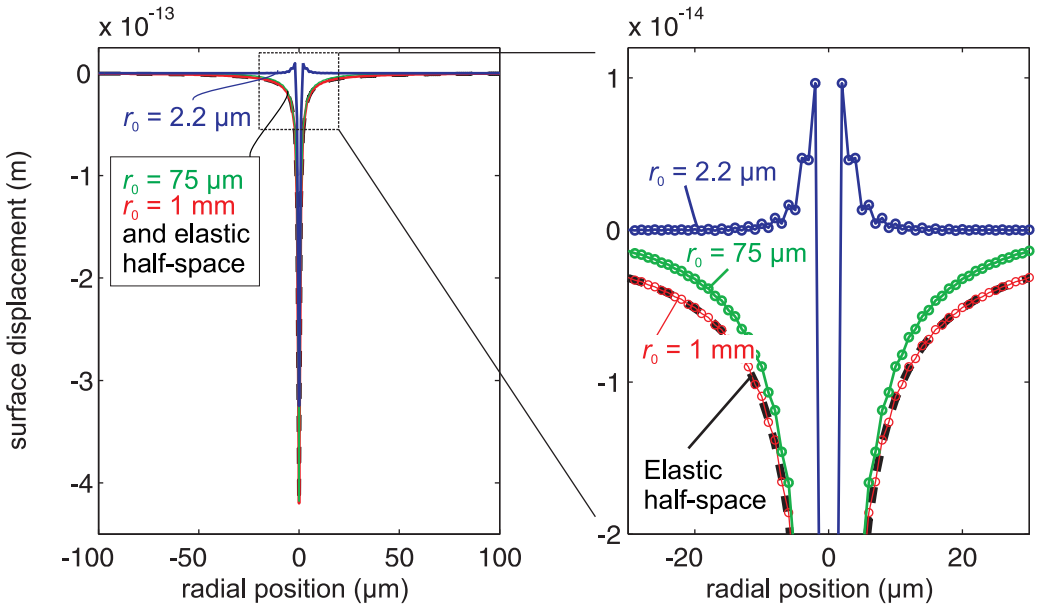

Figure 6.3: Comparison of kernel functions generated for three different layer thicknesses. The functions are discretized with pitch d = 1 µm and describe the displacement of an elastic material's surface in response to unit pressure applied downwards across a region of size $d \times d$, centered at (0, 0). The layer, of thickness r_0, is assumed to have a Young's modulus of 2 MPa and a Poisson's ratio of 0.5. The three function instances for which r_0 is defined were generated following the method described by Nogi and Kato [188]. For r_0 = 1 mm, the finite layer-thickness function is virtually indistinguishable from the analytical function for the surface displacement of an elastic half-space [189]. For r_0 = 75 µm, the shape is appreciably changed, and for r_0 = 2.2 µm, the function has morphed into one with two peaks, indicating upwards displacement of material around the point of loading.

6.1.2. Roughness of function, and impact

While the method for computing the kernel function for a finite-thickness layer produces a smooth result when $r_0 >> d$, the kernel function is noticeably rough when $d \sim r_0$ or $d >> r_0$. Superimposed on the basic two-peak kernel shape is then an oscillating component with a spatial period of $2d$. Although, as will be seen in Section 6.4, rough functions of this kind are usually able to provide smooth and realistic simulated topographies, it may prove desirable to find a way of generating a smoother kernel function.

6.1.3. Sensitivity of simulation results to coarseness of pattern discretization

Next we investigate the sensitivity of simulation results to the pitch of pattern discretization, d. To this end we ran a series of simulations in which an incompressible, elastic layer of thickness r_0 was embossed with a hard stamp having a circular protrusion of radius a_0 = 50 μm. The values of r_0 and of the discretization pitch, d, were varied independently, and contact pressure distributions were simulated to represent a small rigid-body movement of the stamp into the layer. The layer was assumed to be fully adhered to a hard substrate and lateral displacements of the layer with respect to the stamp were considered negligible so that friction could be ignored. The relief of the stamp protrusion was assumed large enough that none of the elastic material pushed outwards from the edges of the compressed region would make contact with the surrounding regions of the stamp.

We see in Figure 6.4b that for elastic layers that are far thinner than the radius of the embossed feature (a_0/r_0 = 50), the contact pressure distribution is approximately parabolic in shape, being almost zero at the edges and reaching a maximum at the center of the embossed region. This simulation result is found to hold, within a few percent, for discretization ratios d/r_0 from 0.3 to 10. Even though the kernel functions generated for these various d/r_0 values might themselves vary greatly in shape, the final simulation results do not.

As the layer thickness r_0 approaches the embossed feature radius, a_0, the parabolic pressure distribution begins to morph into one with peaks at the edges of the contact region. For very thick layers, this pressure distribution would be purely edge-high, as was the case in the simulations of Chapter 2. For these thicker layers, the coarser levels of discretization fail to capture the pressure peaks at the edges of the contact region, but the basic ‘envelope’ of simulated contact pressure outside those edge regions is captured well at all values of d/r_0 investigated. Our findings here are essentially the same in nature as those in Chapter 2 where we investigated the effect of discretization coarseness for thick layers.

In cases where the pressure distribution across the contact region is a combination of center-high and edge-peaked (for a_0/r_0 = 10, for example), there is a small amount of ‘jaggedness’ visible in the pressure simulation (see Figure 6.4c). We attribute these imperfections to the roughness of the generated kernel function. In general, however, artifact-free pressure distribution simulations are produced using the present method, regardless of the ratio of layer thickness r_0 to feature diameter, and independently of the discretization ratio d/r_0.

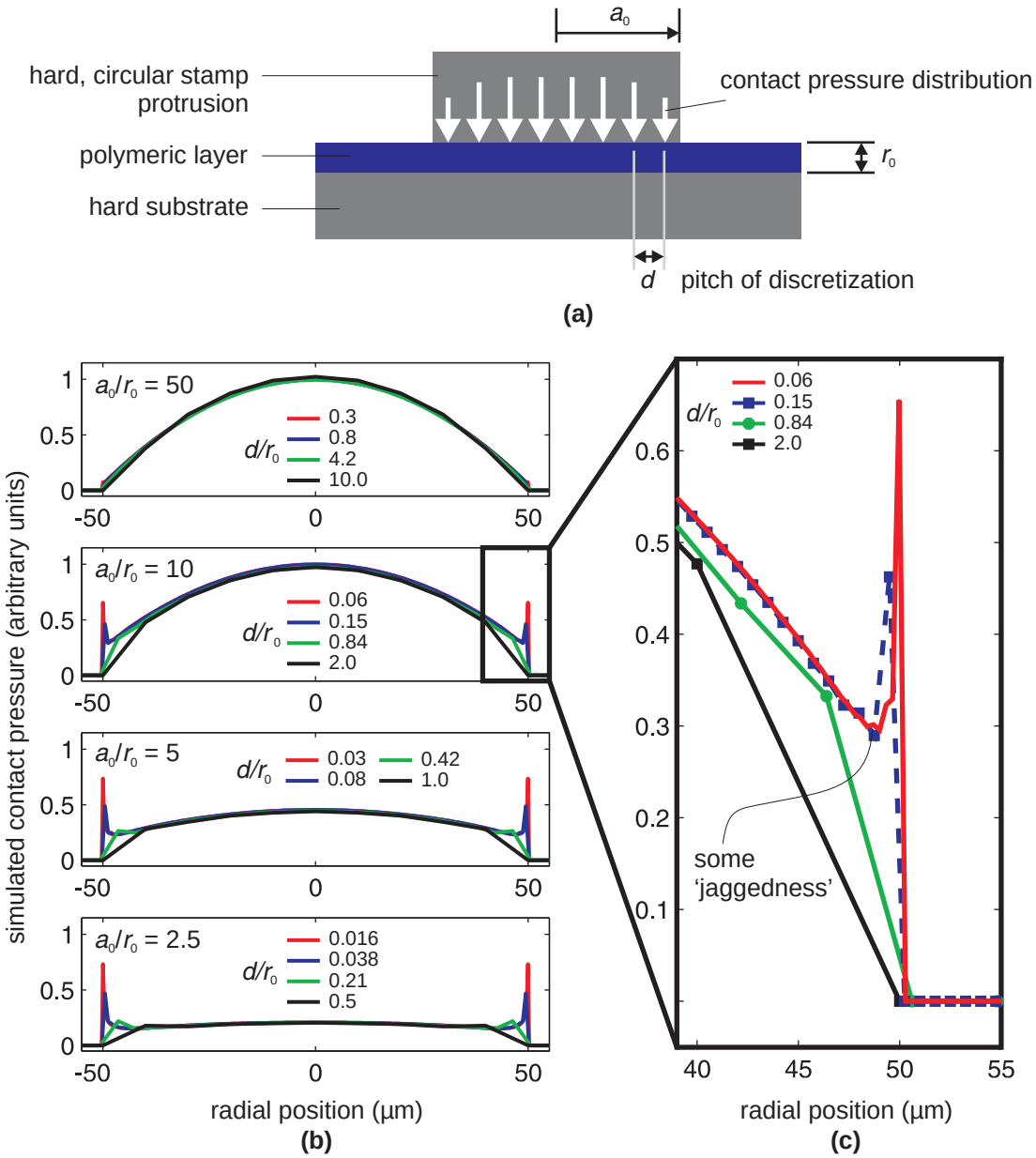

Figure 6.4: Investigation of the sensitivity of simulation results to coarseness of discretization. (a) schematic of simulated geometry; (b) simulated contact pressure distributions for four radius-to-thickness ratios a_0/r_0, and in each case for four different levels of discretization d/r_0; (c) close-up of simulated pressure distributions at the edge of a contact region.

6.2. Extending the approach for viscoelastic or viscous substrates

6.2.1. Generalizing the compliance function

While Nogi and Kato's function above was derived for a purely linear-elastic medium, it is possible for us to adapt its use to simulate the embossing of linear viscoelastic, or even purely viscous, media. To do so we can use the same approach as developed in Section 3.6 for thick layers with compliances that are linear functions of time. All that needs to be done is to compute the following non-dimensional time-integral of the spatial average of the pressure–compliance product:

$$p_{g,0}(t_h) = \int_0^{t_h} p_0(t') \frac{\mathrm{d}J(t-t')}{\mathrm{d}t'} \mathrm{d}t' \,. \tag{6.3}$$

A simulation can then be performed for a 'virtual' elastic layer with unit compliance and an average applied pressure $p_{g,0}(t_h)$. The way in which the virtual layer responds to this effective pressure will, of course, depend on the layer's thickness. If the layer is compressed by more than a small proportion of its thickness, a point-load-response function evaluated for the initial layer thickness will not be applicable for the whole range of the deflection. Ways of dealing effectively with large layer compressions are developed in Chapter 7.

6.2.2. Establishing the 'correct' correspondence between viscosity and elasticity

In Chapter 2 we developed an expression for the effective compliance of a thermoplastic substrate as a function of its elasticity, viscosity, and loading duration. In that derivation it was assumed that the viscosity, η, of a viscous material was directly analogous to the Young's modulus, E, of an elastic medium. Material parameters were fit according to this assumption.

To be strictly correct, however, viscosity is to a viscous medium as *shear* modulus is to an elastic medium. In a viscous medium, shear stress is linked to shear strain rate through the viscosity, η, while in an elastic medium shear stress is linked to shear strain through the shear modulus, $\mu = E/2(1+\nu)$. The quantity for a Newtonian liquid that is truly analogous to Young's modulus, E, of an elastic medium is therefore:

$$\eta_1 = 2\eta(1+\nu) = 3\eta. \tag{6.4}$$

Since liquids are essentially incompressible, we substitute $\nu = 0.5$. This change of definition does not in any way invalidate the results in earlier chapters of this thesis, but becomes important for the following sections.

6.2.3. Agreement of the model with an analytical expression for the squeeze-flow of a Newtonian fluid

In this section we consider the simulation of the imprinting of a Newtonian fluid and demonstrate that our numerical simulation model yields results consistent with an independent analytical model for the squeeze-flow of a disk of fluid.

Firstly we performed a simulation of the contact pressures needed to press a rigid circular die of radius 50 μm into a purely viscous layer of viscosity 10^7 Pa.s and instantaneous thickness 0.5 μm at a speed of 1 nm/s (Figure 6.5a). The quantity substituted into (6.1) for the shear modulus μ_1 was (10^7 Pa.s)/(1 s) and the rigid-body displacement for which a pressure distribution was solved was 1 nm. A biconjugate-gradient algorithm was again used to find the appropriate pressure distribution. The resulting simulated contact pressures are shown as the red dashed line in Figure 6.5c. The point load-response function was

derived by Nogi and Kato assuming no friction at the contact surface, and so this is the assumption inherent in the numerical simulation.

We now consider an analytical expression for the pressure distribution during the squeezing of a disk of Newtonian fluid between two rigid plates when there is, in contrast, *no slip* at the fluid–plate interface. For a disk of instantaneous thickness $2r_0$ and viscosity η, the pressure distribution in the fluid $p(a)$ is given by Byron Bird [213] as a function of radial position, a, by:

$$p(a) = -\frac{3\eta a_0^2}{4{r_0}^3}\frac{\mathrm{d}r}{\mathrm{d}t}\left[1-\left(\frac{a}{a_0}\right)^2\right]. \tag{6.5}$$

where a_0 is the radius of the disk. The layer is assumed so thin that the pressure is a function of only radial position, and does not vary through the thickness. In this no-slip situation, we note that shear stresses in a plane half-way through the thickness of the disk are zero. We exploit this symmetry to observe that the velocities and shear stresses in one half of a disk of thickness $2r_0$ in the no-slip case are almost identical those in a layer of thickness r_0 in the no-friction case. We therefore expect the pressure distributions for a particular value of dr/dt to be almost identical for each of the two cases illustrated in Figure 6.5a–b, and indeed they are, as shown in Figure 6.5c.

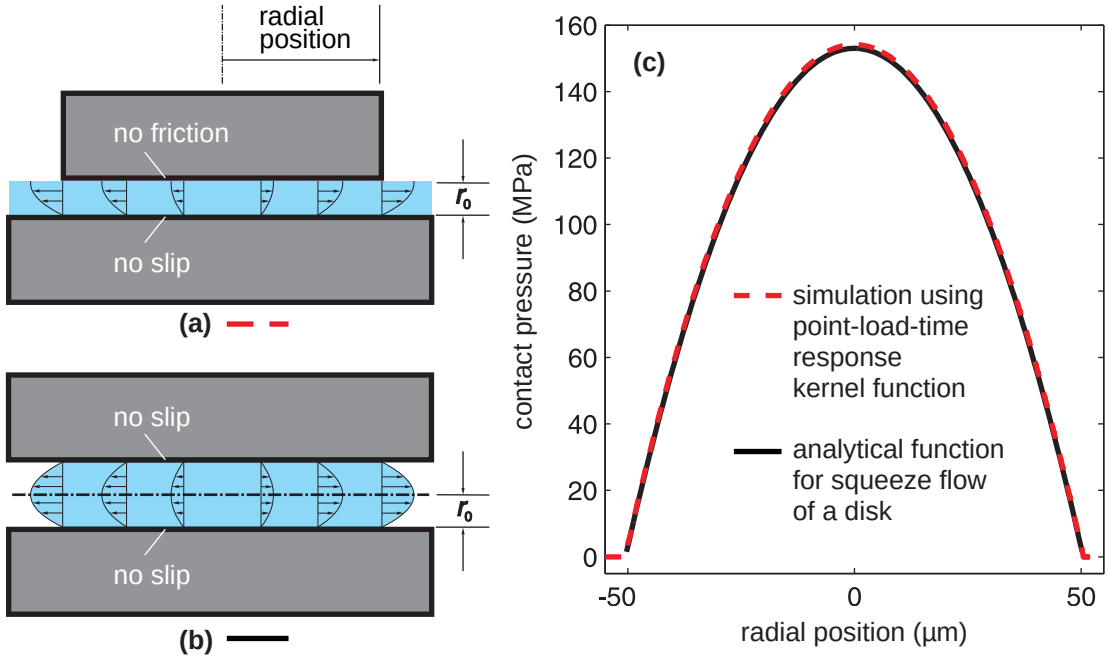

Figure 6.5: Confirmation of agreement between the convolution-based embossing model and an analytical expression for the squeeze-flow of a Newtonian fluid. (a) cross-sectional schematic (not to scale) for the kernel function-based simulation: a layer of thickness r_0 is embossed with a rigid circular punch, and the model assumes no friction between punch and layer. (b) Cross-sectional schematic (not to scale) for a squeeze-flow analysis, with no slip assumed between fluid and rigid plates; the layer must be of thickness $2r_0$ for the contact pressures and dr/dt both to be the same as in (a). (c) Demonstration of equivalence of simulated and analytical results. The geometry simulated is a 50 μm-radius disk. The assumed viscosity is 10^7 Pa.s and the fluid is taken to be incompressible. The instantaneous value of r_0 is 0.5 μm. Contact pressures are for dr/dt = –1 nm/s.

There is a further, subtle, difference between the two modeling cases. The numerical simulation assumes that the layer being compressed is of infinite extent and that the size of the embossing stamp protrusion determines the extent of the region being compressed. The analytical function, meanwhile, assumes that the fluid takes the shape of a disc of finite size, compressed between two rigid plates extending beyond the edges of the fluid. The comparison of the two models indicates that for very thin fluid layers, this difference in edge conditions has a negligible effect on the simulated pressure distributions.

From this analysis it is clear that for thin layers the relationship between applied pressure, layer thickness, and rate of compression of the layer is strongly dependent upon whether the polymer–stamp interface is able to slip. The rate of compression for a given applied average pressure and layer thickness is expected to be four times slower in the no-slip case than in the frictionless stamp–polymer contact case.

6.3. Experimental method

Some experiments were conducted with which to explore pattern dependencies in the embossing of thin polymeric layers. In these experiments we do not attempt to fit the compliances of the embossed materials as functions of time or temperature, but instead fit for each embossing experiment a single *effective* compliance that reflects the particular processing conditions used.

6.3.1. Test-pattern design

The test-pattern illustrated in Figure 6.6 was used to conduct embossing experiments against which to compare simulation results. The pattern comprises a 30 mm square array of identical cells, with each cell having diameter 0.85 mm. The cell design, when transferred to an embossing stamp, incorporates square holes and trenches with diameters and separations ranging from 10 to 100 μm. The design of the pattern is deliberately periodic, to allow for convenient simulation using the method described above.

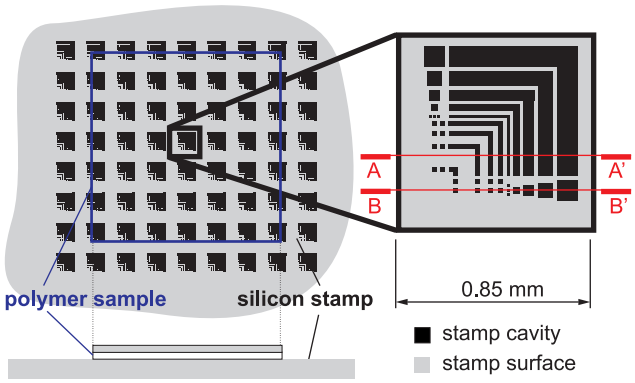

Figure 6.6: Test-pattern for embossing polymeric layers. The design of one unit of the pattern contains square holes, trenches and ridges ranging from 10 to 100 μm in diameter. The relief of the pattern on the test stamp is ~ 30 μm. The stamp is patterned with a square, homogeneous array of these units at a pitch of 850 μm. The array of patterns extends beyond the edges of the polymeric sample. Two sections through the pattern are defined for the analysis of results: A–A', which is through embossed ridges/trenches, and B–B', which is through square posts on the embossed part.

6.3.2. Test stamp fabrication

The test-pattern illustrated was etched into a silicon wafer using deep reactive ion etching to a depth of approximately 30 µm. The etch mask was a 10 µm-thick layer of Clariant (Charlotte, NC) AZ4620 photoresist and after etching this was removed from the wafer by a 30-minute oxygen plasma exposure followed by a 15-minute immersion in a hydrogen peroxide/sulfuric acid 'piranha' mixture.

6.3.3. Embossing of 75 µm-thick PMMA film

Sheets of 75 µm-thick Rohaglas 99845 PMMA were obtained as a gift from Degussa HPP Technical Films (Madison, WI). Two preliminary 15 mm square samples were cut from the film and embossed with the silicon test stamp under the following conditions: (*i*) 75 °C, with a sample-average pressure of *c*. 4 MPa; (*ii*) 80 °C, with a sample-average pressure of 13 MPa. In both cases the load was held for 2 minutes before cooling to 40 °C and unloading. The embossing apparatus used was a Carver (Wabash, IN) 4386 manual hydraulic press equipped with electrically heated platens and water-assisted cooling.

A 1.5 mm-thick polycarbonate plate served as the 'rigid plate' of Figure 1.1a: since the embossing temperature was well below polycarbonate's glass-transition temperature of ~ 137 °C, it was assumed that the Young's modulus of the backing plate was 3 GPa and with a Poisson's ratio of 0.3.

6.3.4. Embossing of spun-on 2.2 µm-thick polysulfone film

Polysulfone (BASF, Florham Park, NJ) was dissolved at a concentration of 15 wt% in N-Methylpyrrolidone, and was spun at 1000 r.p.m. on to silicon wafers on to which had first been deposited a silicon nitride layer using the process detailed by Iliescu *et al.* [214]: it has been found by Iliescu *et al.* that the nitride layer promotes the adhesion of the polysulfone to the wafer's surface. After spinning, the wafers were baked on a hotplate at 110 °C for one minute. A wafer coated in this way was broken into pieces *c*. 15 mm square. As a preliminary test, one of these pieces was embossed at 205 °C with a sample-average pressure of 30 MPa that was held for two minutes before cooling. The embossing temperature was 20 °C above the published value of polysulfone's glass-transition temperature. Because of the high temperature of embossing, it would not have been safe to use the water-cooling capability of the press, and the platens were instead allowed to cool, via radiation and the convection of air, at a much slower rate, taking ~20 minutes to reach the unloading temperature of ~130 °C.

6.3.5. Measurement

The pre-embossing thickness of the spun-on polysulfone film was measured by scratching the film from part of a fragment of a film-coated wafer, sputtering the fragment with ~ 50 nm gold, and profiling the surface with a Zygo (Middlefield, CT) NewView scanning white-light interferometer. The PMMA film's thickness, meanwhile, was measured with a micrometer screw gauge.

The polysulfone sample, post-embossing, was scratched in a small region to reveal the underlying substrate. These samples, and the embossed PMMA films, were sputtered with ~50 nm gold and their surfaces were profiled with the white-light interferometer. Using this interferometer, the area of a single cell could be scanned at a lateral resolution of ~0.5 µm within approximately two minutes. Measurement is quick enough that several measurements can efficiently be made at various positions on a sample, giving an impression of the spatial uniformity of the embossed pattern or of the frequency of defect occurrence. The topography of the etched silicon stamp was also measured by white-light interferometry.

6.4. Results and discussion

6.4.1. 75 μm-thick PMMA layer

We consider first the results of embossing the 75 μm-thick PMMA film. Cross-sections through the measured topographies are plotted in Figure 6.7. For the sample processed at 75 °C with a sample-average pressure of 4 MPa (Figure 6.7a–b), penetration of the stamp cavities was everywhere less than 2 μm. A finite-thickness linear-elastic model of the embossed layer was fit to these experimental results, and the red solid lines in Figure 6.7a–b correspond to an effective elastic modulus of 163 MPa. The effective modulus was the only fitting parameter; the factor k_f was kept equal to 1. The shape and magnitude of the simulated topographies match the measurements closely.

We also plot, as a dashed green line, the topography predicted by an infinite-thickness layer model having an effective Young's modulus of 163 MPa. Interestingly, the infinite-thickness model under-predicts by as much as 30% the degree of penetration of the narrower cavities, but substantially overestimates the degree of penetration of the 100 μm-wide cavity. In other words, for a given applied embossing pressure, cavities narrower than the layer thickness are penetrated further than they would be if the layer were infinitely thick, while cavities wider than the layer thickness are penetrated less far than they would be for a thicker layer. This result is worth noting, because it suggests that for a given stamp pattern there may be a finite polymeric layer thickness that is 'optimal' for embossing in the sense that it requires a minimal pressure to fill all its cavities.

For the sample embossed at 80 °C with a sample-average pressure of 13 MPa, the finite-thickness substrate model tracks well the peak cavity penetration depths when an effective layer modulus of 10.7 MPa is chosen (Figure 6.7c–d and Figure 6.8b). That this modulus is more than a decade smaller than the modulus fitted for the sample embossed at 75 °C indicates that these samples were processed in the glass-transition region of the polymer, in which the viscoelastic parameters vary rapidly with temperature. Extensive further investigation would be needed to place fully in context these point-estimates of effective modulus. Yet the point that can be taken from this experiment is that a linear visco-elastic material representation, using an appropriate effective compliance, can provide a good prediction of embossed topography.

Although the peak depth of cavity penetration is well captured by the model, the *shape* of the material penetrating each cavity is not very closely represented: the simulation implies that material penetrating the narrow cavities adopts a parabolic shape, while a scanning electron micrograph of the embossed part (Figure 6.8c) indicates a more rectangular shape for the 'plug' of material penetrating each cavity. A modified kernel function shape might better capture the embossed topography, although the ability of this simulation technique to establish the necessary embossing pressure for near-complete stamp filling may well prove to be adequate as it stands.

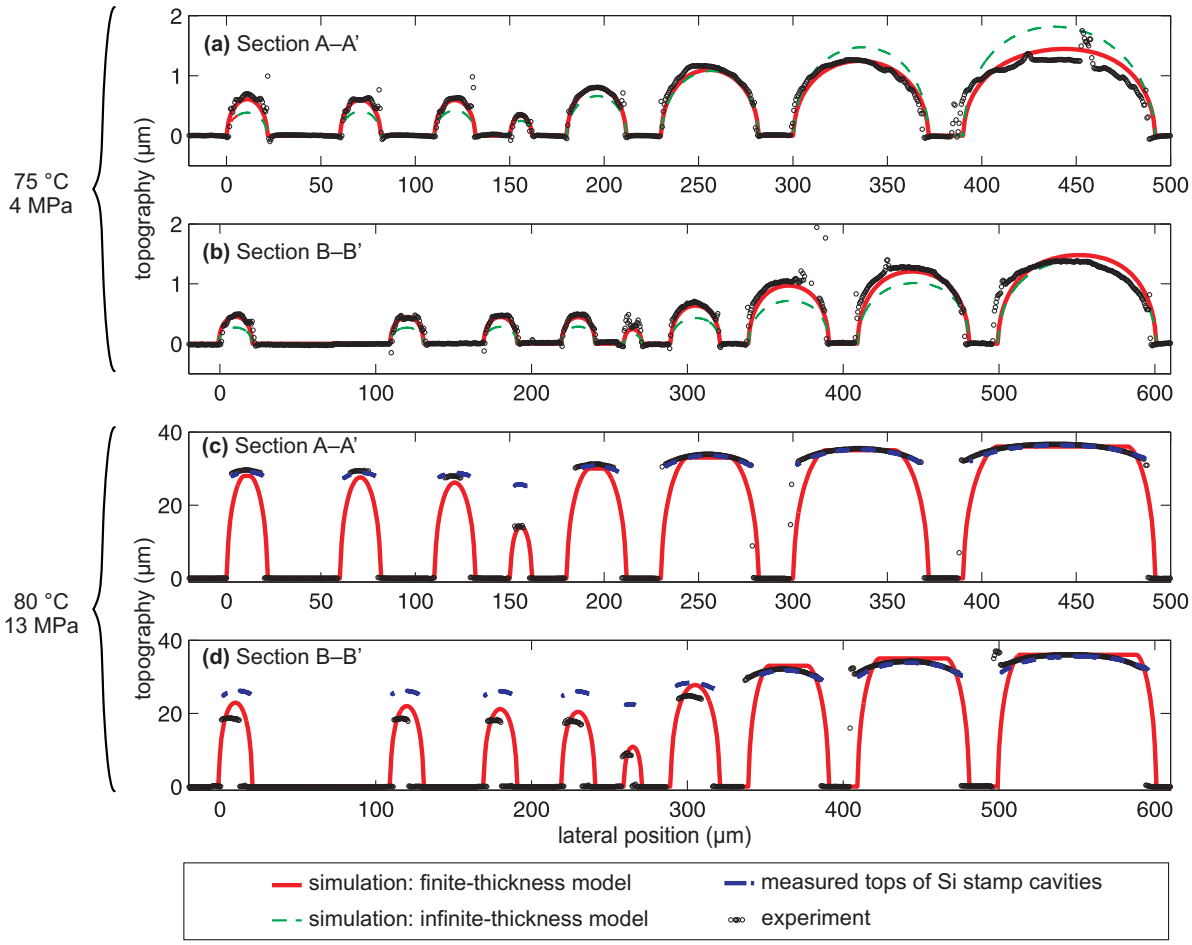

Figure 6.7: Results of embossing two samples of Rohrglas 99845 PMMA. One was embossed at 75 °C and a sample-average pressure of *c.* 4 MPa, and the other at 80 °C and *c.* 13 MPa. The loading duration was 2 minutes in each case. Measured topographies through sections A–A' (ridges) and B–B' (posts), as defined in Figure 6.6, are shown for each sample (black circles), along with the equivalent simulated topographies (red solid lines) and the measured locations of the tops of the stamp cavities (blue dashed lines). In (a) and (b), green dashed lines also show the prediction of an infinite-thickness model of the polymeric layer.

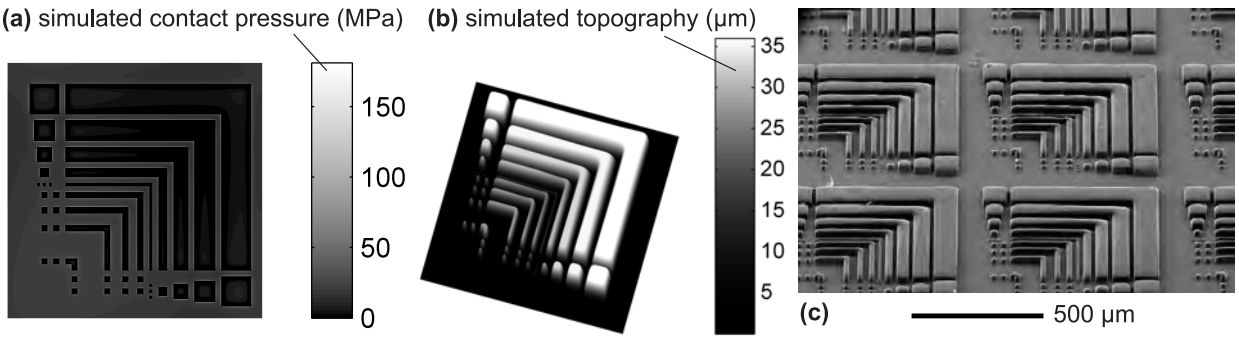

Figure 6.8: Simulation *vs.* experiment for the embossing of Rohrglas 99845 PMMA at 80 °C and a sample-average pressure of *c.* 13 MPa for two minutes. The simulated contact pressure distribution (a) indicates that the contact pressure peaks at the edges of the stamp–substrate contact regions. A 3-D plot of the simulated topography (b) shows that wider features have been penetrated more deeply by polymer. A scanning electron micrograph of a region of the sample (c) demonstrates the reasonable fidelity of the simulation.

6.4.2. 2.2 µm-thick polysulfone layer

We now consider the embossing of the polysulfone film. Figure 6.9 shows topographies measured at two separate sites on the same sample, which was embossed at 205 °C for two minutes under 30 MPa. Whereas, with the 75 µm-thick film, the wider cavities on the stamp filled more readily, in the case of this thinner film the depth of cavity penetration is larger for the *smaller* cavities, and especially for those cavities surrounded by large regions of the stamp without cavities (Figure 6.10a). Moreover, the topography of material penetrating each cavity wider than 10 µm now exhibits separate peaks at the cavity edges, in place of the single central peak seen with layers that are thicker than the cavity widths. This dual-peak filling mode is similar to that observed at the considerably smaller scales of thermal nanoimprint lithography [165, 172, 174].

When assuming $k_f = 1$, the finite-thickness kernel function generated for the measured film thickness of 2.2 µm yielded a simulated topography with peaks that were rather too sharp and too close to the edges of the cavities. By tuning the scaling factor k_f to 2.5, the characteristic diameter of the kernel function is increased by that factor and the shapes of most peaks are now well represented. A corresponding effective elastic modulus of 4 MPa is fit for the layer. The only real shortcoming of this simulation is that it over-predicts the height of the very tall peak of material at the right hand side of the traces in Figure 6.9. The scanning electron micrograph of Figure 6.10c indicates that, in the measured sample, this peak of material has curled over towards the substrate, reducing its height. This curling-over is not behavior that our simulation method would be expected to capture. Additional scanning electron micrographs of the embossed polysulfone film are shown in Figure 6.11.

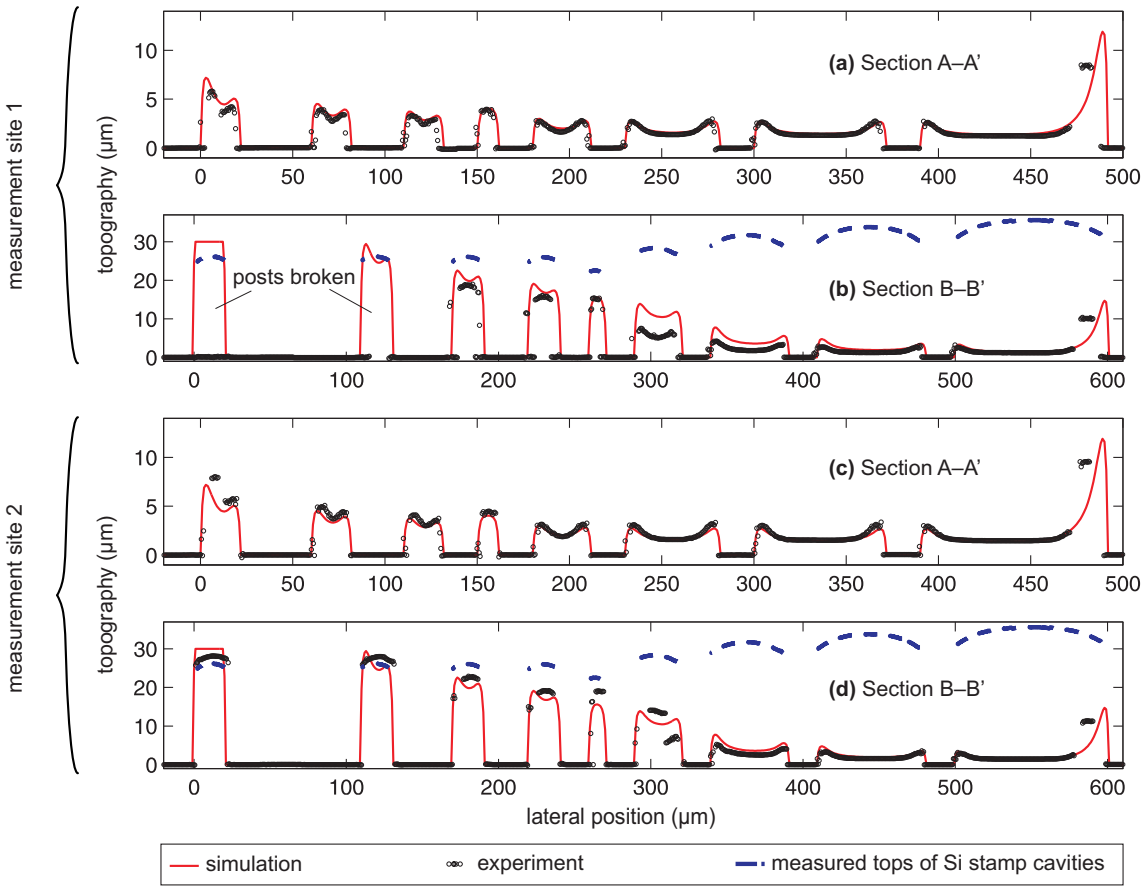

Figure 6.9: Comparison of experimental results and simulation for the embossing of a 2.2 μm-thick spun-on film of polysulfone. The sample was embossed at 205 °C with a sample-average pressure of 30 MPa held for approximately two minutes before cooling to ~120 °C over ~10 minutes and unloading. Measurements from two separate locations on the sample are shown. Measured topographies through sections A–A' (ridges) and B–B' (posts), as defined in Figure 6.6, are shown for each location (black circles), along with the equivalent simulated topographies (red solid lines) and the measured locations of the tops of the stamp cavities (blue dashed lines).

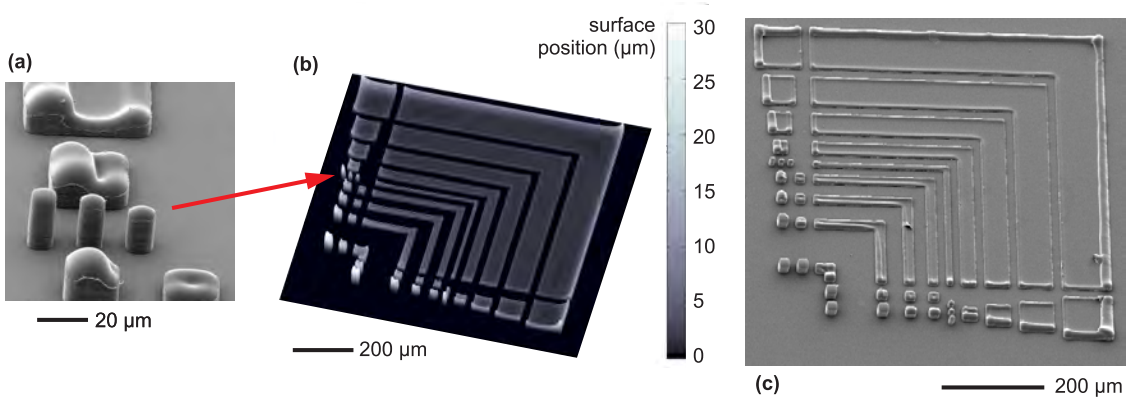

Figure 6.10: Simulation *vs*. experiment for the embossing of a 2.2 μm-thick spun-on film of polysulfone. A 3-D plot of the simulated topography (b) indicates that the narrower cavities, and especially those surrounded by few other cavities, have filled the most deeply. Scanning electron micrographs of the sample (a, c) verify this behavior.

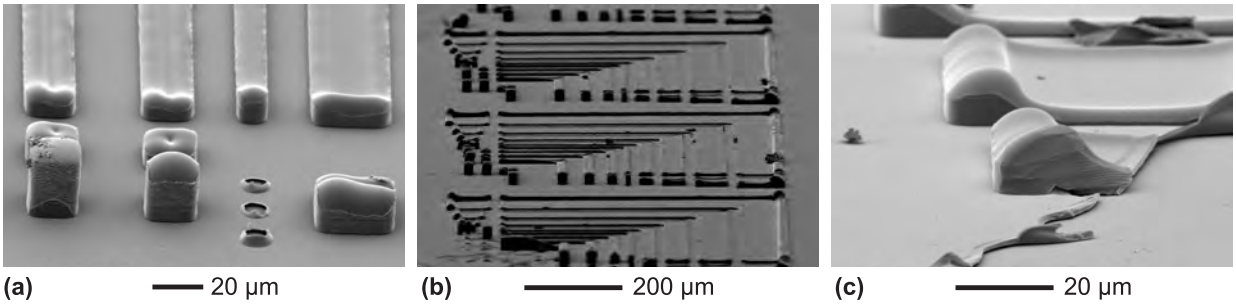

Figure 6.11: Scanning electron micrographs of the embossed polysulfone sample. (a) Close-up of 10 , 20 and 30 µm-diameter posts and ridges, showing the edge-peaks in the topographies of incompletely filled features and the places where 10 µm-diameter posts had been torn from the film during separation of the stamp from the layer. (b) Oblique view of three copies of the test pattern, showing the topography of the embossed layer. (c) Close-up of the ends of two embossed ridges, in a region where part of the film has been scratched away, revealing the SiN substrate and showing the thickness of the compressed layer of polysulfone.

The nature of the simulated contact-pressure distribution is as strongly dependent upon the layer thickness as is the shape of an imprinted topography. With the 75 µm-thick layer, contact pressure exhibits peaks at the boundaries of cavities (Figure 6.8a), while for the 2.2 µm-thick layer, contact pressure is minimal at cavity edges and increases with distance from a cavity (Figure 6.12a).

The location of the peak of the simulated pressure distribution for the 2.2 µm-thick layer corresponds to interesting artifacts in some of the experimental replicates of the test pattern (Figure 6.12b). Profiling of one of these artifacts shows that the layer thickness has apparently sprung back to its original value at the center of the artifact. Further investigation of the causes of these defects is needed.

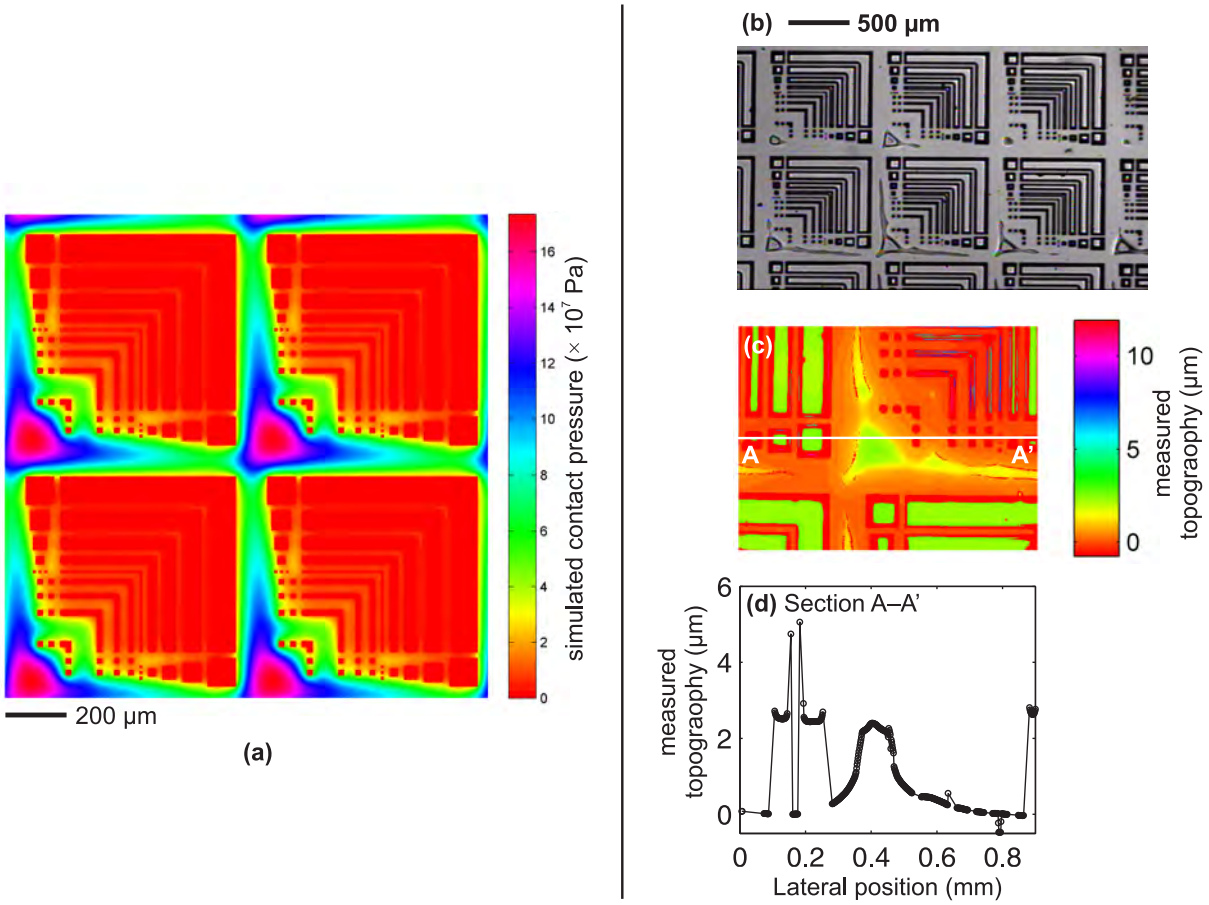

Figure 6.12: (a) Simulation of stamp–polymer contact pressure distribution in the embossing of a 2.2 µm-thick spun-on film of polysulfone. The simulated pressure increases with distance from the edges of the contact region. An optical micrograph of several copies of the test pattern in part of the embossed sample (b) indicates defects in the compressed region of the polysulfone film, corresponding in shape to that of the simulated pressure distribution. Profilometry of one of these defects (c, d) indicates that the compressed layer has 'sprung back' to approximately its original thickness in the center of the defect region.

Our current modeling approach is based on the assumption that, while the layer may be thin, it is compressed by only a small proportion of its thickness. In fact, the minimum post-embossing layer thickness of polysulfone was measured as 1.6 µm, which is around 70% of the starting layer thickness. This is a substantial reduction, and to be modeled properly we might need to consider finding the true final pressure distribution as the superposition of a series of pressure distributions associated with progressively thinner layers. Indeed, this is the approach that we develop in the next chapter. We do not, however, anticipate that such a refinement would deal with the modeling problem that the scaling factor k_f is designed to overcome: thinner layers are associated with narrower load-response kernel functions, while in contrast we found that we needed a *broader* kernel function than was directly predicted by the 2.2 µm initial thickness.

6.4.3. Simulation speed

The test pattern was discretized for simulation on a 1μm-pitch grid of 850 × 850 elements. In cases where the initial guess for the contact set was accurate, the simulation, which was implemented in MatLab (The Mathworks, Natick, MA), completed in between 30 and 90 s using a desktop computer equipped with two 3.2 GHz Intel Pentium 4 processors and 2 GB of RAM. In the case where material had touched the tops of some of the cavities (PMMA embossed at 80 °C), additional iterations to find the contact set extended the simulation time to up to ten minutes.

6.5. Conclusion

We have outlined a computationally inexpensive way of simulating the hot-embossing of thermoplastic layers of finite thickness. A simulation in which the embossed layer is discretized on a grid of size 850 × 850 takes between one and ten minutes to run. The results of such simulations have been shown to capture the key topographical features of real embossed thermoplastic layers having two markedly different layer thicknesses. The thickness of one of these layers, 75 μm, is larger than most of the feature dimensions of the embossed pattern, while the other, at 2.2 μm, is substantially thinner than all feature dimensions.

There remains much work to be done to establish the extent of validity of this modeling approach, but it does appear to be able to predict the embossed topographies of finite-thickness polymeric layers. The use of the scaling factor k_f to 'tune' the kernel function to observed pattern dependencies is not particularly elegant, and further investigation is certainly warranted to establish whether it is really necessary.

The method is also able to predict contact pressure distributions. The outputs of this modeling approach could be used to guide the design of embossed patterns — for example, by informing the introduction of 'dummy' features on embossing stamps to relieve contact pressure concentrations.

The next stage, though, is to extend the method to account for embossing/imprinting processes in which the layer is reduced to a small proportion of its initial thickness.

7. Simulating nanoimprint lithography

In the previous chapters of this thesis, the micron-scale embossing both of bulk thermoplastic plates and of thinner thermoplastic films has been modeled. The purpose of this chapter is to extend the models already presented so that they can be used to describe nanoimprint lithography.

7.1. The need for nanoimprint modeling

Nanoimprint brings several additional modeling challenges. Firstly, a layer of material being nanoimprinted is usually reduced to a small proportion of its initial thickness in certain regions of the pattern, and it will be essential to represent the increasing difficulty of reducing this residual layer's thickness as it becomes progressively thinner. The thin-layer model presented in the previous chapter was constructed on the basis of the *initial* layer thickness alone, and would not be appropriate for describing the full nanoimprint process.

The second new challenge is that deflections of the stamp and the hard substrate underlying the imprinted layer are often of crucial importance. Whereas the deflections of a half millimeter-thick silicon stamp were negligible when compared with the deflections of a softened millimeter-thick plate of PMMA, in nanoimprint they become comparable in magnitude to the deformations of the polymeric resist layer, which might be only 100 nm thick.

A third key difference from the work of previous chapters is that in nanoimprint we are not merely interested in whether every cavity on a stamp is filled with resist material during a particular imprint process. We are often even more concerned with knowing the thickness and uniformity of the residual layer of imprinted resist. This residual layer is what is typically etched through in a post-imprint fabrication step, and any variation in its thickness imposes a need for *over-etching*, whereby the duration of the etching step is prolonged to ensure that even the thickest parts of the residual layer are penetrated. Residual layer thickness variation therefore propagates to variation of the critical dimensions of the underlying etched features, and probably to unwanted device performance variation. It is clearly desirable to be able to control — or at least predict — residual layer thickness variation for a given imprinting pattern and process.

In the introduction to this thesis, two broad modes of stamp-cavity filling were outlined: one in which cavities were much narrower than the imprinted layer thickness, and viscoelastic material penetrated the cavities with a single, central, peak, and a second mode in which cavities were very wide in comparison with the layer thickness, and material entered the cavities with one peak near each wall. In nanoimprint, it may be impossible to categorize geometries this cleanly: cavity widths are often comparable to layer thicknesses and a unified way of modeling the imprinting of viscoelastic layers with arbitrary patterns is desirable.

Several types of nanoimprint machine design were described in the introductory chapter:

- Wafer-scale imprinting of spun-on thermoplastic or thermosetting layers;
- 'Step-and-flash' imprint, in which a die-sized stamp steps across the wafer and freshly sprayed-on liquid resist fills its cavities before being cured with UV light;
- Roll-to-roll nanoimprinting, which is at a much earlier stage of industrial development.

This chapter focuses on the wafer-scale embossing of a spun-on viscoelastic layer. There are two good reasons for selecting this focus. It is a widely-used process, deployed in several commercially available imprint tools and used extensively in academic research. Moreover, the imprinting of a resist layer that is flat and of uniform thickness is more readily described by extending the models of the previous chapters than is either step-and-flash or roll-to-roll imprint. It is therefore the ideal process with which to demonstrate this modeling method. There may well be ways to extend the modeling method further in the future to deal with step-and-flash and with roll-to-roll imprint, but this chapter is confined to imprinting an initially flat viscoelastic layer. An additional, realistic, assumption that can be made is that the wafer will be patterned with a square array of nominally identical dice, such that the pattern can be approximated as being periodic in space and the modeling techniques of the previous chapters are readily applicable.

In the early part of this chapter several possible viscoelastic models are considered for the imprinted resist. The relationships between the time-course of applied pressure, viscoelastic layer parameters, and imprinted layer topographies are then parameterized for three simple types of imprinted geometry: parallel lines, square holes, and circular pads. These simplified relationships are then integrated with a description of stamp and substrate deflections to construct a method for quickly simulating the imprinting of feature-rich patterns.

In the simulations demonstrated later in the chapter, *thermoplastic* imprinted layers are assumed. Viscoelastic material models could, however, also be used to describe thermally- or optically-curing thermosets. While much of the work here centers on a linear material model, a simple approach to modeling shear-thinning is also demonstrated.

7.1.1. Previous nanoimprint simulation work

In Chapter 1, we surveyed previously published work in nanoimprint simulation. It was found that there had been extensive efforts to simulate the imprinting of simple geometries into spun-on resist layers. It was also noted that efforts had been made to simulate step-and-flash imprint lithography, where two additional things needed to be modeled: capillary forces, and the dissolution of trapped pockets of gas into the resist. While these are all important modeling aims, we put to one side considerations of surface tension and gas trapping, and focus only on the deformation of the continuous viscoelastic layers encountered in thermal NIL performed under vacuum.

7.2. Hierarchical modeling approach: outline

The overall objective of this chapter is to provide an equivalent, for thermal wafer-scale nanoimprint, of the hierarchical modeling approach that was presented for bulk micro-embossing in Chapter 4. For nanoimprint, stamp deflections must be introduced and the way in which the finite-thickness layer of resist deforms must be modeled differently from the bulk case. The stamp is modeled as a square array of identical dice, each of size $D \times D$. In the case of a hierarchical stamp representation, each die is split into an array of homogeneously patterned regions of diameter d. The reference displacement of the stamp is equal to Δ in each $d \times d$ region and is the sum of stamp, substrate and polymer layer deflections. In a model accounting for wafer-scale nonuniformity, Δ would be allowed to vary from die to die.

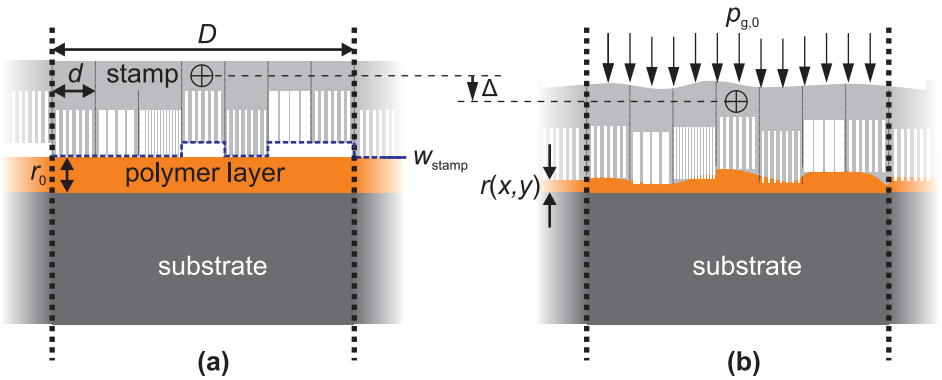

Figure 7.1: Outline of hierarchical modeling approach for wafer-scale thermoplastic embossing: (a) before imprinting pressure is applied; (b) after a pressure–compliance of $p_{g,0}$ is applied hydrostatically to the back-side of the stamp.

In this chapter we begin by modeling the deformation behavior of the resist itself, then establish how the stamp and substrate deform, and finally bring these together in the hierarchical manner hinted at in Figure 7.1.

7.3. Thermoplastic nanoimprint resists: material models

Before proceeding with resist-deformation modeling, it is important to understand the properties of commonly-used imprint resists.

7.3.1. Thermoplastic resists used, and phenomena noted

Extensive use of the well known materials PMMA and PS is reported in the nanoimprint literature. The use of molecular weights from 75 kg/mol to 950 kg/mol is widely reported: there has been much experimental work to characterize these materials' glass-transition temperatures, as well as their viscosities as functions of temperature and molecular weight [215].

A important concern in the selection of an imprint resist and process is the possibility of 'springback', whereby a portion of the resist deformation obtained during imprinting is recovered either immediately after imprinting [105] or gradually — for example over several weeks after imprinting [216]. Springback presents a challenge because a supposedly thin residual layer can, in some regions, recover to its initial spun-on thickness and impede etching of the underlying material. In general, springback has been observed to be more severe the closer the temperature of imprinting to the material's glass-transition (*e.g.* [216]) and the larger the diameter of the imprinted feature (*e.g.* [106]). The 'fingerprint stamp' of Scheer *et al.*, which includes a variety of micron-scale lines of varying width, has been used to explore these size- and temperature-dependent springback effects in detail for 350 kg/mol PS [217].

There has been interest in particularly low-molecular-weight polymers: it has been suggested that they might be amenable to room-temperature imprinting and that they would be less prone to elastic springback. One thorough exploration of 10 kg/mol PS and 30 kg/mol PMMA was unsuccessful, however, in finding processing conditions under which both elastic springback and parasitic 'self-assembly' could be avoided [218]. Moreover, the fact that lower-molecular-weight polymers are more brittle than higher molecular-weight materials when in their glassy state renders them more prone to fracture during removal of the stamp [217].

Viscosity measurements have often been done using bulk samples of material and standard rheological techniques, although the possibility of non-continuum effects in sub-100 nm-thickness layers has inspired

the use of measurements directly from nanoimprinted patterns to determine viscosity estimates. For example, Scheer *et al.* extracted viscosity estimates for 350 kg/mol PMMA and PS from the measured time-courses of residual layer thickness during the imprinting of their 'fingerprint stamp' pattern [217, 219]. As well as measuring viscosity, they characterized elastic recovery behavior and parsasitic self-assembly effects, concluding that the optimal resist viscosity for thermal nanoimprint is ~10^6 Pa.s. Leveder *et al*. performed a similar viscosity characterization for Sumitomo NEB22 resist [220]. In the work of Soles *et al*., meanwhile, imprinted gratings were annealed and the resulting re-flow of the patterns was observed via scatterometry; viscoelastic parameters as well as surface tension estimates were extracted from the re-flow data [42, 221–223]. A similar approach was taken by Buck *et al*., who used atomic force microscopy instead of scatterometry to measure the surface tension-driven decay of imprinted gratings [224].

Etch-resistance, too, is of concern when selecting an imprint resist: in most processes, nanoimprinted resist layers need to withstand reactive ion etching well enough for the underlying layer to be successfully patterned by the etch process before the resist is destroyed. Certainly the author's experience is that PMMA's resistance to reactive ion etching is rather poor. Superior etch resistance could come, for example, from the use of cross-linked resist materials such as SU-8. The thermal imprinting of partially-cured SU-8 film has been successfully demonstrated by others [65].

For biomedical and photonic applications in which broad chemical resistance and ultraviolet transmissivity are often desired, the nanoimprinting of cyclic olefin polymers, including Topas, has also been reported [6]. In that work, Topas was also discovered to offer a resistance to both oxygen and SF_6 plasma etching that was greatly superior to that of PMMA and comparable to that of SU-8.

In addition, several dedicated nanoimprint resist formulations have emerged, claiming to offer a superior mix of 'flowability' during imprint with resistance to subsequent etching. Some of these materials can be made more etch-resistant by being chemically cross-linked after imprinting [88]. Among those offering such resists is the German company MicroResist [225]; rheological [226] and etch-resilience [227] characterizations of their products have been published.

7.3.2. Candidate material models

Because one of our primary aims is to provide a simulation technique that is exceptionally quick to run, the use of a linear material model is to be desired whenever possible. At sufficiently high temperatures, experimental results reported in the literature imply that a Newtonian model with temperature-dependent viscosity is often sufficient. A Williams-Landel-Ferry temperature-dependence [200] of the resist's viscosity has often been used.

In imprinting cases only moderately far above the material's glass-transition temperature, meanwhile, a Maxwell model might be desirable because of its ability to capture the elastic 'springback' that has been observed to occur immediately after unloading. A Maxwell model would also allow for the possibility of continuous and permanent flow of the resist while under load — deformation associated with slipping of the entanglements of the polymer network [228].

There has, however, been observed by some NIL researchers elastic springback developing over a period of several *weeks* after unloading [216]. This observation suggests that the delayed elasticity of a Voigt model might still be needed for a more complete description of some resists. Perhaps a hybrid three- or four-element viscoelastic model will ultimately be needed.

Any or all of the models described above and in Figure 7.2 might be appropriate for thermoplastic resists — where the viscoelastic parameters would be functions of temperature — and could perhaps also be applied to thermally or optically-curing resists, in which viscosity would increase by several orders of magnitude during the curing process.

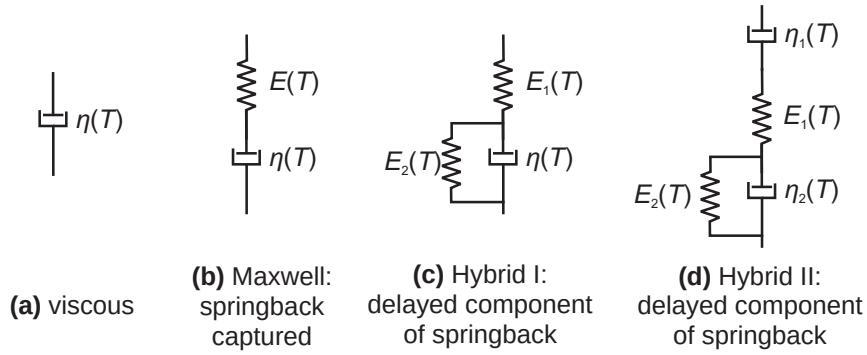

Figure 7.2: Possible thermoplastic resist models for nanoimprint. The simplest is a purely viscous model (a), which may be either Newtonian or shear-thinning. A Maxwell model (b) would additionally capture spring-back of the topography that is instantaneous upon unloading. A hybrid Maxwell/Voigt model (c) would allow for the gradual recovery of the imprinted topography over time. A four-element hybrid model (d) would allow for some of the imprinted topography to be permanent and some to recover over time.

7.3.3. Extent of validity of a linear material model

Before developing a simulation approach that assumes a linear material model, it is important to establish the limits of validity of such a model. In this section we show how to gain an impression of whether substantial shear-thinning will occur in the imprinting of a particular feature.

Suppose for the moment that a purely viscous model is to be adopted for the resist. It is well known that nanoimprint resists such as PMMA exhibit shear-thinning behavior at sufficiently large shear strain rates. The specific strain-rate at which the transition to shear-thinning occurs will depend on the type of polymer and its molecular weight distribution. As an example, Figure 7.3 shows viscosity–strain-rate data for a bulk PMMA, Rohm and Haas Plexiglas V825 [229, 230]. Although the molecular weight distribution of this grade of material is unknown, we take the data to be representative of a typical nanoimprintable PMMA resist. In the temperature range 160–190 °C, which is usual for NIL, a transition from essentially Newtonian to shear-thinning behavior is observed in the strain rate range of about 0.03–0.5 /s At strain-rates above the transition, the relationship between shear stress and strain rate is often modeled using a power law [228].

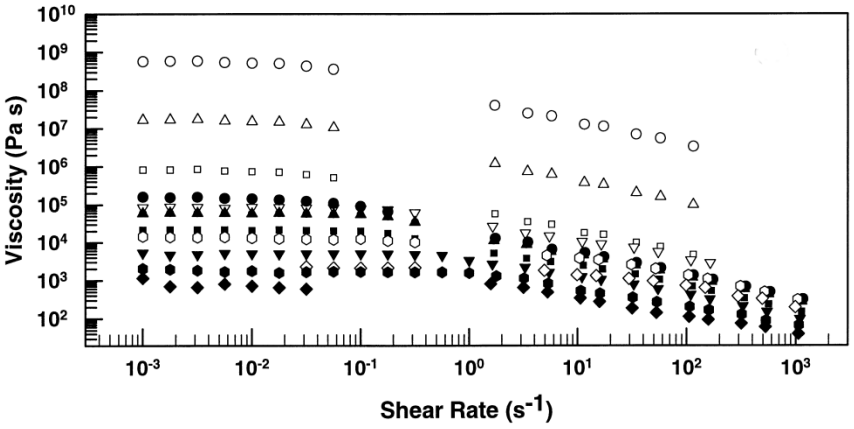

Figure 7.3: Viscosity as a function of shear rate for Rohm and Haas Plexiglas V825 PMMA (open symbols) and Dow Chemical Styron 615PR PS (filled symbols) at various temperatures (°C): circles — 160; upward-pointing triangles — 170; squares — 180; downward-pointing triangles — 200; hexagons — 220; diamonds — 240. Reprinted from Han [230].

A relationship is now developed between the rate of squeezing of a disk of Newtonian liquid and the peak shear strain rate occurring in that liquid disk. Figure 7.4 illustrates a cross-section through a disk of liquid of thickness 2*r* and diameter *a* squeezed between two rigid plates whose separation changes at a rate of 2d*r*/d*t*. Considering the liquid to be incompressible, the outwards radial volume flow rate of liquid at the edge of the disk — where the largest strain rates are expected — is

$$\dot{V} = -\frac{\pi a^2}{2}\frac{\mathrm{d}r}{\mathrm{d}t}. \tag{7.1}$$

The velocity profile of fluid at the edge of the disk may be approximated by

$$v(z) = k\left[1-\left(\frac{z}{r}\right)^2\right] \tag{7.2}$$

and from continuity we have:

$$\dot{V} = -\frac{\pi a^2}{2}\frac{\mathrm{d}r}{\mathrm{d}t} = \pi a\int_{-r}^{r} v(z)\mathrm{d}z \tag{7.3}$$

which simplifies to

$$\dot{V} = -\frac{\pi a^2}{2}\frac{\mathrm{d}r}{\mathrm{d}t} = \pi a\int_{-r}^{r} v(z)\mathrm{d}z = \frac{4}{3}\pi a k r. \tag{7.4}$$

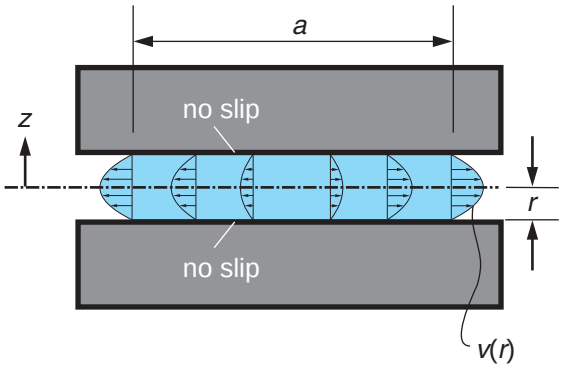

Figure 7.4: Modeling strain rates in a disk of fluid compressed with a rigid plate

The peak shear strain rate is located at the edge of the disk where $z = \pm r$:

$$\dot{\gamma}_{pk} = \dot{\gamma}(z=\pm r) = \left.\frac{\mathrm{d}v}{\mathrm{d}z}\right|_{z=\pm r} = \frac{\pm 2k}{r} = \frac{\mp 3a}{4r^2}\frac{\mathrm{d}r}{\mathrm{d}t} \tag{7.5}$$

For example, a 200 nm-thick polymer layer being imprinted with a feature of diameter 10 μm at a rate of 1 nm/s would experience a maximal strain rate, at the edges of the contact region, of approximately 0.75/s — well within the expected shear-thinning regime for PMMA in the temperature range considered here. Materials such as the Microresist mr-I series, with lower glass transition temperatures than PMMA, can easily be processed much further above their T_g values than can PMMA, and might therefore be less likely to exhibit shear-thinning in the course of processing.

Even if the *peak* strain-rate is in the shear-thinning range, though, the overall behavior of the feature may not in fact deviate significantly from that implied by a Newtonian model: the average strain rate in the material is substantially lower than the peak values at the edges of the disk. It would be possible with a

simple extension of this analysis to determine what *proportion* of the volume of resist beneath a stamp protrusion was in a shear-thinning regime.

As models are developed and tested experimentally in the following sections, this crude estimate of the extent of validity of a linear material model will be borne in mind.

7.4. Pattern dependencies in incompressible resist

In this section we generate and then non-dimensionalize simulation results for the imprinting of three types of simple, regular patterns into finite-thickness layers.

The analysis presented here is valid for any linear viscous, elastic, or viscoelastic material. As long as the material model is linear, we can use the simplifying approach that was demonstrated in Chapter 2. The imprinting of a linear viscoelastic layer with time-evolving compliance $J(t)$ and exposed to a stamp-average pressure $p_0(t)$ produces the same topography at time t_h as does the imprinting of a 'virtual', *purely elastic* layer having a dimensionless elastic modulus of $(1–\nu^2)$ and loaded instantaneously with the dimensionless, spatial-average pressure quantity $p_{g,0}$:

$$p_{g,0}(t_h) = (1-\nu^2)\int_0^{t_h} \frac{1}{D^2}\int_0^D\int_0^D p(x,y,t')\,\mathrm{d}x\mathrm{d}y\,\frac{\mathrm{d}J(t-t')}{\mathrm{d}t'}\,\mathrm{d}t' = (1-\nu^2)\int_0^{t_h} p_0(t')\frac{\mathrm{d}J(t-t')}{\mathrm{d}t'}\,\mathrm{d}t' \qquad (7.6)$$

.

This equivalence implies that the 'real' and 'virtual' imprinted layers and stamps have identical geometries. Henceforth in this analysis, imprinted topographies will be described in terms of $p_{g,0}$.

7.4.1. Assumptions

In these initial simulations, the layer material is assumed incompressible, which is realistic for a liquid resist or for one in a rubbery state.

The stamp and the substrate underlying the imprinted layer are assumed to be perfectly rigid. While this is not a strictly realistic assumption, we adopt it for convenience, knowing that stamp and substrate deflections will be introduced later when the full die-scale simulation procedure is constructed.

The simulated patterns are assumed to be periodic — and infinite in extent — in the two dimensions of the plane of the imprinted layer. As a result, the stamp is assumed to be able to translate as a rigid body, but not to rotate.

Finally, the point-load response used in this section assumes that no lateral tractions are applied to the layer — *i.e.* that there is no friction between stamp and layer.

7.4.2. Pressure–residual layer relationships without cavity filling

Firstly we consider the case in which the cavities of a stamp are tall enough that material does not reach the top of them even when the thickness of the compressed parts of the polymer layer approaches zero. We will call this the 'squeezing' mode of material deformation. The relationships between pressure and residual layer thickness are simulated using the approach illustrated in Figure 7.5. The layer thickness, r, in the stamp–substrate contact region is reduced, through a series of steps, towards a very small proportion of its initial value. In our implementation, r_k follows a geometric series with term-to-term ratio 0.9. At each step k, the point-load response for a layer of thickness r_k is computed, following the analytical form given by Nogi and Kato [188]. The factor k_f of (6.2) is kept equal to one from this point onwards. A biconjugate gradient algorithm is used to find the contact pressure distribution $p_{g,0,k}$ that, when

convolved with the current point-load response, causes the stamp to move down into the layer by a distance $r_k - r_{k-1}$. The total pressure distribution under which r is reduced from its starting value to r_k is given by the superposition of all pressure distributions $p_{g,0,1} \ldots p_{g,0,k}$.

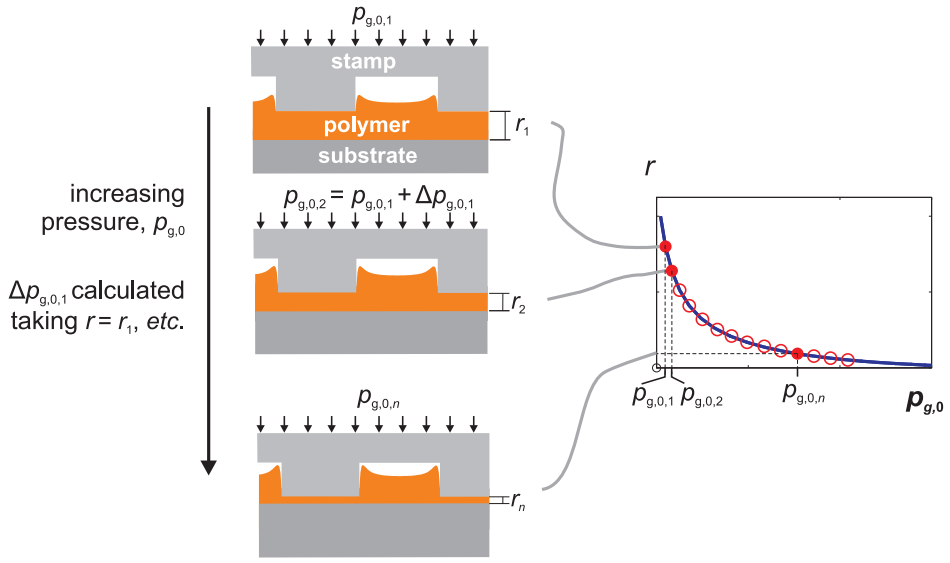

Figure 7.5: Residual layer thickness-stepping method for determining the relationship between applied pressure and residual thickness *r*.

This stepping method has been performed for the three types of pattern geometry illustrated in Figure 7.6: parallel lines, square holes etched into the stamp, and circular protrusions from the stamp. Table 7.1 relates four geometrical parameters describing these patterns: the areal density of protrusions from the stamp, ρ, the lateral pitch of features, s, the diameter of protrusions, a, and the space between protrusions, w.

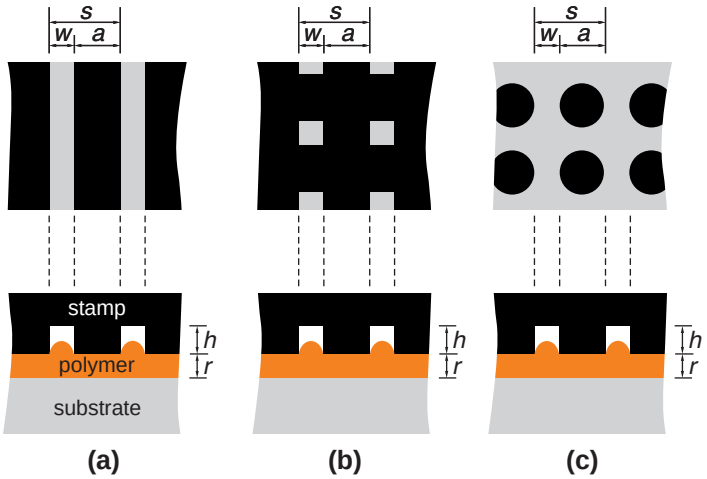

Figure 7.6: Nomenclature of finite-thickness layer embossed with a homogeneous array features of infinite lateral extent. Dimensions are labeled for (a) parallel lines, (b) square holes and (c) circular pads on the stamp.

Table 7.1: Relationship between (*w*/*s*), feature diameter *a* and areal feature protrusion density ρ for three example geometries.

	Lines	Square holes	Circular pads
a	$s-w$	$s-w$	$s-w$
ρ	$a/s = (s-w)/s$	$1-(w/s)^2$	$\pi a^2/4s^2$
w/s	$1-\rho$	$\sqrt{1-\rho}$	$1-\sqrt{\frac{4\rho}{\pi}}$

For each geometry type, simulations were performed for a range of areal densities of stamp protrusions. Simulation results were then non-dimensionalized and are plotted in Figure 7.7, Figure 7.8, and Figure 7.9. The dimensionless residual layer thickness r' is defined as r/a, and in these figures the dimensionless pressure–layer thickness gradient, $\mathrm{d}p_{g,0}/\rho\mathrm{d}r'$, is plotted against r'. The quantity $\mathrm{d}p_{g,0}/\rho\mathrm{d}r'$ gives an impression of how 'stiff' the overall pattern appears for a particular value of r' — in other words, it indicates what incremental increase in stamp-average pressure would be required to obtain a further incremental reduction of layer thickness.

When the instantaneous layer thickness is very small ($r' << 1$), simulations show that $\mathrm{d}p_{g,0}/\rho\mathrm{d}r'$ is proportional to the cube of the layer thickness: this relationship is fully in keeping with the Scott equations for squeezing flow of films of viscous, incompressible liquids. In contrast, when the instantaneous layer thickness is very large ($r' >> 1$), $\mathrm{d}p_{g,0}/\rho\mathrm{d}r'$ ceases to depend on layer thickness and the problem reduces to the bulk-embossing case explored in Chapter 2. For layer thicknesses comparable with imprinted feature diameters ($r' \sim 1$), there is a transition between the extreme 'thick'- and 'thin'-layer regimes.

For each feature type, the relationship between the layer thickness and the pressure–layer thickness gradient is found to be well approximated by the following relationship:

$$-\frac{\mathrm{d}p_{g,0}}{\rho\,\mathrm{d}r'} = F_1(r')^{-3} + F_2(r')^{-2} + F_3 . \tag{7.7}$$

$F_{1\text{–}3}$ are pattern shape- and density-dependent constants. F_1 governs the behavior for $r' << 1$, while F_3 describes the behavior for comparatively very thick layers where $r' >> 1$. The magnitude of F_2, meanwhile, determines the smoothness of the transition between the very-thick and very-thin layer regimes.

Where protrusions from the stamp are discrete (*i.e.* they do not touch), and pattern density is consequently determined only by the number of them within a given area, the value of F_1 — the effective pattern stiffness coefficient for $r' << 1$ — is independent of pattern density. This situation applies, for example, in the case of parallel lines and circular pads. For these two geometry types, the values of F_1 extracted from simulations and noted in Table 7.2 exactly match those predicted by the Scott equations [213, 215] after correction by a factor of four to allow for the no-friction assumption inherent in our simulations. The reasoning behind this factor-of-four correction is explained in the previous chapter.

In the case of square holes, however, patterns of different areal protrusion densities are geometrically quite different. The regions of the stamp lying diagonally between cavities (labeled R_1 in Figure 7.6) account for an increasing proportion of the protrusion area of the stamp as ρ increases, and since it is harder to squeeze material from the centers of these regions than from other parts of the pattern, F_1 is an increasing function of pattern density. Figure 7.10 illustrates the fitting of the function $F_1 = 0.0625 + 0.053\rho$ to simulation data for stamps with square holes. For very low values of ρ, the

function chosen for F_1 tends to the value of 0.0625 predicted by the Scott equation for parallel lines of width a. Simulated values of F_1 for very small and very large values of ρ, however, deviate somewhat from the functional relationship chosen. The deviations at large values of ρ could occur because the linear model chosen is not a true representation of reality. The deviations at very *small* values of ρ, meanwhile, are more likely to have occurred because the spatial discretization of the simulation region used was too coarse, or because the simulation was not allowed to converge sufficiently far for completely accurate answer to be given.

Considering the transitions between thick- and thin-layer regimes for the three pattern types investigated, a reasonable approximation to simulation results is obtained with F_2 set to the constant values given in Table 7.2.

F_3, meanwhile, is a direct function of the geometry of the stamp but not of the layer thickness: it is directly related to the dimensionless parameter B obtained in Chapter 2 for infinitely thick polymeric layers, as shown in Table 7.2. Quintic fits of parameters A and B as functions of cavity opening density w/s are also illustrated in Figure 7.11.

For pattern regions with very small values of w/s (and correspondingly large values of ρ), even tiny rms deviations of the overall fitted relationships from the true values of A and B could lead to substantial errors in simulation. Several manual corrections to the values of B are proposed for parallel lines and square holes at the particular pattern densities of 0.7 and 0.9: these corrections are given in Table 7.3. Such *ad hoc* corrections are undesirable, and future work should aim to provide a more faithful model fit.

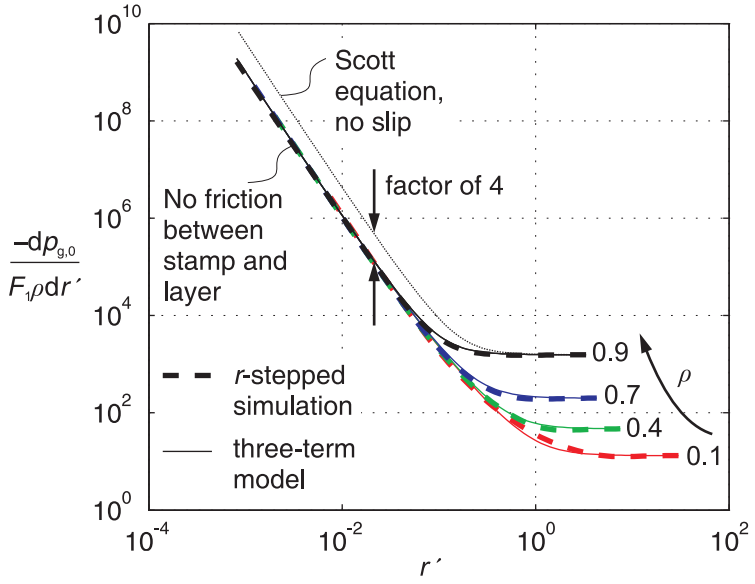

Figure 7.7: Relationship between $dp_{g,0}/\rho dr'$ and r' for embossing with a stamp having an infinitely large array of parallel lines and trenches.

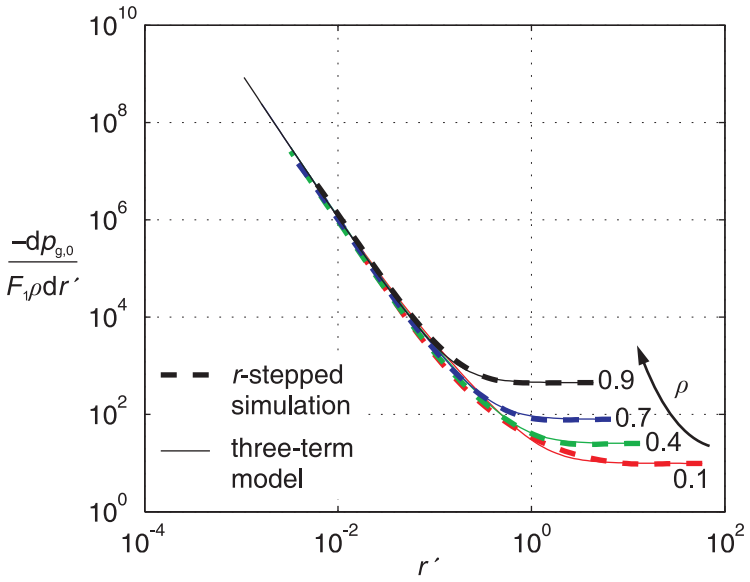

Figure 7.8: Relationship between $dp_{g,0}/\rho dr'$ and r' for embossing with a stamp having an infinitely large array of square holes.

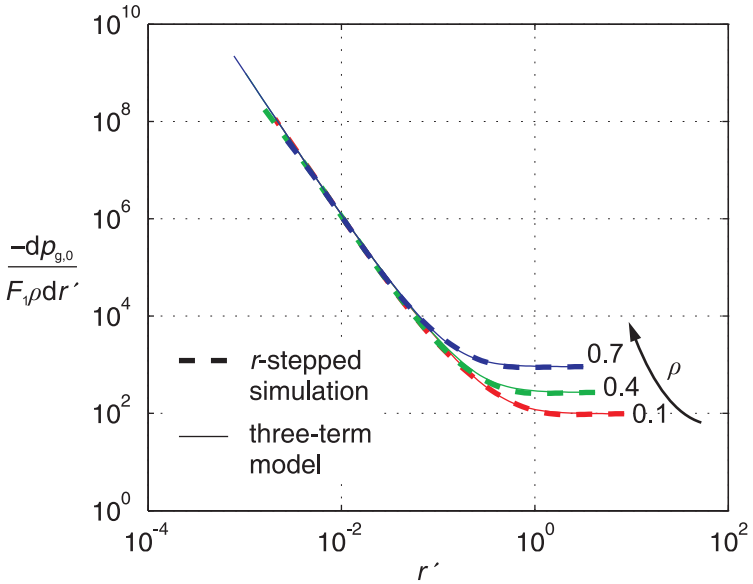

Figure 7.9: Relationship between $dp_{g,0}/\rho dr'$ and r' for embossing with a stamp having an infinitely large array of circular protrusions arranged on a square grid.

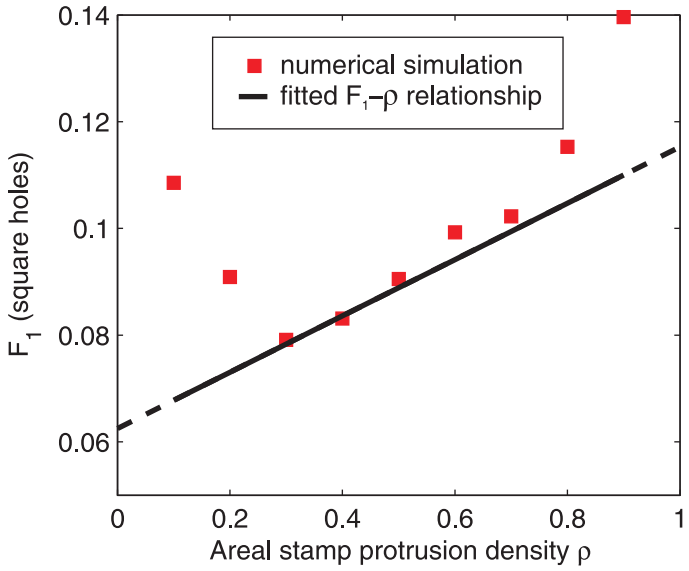

Figure 7.10: Linear fitting of a relationship between F_1 and ρ for a stamp with an infinitely large array of square holes. Symbols: F_1 values extracted from simulations; line: model fit to simulations.

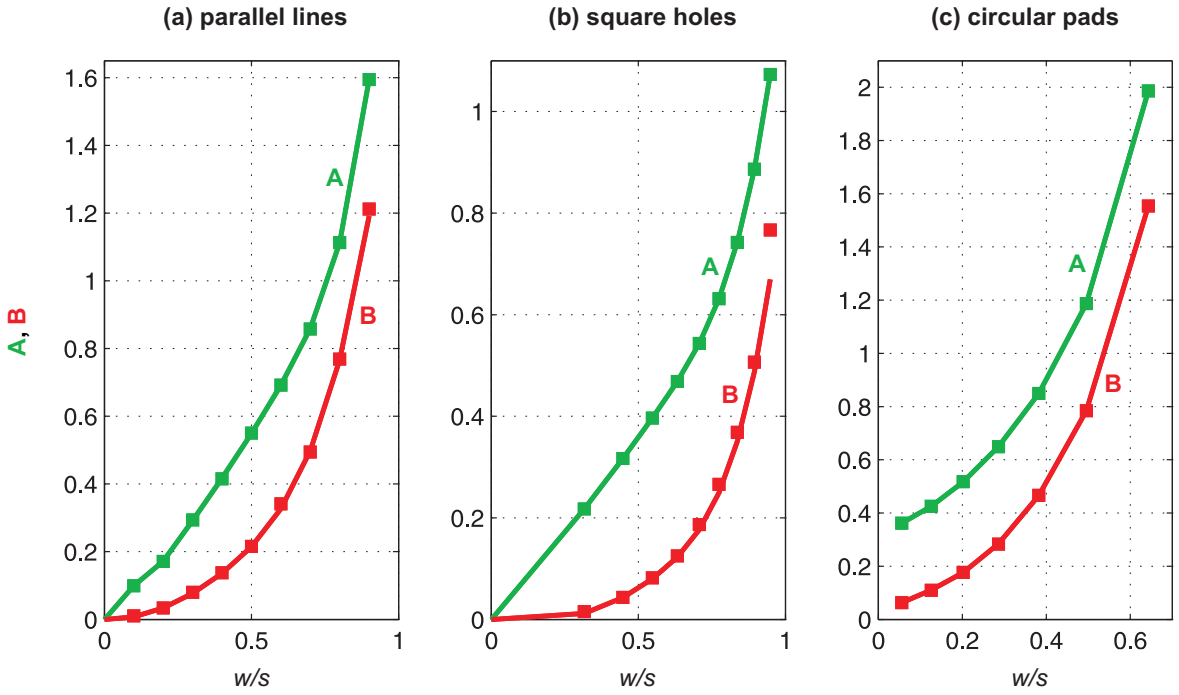

Figure 7.11: Fitting of a polynomial relationship between *A*, *B* and *w/s* for three elemental patterns: (a) parallel lines, (b) square holes, and (c) circular pads.

Table 7.2: Expressions for non-dimensional parameters in the abstracted representations of the imprinting of three example geometries. It is assumed here that no friction exists between stamp and polymer layer.

	Lines (coef's valid for $0.1 < \rho < 0.9$)		Square holes (coef's valid for $0.1 < \rho < 0.9$)		Circular pads (coef's valid for $0.1 < \rho < 0.7$)	
	q	Coef. of $(w/s)^q$	q	Coef. of $(w/s)^q$	q	Coef. of $(w/s)^q$
A	5	12.0	5	6.19	5	20.9
	4	–18.5	4	–11.3	4	–21.8
	3	8.38	3	7.59	3	10.1
	2	0.217	2	–2.07	2	–0.113
	1	0.362	1	0.875	1	0.731
	0	0.0536	0	0.0011	0	0.320
	q	Coef. of $(w/s)^q$	q	Coef. of $(w/s)^q$	q	Coef. of $(w/s)^q$
B	5	6.89	5	64.7	5	35.4
	4	–11.0	4	–190	4	–49.3
	3	7.16	3	220	3	29.0
	2	–1.37	2	–123.8	2	–5.64
	1	0.310	1	33.9	1	1.10
	0	–0.0135	0	–3.58	0	0.0145
F_1	1/16		$0.0625 + 0.053\rho$		3/128	
F_2	0.8		1.3		0.5	
F_3	$\frac{1}{B}$		$\frac{1}{B\left(1+\frac{w}{s}\right)}$		$\frac{4}{\pi B\left(1-\frac{w}{s}\right)}$	

Table 7.3: Some corrections to the values of *B* generated using the fitted polynomials of Table 7.2: *B* as generated by the polynomial should be multiplied by the factors in this table to yield a more accurate value of *B*. Clearly, the use of these correction factors is not convenient and it would be desirable to achieve superior fitting of functions for *A* and *B* to the simulation results.

ρ	Lines	Square holes
0.7	0.97	1.15
0.9	0.853	1.13

7.4.3. Stamp–layer friction

In the case of no-slip between the stamp and the polymer layer, the values of F_1 would be four times higher than those modeled assuming no friction, for the reasons discussed in the previous chapter. The expected relationship between $\mathrm{d}p_{g,0}/\rho\mathrm{d}r'$ and r' in the no-slip case is indicated by a dotted line in Figure 7.7: while F_1 would be four times higher than in the no-friction case, we do not expect F_3 to be substantially influenced by the amount of stamp–layer friction.

For thin layers, then, it is clearly very important to know the amount of friction between the layer and the stamp. For intermediate friction cases, F_1 would lie between the two extremes plotted and its value could be obtained experimentally for particular layer/stamp material combinations.

7.4.4. Functional relationship between average applied pressure–compliance integral and residual layer thickness

It would be helpful to have a closed-form relationship between the total applied stamp-average pressure–compliance and the instantaneous residual layer thickness. Integrating (7.7) for r' between its initial value r'_0 and its final value r'_f, we obtain:

$$-\int_0^{p_{g,0}} \mathrm{d}\,p_{g,0} = \rho \int_{r'_0}^{r'_f} F_1 (r')^{-3} + F_2 (r')^{-2} + F_3 \,\mathrm{d}r'\,; \tag{7.8}$$

$$-\frac{p_{g,0}}{\rho} = \left[-\frac{F_1}{2}(r')^{-2} - F_2 (r')^{-1} + F_3 r' \right]_{r'_0}^{r'_f}. \tag{7.9}$$

Multiplying through by $r'_f{}^2$, we have a cubic equation in r'_f whose real root gives the residual layer thickness resulting from the application of the spatial-average pressure–compliance $p_{g,0}$:

$$\frac{F_1}{2} + F_2 (r'_f)^1 + \left[-\frac{p_{g,0}}{\rho} - \frac{F_1}{2}(r'_0)^{-2} - F_2 (r'_0)^{-1} + F_3 r'_0 \right](r'_f)^2 - F_3 (r'_f)^3 = 0. \tag{7.10}$$

The real root is given by the following expression:

$$\left.\begin{aligned} r'_f &= S + T + \frac{\beta}{3F_3} \\ &\text{where} \\ S = \sqrt[3]{R + \sqrt{Q^3 + R^2}} &\qquad T = \sqrt[3]{R - \sqrt{Q^3 + R^2}} \\ &\text{and} \\ Q = \frac{-3F_3F_2 - \beta^2}{9F_3{}^2}; \quad R = \frac{-9F_2F_3\beta - \frac{27}{2}F_3{}^2F_1 - 2\beta^3}{-54F_3{}^3}; &\quad \beta = -\frac{p_{g,0}}{\rho} - \frac{F_1}{2}(r'_0)^{-2} - F_2(r'_0)^{-1} + F_3 r'_0. \end{aligned}\right\} \tag{7.11}$$

Figure 7.12 illustrates the correspondence of this cubic-solution approach with the numerical simulations already performed. Normalized residual layer thickness r' is plotted against the cumulative pressure–compliance integral $p_{g,0}$ applied to the stamp. Results are plotted for four pattern-density values and for three values of initial layer thickness, r'_0. In each case, the position of the data on the pressure–compliance axis is shifted such that $p_{g,0} = 0$ for $r' = 0.02$. Our assumption of a linear material model means that the *incremental* pressure distribution needed to bring about an *incremental* reduction of residual layer thickness is dependent solely on the instantaneous layer thickness and the pattern, and not

on the starting layer thickness r'_0 or on the history of deformation. Figure 7.12 shows that the cubic-solution approach of (7.11) does indeed faithfully describe the relationship between $p_{g,0}$ and r'.

The portion of Figure 7.12b that corresponds to the thin-film regime is analogous to the film-thickness–time graphs that Schulz *et al*. show for their simulations of the imprinting of Newtonian resist [216]. In the case of a Newtonian resist at constant temperature and loaded with a constant stamp-average pressure, the pressure–compliance integral $p_{g,0}$ is simply proportional to the elapsed loading time. The modeling method presented here goes beyond the simple Newtonian case, though: it is applicable to any linear viscoelastic material layer, and represents not just the thin-film case but the thick-to-thin transition as well.

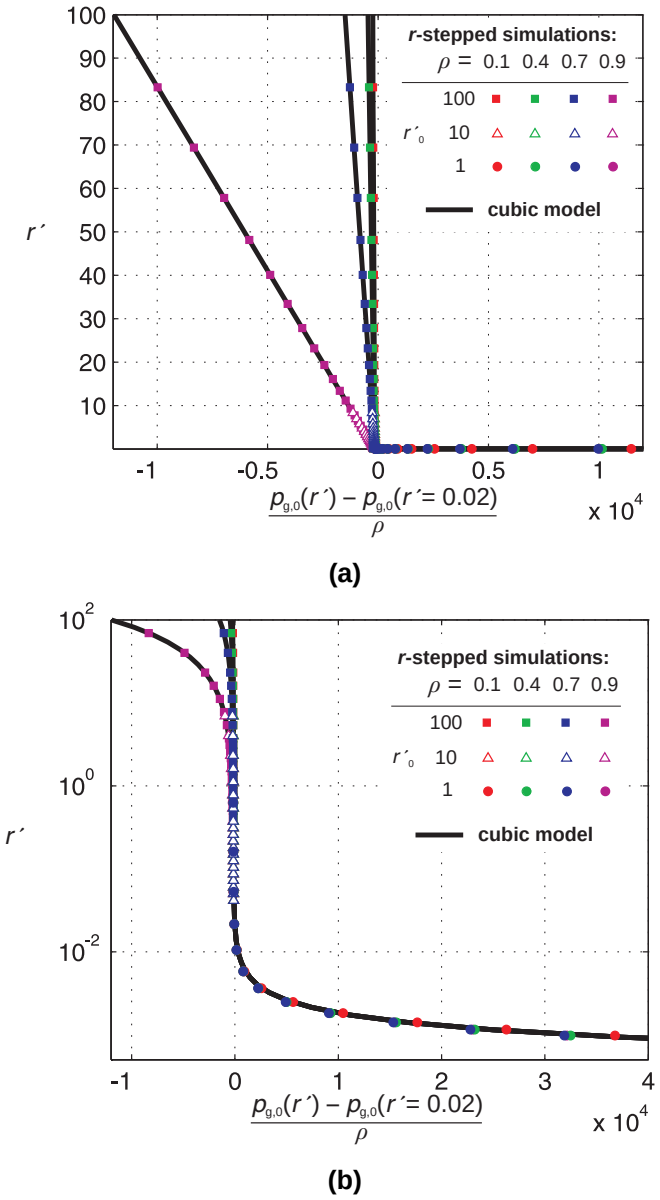

Figure 7.12: Relationship between $p_{g,0}/\rho$ and r' for embossing with a stamp having an infinitely large array of parallel lines and trenches. The relationships for three pattern densities and in each case for three initial layer thicknesses are superimposed; for each simulation the relationships are shifted along the $p_{g,0}/\rho$ axis to give $p_{g,0}/\rho = 0$ at $r' = 0.02$. The r'-axis is plotted both (a) linearly and (b) logarithmically.

7.4.5. Modeling cavity filling during nanoimprinting

Next we consider cases in which the cavities of the stamp are filled with polymer before the residual layer thickness is reduced to zero. At first it might seem logical to make stamp cavities tall enough that material *never* fills them, so that residual layers can be made arbitrarily thin, but there are several reasons why this is unlikely to be sensible. Firstly, stamp fabrication technology might not be able to produce sufficiently tall cavities to achieve that objective in stamp regions with a very small areal density of cavities. Secondly, in real imprint processes, partially filled cavities tend not to have the smooth resist topographies that are predicted by the simulations presented so far in this chapter. There is an element of chaos in the way resist occupies the cavity, with capillary 'bridges' often forming between the resist and the top of the stamp cavity [216]. These instabilities can lead certain portions of the resist to become very thin where they are supposed to remain thick, resulting in defects during etching [98]. Consequently, it is important to be able to model cavity filling and to develop an ability to design stamps that can be *completely* filled with material without excessive residual layer variation.

Since we are currently making an assumption that the imprinted layer is incompressible, there is implied for any stamp geometry and starting layer thickness a particular residual layer thickness, r'_f, for which every cavity on the stamp is filled and further reduction of the residual layer is impossible (Figure 7.13). On a $p_{g,0}$–r' graph this could be visualized as a horizontal line at $r' = r'_f$, 'clipping' the $p_{g,0}$–r' relationship that was derived above in the absence of cavity filling.

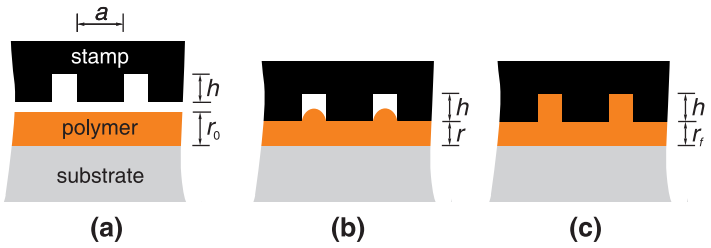

Figure 7.13: Nomenclature for minimum local layer thickness *r* (a) initially, before imprinting; (b) during imprinting; (c) upon filling: *r′* = *r*/*a*.

Such a clipping approach, however, would not convey any information about the sharpness or smoothness of the true transition from the 'no-filling' $p_{g,0}$–r' curve to the asymptote $r' = r'_f$. Knowing the shape of this transition is important in order to be able to produce realistic simulations.

The shape of the transition depends, in fact, on the initial layer thickness r'_0, with thicker initial layers giving rise to more gradual transitions from the 'squeezing' mode to the 'filling' mode. Figure 7.14 illustrates the results of a set of r'-stepped simulations that illustrate this trend. The stamp simulated is an array of parallel lines with $\rho = 0.5$. $p_{g,0}$–r' relationships were simulated for three values of initial layer thickness: $r'_0 = \{1, 10\ 100\}$. For each simulation, the cavity height h was recalculated so that cavities would be completely filled with material for $r'_f = 0.5$. During each simulation, r' was gradually reduced in a series of steps and an incremental pressure distribution $\Delta p_g[m, n]$ was calculated that was consistent with each step down in r'. For each step, the incremental change in topography of the layer was computed, and where material came newly into contact with the tops of the stamp cavities as a result, those regions were added to the contact region, C. Because the absolute layer thickness *inside* filled regions of the cavities is $r'a + h$ and that outside the cavities is only $r'a$, the convolution expression that needs to be solved to find the incremental pressure distribution is split into two parts. The solution itself is performed in terms of real incremental pressures, $\Delta p[m, n]$, and displacements, Δr, consistent with chosen 'dummy' values of layer stiffness and of feature diameter, a:

$$\left(\Delta p[m,n]k_{bottom}[m,n]\right)*g_{bottom}[m,n]+\left(\Delta p[m,n]k_{top}[m,n]\right)*g_{top}[m,n]=-\Delta r \qquad \forall m,n\in C \tag{7.12}$$

In this expression, g_{bottom}[m, n] is the point-load response computed for a layer thickness of r, and g_{top}[m, n] is computed for a layer thickness of $r + h$. The function k_{top}[m, n] is set to 1 inside cavity regions and zero outside, and k_{bottom}[m, n] = 1 – k_{top}[m, n]. $\Delta p[m, n]$ is zero outside C.

In Figure 7.14 the black dashed line shows the simulated relationship between $p_{g,0}$ and r' in the absence of cavity filling, while the other, colored, lines show simulated relationships *including* cavity filling, for the three different values of r_0' explored. In all three of these cases, the simulated relationships asymptotically approach $r' = r_f' = 0.5$, as expected. The thicker the layer, the larger the range of $p_{g,0}$ over which the transition from 'squeezing' to 'filling' behavior occurs. This trend can be understood by considering that as r'_0 increases, a greater proportion of the work done on the layer is associated with the deformation of material *well away* from the polymer–substrate interface; in other words, the larger r'_0, the less impact the squeezing flow of material near the interface has on the overall $p_{g,0}$–r' relationship. For extremely large r'_0, of course, we approach the thick-layer case and the $p_{g,0}$–r' relationship is as explored in Chapter 2.

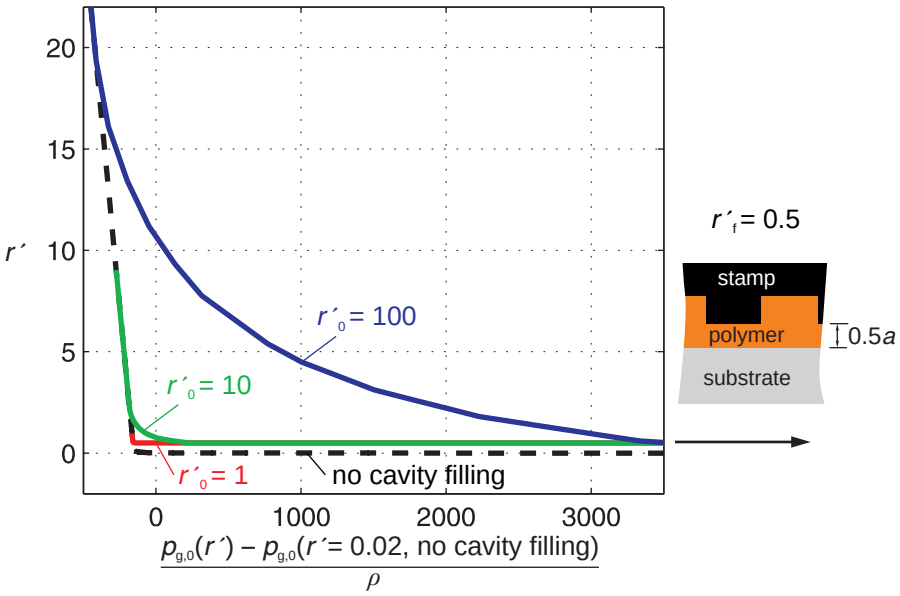

Figure 7.14: Relationship between dimensionless residual layer thickness, *r′*, and dimensionless applied pressure for the imprinting of an array of parallel lines of infinite extent, with ρ = 0.5. Simulations were performed (i) for the case in which stamp cavities are so tall that material never touches the tops of the cavities (black dashed line) and (ii) for three cases in which the cavities do begin to fill. These three cases are differentiated by the ratio of initial layer thickness to feature width. In each case the cavity height is chosen to be consistent with complete cavity filling occurring when *r* = 0.5*a*. As the initial layer thickness increases, reaching a given residual layer thickness requires a larger pressure.

To build an efficient simulation method, we need a faithful functional representation of the $p_{g,0}$–r' relationship that is valid for each type of regular pattern that might be encountered as well as for any value of r'_0. One promising approach is to use a thick-layer model to approximate the part of the $p_{g,0}$–r' relationship dominated by cavity filling, and to model the actual value of r' for a given $p_{g,0}$ using the *maximum* of the values predicted by that thick-layer relationship and by a purely squeezing-governed relationship computed in the absence of cavity filling. This approach is illustrated schematically in Figure 7.15.

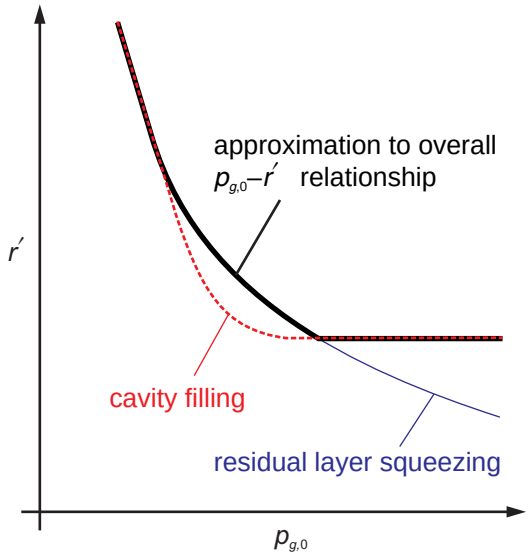

Figure 7.15: Proposed method for approximating the $p_{g,0}$–r' relationship where both residual layer squeezing and cavity filling are relevant.

To examine the validity of this approach, two sets of simulations were performed for a stamp patterned with an array of parallel lines of infinite extent. Half of the simulations assumed a finite-thickness layer (Figure 7.16a) whose residual thickness r' was reduced from r'_0 to r'_f in a series of steps following a geometric series, as described above. In the remaining simulations, the polymer was assumed to be an elastic half-space (Figure 7.16b) while the series of stamp displacements followed was specified to be exactly the same as in the finite-thickness layer simulations.

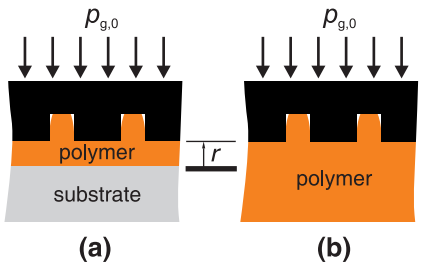

Figure 7.16: Schematic representation of the two simulation cases represented in Figure 7.15. In simulations following model (a), r is stepped in a geometric series from r_0 to r_f, and $p_{g,0}$ is computed at each step using a model for a finite-thickness polymer layer on a hard substrate. In (b), the same series of r values is used, and values for $p_{g,0}$ are computed at each step, but the polymer model is for a notional half-space.

This comparison — of the finite-thickness and infinite-thickness pressure–displacement relationships — was performed for stamp patterns having ρ values of 0.1, 0.4, 0.7 and 0.9, and for values of r'_0 of 1, 10 and 100. The results are plotted in Figure 7.17, together with $p_{g,0}$–r' relationships simulated for very tall cavities and therefore without any cavity filling. For $r'_0 = 100$, the results assuming a finite-thickness layer and an infinite-thickness layer are indistinguishable: the presence of the layer–substrate interface has no noticeable influence on the pressure–displacement relationship of the stamp. In the case of $r'_0 = 10$, the two relationships are indistinguishable except for small differences in the case of $\rho = 0.1$. For $r'_0 = 1$, meanwhile, clear differences are observed between the two simulations for $\rho = 0.4$ and below. In these cases, the value of r' given by the thin-layer simulation for lower values of $p_{g,0}$ exceeds that predicted by the infinite-thickness layer simulation, and instead follows quite closely the 'squeezing' relationship derived for no cavity filling, which is plotted in Figure 7.17 using black dashed lines. A notional division of the r'_0–r'_f space into squeeze-dominated and bulk deformation-dominated regimes is illustrated, for the imprinting of arrays of parallel lines, in Figure 7.18. Meanwhile, a comparison of finite- and infinite-thickness-layer simulations is illustrated in Figure 7.19 for stamps carrying arrays of square holes, rather than the parallel lines of Figure 7.17.

What all this means is that a reasonable approximation to the $p_{g,0}$–r' relationship is usually found by taking the maximum of the values of r' predicted by (*i*) a thin-layer simulation assuming tall cavities that never fill, and (*ii*) an infinite-thickness-layer simulation that does allow for cavity filling and assumes the same polymer material properties and stamp geometry as (*i*). This observation is useful, because if we can find a functional pressure–displacement relationship for a stamp being imprinted into an infinite-thickness layer, we will then have enough, combined with the squeezing relationship already derived, for a reasonable model of the imprinting process.

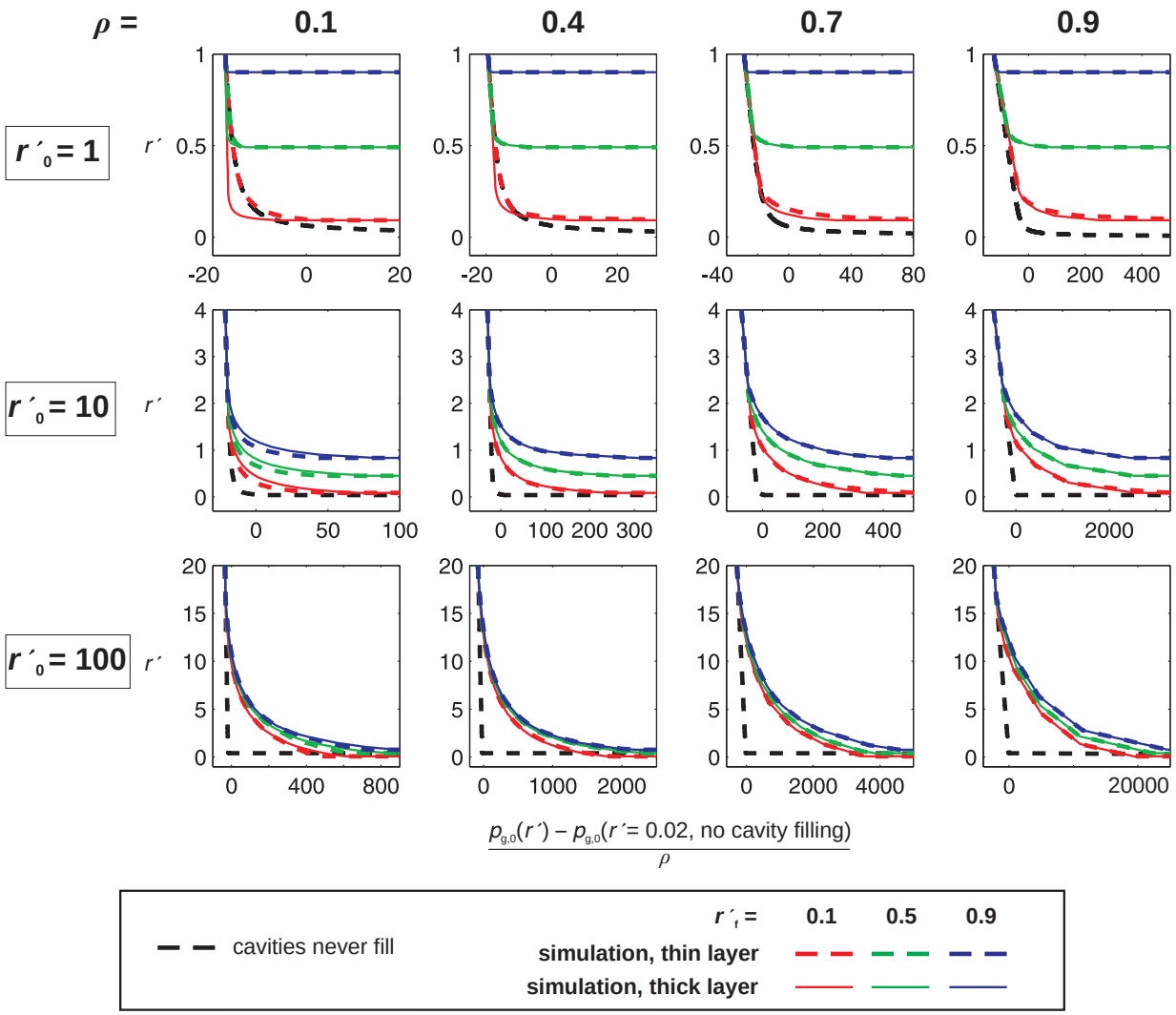

Figure 7.17: Simulated residual layer–pressure relationships for three values of initial layer thickness and four pattern densities. The pattern simulated is an array of parallel lines of infinite extent. Heavy dashed lines correspond to finite layer-thickness simulations; thin solid lines represent simulation case (b) in Figure 7.16, *i.e.* a very thick polymer layer. The thin-layer case in which cavities are so tall that they never begin to fill is shown as a black dashed line.

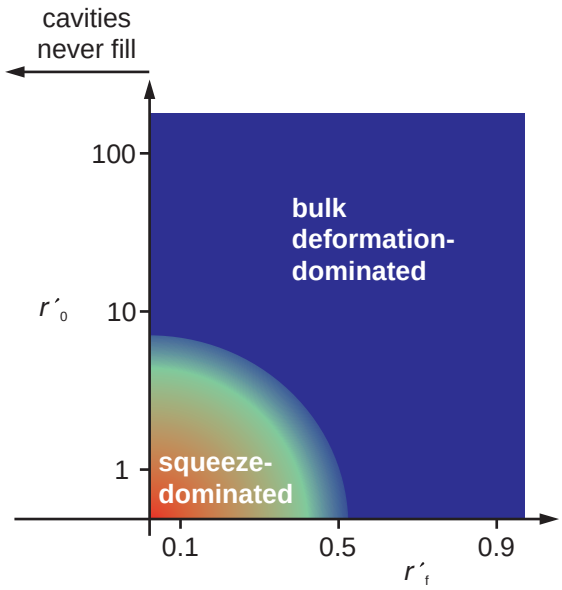

Figure 7.18: Map of squeeze- and bulk deformation-dominated pressure–cavity-filling relationships for various layer initial thicknesses and filling thicknesses.

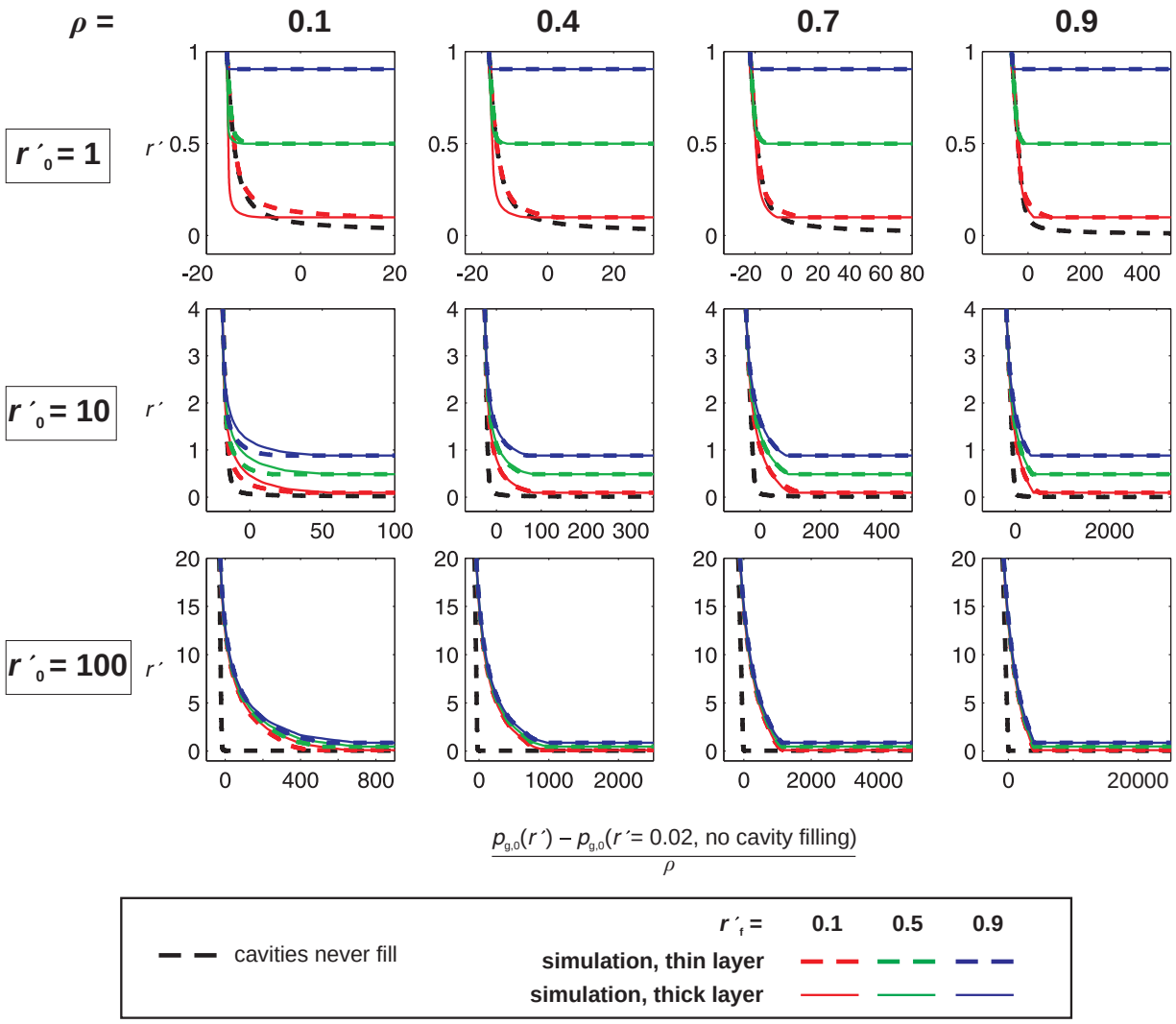

Figure 7.19: Simulated residual layer–pressure relationships for three values of initial layer thickness and four pattern densities. The pattern simulated is an array of square holes of infinite extent. Heavy dashed lines correspond to finite layer-thickness simulations; thin solid lines represent simulation case (b) in Figure 7.16, *i.e.* a very thick polymer layer. The thin-layer case in which cavities are so tall that they never begin to fill is shown as a black dashed line.

We have already proposed, in Chapter 4, an extremely simple way of modeling the pressure–displacement relationship for a patterned stamp being embossed into an elastic half-space. In that model, the pressure–displacement curve was split into three linear regions: one corresponding to displacement before any material touches the tops of the cavities, a second representing progressive filling of the cavities, and a third in which the cavities were modeled as being essentially filled and no further stamp displacement was possible.

Now, however, we propose a potentially more accurate model that does away with that previous piecewise-linear approximation. The pressure–displacement relation is now split into two sections: a linear pre-filling section and an exponential region, as illustrated in Figure 7.20.

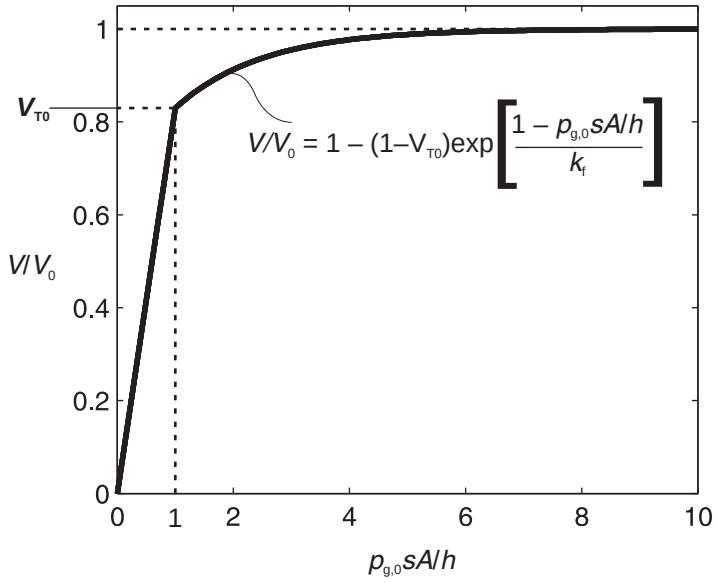

Figure 7.20: Modified functional form for the relationship between dimensionless applied pressure–compliance integral and proportion of cavity filled, for thick layers.

The proportion of cavity volume filled, V/V_0, is always proportional to rigid-body stamp displacement downwards into the polymer. Since we assume the polymer to be incompressible, V_{T0}, the value of V/V_0 at which material first touches the tops of the cavities, is given by:

$$V_{T0} = \frac{B}{A(1-\rho)} \tag{7.13}$$

and V/V_0 is then given as a function of $p_{g,0}$ by:

$$\frac{V}{V_0} = \begin{cases} \dfrac{p_{g,0}sA/h}{V_{T0}} & p_{g,0}sA/h < 1 \\ 1-(1-V_{T0})\exp\left[\dfrac{1-p_{g,0}sA/h}{k_f}\right] & p_{g,0}sA/h > 1 \end{cases} . \tag{7.14}$$

For parallel lines, we find that the constant k_f is well modeled by the relationship:

$$k_f = 2(0.8 - 0.5\rho). \tag{7.15}$$

For square holes, a slightly different relationship is found to give satisfactory fitting:

$$k_f = 2(0.8 - 0.65\rho). \tag{7.16}$$

This new functional relationship is plotted in Figure 7.21 for arrays of parallel lines of three pattern densities, and in Figure 7.22 for arrays of square holes.

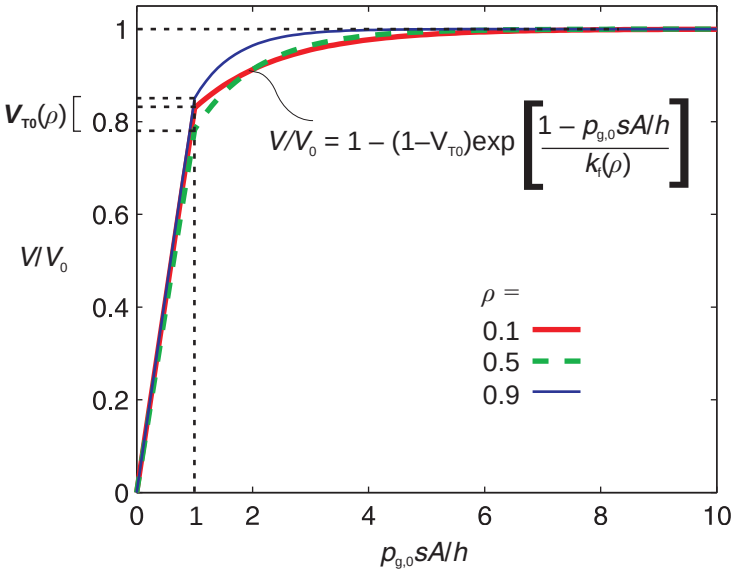

Figure 7.21: New functional relationship between $p_{g,0}sA/h$ and V/V_0 for arrays of parallel lines of three example pattern densities.

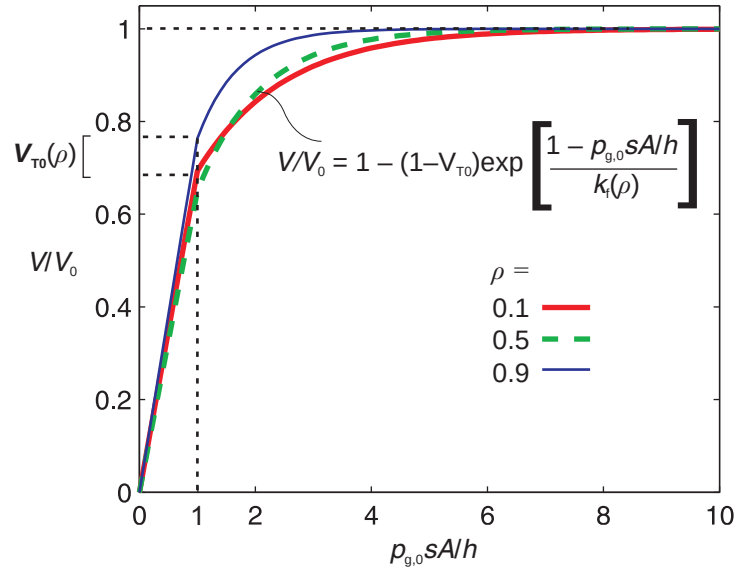

Figure 7.22: New functional relationship between $p_{g,0}sA/h$ and V/V_0 for arrays of square holes of three example pattern densities.

These relationships between $p_{g,0}sA/h$ and V/V_0 can be transferred directly to the $p_{g,0}$–r' graphs through a simple flipping and scaling. Figure 7.23 and Figure 7.24 plot the r'-stepped simulation results for finite-thickness layers together with the $p_{g,0}$–r' relationships for infinite-thickness layers that are given by the exponential function developed above. The predictions of the exponential-filling function follow reasonably closely the simulated results in those regions where bulk deformation dominates. The

agreement is least good for $\rho = 0.1$ and $r'_0 = 10$, where the developed function substantially overestimates the value of r' for a given $p_{g,0}$. Other than in this case of very low pattern density, though, it does appear that a good approximation to the $p_{g,0}$–r' relationship of imprinted finite-thickness layers can be obtained by taking the *maximum* of the values of r' given by the squeezing expression of (7.11) and a flipped and scaled version of the bulk filling model of (7.14).

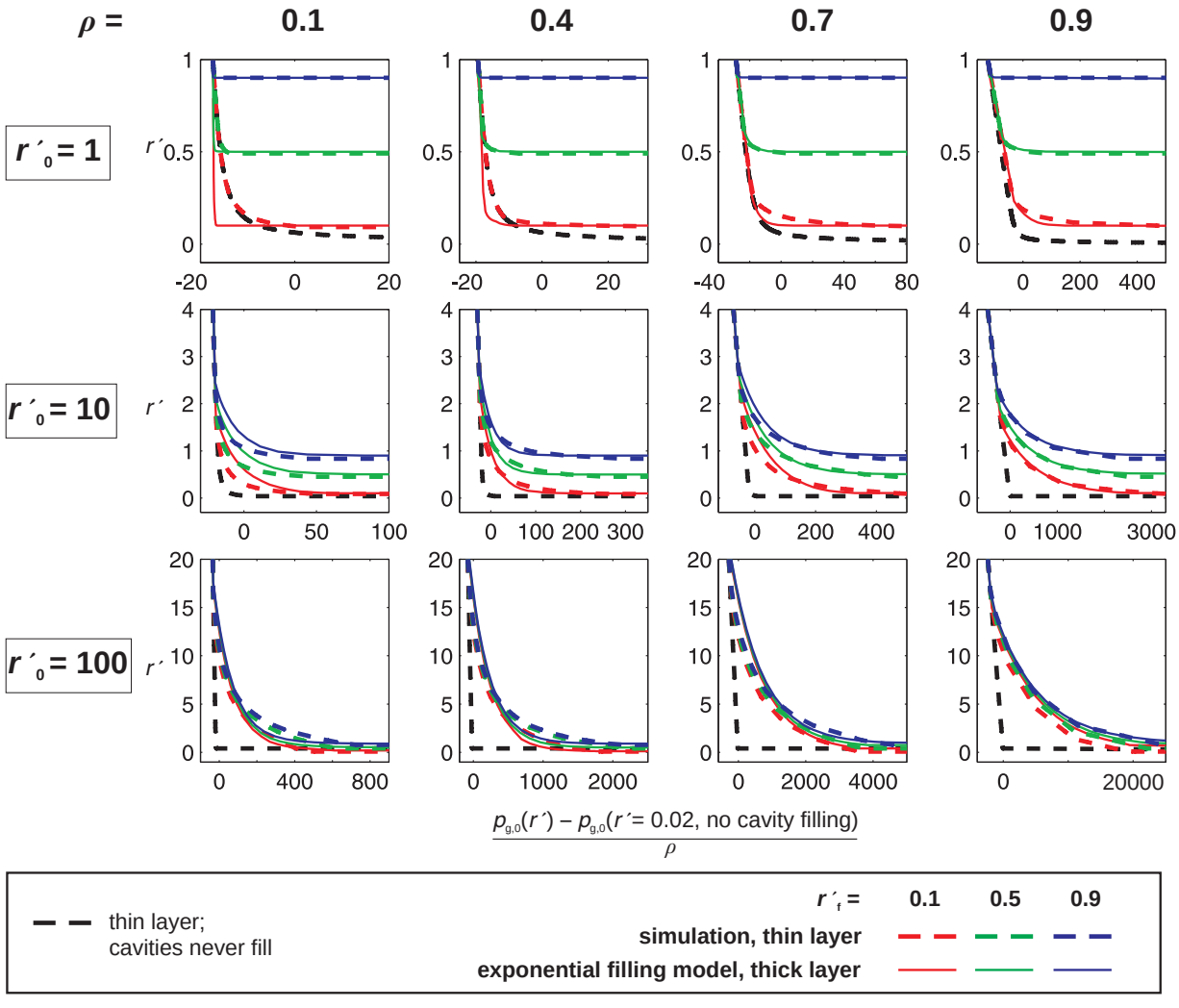

Figure 7.23: Demonstration of the ability of the exponential pressure–filling model derived for thick polymeric layers to capture the salient features of cavity-filling behavior for imprinted arrays of parallel lines.

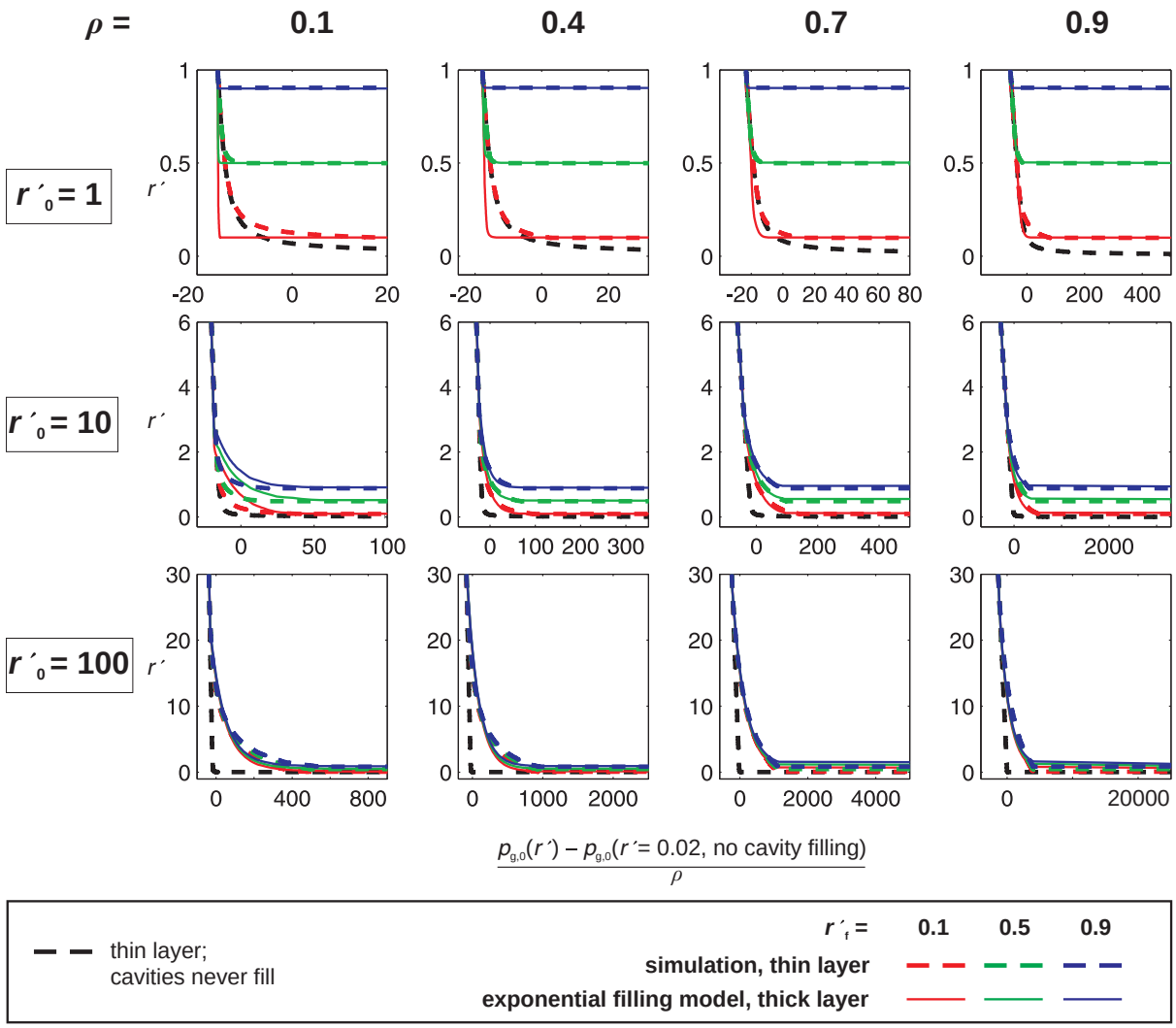

Figure 7.24: Demonstration of the ability of the exponential pressure–filling model derived for thick polymeric layers to capture the salient features of cavity-filling behavior for imprinted arrays of square holes.

7.4.6. Incorporating non-continuum effects

The modeling so far presented has assumed a continuum model of the imprinted resist. In reality, residual layers are likely to be comparable in thickness with the coiled diameter of polymer chains in melted resist. Chukalina *et al.* estimate these coiled polymer diameters to be ~100 nm for 950 kg/mol PMMA and ~10 nm for 25 kg/mol PMMA [231, 232]. They further suggest that molecular diameters will impose a lower limit on the residual layer achievable in thermal NIL. In our simulation method, a lower limit to the layer thickness could be represented by 'clipping' the r–p_g curve at an appropriate limiting value of r.

7.4.7. Linking to the die-scale

The relationships obtained above assume no stamp or substrate deflection. In reality, these deflections can be of crucial importance and might, in a more refined approach, need to be factored directly into the

derivation of the $p_{g,0}$–r' relationships. In the next section, however, we choose to represent stamp and substrate deflections at a higher level of the modeling hierarchy, where deflections are not necessarily described at the feature-scale but rather at the die-scale with a spatial resolution of d as defined in Figure 7.1.

7.5. Modeling stamp and substrate deflections

In the imprinting system that we are modeling, the polymer layer to be imprinted sits on a substrate which is relatively hard and perfectly elastic, and which may be regarded as a half-space consisting of the wafer on to which the resist has been spun and the underlying platen (made, for example, of steel). Meanwhile, a patterned elastic stamp of *finite* thickness is pressed hydrostatically into the resist. The use of a hydrostatic pressure to press the stamp against the imprinted layer (the so-called 'air cushion' press design [233, 234]) is intended to counteract wafer-scale nonuniformity by allowing the stamp to bend and conform to long-range non-flatness of the stamp or substrate.

To model the deflections of stamp and substrate within our framework, we require expressions for the responses of their surfaces to unit contact pressure applied uniformly across one $d \times d$ region.

In the following analysis, we neglect any compression of individual feature protrusions from the stamp: since their heights are a tiny fraction of the stamp thickness, and they are in almost all cases much harder than the resist itself, individual stamp feature compression can usually be safely neglected.

7.5.1. Substrate deflections

The deflections of the substrate may be modeled with the same expression that was used for the embossing of thick polymeric layers in Chapter 2:

$$\left.\begin{aligned} g_{substrate}[m,n] &= \frac{1-\nu_{substrate}^{\,2}}{\pi E_{substrate}}\left[f(x_2,y_2) - f(x_1,y_2) - f(x_2,y_1) + f(x_1,y_1)\right] \\ \text{where} \quad f(x,y) &= y\ln\left(x+\sqrt{x^2+y^2}\right) + x\ln\left(y+\sqrt{x^2+y^2}\right) \\ \text{and} \quad & x_1 = md - d/2;\ \ x_2 = md + d/2;\ \ y_1 = nd - d/2;\ \ y_2 = nd + d/2. \end{aligned}\right\} \tag{7.17}$$

Appropriate values for $E_{substrate}$ and $\nu_{substrate}$ would be those of silicon: ~120 GPa and 0.27 respectively.

7.5.2. Stamp deflections

The deflections of the stamp, meanwhile, may be regarded as having two components: an 'indentation' component, and a 'bending' component. The indentation component will dominate in cases where the characteristic spatial period of the contact pressure distribution is smaller than the thickness of the stamp. A good approximation for the kernel function describing the indentation component, $g_{stamp,indentation}[m, n]$, has the same form as that given in (7.17) for substrate indentations. The values of E and ν would be those of the stamp material; since stamps are often made from silicon, $g_{stamp,indentation}[m, n]$ and $g_{substrate}[m, n]$ will frequently be identical in magnitude.

The stamp's bending mode, in contrast, would be expected to dominate deflections where the characteristic spatial period of the contact pressure distribution is larger than approximately the stamp thickness. While most patterns imprinted using NIL have lateral feature separations that are far smaller than the stamp thickness, there may be pattern *density* variations that occur over distances greater than a stamp thickness, so we do wish to allow for the possibility of stamp bending.

We derive the stamp bending kernel by exploiting the assumption of spatial periodicity that is implicit in our simulation approach. The application of unit stamp–substrate contact pressure across a given $d \times d$ region of the stamp is balanced by a hydrostatic pressure of d^2/D^2 applied to the backside of the stamp, assuming that the spatial period of the stamp is D in each direction. Because of the assumption of spatial periodicity, the application of unit pressure in one $d \times d$ region of the simulated pattern is equivalent to the application of unit pressure at an infinite array of $d \times d$ regions, spaced D apart in both directions across an infinitely large stamp. Looking at one particular $D \times D$ period of this imagined infinite stamp, the stamp's deformed shape is identical to that of an edge-clamped square plate of size $D \times D$, experiencing uniform pressure of d^2/D^2 on one side and unit pressure applied on the other side to a $d \times d$ region at its center. The deflections of this equivalent clamped plate can be found using the standard analytical results of Timoshenko [235] and Reddy [236]. We superimpose the following two plate topographies: (*i*) $g_{\mathrm{U}}(x, y)$, that resulting from the hydrostatic applied pressure of d^2/D^2, and (*ii*) $g_{\mathrm{P}}(x, y)$, that resulting from the localized load at the center of the plate:

$$g_{stamp,bending}(x,y) = g_{\mathrm{U}}(x,y) - g_{\mathrm{P}}(x,y) \tag{7.18}$$

The localized load is modeled as a point load of magnitude d^2 to enable the ready use of standard formulae.

Following the methods used by Timoshenko and Reddy, $g_{\mathrm{U}}(x, y)$ and $g_{\mathrm{P}}(x, y)$ are each given by the superposition of two sets of deflections: the deflections $g_{\{\mathrm{U|P}\},\mathrm{s}}(x, y)$ of a simply supported plate exposed to the loads just described, and the deflections $g_{\{\mathrm{U|P}\},\mathrm{m}}(x, y)$ in response to edge clamping moments that satisfy the condition of no edge rotations of the plate. The function $g_{\{\mathrm{U|P}\},\mathrm{m}}(x, y)$ describes the deflections resulting from clamping moments applied to only *two* opposite edges of the plate's four edges, whereas in fact clamping moments are experienced at all four edges so that the overall deflections $g_{\{\mathrm{U|P}\}}(x, y)$ include both $g_{\{\mathrm{U|P}\},\mathrm{m}}(x, y)$ and its transpose, $g_{\{\mathrm{U|P}\},\mathrm{m}}(y, x)$.

$$\left.\begin{aligned} g_{\mathrm{U}}(x,y) &= g_{\mathrm{U,s}}(x,y) + g_{\mathrm{U,m}}(x,y) + g_{\mathrm{U,m}}(y,x) \\ g_{\mathrm{P}}(x,y) &= g_{\mathrm{P,s}}(x,y) + g_{\mathrm{P,m}}(x,y) + g_{\mathrm{P,m}}(y,x) \end{aligned}\right\} \tag{7.19}$$

The functions composing the overall plate-bending kernel $g_{\mathrm{plate}}(x, y)$ are summarized diagrammatically in Figure 7.25. The stamp's discretized bending kernel, $g_{\mathrm{stamp,bending}}[m, n]$ is simply $g_{\mathrm{plate}}(x, y)$ sampled at spatial intervals of d.

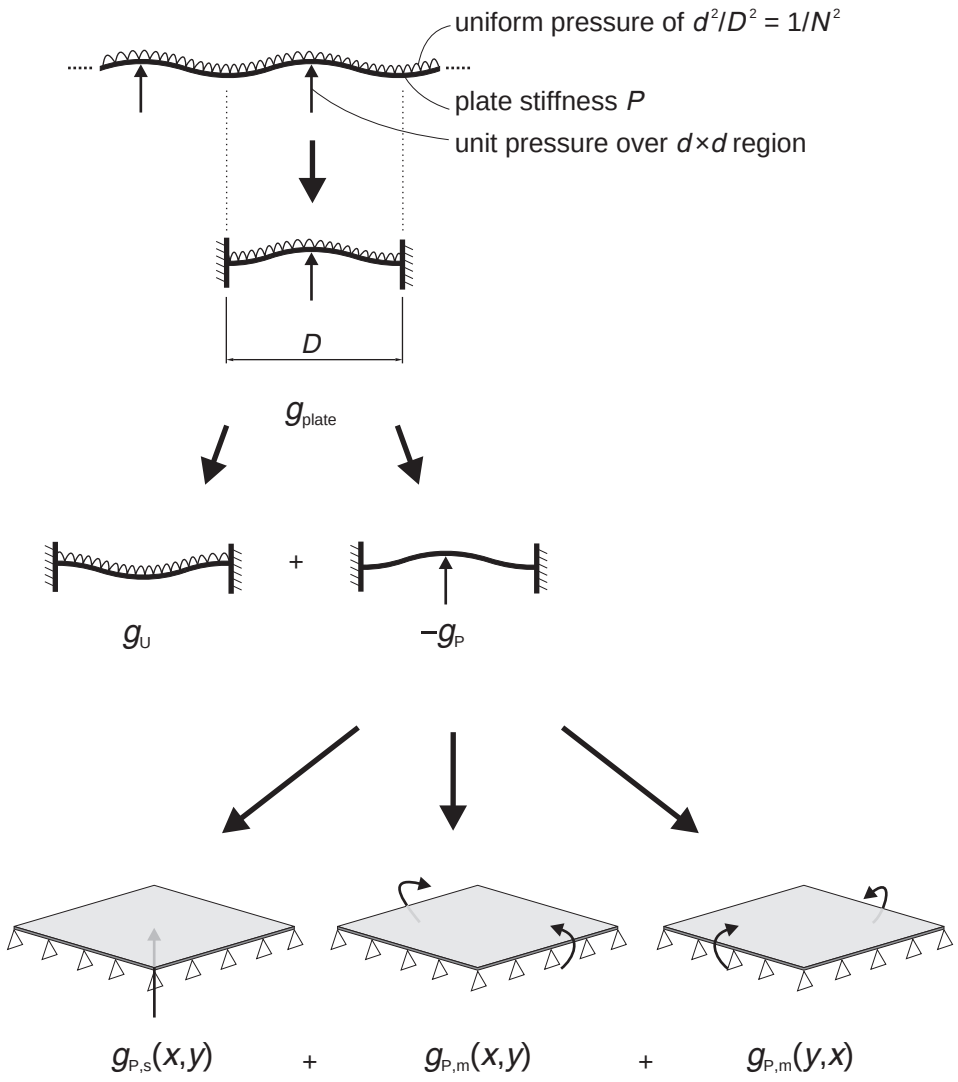

Figure 7.25: Method for deriving the kernel function appropriate for stamp bending.

Expressions for $g_{\{U|P\},m}(x, y)$ and $g_{\{U|P\},s}(x, y)$ are given below:

$$w_{U,s}(x,y) = \frac{4D^4}{N^2\pi^5 P} \sum_{m=1,3,5,7} \frac{(-1)^{\frac{m-1}{2}}}{m^5} \cos\left(\frac{m\pi x}{D}\right)\left[1 - \frac{\alpha_m \tanh\alpha_m + 2}{2\cosh\alpha_m}\cosh\left(\frac{m\pi y}{D}\right) + \frac{m\pi}{2D\cosh\alpha_m} y \sinh\frac{m\pi y}{D}\right] \tag{7.20}$$

$$w_{U,m}(x,y) = -\frac{2D^4}{N^2\pi^5 P} \sum_{m=1,3,5,7} \frac{Q_m(-1)^{\frac{m-1}{2}}}{m^2\cosh\alpha_m} \cos\left(\frac{m\pi x}{D}\right)\left[\frac{m\pi}{D} y \sinh\left(\frac{m\pi y}{D}\right) - \alpha_m \tanh\alpha_m \cosh\left(\frac{m\pi y}{D}\right)\right] \tag{7.21}$$

$$w_{P,s}(x,y) = \frac{4d^2}{D^2 P} \sum_{n=1}^{7}\sum_{m=1}^{7} \frac{1}{k_{mn}} \sin\left(\frac{m\pi}{2}\right)\sin\left(\frac{n\pi}{2}\right)\sin\left(\frac{m\pi\left(x - \frac{D}{2}\right)}{D}\right)\sin\left(\frac{n\pi\left(y - \frac{D}{2}\right)}{D}\right) \tag{7.22}$$

$$k_{mn} = \left(\frac{\pi}{D}\right)^4 \left(m^4 + 2m^2n^2 + n^4\right) \tag{7.23}$$

$$w_{\mathrm{P,m}}(x,y) = -\frac{D^2 d^2}{2\pi^2 P} \sum_{m=1,3,5,7} \frac{R_m (-1)^{\frac{m-1}{2}}}{m^2 \cosh\alpha_m} \cos\left(\frac{m\pi x}{D}\right)\left[\frac{m\pi}{D} y \sinh\left(\frac{m\pi y}{D}\right) - \alpha_m \tanh\alpha_m \cosh\left(\frac{m\pi y}{D}\right)\right] \tag{7.24}$$

$$\alpha_m = \frac{m\pi}{2} \tag{7.25}$$

$$P = \frac{E t_{plate}^3}{12(1-\nu^2)} \tag{7.26}$$

In (7.20) and (7.21), $N = D/d$. The values of Q_m and R_m referred to in (7.21) and (7.24) respectively are given by Timoshenko and are shown in Table 7.4.

Table 7.4: Values of Q_m and R_m for the construction of the plate-bending kernel function. From Timoshenko [235].

m	1	3	5	7
Q_m	–0.3722	0.0380	0.0178	0.0085
R_m	–0.1025	0.0263	0.0042	0.0015

It has been found that the introduction of the $m = 7$ terms makes no appreciable difference to the shapes of the final kernels, compared to the case of using all lower terms but not $m = 7$ itself. It is therefore concluded unnecessary to add terms above $m = 7$.

The plate-bending expressions thus derived are for a uniform-thickness, isotropic plate; other expressions can be found for layered or composite plates and the expressions for the kernel functions could if necessary be generalized to deal with anisotropic materials.

7.5.3. Quantifying the relative magnitudes of stamp indentation and bending

It is suggested above that stamp indentation would dominate deflections when the characteristic spatial period of the imprinted pattern was lower than approximately a stamp thickness, and that bending would dominate for larger spatial periods. Here we quantify the relative importance of these two modes through simulations that use the kernel functions just derived.

Hard surfaces of topography $z(x, y)$ are defined as follows, and then discretized:

$$z(x,y) = z_0 \sin\left(2\pi\frac{x}{\lambda}\right)\sin\left(2\pi\frac{y}{\lambda}\right). \tag{7.27}$$

Here, λ represents the characteristic spatial period of the topography. We perform simulations in which an initially flat layer of material having the elastic properties of the stamp is forced to conform to this hard topography. Firstly, only the indentation mode of the stamp is considered. For each of a range of values of λ, we find the contact pressure distribution that would be required to pull the stamp fully into contact with the surface $z(x, y)$. The pressure distributions are found by deconvolving the discretized $z[m, n]$ with $g_{\mathrm{stamp,indentation}}[m, n]$. Dummy values are used for z_0 and for the stamp's plate modulus, E'. For each calculation, the amplitude of the pressure distribution, $p_{z0,i}$, is recorded.

The procedure is then repeated but this time considering only the *bending* mode of the stamp. The pressure distributions are found by deconvolving the discretized $z[m, n]$ with $g_{\text{stamp,bending}}[m, n]$. A dummy value is adopted for the stamp thickness, t_{stamp}. For each calculation the amplitude of the pressure distribution, $p_{z0,b}$, is recorded.

It is noted that $p_{z0,i}$ is inversely proportional to the wavelength of the surface, while $p_{z0,b}$ is inversely proportional to the fourth power of the wavelength. The constants k_i and k_b are then defined as follows:

$$p_{z0,i} = \frac{k_i z_0 E'}{\lambda}; \tag{7.28}$$

$$p_{z0,b} = \frac{k_b z_0 E' t_{\text{stamp}}^3}{\lambda^4}; \tag{7.29}$$

$$E' = \frac{E}{1-\nu^2}. \tag{7.30}$$

The values of these constants are extracted from the numerical simulations: k_i is found to be 4.28 and k_b to be 336 (3 s.f.). By defining the value of λ at which $p_{z0,b} = p_{z0,i}$ to be that at which bending and indentation are of equal importance, we find that stamp bending begins to play a larger role than bulk indentation in conforming to the surface when

$$\frac{\lambda}{t_{\text{stamp}}} > \sqrt[3]{\frac{k_b}{k_i}} \approx 4. \tag{7.31}$$

Since stamp compliance is what enables residual layer nonuniformity to arise, it might seem desirable — from the perspective of minimizing pattern dependencies — to make stamps as stiff as possible. One good reason for not wishing to make a stamp infinitely stiff, however, is that stamps, substrates, and polymeric layers may not be perfectly flat at the start of the imprinting process: they may be wavy, or bowed, or have a certain roughness, or have dust particles sitting on their surface. A stamp with a certain amount of compliance can conform to these imperfections and reduce the lateral extent of their influence; that indeed is the purpose of the air cushion press design.

As a proxy for the ability of a stamp to conform to layer topography imperfections, we can use the level of contact pressure uniformity that arises when an elastic layer having the properties of the stamp is pressed against a hard topography representing the uneven layer. Suppose that a specification is placed on the pressure nonuniformity arising from layer waviness of a certain wavelength, such that it must not exceed a fraction α of the average contact pressure p_0. A pressure distribution that satisfies this specification is illustrated in Figure 7.26. For an incompressible layer material, the total contact pressure distribution is equal to the zero-mean pressure distribution required to *just* bring the elastic layer into contact with all points of the topography, plus a constant p_0.

At the wavelength at which stamp bending becomes more significant than indentation, the largest allowable roughness amplitude z_0 that will keep the pressure within its nonuniformity specification will therefore be given by:

$$\frac{z_0}{t_{\text{stamp}}} = \sqrt[3]{\frac{k_b}{k_i}}\left(\frac{\alpha\, p_0}{E' k_i}\right). \tag{7.32}$$

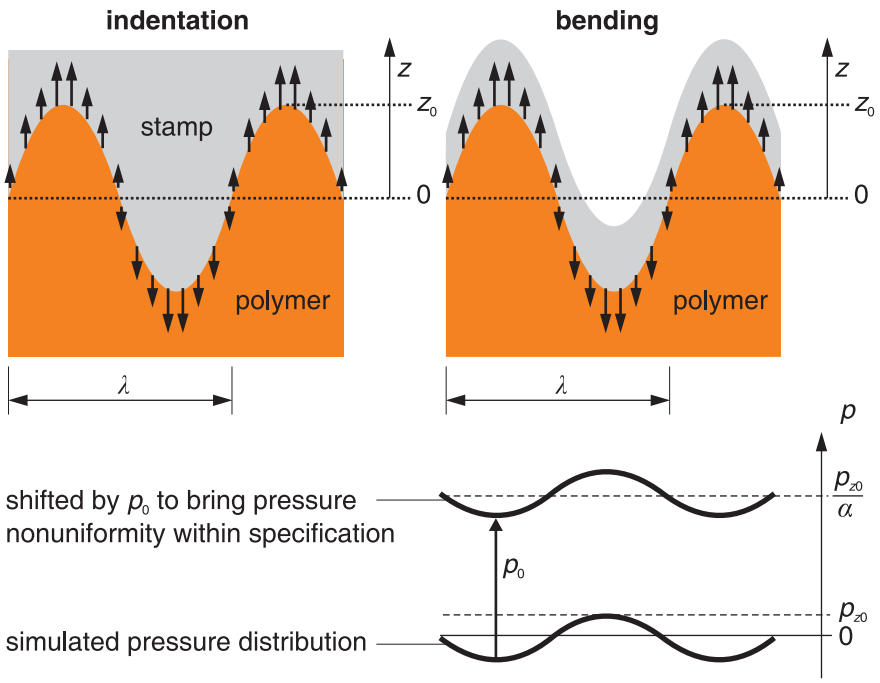

Figure 7.26: Simulations of contact pressure nonuniformity for hard rough surface and a stamp that can either bend or be indented.

The maximum allowable surface waviness amplitude can then be plotted against the characteristic wavelength of the layer imperfections, as shown in Figure 7.27. Near the transition region, both indentation and bending are in fact relevant, and the dashed line in Figure 7.27 suggests how the maximum acceptable z_0 might, in reality, change with λ.

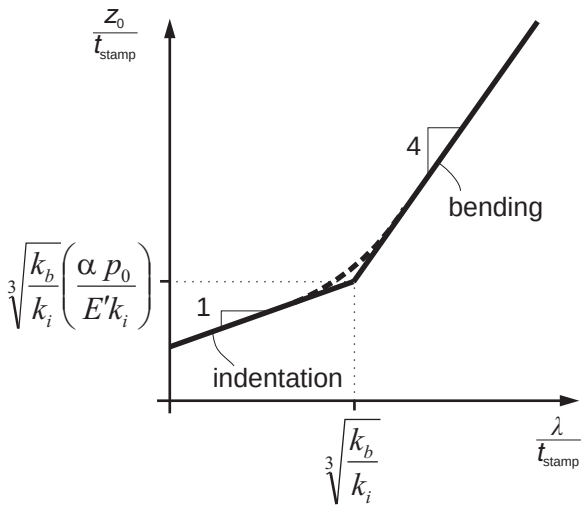

Figure 7.27: Schematic graph, on logarithmic axes, of the maximum surface waviness to which a stamp can conform as a function of the applied average pressure, the pressure nonuniformity specification, the material properties and the characteristic wavelength of surface roughness.

7.5.4. Modeling the use of layered stamps

Given the dual aims, when designing a stamp, of minimizing pattern-dependent residual layer nonuniformity and accommodating any initial layer imperfections, one might imagine that it would be useful to tailor the wavelength–compliance spectrum of the stamp — *i.e.* the shape of the curve illustrated in Figure 7.27. For example, stamps composed of two of more layers of varying stiffness, or stamps with graded, depth-varying stiffness, might provide better performance than a single, thick elastic layer.

If, for example, polymer layers of a certain type were known to exhibit bow or waviness but very little roughness below a particular characteristic wavelength, it might be valuable to produce a stamp in which the features were patterned on a relatively stiff surface layer attached to a more compliant support layer. This way, initial layer waviness could be accommodated while residual layer nonuniformity would be suppressed at length scales smaller than that of the waviness. Such an approach has been demonstrated by Suh *et al.* [237].

Conversely, if the layer being imprinted is particularly rough at small length-scales, it could be beneficial to make the stamp with a soft surface layer on a harder support material. McClelland *et al.* report the use of this approach for the patterning of resist spun on to rough magnetic layers [238].

In general, a good approach would seem to be to tailor the compliance of the stamp so that the shape of its wavelength–compliance (z_0–λ) spectrum hugs as closely as possible the characteristic spectrum of any parasitic roughness/waviness of the stamp and substrate. This way, the stamp does not deform any more than is needed to counteract these parasitic topographies, and so pattern-dependent residual layer variation is no larger than it needs to be. In fact, there is likely to be a trade-off between accommodating any parasitic roughness/waviness of the stamp and substrate and limiting pattern-dependent stamp deflections.

Next we examine the use of two-layer stamps as a way of tailoring stamp compliance. Figure 7.28 illustrates the factors determining the wavelength–compliance spectrum of a stamp with a coating layer of thickness t_{layer} and elasticity E_1 attached to a thick backing layer of stiffness E_2. The kernel function described by Nogi and Kato [188] for the point load response of a layered elastic substrate was used in the numerical simulations that yielded these results.

Where $E_1 < E_2$, stamp compliance is large for $\lambda << t_{layer}$, exhibits a plateau around $\lambda = t_{layer}$, and begins increasing again for $\lambda >> t_{layer}$, corresponding to substantial indentation of the backing layer. Where $E_1 > E_2$, the thin layer exhibits indentation behavior for $\lambda << t_{layer}$, behaves as a plate on an elastic support for $\lambda = t_{layer}$, and transmits loads fairly directly to the soft support layer for $\lambda >> t_{layer}$.

By tuning the thickness of the coating layer and the elasticity of both layers, it may therefore be possible to ‘hug’ the parasitic roughness/waviness spectrum of a stamp and substrate more closely than can be done with a single-layer substrate. Multi-layer or graded-stiffness substrates could offer even better tailoring than two-layer stamps, although the analysis would be substantially more complicated and is left for the future.

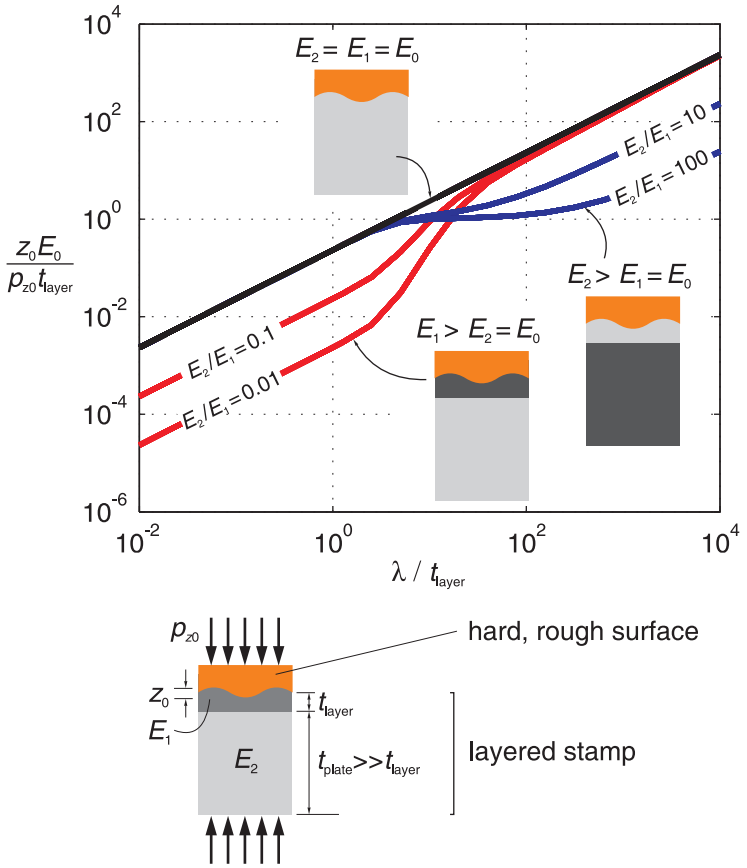

Figure 7.28: The ability of a two-layer stamp to conform to surface roughness.

Stamp compliance could be tailored in other ways, too. Several researchers have proposed introducing backside grooves into nanoimprint stamps — usually aligned with the edges of dice [239–241]. These grooves increase the bending compliance of the stamp at length scales greater than that of the die size, and are claimed to enhance wafer-scale imprint uniformity. In step-and-flash imprint lithography, meanwhile, because the stamp is the size of a single die, it is possible to reduce wafer-scale nonuniformity by using mechanical systems that maneuver the stamp to be parallel to the local surface of the wafer before each imprint is made [242].

Finally, if it is inconvenient to tailor the stamp compliance, it may be possible to improve conformality of stamp and substrate by placing a compliant layer beneath the substrate itself. Bergmair *et al.* report on such a scheme [243]. This approach is applicable for counteracting stamp or substrate waviness at length scales larger than the substrate thickness: the substrate is required to bend for this approach to work.

7.6. Implementing the hierarchical simulation approach

We now bring together the models for polymer layer deformation and stamp/substrate deflections to construct a die-scale, hierarchical simulation method. As shown in Figure 7.1, each (identical) $D \times D$ die on the stamp is discretized into regions of size $d \times d$. The die design is described by a 'coarse' topography $w_{\text{stamp}}[m, n]$ that takes a uniform value within any given $d \times d$ region, upon which is superimposed a 'fine' topography characterized within each $d \times d$ region by a homogeneous, regular pattern of a particular pitch, shape, and areal density. In this way, we can use a single simulation approach both for large, feature-rich patterns and for intricate custom patterns discretized at the sub-feature scale.

Since our model considers a large square array of identical dice, we neglect for the time being any wafer-scale components of stamp and layer deformation. We believe wafer-scale variation only to become significant when all cavities within the die have been substantially filled. We therefore have the following kinematic relationship between the reference displacement of the stamp, Δ, and the deflections of stamp, substrate and polymer layer inside the stamp–layer contact region C:

$$w_{stamp}[m,n] + w_{D,die}[m,n] + w_{D,substrate}[m,n] + w_{local}[m,n] + w_{die}[m,n] = \Delta \qquad \forall\ m,n \in C \tag{7.33}$$

The reference displacement of the stamp, Δ, is defined positive-downwards into the polymeric layer. The coarse stamp topography $w_{\text{stamp}}[m, n]$ is fixed for a given stamp and is defined positive upwards from the surface of the stamp that is in contact with the polymeric layer at the start of imprinting. Intra-die deflections of the surface of the stamp, $w_{\text{D,die}}$, are defined positive-upwards. Deflections of the substrate, $w_{\text{D,substrate}}$, are defined positive-downwards. Both $w_{\text{D,die}}$ and $w_{\text{D,substrate}}$ are assumed here to be periodic at the die level and to have no wafer-scale variation. Because the substrate is assumed elastic, substrate deflections consistent with the final imprinting pressure distribution will spring back when the stamp is removed.

Deformations of the polymeric layer are defined such that the residual layer thickness $r[m, n]$ — *i.e.* the thickness of the thinnest part of material within that region — is given by the following relation:

$$r[m,n] = r_0 - w_{local,u}[m,n] - w_{die,u}[m,n] \tag{7.34}$$

where r_0 is the initial layer thickness. The quantity $w_{\text{local}}[m, n]$ represents the reduction of residual thickness that is associated with the filling of any fine features *within* the region $[m, n]$. Meanwhile, $w_{\text{die}}[m, n]$ represents any reduction of layer thickness that is consistent with the exchange of layer material between adjacent $d \times d$ regions. The quantity $w_{\text{die}}[m, n]$ is therefore responsible for capturing intra-die pattern interactions.

Our objective is to find the values of three particular quantities at the end of the imprinting cycle: (*i*) the residual layer thickness everywhere in the contact region, C; (*ii*) the proportions of the volumes of cavities constituting the 'fine' topography that are filled with polymer; (*iii*) the topography of material outside the contact region.

We perform the solution for these three quantities in terms of the dimensionless contact pressure–compliance, $p_{\text{g}}[m, n]$. The simulation procedure involves gradually increasing this quantity's spatial average, $p_{\text{g,0}}$, in a series of steps, labeled $u = 1..U$, towards the final value $p_{\text{g,0,U}}$. This final value is as defined in (7.6): it is a function of the linear viscoelastic properties of the imprinted layer and the pressure–time profile of the imprinting process being simulated.

This stepping procedure serves to deal with the geometric nonlinearities that exist in the imprinting of a finite-thickness layer. At each step, the 'resistance' to imprinting is recomputed as a function of position, according to the instantaneous maps of $r[m, n]$ and $p_{\text{g}}[m, n]$ obtained in the previous step.

If the resist model is a Newtonian viscosity and the applied average pressure remains constant with time, then the value of $p_{g,0}$ at a given step is proportional to the imprinting time that has elapsed. In the cases of different viscoelastic models or different pressure–time courses, the value of $p_{g,0}$ is a function of both elapsed time and applied pressure history.

For step $u = 1$, the values of relevant variables are defined in Table 7.5.

Table 7.5: Initial values of variables involved in nanoimprint simulation

Quantity	Meaning	Initial value
$r_1[m, n]$	Residual layer thickness	r_0 everywhere
$w_{die,1}[m, n]$	Die-scale layer deformation	0 everywhere
$w_{local,1}[m, n]$	Local layer deformation associated with filling of the fine-featured topography	0 everywhere
$S_1[m, n]$	Switch that determines whether filling of fine-topography cavities is squeeze-dominated (value is 1) or dominated by bulk deformation of material (value is 0).	1 everywhere
$k_{die,1}[m, n]$	Local thickness-correction factor	1 everywhere (layer thickness begins uniform)
$p_{g,1}[m, n]$	Contact pressure–compliance integral	0 everywhere ($p_{g,0}$ ramps up from zero)
Δ_1	Reference displacement of stamp	0 everywhere
C	Contact set	1 where w_{stamp} is equal to its minimum value across the whole stamp; 0 otherwise.

For subsequent steps $u = 2..U$, the following procedure (enumerated in Sections 7.6.1 to 7.6.9) is followed:

7.6.1. Compute $g_{die,u-1}[m, n]$

A kernel $g_{\text{die},u-1}[m, n]$ is generated for an elastic layer on a perfectly hard substrate, using the expressions presented by Nogi and Kato [188] and in the previous chapter. The thickness of the layer is set to the mean value of $r_{u-1}[m, n]$. The kernel is generated on a lateral grid of pitch d. Spatial variation of the residual layer thickness is encapsulated in the quantity $k_{\text{die},u-1}[m, n]$, discussed below. Because we are working in terms of the dimensionless pressure–compliance quantity $p_g[m, n]$, we generate the kernel assuming a dimensionless Young's modulus of $(1–\nu^2)$ and a Poisson's ratio of $\nu = 0.5$.

7.6.2. Compute $k_{inst,u-1}[m, n]$

The value of $k_{\text{inst},u-1}[m, n]$ at each step is defined in (7.35) and illustrated in Figure 7.29.

$$k_{inst,u-1}[m,n] = \left.\frac{-\mathrm{d}w_{local}}{\mathrm{d}p_g}[m,n]\right|_{r=r_{u-1}} \tag{7.35}$$

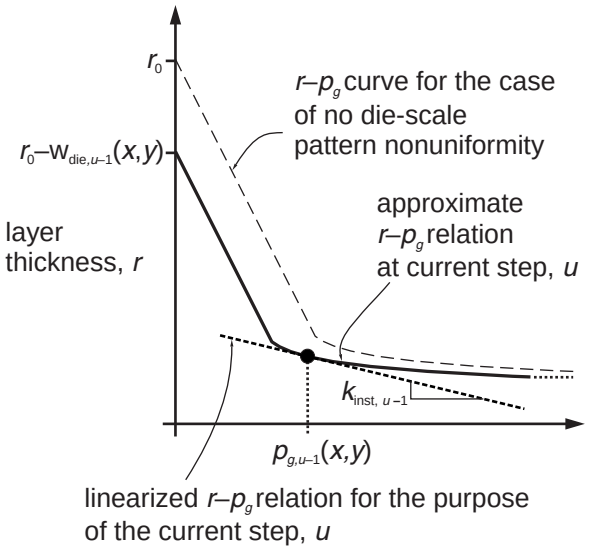

Figure 7.29: Relationship between r and p_g at a particular location within a pattern and for a particular step u.

If $S_{u-1}[m, n]$ equals 1 (*i.e.* the region is in squeezing-dominated mode), then $k_{\text{inst},u-1}[m, n]$ is calculated using the appropriately scaled dp_g/dr' as defined in (7.7); if $S_{u-1}[m, n]$ equals 0 (*i.e.* the region is in bulk deformation-dominated mode), then $k_{\text{inst},u-1}[m, n]$ is calculated using the appropriately scaled derivative of $V/V_0[m, n]$ with respect to $p_g[m, n]$, as defined in (7.14).

7.6.3. Solve for $p_{g,u}[m, n]$ and the corresponding value of Δ_u

At each step, we have specified the spatial-average of the virtual pressure $p_{g,0,u}$. We decompose the solution for $p_{g,u}[m, n]$ into two parts:

$$p^f_{g,u}[m,n]*\left\{\frac{p_0(t_h)}{p_{g,0,u}}g_{ss}[m,n]\right\}+\left\{k_{die,u-1}[m,n]p^f_{g,u}[m,n]\right\}*g_{die,u-1}[m,n]-p^f_{g,u}[m,n]k_{inst,u-1}[m,n]=$$
$$-w_{stamp}[m,n]-r_0+r_{u-1}[m,n]-p_{g,u-1}[m,n]k_{inst,u-1}[m,n]+g_{die,u-1}[m,n]*\left(k_{die,u-1}p_{g,u-1}[m,n]\right) \quad (7.36)$$

and

$$p^e_{g,u}[m,n]*\left\{\frac{p_0(t_h)}{p_{g,0,u}}g_{ss}[m,n]\right\}+\left\{k_{die,u-1}[m,n]p^e_{g,u}[m,n]\right\}*g_{die,u-1}[m,n]-p^e_{g,u}[m,n]k_{inst,u-1}[m,n]=1 \quad (7.37)$$

We have the additional constraint that contact pressure is zero outside C:

$$p_{g,u}[m,n]=0 \qquad \forall \;\; m,n\notin C. \quad (7.38)$$

Pressure distributions $p^f_{g,u}[m, n]$ and $p^e_{g,u}[m, n]$ are found using the stabilized biconjugate gradient algorithm implemented in Matlab. Having found these two distributions, we solve for the stamp reference displacement Δ_u such that:

$$p^{e}_{g,u}[m,n] + \Delta_u p^{f}_{g,u}[m,n] = p_{g,u}[m,n] \tag{7.39}$$

subject to the constraint that:

$$\sum_{m=1}^{M}\sum_{n=1}^{N} p_{g,u}[m,n] = MNp_{g,0,u}. \tag{7.40}$$

Equations (7.36) and (7.37) encapsulate the idea that in each simulation step the layer deformation at each location [*m*, *n*] can experience change from two sources: (*i*) the forcing of material from the residual layer into the finely patterned cavities *within* the region [*m*, *n*], as governed by the 'stiffness' coefficient $k_{\text{inst},u-1}[m, n]$, and (*ii*) the displacement of material laterally between adjacent regions, as governed by $g_{\text{die},u-1}[m, n]$.

The use of a single kernel, $g_{\text{die},u-1}[m, n]$, to represent the lateral transport of material between regions allows the procedure for finding $p_{g,u}[m, n]$ to consist of a simple series of convolutions and multiplications, but does not in itself capture the fact that it requires a larger pressure to force material away from a region with thinner $r_{u-1}[m, n]$ than from a region in which $r_{u-1}[m, n]$ is thicker. The pre-multiplication factor $k_{\text{die},u-1}[m, n]$ is designed to reflect any spatial variation of $r_{u-1}[m, n]$: in (7.36) and (7.37) it is multiplied by the trial pressure distribution $p_{g,u}[m, n]$ before convolution with $g_{\text{die},u-1}[m, n]$. In this way, residual layer thickness variation can be approximately accounted for without slowing down the solution procedure. In layers where $r_{u-1}[m, n]$ is everywhere substantially smaller than the lateral pitch *d* at which $g_{\text{die},u-1}[m, n]$ is defined, $k_{\text{die},u-1}[m, n]$ would be proportional to the cube of $r_{u-1}[m, n]$, as detailed in Section 7.6.7.

In the convolution expressions of (7.36) and (7.37), the kernel $g_{ss}[m, n]$ incorporates both substrate and stamp deflections: since all substrate deflections spring back upon unloading, it is convenient to fold the substrate and stamp deformations into a single kernel. The individual kernels for bending and indentation are as defined in Section 7.5.

$$g_{ss}[m,n] = g_{stamp,bending}[m,n] + g_{stamp,indentation}[m,n] + g_{substrate}[m,n] \tag{7.41}$$

The sum of stamp and substrate deflections is then given by the following convolution:

$$w_{D,die,u}[m,n] + w_{D,substrate,u}[m,n] = \frac{p_0(t_h)}{p_{g,0,u}} p_{g,u}[m,n] * g_{ss}[m,n]. \tag{7.42}$$

As seen in (7.36), (7.37), and (7.42), the convolution that yields the stamp and substrate deflections re-scales the trial pressure–compliance distribution, $p_g[m, n]$, to a *real* instantaneous pressure distribution by using the factor $p_0(t_h)/p_{g,0,u}$. This re-scaling is necessary because the responses of the stamp and substrate are instantaneous and not time-dependent, and their kernels are generated using their *true* elastic moduli.

7.6.4. Compute $w_{die,u}[m, n]$ and $w_{local,u}[m, n]$

Updated local (feature-level) polymer layer deformations are calculated as follows within the contact region *C*:

$$w_{local,u}[m,n] = r_0 - r_{inst,u-1}[m,n] - w_{die,u-1}[m,n] - k_{inst,u-1}[m,n]p_{g,u}[m,n] \tag{7.43}$$

and the updated polymer layer deformations associated with intra-die interactions are given by:

$$w_{die,u}[m,n] = w_{die,u-1}[m,n] + k_{die,u-1}\left[p_{g,u}[m,n] - p_{g,u-1}[m,n]\right] * g_{die,u-1}[m,n]. \tag{7.44}$$

7.6.5. Compute $r_u[m, n]$ according to $p_{g,u}[m, n]$

The updated residual layer expression $r_u[m, n]$ is found as an incremental change from $r_{u-1}[m, n]$:

$$r_u[m,n] = r_{u-1}[m,n] + k_{inst,u-1}[m,n]\left(p_{g,u}[m,n] - p_{g,u-1}[m,n]\right) - \left[k_{die,u-1}[m,n]\left(p_{g,u}[m,n] - p_{g,u-1}[m,n]\right)\right] * g_{die,u-1}[m,n] \tag{7.45}$$

7.6.6. Compute V/V_0 [m, n]

In any regions of the stamp that are defined with finely patterned features, the filled proportion of their volume can be estimated according to the conservation of resist volume, using the following relation:

$$\frac{V}{V_0}[m,n] = \frac{w_{local}[m,n]h[m,n]}{1-\rho[m,n]} \tag{7.46}$$

where $h[m, n]$ is the cavity height, and $\rho[m, n]$ is the areal density of protrusions from the stamp. In places where this solution implies $V/V_0[m, n] > 1$, we clip $V/V_0[m, n]$ to equal 1 and clip $w_{\text{local},u}[m, n]$ correspondingly, to $(1–\rho)/h$.

7.6.7. Compute $k_{die,u}[m, n]$

The scale factors $k_{\text{die},u-1}[m, n]$ account approximately for the effect of the spatial variation of r. Where the spatial average of r is much smaller than d, values of $k_{\text{die},u-1}[m, n]$ will be proportional to the cube of $r_{u-1}[m, n]$; where r is much larger than d, $k_{\text{die},u-1}[m, n] \approx 1$. Where $r \sim d$, $k_{\text{die},u-1}[m, n]$ could perhaps be calculated using the relationships in Figure 7.7, Figure 7.8, and Figure 7.9 where the 'feature diameter' a would be assumed to be given by the discretization pitch d and $k_{\text{die},u-1}[m, n]$ would be assumed to be inversely proportional to $\mathrm{d}p_g/\mathrm{d}r'$.

This approach will lose validity if layer thickness variation is a large proportion of the average thickness, and in cases where $d << r$ but material is displaced laterally at the die-scale over distances that are comparable with or much greater than r.

7.6.8. Update the squeeze-/bulk-deformation switch $S_u[m, n]$

It is now necessary to update the estimate of which regions of the layer are operating in a squeeze-dominated mode and which are bulk-deformation-dominated. Firstly, the calculated pressure–compliance distribution $p_{\text{g}}[m, n]$ is substituted into the relation of (7.11), together with pattern information, to give residual layer-thickness values $r_{squeeze}[m, n]$ that correspond to squeeze-dominated deformation of the layer (*i.e.* no cavity filling is considered). Secondly, $p_{\text{g}}[m, n]$ is substituted into (7.14). The resulting values of $V/V_0[m, n]$ are scaled to give absolute stamp displacements, which are subtracted from r_0 to give a set of residual layer-thickness values $r_{bulk}[m, n]$ corresponding to bulk deformation of the layer. In calculating $r_{bulk}[m, n]$, squeezing-limited flow of the residual layer is ignored.

Where $r_{squeeze}[m, n] > r_{bulk}[m, n]$, it is deduced that resistance to squeezing flow of the residual layer is limiting the ability of the stamp to penetrate the layer, and $S_u[m, n]$ is set to 1. Otherwise, it is concluded that movement of the stamp into the layer is bulk deformation-dominated — *i.e.* limited by forces distributed throughout the *whole* layer — and $S_u[m, n]$ is set to zero. In this calculation, any lateral displacement of material, $w_{\text{die}}[m, n]$, is ignored; the estimate of $S_u[m, n]$ is based solely on the current pressure–compliance distribution.

7.6.9. Update the contact set C

At the end of each step, the contact region C is also revised, subject to the constraint that regions $[m, n]$ with a negative pressure in the current solution must be removed from C, while those regions in which the simulated polymer topography overlaps the stamp topography are added to C.

7.6.10. A strategy for choosing step-size

In order to minimize the number of steps U necessary to complete a simulation, the following approach could be adopted. An initial step size for $p_{g,0}$ is chosen that is typically around 5 or 10% of $p_{g,0,U}$. The solution for that step is performed. If any value of $r[m, n]$ is negative in this new solution, this is taken to indicate that the step-size was too large to represent reality, and the step solution is re-done using a step-size half as large as previously. If, on the other hand, no value of $r[m, n]$ is negative in the new solution, the algorithm advances to the next step by incrementing $p_{g,0}$ twice as much as for the previous step. In this way, the algorithm should gravitate towards the largest step-size that allows the solution to proceed in a stable fashion.

We would however expect the fidelity of simulation results to reduce as the step-size is increased: the pressure–displacement relations of the polymeric layer are linearized at each step, and the larger the step, the further a linearized solution will deviate from reality. Care therefore needs to be taken to restrict the maximum allowable step-size for $p_{g,0}$.

7.7. Demonstration of die-scale simulation in ‘flat’ mode

As a demonstration of the simulation method, we now compare experimental results from the imprinting of a simple test pattern with the results of a simulation assuming a Newtonian resist model. The simulation is operated here in ‘flat’ mode, whereby the design of the stamp is discretized at the sub-feature scale and there is no fine topography included in the stamp’s description.

7.7.1. Test pattern

The test pattern used is similar in design to that of the previous chapter. Here, though, it is scaled down in lateral dimensions by a factor of two, so that features are 5 to 50 μm in diameter and the pattern is arrayed on a square grid with pitch 425 μm. The polarity of the pattern is also reversed from the previous chapter, so that the stamp now contains a series of square and rectangular protrusions.

7.7.2. Experimental method

The test pattern was transferred to 1 μm of OCG825 photoresist on a 6” silicon wafer. The silicon was etched to a depth of ~1 μm using SF_6 chemistry and the resist was stripped using an oxygen plasma.

The layer to be imprinted was prepared as follows. 950 kg/mol PMMA, dissolved 3% by weight in anisole, was spun on to a fragment of silicon that was ~ 10 mm square. The spinning conditions were 2000 rpm for 1 minute. The prepared substrate was baked in an oven at 170 °C for 30 minutes.

The PMMA layer on silicon was then placed into contact with part of the array of test patterns on the silicon stamp. A piece of Neoprene rubber, ~ 8 mm square and 1 mm thick, was placed on the back of the 10 mm square silicon sample. The stamp/substrate/Neoprene stack was placed between the platens of the hot embossing apparatus described in Chapter 2. The platens were heated to 165±1 °C and a sample-

average pressure of 40 MPa was applied for two minutes. The platens were then cooled to approximately 90 °C and the load was removed.

7.7.3. Metrology

A few small scratches were made through the imprinted resist layer to enable the position of the PMMA/silicon interface to be determined. Several regions of the sample were photographed in an optical microscope and the interferogram obtained from one particular copy of the test pattern near the center of the sample is shown in Figure 7.30, column (a). The color of each region of the interferogram can be used to infer the approximate thickness of the imprinted layer, as outlined in Appendix B.

To gain more precise measurements of the imprinted topography, a white-light interferometer (Zygo NewView) was used. The PMMA layer is transparent and its thickness is too small to use white-light interferometry directly on the sample: reflections from the PMMA/Si interface would have made it impossible for the interferometer's software to determine the true position of the PMMA/air interface. Depositing a reflective layer (*e.g.* sputtered gold) on the sample to stop light from penetrating the PMMA layer was also not feasible: the required thickness of the deposited layer would have been comparable to the relief of the imprinted topography. Instead, Sylgard 184 PDMS was cast on to the imprinted sample, cured at 80 °C for six hours, and then peeled from the sample. This PDMS casting was sufficiently thick that white-light interferometry could be used directly on the surface of the casting without encountering parasitic reflections from the flat back-side of the PDMS layer. The topographies obtained were then simply flipped to give a representation of the imprinted PMMA topography.

It is known that white-light interferometry can produce erroneous data near step-changes in topography, and indeed the data obtained from this sample do exhibit sharp spikes near feature edges. We cannot be sure whether these spikes are real or artifacts of the measurement procedure, and so the data were smoothed before being plotted in Figure 7.30, column (a).

The spun-on PMMA layer thickness was determined to be approximately 260 nm by looking at the step-height of PMMA at the edge of one of the scratches introduced to the PMMA samples (Figure 7.31). This measurement was performed in a region of the sample that had not made contact with any part of the stamp.

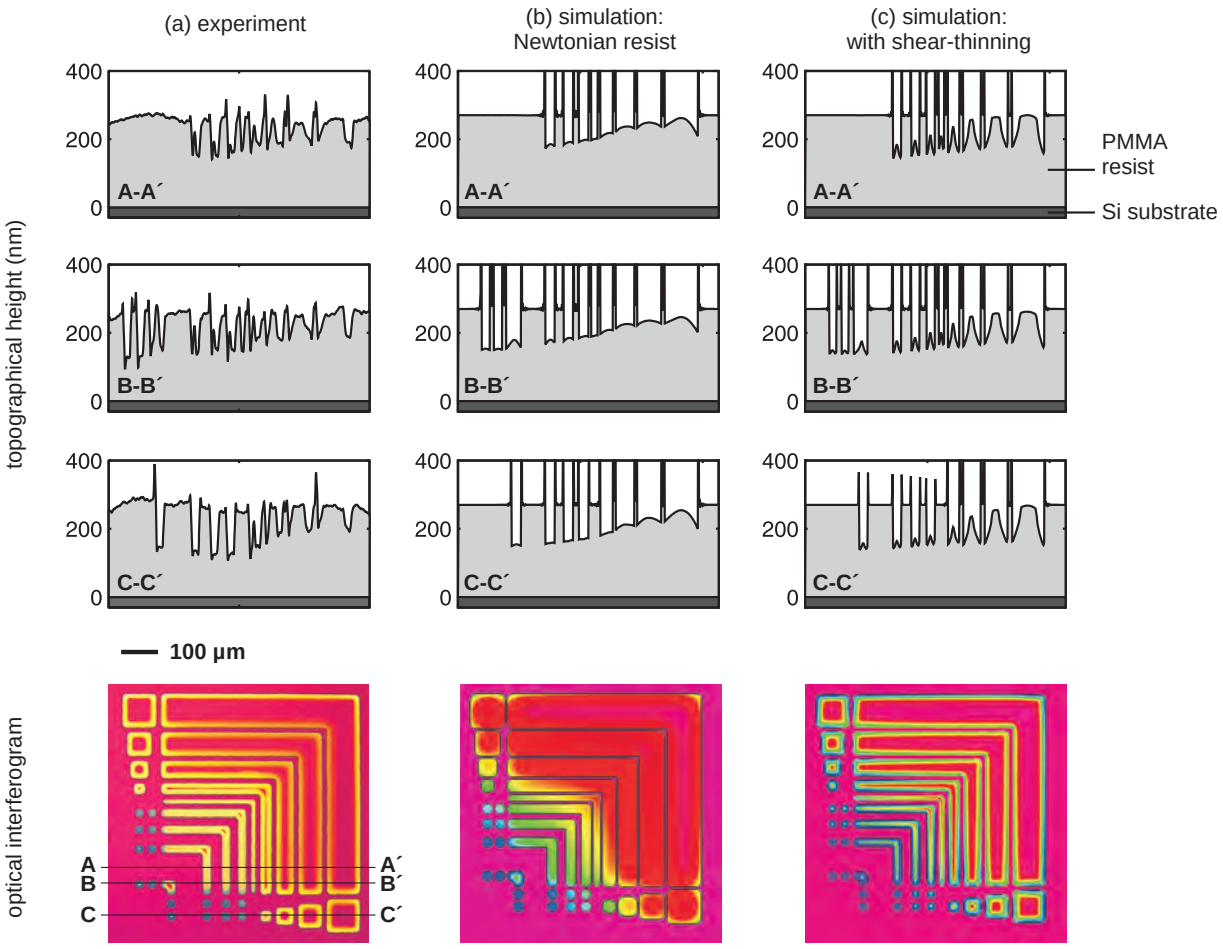

Figure 7.30: Optical micrographs and white-light interferometry cross-sections of test patterns imprinted into 260 nm-thick 950 kg/mol PMMA under 165 °C, 40 MPa, 2 min: (a) experimentation (b) linear viscous simulation (c) shear-thinning model.

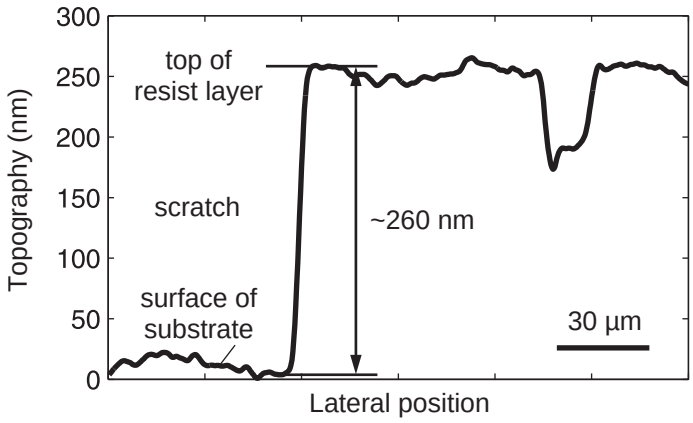

Figure 7.31: Determination of initial PMMA layer thickness using scanning white-light interferometry results.

7.7.4. Newtonian simulation

The simulation method described in Section 7.6 was used to simulate the embossing of this PMMA sample. A Newtonian resist model was chosen with a viscosity of 5×10^7 Pa.s, which is a plausible value for PMMA at 165 °C according to the data reported by Han [230]. The stamp and substrate, which are both silicon, were modeled with Young's modulus 160 GPa and Poisson's ratio 0.27. The nominal number of simulation steps, *U*, was set to 10.

The simulation results are plotted in Figure 7.30, column (b). The simulated optical interferogram was constructed according to the method described in Appendix B and assuming a refractive index of 1.49 for PMMA. The simulation, which was discretized at a lateral pitch of 1 μm, took approximately six minutes to run.

Substantial stamp/substrate deformation is predicted by the simulation, leading to variation of the simulated depth of imprinting by more than a factor of two across the pattern. The general shape of these stamp deflections — whereby the larger features are imprinted to a much shallower depth than the narrower ones — roughly follows that of the experimental data. Tracking the simulated contact pressure distribution over time (Figure 7.32), we see that the pressure is initially higher in the region of the small, sparse stamp protrusions near the lower left corner of the pattern, but that as the resist is progressively imprinted in these regions the bulk of the contact pressure transfers to the wider features on the upper and right-hand sides of the pattern.

It is important to note that this topographical nonuniformity is predicted in the absence of any 'springback' of the resist material itself: the nonuniformity is entirely attributable to deflections of the stamp and substrate.

Since it would be difficult to increase the stiffness of the stamp much above that of silicon, it is apparent that, for a pattern of this nature, an improvement of residual layer uniformity would require either a substantial extension of imprinting time, or a substantial reduction of resist viscosity enabling imprinting to be carried out at much lower pressures.

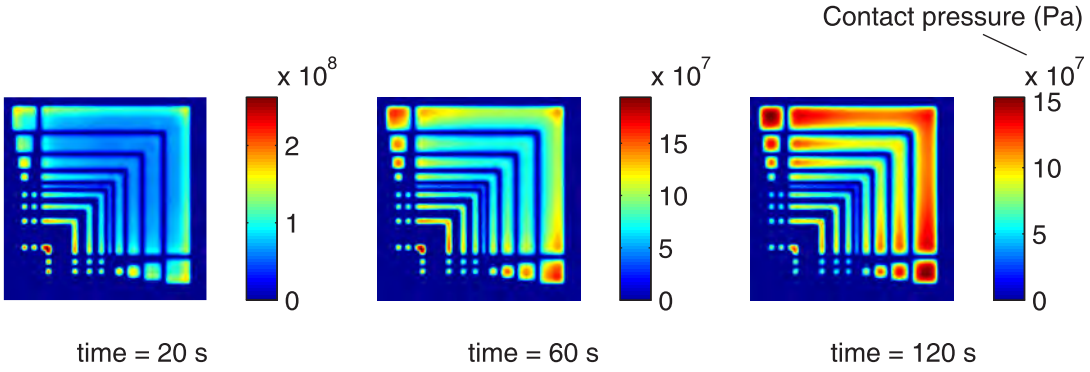

Figure 7.32: Evolution of contact pressure in a simulation assuming a Newtonian resist. During the loading cycle the contact pressure redistributes from being highly concentrated in the region of the smallest, sparsest features to being higher in the largest features.

The prediction of this Newtonian resist model is far from perfect, however: the exact measured topography of resist within each of the larger features is not well captured. The experimental data in fact show much sharper gradients of topography near the edges of these larger features, indicative of shear-thinning behavior.

7.8. Modeling shear-thinning

We now outline a possible way of representing shear-thinning in simulation. The proposed scheme deals only with viscous (not viscoelastic) resist materials. The idea is to perform the simulation in a series of explicit time-steps, with each step u made up of two components. In the first component, the contact pressure distribution is estimated using a *linear* viscous model for the resist and taking as one of its inputs the layer topography $r_{u-1}[m, n]$ from the previous step, u–1. The following equations are defined in terms of real pressures $p[m, n]$:

$$p_u^f[m,n] * g_{ss}[m,n] + \left\{k_{die,u-1}[m,n]\, p_u^f[m,n]\right\} * g_{die,u-1}[m,n]\Delta t = -w_{stamp}[m,n] - r_0 + r_{u-1}[m,n] \tag{7.47}$$

and

$$p_u^e[m,n] * g_{ss}[m,n] + \left\{k_{die,u-1}[m,n]\, p_u^e[m,n]\right\} * g_{die,u-1}[m,n] = 1. \tag{7.48}$$

Δt is the length of step u, and k_{die} and g_{ss} are as defined in Section 7.6. Here, $g_{\text{die},u}$ is generated by substituting a 'Young's modulus' of $3\eta_0$ into the function defined by Nogi and Kato and presented in the previous chapter, where η_0 is the zero-shear viscosity of the layer. The layer thickness substituted is the spatial average of the layer thickness $r_{u-1}[m, n]$ from the previous step. We have the additional constraint that contact pressure is zero outside C:

$$p_u[m,n] = 0 \qquad \forall\ m,n \notin C. \tag{7.49}$$

Pressure distributions $p^f{}_u[m, n]$ and $p^e{}_u[m, n]$ are found using the stabilized biconjugate gradient algorithm implemented in Matlab. Having found these two distributions, we solve for the incremental stamp reference displacement Δ_u such that:

$$p_u^e[m,n] + \Delta_u\, p_u^f[m,n] = p_u[m,n] \tag{7.50}$$

subject to the constraint that:

$$\sum_{m=1}^{M}\sum_{n=1}^{N} p_u[m,n] = MNp_{0,u}. \tag{7.51}$$

An amount of linear viscous flow consistent with this pressure distribution $p_u[m, n]$ and with the length Δt of the time-step is then computed:

$$\Delta r_{lin,u}[m,n] = -\left(p_u[m,n]k_{die,u-1}[m,n]\right) * g_{die,u}[m,n]\Delta t. \tag{7.52}$$

In the second component of each step, an *additional* amount of plastic flow associated with shear-thinning is computed. We expect the rate of additional flow at a given location in the resist to be related to the magnitude of in-plane shear stress at that location. The magnitude of in-plane shear stress can readily be calculated from the contact-pressure distribution $p_u[m, n]$ by way of two additional kernel functions defined by Nogi and Kato. Where the plane of the resist is x–y, the Fourier transforms of the in-plane shear stresses in the layer arising in response to unit pressure applied at location [0, 0] are given by:

$$\left.\begin{aligned} S_{yz}[m,n] &= -\sqrt{-1}\left[\frac{m\pi}{Nd}\alpha\left(A-\tilde{A}\right) + z\frac{n\pi}{Nd}\alpha\left(B-\tilde{B}\right)\right] \\ S_{zx}[m,n] &= -\sqrt{-1}\left[\frac{n\pi}{Nd}\alpha\left(A-\tilde{A}\right) + z\frac{m\pi}{Nd}\alpha\left(B-\tilde{B}\right)\right] \end{aligned}\right\} \tag{7.53}$$

where

$$\left.\begin{aligned} \alpha &= \sqrt{\left(\frac{m\pi}{Nd}\right)^2 + \left(\frac{n\pi}{Nd}\right)^2}; \quad \lambda = -1; \quad \kappa = -1 \\ A &= \left[0.5\left(\kappa - \lambda - 4\kappa\alpha^2 r_{mean}{}^2\right)\exp\left(-2\alpha r_{mean}\right)\right]R\exp\left(-\alpha z\right) \\ \tilde{A} &= \left[0.5\left(\kappa - \lambda - 4\kappa\alpha^2 r_{mean}{}^2\right)\exp\left(-2\alpha r_{mean}\right)\right]R\exp\left(\alpha z\right) \\ B &= \left[1-\left(1-2\alpha r_{mean}\right)\kappa\exp\left(-2\alpha r_{mean}\right)\right]\alpha R\exp\left(-\alpha z\right) \\ \tilde{B} &= \left[1+2\alpha r_{mean} - \lambda\exp\left(-2\alpha r_{mean}\right)\right]\kappa\exp\left(-2\alpha r_{mean}\right)\alpha R\exp\left(-\alpha z\right) \\ R &= -\left[1-\left(\lambda+\kappa+4\kappa\alpha^2 r_{mean}{}^2\right)\exp\left(-2\alpha r_{mean}\right) + \lambda\kappa\exp\left(-4\alpha r_{mean}\right)\right]^{-1}\alpha^{-2}. \end{aligned}\right\} \quad (7.54)$$

The thickness defined for the layer, r_{mean}, is the spatial average of $r_{u-1}[m, n]$. The functions above are defined for an incompressible layer and a perfectly stiff substrate (substrate compliance is allowed for elsewhere, in $g_{ss}[m, n]$). The quantity z is the distance between the top surface of the layer and the plane in which shear stresses are expressed; shear stress at a particular location $[m, n]$ is proportional to z, provided that $z \leq r_{\text{mean}}$. $S_{yz}[m, n]$ and $S_{zx}[m, n]$ are evaluated over a range of $2N$ in both m and n, taking $z = 0.5r$ so that the shear stresses computed are those half-way through the thickness of the layer. The values of $S_{yz}[0,0]$ and $S_{zx}[0,0]$ are undefined according to (7.53); however, the average value of shear stress in the layer in response to a normally applied load is zero, so we set both $S_{yz}[0,0]$ and $S_{zx}[0,0]$ to zero. After inverse Fourier transformation of $S_{yz}[m, n]$ and $S_{zx}[m, n]$, the central $N \times N$ regions of the resulting matrices are taken as the kernel functions, $s_{yz}[m, n]$ and $s_{zx}[m, n]$, for use in simulation.

The in-plane shear stress components are then given by convolution:

$$\tau_{yz}[m,n] = s_{yz}[m,n] * p_u[m,n]; \quad \tau_{zx}[m,n] = s_{zx}[m,n] * p_u[m,n]. \quad (7.55)$$

We define the magnitude of in-plane shear stress as follows:

$$\bar{\tau}_u[m,n] = \sqrt{\tau_{yz}^2[m,n] + \tau_{zx}^2[m,n]}. \quad (7.56)$$

From the strain-rate–viscosity relations for PMMA illustrated in Figure 7.3, it is seen that for any given temperature there is a breakpoint in strain-rate above which a Newtonian model ceases to hold and viscosity falls with increasing strain rate. From the perspective of shear *stress*, this behavior can be described in terms of the existence of a yield stress, below which the rate of resist flow is proportional to stress and above which it increases super-linearly with stress. Since we are trying to express an *additional* incremental amount of plastic flow $\Delta r_{thinning,u}[m, n]$ *beyond* that implied by a Newtonian model, we propose the following expression:

$$\Delta r_{thinning,u}[m,n] = -\left(p_u[m,n]k_{die,u-1}[m,n]\right)\max\left[\bar{\tau}_u[m,n] - \tau_{yield}, 0\right]^b \frac{k_{shear}\Delta t}{\eta_0}. \quad (7.57)$$

where τ_{yield} is a yield shear stress for the layer, k_{shear} is a constant depending on the thickness of the layer and the pitch d of discretization, and b is an exponent describing the shear strain rate's dependence on shear stress.

The layer topography $r_u[m, n]$ that is carried forward to the next step is then given by:

$$r_u[m,n] = r_{u-1}[m,n] + \Delta r_{lin,u}[m,n] + \Delta r_{thinning,u}[m,n] \quad (7.58)$$

The overall idea of this approach is that by calculating the evolving pressure distribution with a linear model, we can still use the convolution approach of the previous sections, and the speed of solution will

be much greater than if the non-linear shear-thinning model were to be integrated in the pressure-solution step. The value of $r_u[m, n]$ is updated separately at the *end* of each step, in order to keep track of the additional, shear-thinning-related flow.

In trying to implement this approach, it was found that after the first complete solution step the calculated pressure distributions started to become very rough indeed. Further work is needed to resolve these numerical problems. An illustration of the scheme, however, can be provided by looking at the output of the model after just one step, where that step has been specified to have a length equal to the entire duration of the imprinting cycle. Such an illustration is given in Figure 7.30, column (c). The simulation was performed at a lateral discretization, d, of 1 μm. The value of b found to represent experimental results effectively was 0.4, that of τ_{yield} was 0.45 MPa, and that of k_{yield} was 5.1×10^{-5} m/(Pa$^{0.4}$). The duration of the loading cycle was 120 s, the pattern-average applied pressure was 40 MPa, and the zero-shear viscosity specified was 5×10^7 Pa.s. Elastic properties of the stamp and substrate were as in Section 7.7.

The simulation results shown in Figure 7.30, column (c), bear a substantially closer resemblance to the experimentally obtained topography (column (a)) than does the simulation that assumes a Newtonian resist (column (b)). The shear-thinning simulation successfully represents the bands of ~10 μm width around the edges of the larger features have been imprinted deeply into the resist layer. These bands correspond to the locations of in-plane shear stresses that exceeded the fitted yield stress of 0.45 MPa (Figure 7.33b).

Because only one simulation step was used here, we cannot expect the accuracy of the simulated topography — or indeed the validity of the extracted values of b, τ_{yield} and k_{yield} — to be particularly high. Even so, the proposed method of using in-plane shear stresses to compute the locations of shear-thinning behavior does appear promising. The total simulation time for this crude, single-step solution was only two minutes.

The PMMA sample analyzed here was processed under conditions where a great amount of shear thinning evidently occurred. In many realistic imprint cases, though, the resist would be processed much further above T_g, so that its behavior would in general be much closer to Newtonian. Therefore, we expect the incorporation of shear-thinning computations to be required in some, but by no means all, nanoimprint simulations.

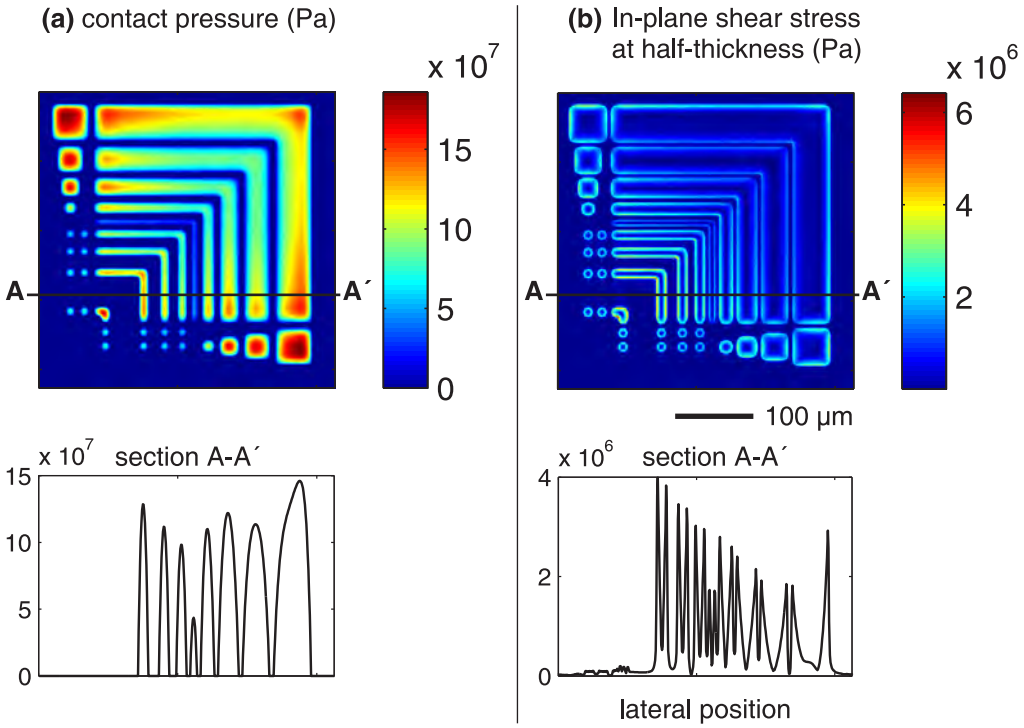

Figure 7.33: Simulated maps of contact pressure distribution (a) and in-plane shear-stress distribution (b) after a single step's worth of linear viscous flow has occurred but before any shear-thinning-related plastic flow has occurred. The cross-sections show section A-A′. The case simulated is for initially 260 nm-thick 950 kg/mol PMMA/Si, at 165 °C, with 40 MPa average applied pressure, and a two-minute loading duration.

7.9. Demonstrations in 'hierarchical' mode

We now return to a *linear*-viscous material model to demonstrate the hierarchical mode in operation. Firstly, we demonstrate an attempt to reproduce the published experimental and simulation results of Kehagias *et al.*, and secondly we show the hierarchical nanoimprint model in conjunction with the test pattern used in Chapter 2 of this thesis.

7.9.1. Comparison with the results of Kehagias et al.

Kehagias report the use of a silicon test-stamp with micron-scale features to imprint a spun-on layer of 75 kg/mol PMMA [89]. The layer is reported to have an initial spun-on thickness of 340 nm and to have been imprinted with a silicon stamp having cavity depths of 300 nm. The imprinting was done at 190 °C under a sample-average pressure of 6 MPa for 5 minutes. According to the published description, no contact was made between stamp and PMMA outside the edges of the 2.5 mm square pattern defined. By measurement from Kehagias's figures, the pitches and cavity densities of the arrays of parallel lines patterned on the stamp were estimated and are plotted in Figure 7.34.

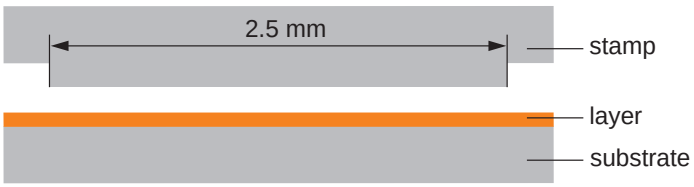

50	50	50	50	50	50	50	50	50	50	50	50
50	50	50	50	50	50	50	50	50	50	50	50
50	50	80	70	40	20	20	20	30	70	50	50
50	50	80	70	40	20	20	20	30	70	50	50
50	50	20	20	20	20	20	30	20	20	50	50
50	50	20	20	20	20	20	30	20	20	50	50
50	50	50	50	50	50	50	50	50	50	50	50
50	50	50	50	50	50	50	50	50	50	50	50
50	50	50	50	50	50	50	50	50	50	50	50
50	50	50	50	50	50	50	50	50	50	50	50
50	50	50	50	50	50	50	50	50	50	50	50
50	50	50	50	50	50	50	50	50	50	50	50

(a) cavity density map (%)

25	25	25	25	25	25	25	25	25	25	25	25
25	25	25	25	25	25	25	25	25	25	25	25
25	25	50	50	50	50	50	50	50	50	25	25
25	25	50	50	50	50	50	50	50	50	25	25
25	25	25	50	50	50	50	25	25	50	25	25
25	25	25	50	50	50	50	25	25	50	25	25
25	25	50	75	100	125	125	125	125	125	25	25
25	25	50	75	100	125	125	125	125	125	25	25
25	25	50	50	30	25	25	30	50	50	25	25
25	25	50	50	30	25	25	30	50	50	25	25
25	25	25	25	25	25	25	25	25	25	25	25
25	25	25	25	25	25	25	25	25	25	25	25

(b) feature pitch map (μm)

Figure 7.34: Pattern for simulations emulating the results of Kehagias *et al.* Feature pitches and cavity densities are shown for each region of the stamp.

Using the hierarchical simulation approach developed in Section 7.6, this imprinting process was simulated, and results were compared with Kehagias's experiments and their own reported simulations.

The viscosity of 10^4 Pa.s reportedly used by Kehagias *et al.* for their simulations seems rather low; they claim to have fit this quantity to make their simulation match experimental results, but according to a viscosity–temperature curve reported by Romero *et al.*, the viscosity of 75 kg/mol PMMA at 190 °C is approximately 2×10^5 Pa.s [226]. We use this latter value and obtain reasonably realistic results. Moreover, Kehagias uses a value of 100 GPa for the Young's modulus of silicon, and a Poisson's ratio of 0.2; more realistic values are 120–160 GPa for Young's modulus and 0.27 for Poisson's ratio. E = 120 GPa and ν = 0.2 are used in our simulation here.

In Figure 7.35a is shown an optical micrograph of part of one of the samples imprinted by Kehagias. The darker regions of the micrograph correspond to thicker residual-layer regions. In the upper corners of the micrograph, in the vicinity of the narrowest features on the second and third visible rows, and between the two lower rows of large features, there is evidence of defects in which stamp cavities have not completely been filled with resist. Superimposed on the micrograph is a contour map of Kehagias's simulated elastic deflections of the stamp plus those of the silicon substrate. Figure 7.35b, meanwhile, shows a simulation of stamp-plus-substrate deflections made using the method of this thesis. The distribution and magnitudes of stamp deflections simulated using our method agree broadly with those of Kehagias: stamp deflections are largest in the regions of low cavity-opening density. The prediction of our method does, however, show a rather sharper falling-off of the magnitude of stamp deflections outside of these areas.

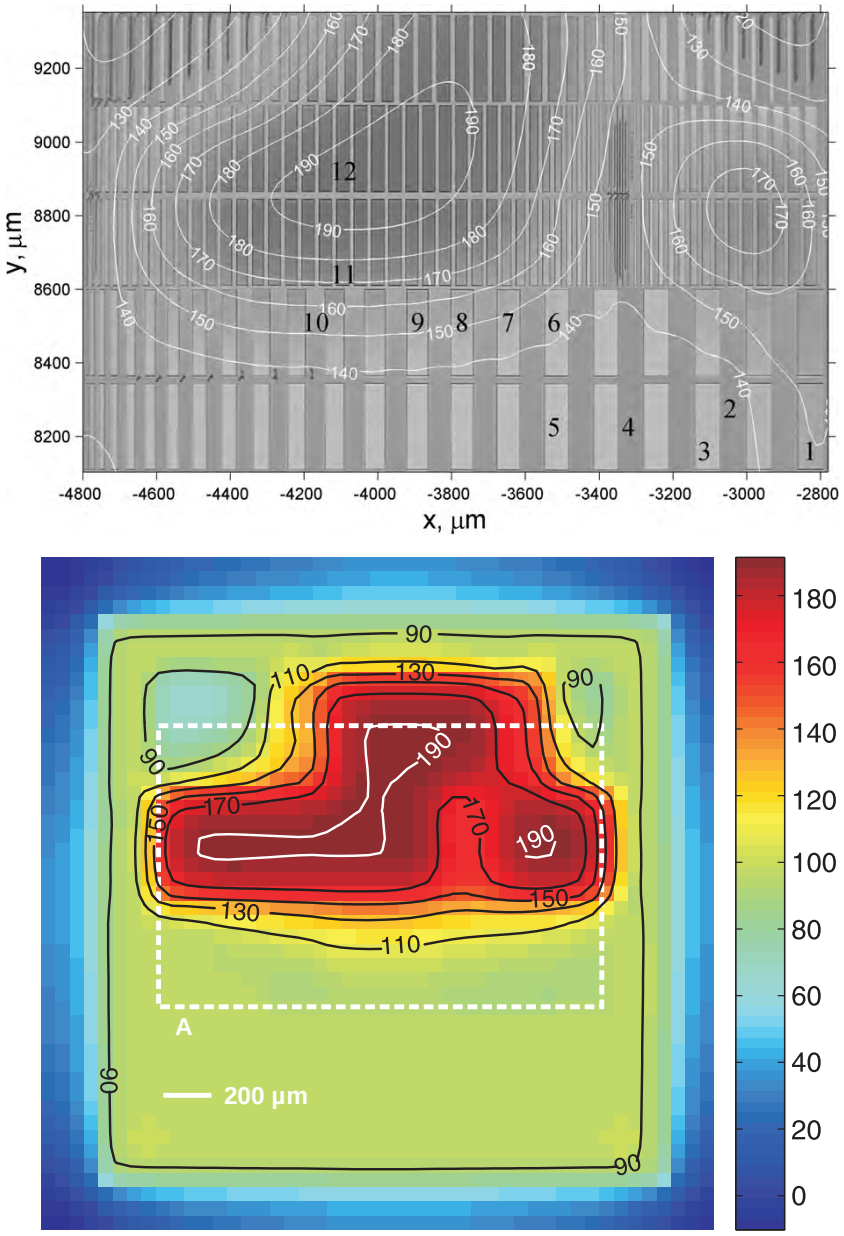

(a)

Optical micrograph of imprinted pattern

Reproduced from Kehagias

Kehagias's simulated stamp + substrate deflections (nm) are superimposed.

(b)

Simulated stamp + substrate deflections (nm) using the method of this thesis.

Region A corresponds to field-of-view of **(a).**

Figure 7.35: Comparison of (a) the experimental results of Kehagias *et al.* with (b) a hierarchical simulation using the method presented in this thesis. In (a), contours of the sum of simulated stamp and substrate deflections are superimposed on an optical micrograph of an imprinted sample of 75K PMMA. In (b), simulated values of the sum of stamp and substrate deflections are plotted.

In Figure 7.36a–b, meanwhile, experimentally measured values of residual layer thickness are compared with Kehagias's simulated values and with the values given by our simulation method. In the region of higher residual layer thickness (points 10 and 12 in Figure 7.36b), our method overestimates the residual thickness by 10–15%. Figure 7.36c shows a simulation made, using our method, of the proportions of cavity volume that are filled with resist at the end of the imprinting cycle. The simulation does manage to identify the upper corners of the pattern as being those in which filling is least complete. Meanwhile, Figure 7.36c shows the final solution for stamp–resist contact pressure distribution. Figure

7.36d is a map of the final values of $w_{die}[m, n]$, indicating the extent to which resist material has been transferred laterally between patterned regions instead of simply being forced into local pattern cavities. The value of $w_{die}[m, n]$ is positive in a particular location when material has, on average, been driven away from that location, and we see that in the region of the stamp with low cavity-opening densities and a correspondingly large residual layer thickness, the amount of lateral displacement of resist material is at its greatest.

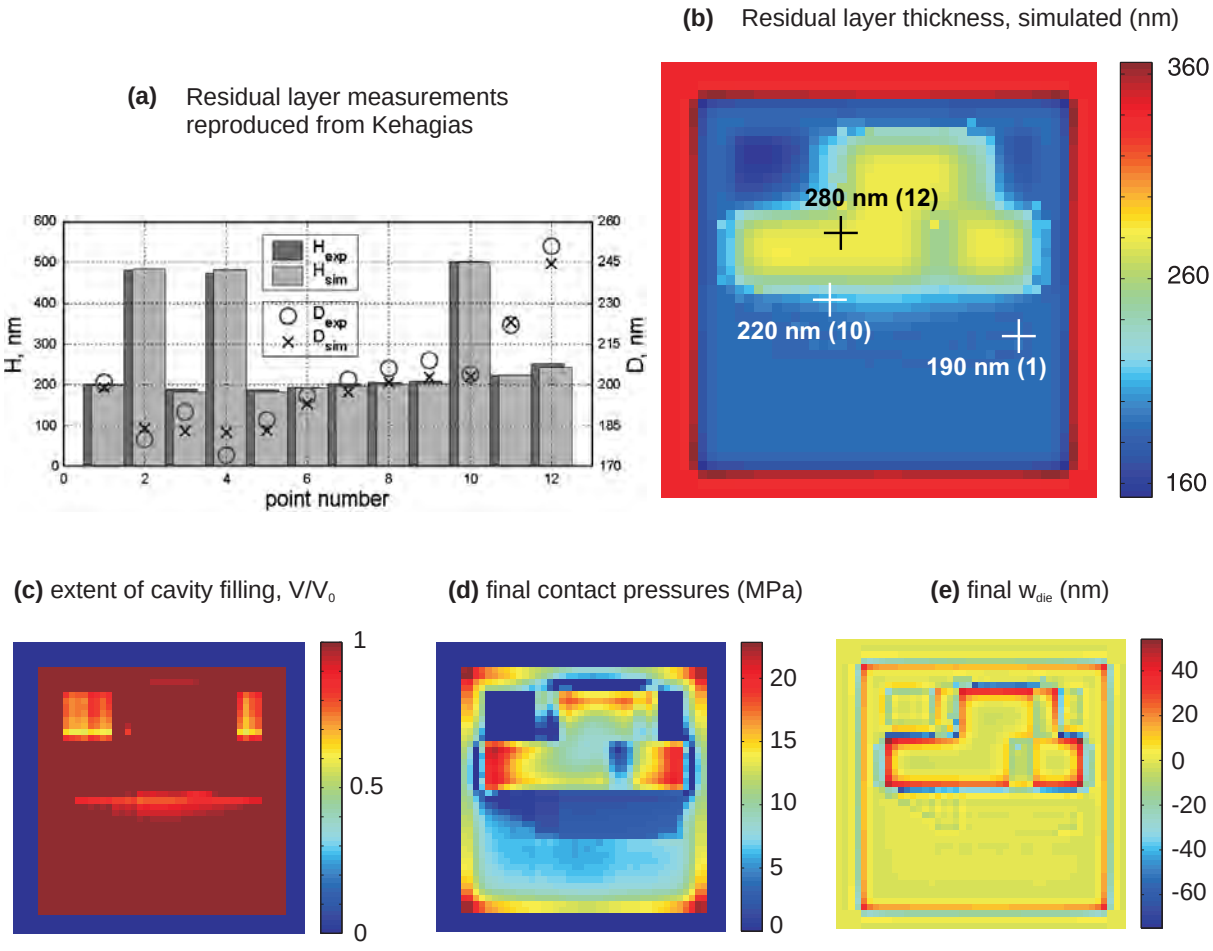

Figure 7.36: Further comparison of the modeling method presented in this thesis with the results of Kehagias. Plot (a) is reproduced from Kehagias: D_{exp} and D_{sim} are experimentally measured and simulated values of the residual layer thickness of resist at the twelve numbered locations marked in Figure 7.35a. In (b), a map is shown of residual layer thicknesses simulated using the method of this thesis. Simulated residual layer thicknesses at three locations are plotted together with the location number corresponding to pane (a). In (c), the simulated proportion of cavity volume filled is mapped. The contact pressure distribution simulated for the end of the five-minute loading cycle is shown in (d). The net intra-die displacement of material at the end of the imprinting cycle is mapped in (e).

As an input to our simulation, the stamp was described with a 12 × 12 array of regions (Figure 7.34), the outer ring of regions corresponding to a rebate on the stamp that was not in contact with the resist. In the simulation that we performed, each of these 144 regions was split into 4 × 4 sub-regions, so that the matrix actually used for solution was 48 × 48 in size. The number of steps U initially allowed for the simulation was 1000, but because the step-size was allowed to vary dynamically, the actual number of

steps required was only 19 and the simulation completed in 48 s. It is not clear how finely Kehagias discretized their simulation region, nor how long their simulation took to run, but based on another of their publications [185], it appears that their simulation times are on the order of 20 minutes for a simulation region discretized on a 128 × 128 matrix.

7.9.2. Demonstration in hierarchical mode: prediction for a feature-rich test pattern

We now demonstrate that our hierarchical mode of nanoimprint simulation can readily be used in conjunction with the feature-rich test pattern that was introduced in Chapter 2. Although we do not yet have experimental results with which to corroborate these simulations, the simulations illustrated do at least provide an indication of the magnitudes of simulation times that can be expected, and of the fact that simulations performed at different levels of spatial discretization produce self-consistent results.

Figure 7.37a shows the test-pattern that has been simulated. It is modeled as being etched to a relief of 200 nm into silicon, and is assumed to be spatially periodic in both directions of the plane of the stamp. The pattern is scaled to have a period of 3.2 mm in both directions. The resist layer that is simulated is initially 270 nm thick on a silicon substrate and is assumed to have a viscosity of 3.3×10^6 Pa.s during imprinting. Simulations have been performed at two levels of discretization: at one level, each homogeneous patch of features is represented by only one matrix element, and at the other level each patch is split into an 8 × 8 sub-matrix such that the simulated region is a 64 × 64 matrix. Figure 7.37b–e show that the simulated values of residual layer thickness, final contact pressure, and proportion of cavity volume filled are consistent between the two levels of discretization: the finer level simply provides more detail.

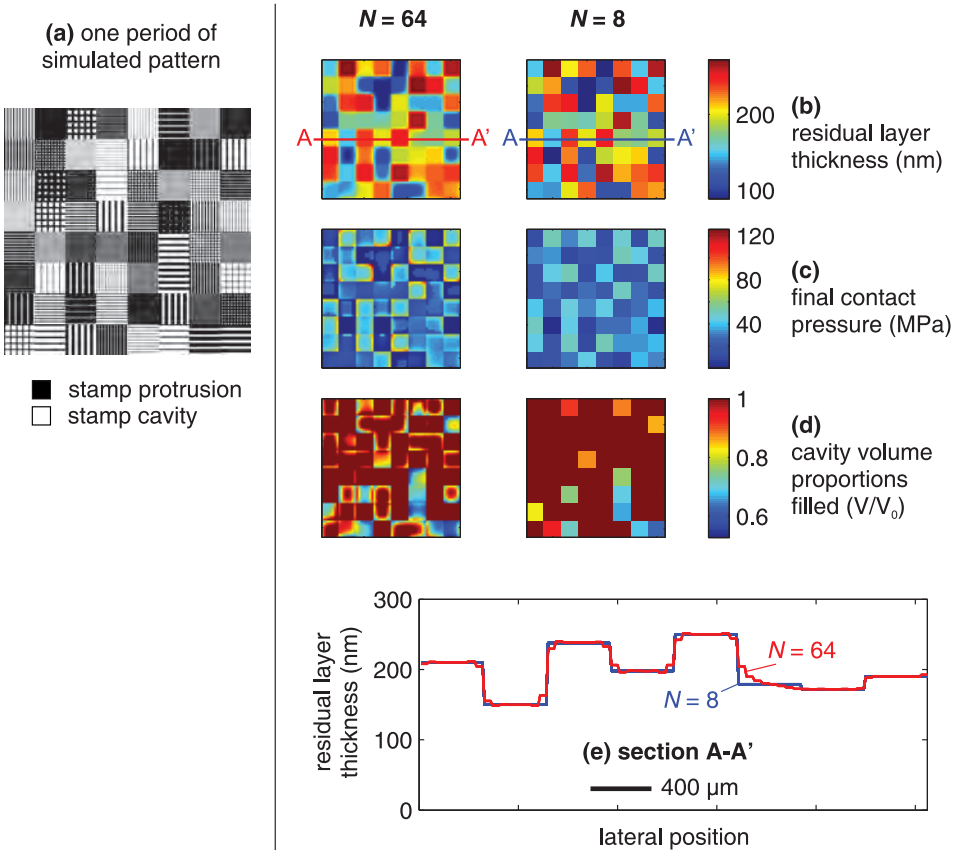

Figure 7.37: Prediction of a hierarchical simulation for NIL performed with the same feature-rich test pattern used in the bulk embossing work of Chapter 2. For *N* = 64, simulation was completed in 17 s and for *N* = 8, simulation took 8 s.

7.10. Computing stamp deflections when cavities fill quickly with resist

In some imprint cases, the viscosity of the resist upon application of the stamp is sufficiently low that all stamp cavities are readily filled during the loading cycle. In these cases, it may be safe to begin with the assumption that every part of the stamp is in contact with resist material and to proceed from there with a solution for the deflections of the stamp and substrate. When this assumption is possible, we can avoid the simulation time that would have been taken in the method of Section 7.6 to estimate the size and shape of the contact region.

In cases where the cavities of the stamp are completely filled with polymer, and assuming that the resist material is a viscous incompressible fluid (which is to be expected if the resist is able to fill the stamp quickly), the only net motion of stamp towards substrate will be that associated with global squeezing of resist towards the edges of the wafer. Within a small, die-sized region of the stamp or wafer, we could characterize the velocity of the stamp as being infinitesimally small and uniform across the region.

Our current simulation methods implicitly assume any modeled pattern to be both periodic and infinite in lateral extent, and it is impossible within this framework for there to be a non-zero steady-state uniform velocity of the stamp when all cavities are filled and the resist is incompressible: net lateral transport of material into or out of the simulation region is inconsistent with its boundary conditions. Yet we know this to be an imperfect representation of a wafer being imprinted: some small amount of material *can* be squeezed laterally from die to die, towards the edge of the wafer.

We therefore make the approximation of neglecting the very small global squeezing motion of the stamp and finding a quasi-steady-state pressure distribution that gives *zero* stamp velocity at every location within the simulation region.

In the 'flat' simulation approach described in the previous section, the contact pressure scaling factor k_{die} was introduced to capture the idea that, for a particular pressure applied to any given region of a resist layer, the region squeezes down more slowly the thinner it is. Where the lateral dimensions of the imprinted pattern are substantially larger than the layer thicknesses, it was proposed that k_{die} should be proportional to the cube of local thicknesses, reflecting the known properties of squeeze-film flow. The concept of k_{die} is also applied here in the filled-stamp case, the reason being that *just before* quasi-steady-state was achieved, there *was* the possibility of motion of the stamp and these squeezing rules would have applied. The following relation is considered to hold for step u of an iterative solution process:

$$(k_{die,u-1}[m,n]p_u[m,n]) * g_{die,u-1}[m,n] = \mathbf{0} \tag{7.59}$$

If the layer were uniform in thickness, k_{die} would be 1 everywhere and p_u would be uniform, whatever the shape and amplitude of g_{die}. Based on (7.59) alone, the magnitudes of $p_{\text{u}}[m, n]$ are indeterminate, but their spatial average is usually specified for any imprinting process.

If we have an estimate of the current residual layer thickness $r_{\text{u}-1}[m, n]$, we can directly estimate $k_{\text{die,u}-1}[m, n]$, and hence $p_{\text{u}}[m, n]$, which is expected to be inversely proportional to $k_{\text{die,u}-1}[m, n]$ and is subject to the constraint that its spatial average must equal the applied imprinting pressure. The deflections of the stamp and substrate can then be straightforwardly computed by convolving $p_{\text{u}}[m, n]$ with the elastic point-load response function of silicon. Based on stamp and substrate deflections, revised estimates of $r_{\text{u}}[m, n]$ and hence $k_{\text{die,u}}[m, n]$ can be made. The more iterations performed, the more accurate the simulation is expected to be.

The initial values of the resist layer thicknesses $r_1[m, n]$ are estimated by assuming the stamp to be undeformed but embedded in the resist such that the resist's initial volume is displaced to fill all stamp cavities.

It is important to note that is it not necessary to know the absolute viscosity of the resist to employ this method: merely the topography and elasticity of the stamp and substrate, the initial resist layer thickness, and the spatial average of $p[m, n]$.

This approach was used in an attempt to simulate the reported experimental results of Pedersen *et al.*, who used a silicon stamp to imprint simple patterns into mr-I 7030 resist [90]. Imprinting was performed at 140 °C under 0.65 MPa for 5 minutes. The relief of the stamp was 300 nm and the apparent initial polymer layer thicknesses approximately 360 nm. Pedersen *et al.* measured the residual layer thickness variation across the resist patterns after removal of the stamp. Their experimental results are reproduced in Figure 7.38.

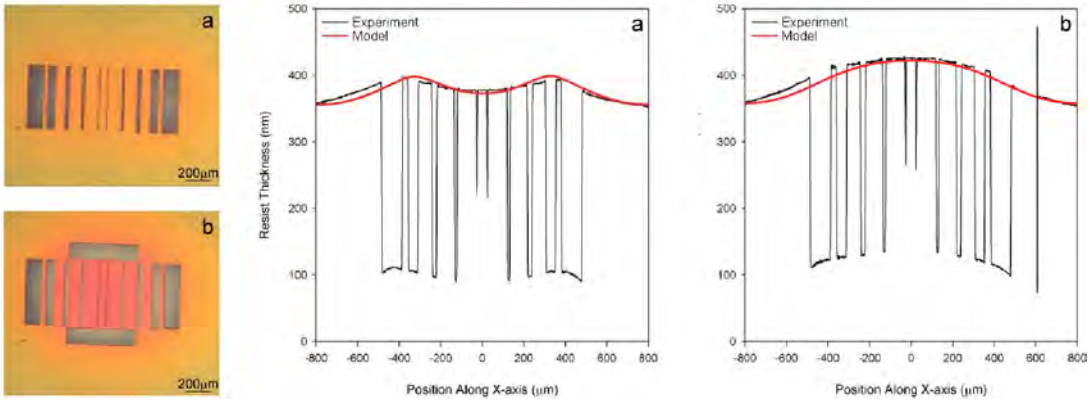

Figure 7.38: Optical micrographs (left) and center-line stylus profilometer scans of patterns imprinted by Pedersen *et al.* [90] into a ~360 nm-thick layer of mr-I 7030 resist at 140 °C under *c*. 0.65 MPa. Stamp cavities have apparently completely filled with resist and stamp deflections are evident in the final topographies of the resist. Pedersen's finite-element simulations of stamp deflection are shown as red lines on the cross-sections.

The reported imprinting temperature is well above the literature value of 60 °C for this particular resist's glass-transition temperature. There is no evidence in the reported results of elastic springback of the residual layer (even though the authors refer to it), so it seems appropriate to adopt a purely viscous model for this simulation. The zero-shear viscosity of mr-I 7000-series resists at 140 °C has been reported by its manufacturers to be 4×10^3 Pa.s [226]. This viscosity is about four orders of magnitude lower than that of the PMMA processed at 165 °C in the previous section, so it is reasonable that stamp cavities would be expected to fill comparatively quickly with this mr-I resist.

The lateral extent of the patterns shown in Pedersen's work is ~1.5 mm, and we assume that there were no stamp protrusions in the region surrounding them, so we choose to model a region that is 3 mm square and otherwise empty, with the expectation that the pattern periodicity implicit in our approach will then not substantially perturb results. For the silicon stamp and substrate, a Young's modulus of 130 GPa and a Poisson's ratio of 0.27 are assumed.

Our simulation of the imprinting of Pedersen's simple chirped grating is shown in Figure 7.39a: the shape and magnitude of stamp deformation have been modeled quite successfully using the known properties of the silicon stamp and substrate and the known applied average pressure.

In attempting to represent the imprinting of a modified grating with dummy features at the sides, the approach as described so far in this section is less successful. In Figure 7.39b (Approach 1), the results of the basic simulation method are shown: they do not fully capture the observed center-high 'bulge' of residual layer thickness (Figure 7.38b). In this experimental case, resist material in the central five stamp cavities is laterally enclosed on *all* four sides by stamp protrusions. It might therefore be appropriate to regard this material as being 'unavailable' for lateral flow. In that case, k_{die} in these regions should be set to the value consistent with a residual layer thickness that does not include this unavailable material: this concept is illustrated in Figure 7.40. The effect of this modeling change is to increase substantially the simulated contact pressure in the regions containing resist material that is 'unavailable' for flow. At each iteration step, any material 'unavailable' for flow does of course continue to contribute to the total volume of resist under the stamp.

Making this change manually to the simulation approach, a stamp deflection profile is obtained that is much closer to that measured experimentally: Figure 7.39b (Approach 2). Ten iteration steps u were found to be ample to obtain a stable solution, and each of the simulations shown was computed within ~10 s using the equipment described earlier in this thesis. Because the contact set is full, there is no need to solve iteratively for a pressure distribution at each step u: the simulation simply consists of a series of forward convolutions followed by direct recomputation of k_{die} and r.

While no firm conclusions can be drawn by studying this single experimental sample, the example presented here suggests three things. Firstly, it is possible that when a resist material readily fills stamp cavities, stamp deflections and hence residual layer nonuniformity can be computed much more quickly than in cases where the contact region has to be predicted through simulation. Secondly, although Pedersen *et al.* interpret 'springback' of the resist layer itself as a cause of the residual layer thickness nonuniformity, our model indicates that stamp and substrate deflection alone can explain the profiles observed. Thirdly, in cases where the stamp cavities are completely filled, it may be necessary to distinguish between cavities that are completely laterally enclosed and those that are open on one or more sides.

This third observation, if correct, potentially creates the need for additional algorithms to detect fully laterally enclosed cavities in arbitrary patterns. Further experimentation will clearly be needed to establish how best to model filled-stamp cases.

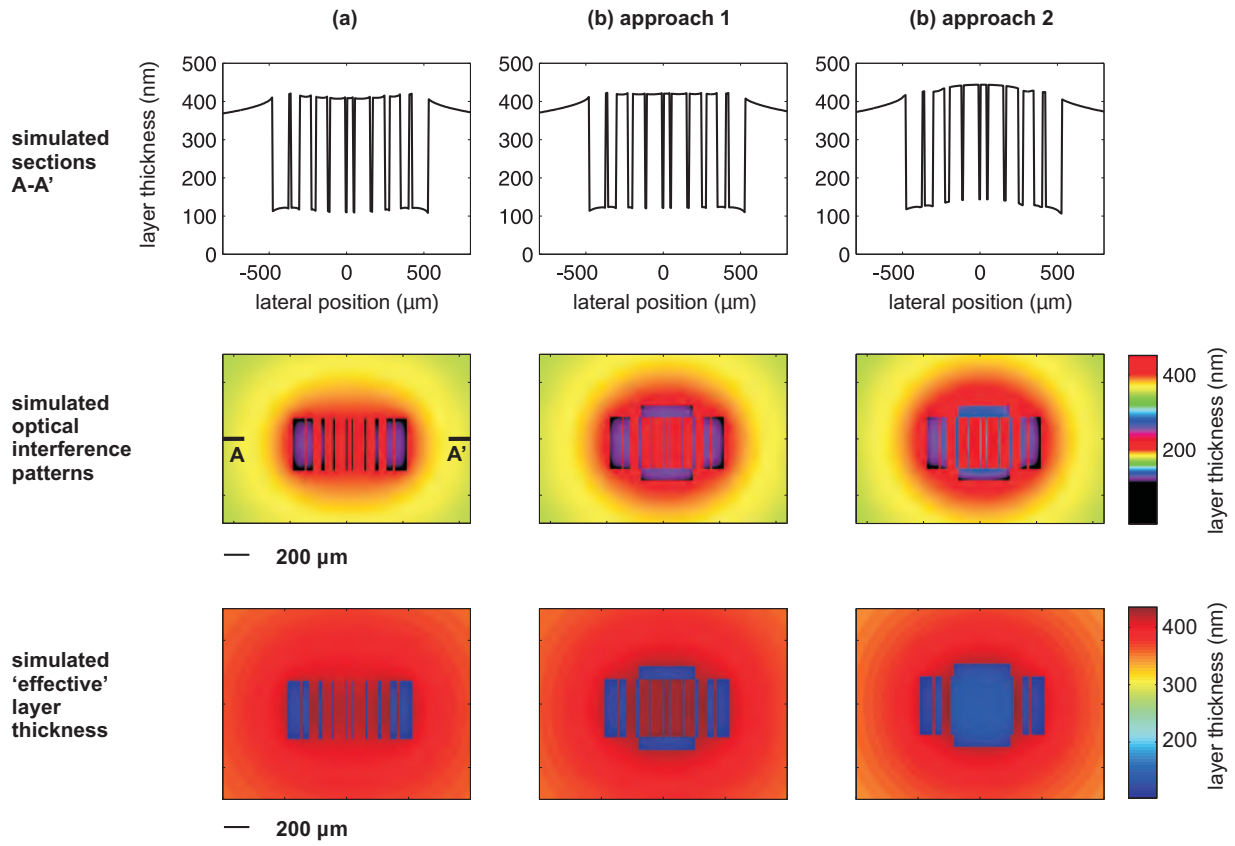

Figure 7.39: Results of our filled-cavity simulation applied to the geometries and experimental conditions of Pedersen *et al.* [90]. Simulated optical interference patterns were generated from the simulated residual layer maps using the conversion procedure detailed in Appendix B. The refractive index of the mr-I 7030 resist is taken to be 1.6 [244].

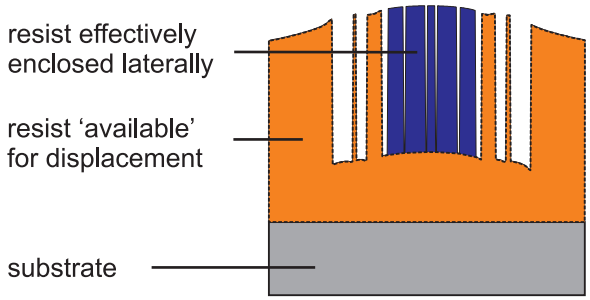

Figure 7.40: The concept of a region of laterally enclosed resist in a filled cavity or cavities. The geometry shown is that of Figure 7.39b, approach 2.

7.11. A refined approach to die-scale NIL simulation

The above analysis of Pedersen's experimental results indicated that when a layer of material being imprinted varies laterally in thickness, the pressure at a particular point in the layer depends not only on the local thickness but also on the extent to which that material is laterally constrained. For example, a particularly thick portion of a layer fully surrounded by much thinner portions will be rather harder to reduce in thickness by squeezing than will a region of that particular thickness surrounded by thicker regions.

In Section 7.6 a die-scale simulation approach was developed in which the quantity $k_{die}[m, n]$, linking local contact pressure to the resulting displacement of material away from point $[m, n]$, was defined as a function of the instantaneous layer thickness at point $[m, n]$ alone. For layers much thinner than the lateral pitch of the simulation grid, $k_{die}[m, n]$ was proposed to be proportional to the cube of the local layer thickness. If residual layer thickness changes very gradually with lateral position, this existing approach can be satisfactory, but in cases where stamp cavities and hence layer thicknesses exhibit step-changes in height (as in almost any feature-scale simulation) the existing approach implies step changes in local pressure and is not likely to produce realistic results. What is needed instead is a method that accounts for the degree of lateral confinement of each portion of an imprinted layer.

A simple way of accounting for the lateral confinement of material is suggested here. We present the idea in two-dimensional form although it is expected that the method could be readily extended to three dimensions. For comparison, Figure 7.41a shows the method that has been employed thus far: the mechanical impulse response function of a viscous imprinted layer effectively takes the form of a triplet, provided that the pitch of lateral discretization is much larger than the layer thickness. For the squeezing of an infinitely long strip of material between a rigid stamp protrusion and a rigid substrate, a parabolic pressure distribution is consistent with this kernel function and with theory. In Figure 7.41b, in contrast, we consider the case in which the same layer material is in contact with a rigid stamp protrusion having half the width of that in Figure 7.41a. The left-hand side of the layer material is prevented from moving leftwards by a 'sluice', attached to the stamp, that is imagined to mate with the substrate, forming a perfect seal. By symmetry, therefore, we expect the pressure distribution in this layer to be identical to that in one half of the layer illustrated in Figure 7.41a.

We now decompose the impulse response of the layer into two parts: one, $g_A[n]$, representing the displacement of material rightwards from the point of application of a load, and another, $g_B[n]$, representing leftwards displacement. Note that the sum of these sub-kernels equals the triplet kernel in Figure 7.41a. We also define two so-called 'masking' functions, $k_A[n]$ and $k_B[n]$, which describe any lateral constraints on rightwards and leftwards material displacement respectively. In this simple case, there are no constraints on rightwards material displacement, and $k_A[n]$ equals 1 everywhere, but there is a constraint preventing leftwards displacement of material from the leftmost region of the imprinted layer, and k_B consequently equals zero in that region and one elsewhere. We then find the pressure distribution $p[n]$ that is the solution to the following set of linear equations:

$$\frac{\mathrm{d}r[n]}{\mathrm{d}t} = g_A[n] * \left(k_A[n]p[n]\right) + g_B[n] * \left(k_B[n]p[n]\right) \tag{7.60}$$

where $r[n]$ is the topography of the upper surface of the imprinted layer, and the material is assumed to exhibit Newtonian viscosity. Additionally, $p[n]$ is constrained to be zero outside the region of stamp–layer contact. As shown in the figure, the pressure distribution found with this method is the half-parabola expected.

In cases where there are step changes in layer thickness rather than the complete blockage of lateral material flow, $k_A[n]$ and $k_B[n]$ could take values other than zero or one. We suggest the following rule for setting their values based on instantaneous layer thicknesses $r[n]$:

$$k_A[n] = \frac{\min\left(r[n]^3, r[n+1]^3\right)}{r_0^{\,3}}$$
$$k_B[n] = \frac{\min\left(r[n]^3, r[n-1]^3\right)}{r_0^{\,3}} \tag{7.61}$$

where r_0 is the average layer thickness across the simulation region and the amplitudes of $g_A[n]$ and $g_B[n]$ are computed for a layer of thickness r_0. This approach to calculating $k_A[n]$ and $k_B[n]$ was used to produce the pressure simulations that are illustrated in Figure 7.42. Figure 7.42(a) and (b) reiterate the cases illustrated in Figure 7.41; meanwhile (c) shows a case in which the 'sluice' at the left-hand side of the contact region has a finite opening height and is able to transmit some material. In (d) is illustrated a split-level stamp where simulations have been performed for a range of height ratios. Finally, (e) illustrates a case in which a stamp protrusion has had a taller cavity introduced at its center, and we see that as the height of the cavity increases, the pressure within that cavity approaches a uniform distribution.

As in previous sections, this simulation method would be performed iteratively, with small steps in layer thickness being computed along with evolution of the stamp–layer contact set. Validation of this method could be provided by comparing its predictions to those of full solutions of the Navier-Stokes equations for some test geometries. We anticipate that this method could be extended to three-dimensional simulation by employing four or eight sub-kernels, one corresponding to each topographical cell neighboring any given location.

In cases where the pitch of lateral discretization is comparable to or less than the layer thicknesses, the kernel is not able to be simplified to a triplet as it was in Figure 7.41a. It may however still be possible to use a modified form of this approach and to decompose an appropriate *non*-triplet kernel function into several directional sub-kernels.

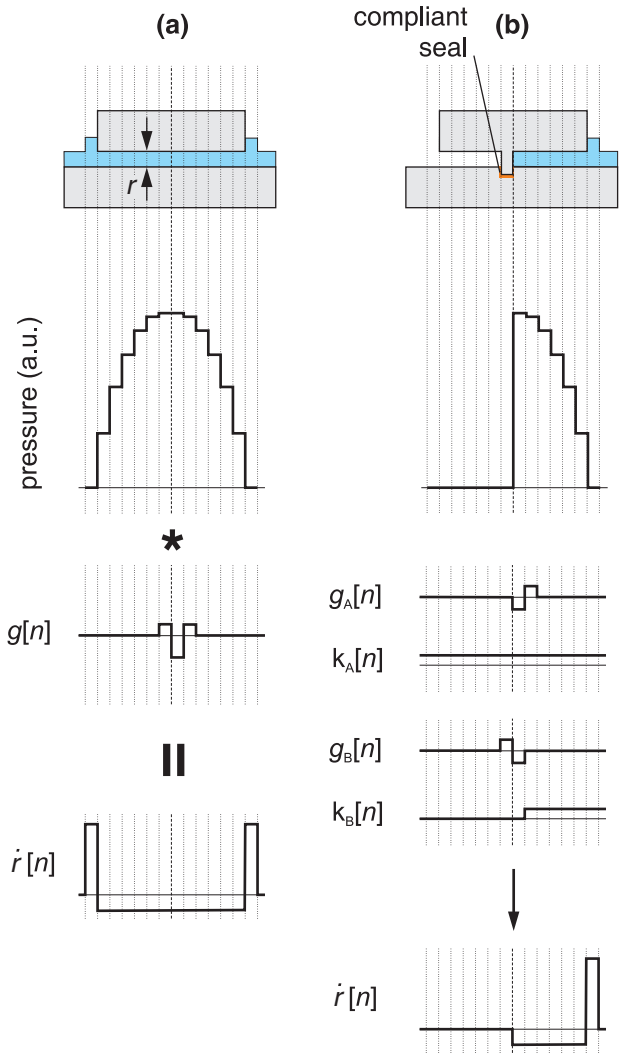

Figure 7.41: Generalizing the simulation of thin-layer squeezing for varying layer thicknesses and lateral constraints (1-D case). In (a), the kernel function linking pressure to local velocity for a viscous layer takes the form of a triplet and successfully represents unconstrained lateral squeezing. In (b), the kernel function is decomposed into two sub-kernels, and those, in concert with the 'masking' functions k_A and k_B, capture lateral constraints on flow. The geometry shown here is equivalent, by symmetry, to one side of the squeezed region illustrated in (a).

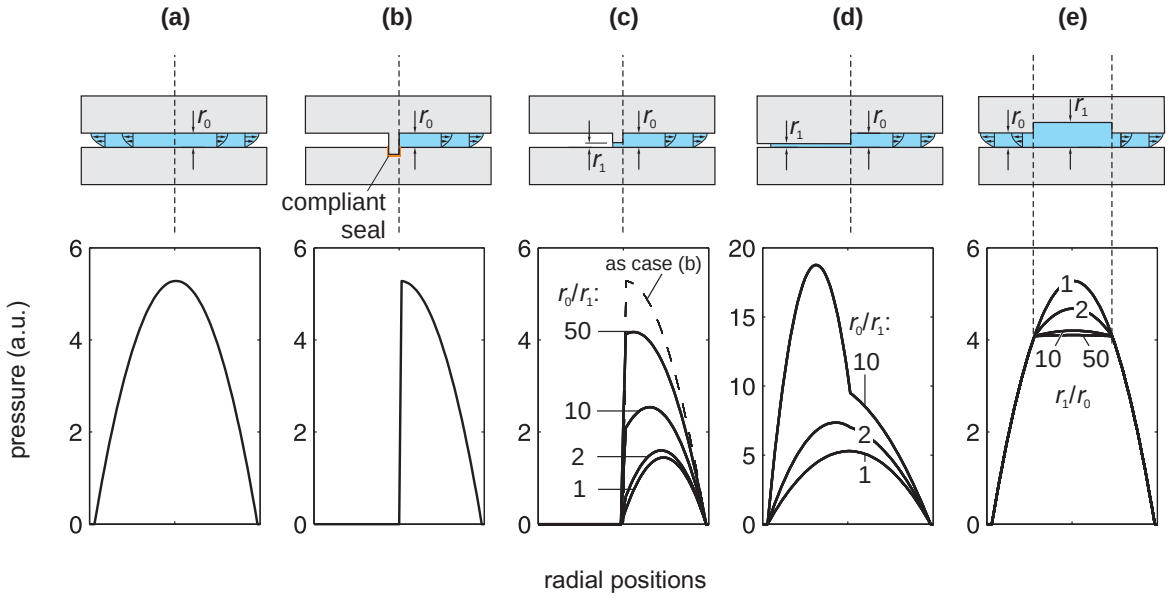

Figure 7.42: Examples of uses of the decomposed-kernel approach to simulate several one-dimensional geometries. Simulated instantaneous pressure distributions are plotted. (a) squeezing of an unconstrained uniform-thickness layer; (b) squeezing of a uniform-thickness layer constrained at one edge; (c) squeezing of a layer largely uniform in thickness, partially constrained at one edge where material can flow through a gap of varying height; (d) squeezing of a layer with two distinct thicknesses; (e) squeezing of a layer using a stamp with a tall internal cavity. Diagrams not to scale: in reality, all lateral dimensions are far larger than layer heights.

7.12. Exploiting stamp compliance as an imprint resolution-doubling technique

Most nanoimprint work reported in the literature is carried out either with glass or silicon stamps having Young's moduli ~ 100 GPa, or, in some cases, with polymeric stamps having Young's moduli of a few GPa. Here, however, we explore what happens when the stamp is made from an elastomer that is much softer than either of these commonly used types of materials. In short, what we have observed is that it is only near the edges of protrusions from elastomeric stamps that the resist layer is substantially deformed: we suggest that this behavior can be used to create features that are much smaller than any individual feature on the elastomeric stamp.

7.12.1. Experimental method

The test-pattern that was introduced in the previous chapter was transferred to an approximately one micron-thick layer of AZ5214 image-reversal resist that had been spun on to a 6" silicon wafer. The pattern consisted of a square array of copies of the pattern, and the array's pitch was 850 μm in both directions. The polarity of the pattern was such that the film of resist, when developed, contained a series of square holes and L-shaped trenches with diameters ranging from 10 to 100 μm. Sylgard 184 PDMS was then cast on to the patterned resist, cured for ~6 hours and peeled from the wafer, producing a soft elastomeric stamp with square and L-shaped protrusions.

This stamp was imprinted into a film of 950 kg/mol PMMA that had been spun on to silicon using the procedure described in Section 7.7.2. The imprinting was carried out at 160 °C, under 20 MPa sample-average pressure applied for 10 minutes. The sample was then cooled to ~90 °C before unloading.

7.12.2. Experimental results

Figure 7.43a shows an optical micrograph of part of the sample: the pink color of most of the image indicates that the resist is close to its original thickness everywhere except at the edges of the features. Figure 7.43c shows a cross-section through part of this pattern, obtained via white-light interferometry from a PDMS casting of the imprinted sample. The cross-section indicates that resist material has been 'punched down' near the edges of the stamp protrusion, and that this displaced material has formed small ridges adjacent to the imprinted lines.

7.12.3. Simulation

The observed behavior can be reasonably well captured by a simple simulation using the method of Section 7.6. The resist was assumed to be initially 260 nm thick and to have a viscosity during imprinting of 2×10^8 Pa.s; the stamp meanwhile was taken to be incompressible with a Young's modulus of 700 kPa, following PDMS measurements reported in the literature. The specification of this very soft stamp was found to introduce numerical difficulties such that the simulated resist profile became very rough if more than one simulation step was performed. The simulation result shown in Figure 7.43d is therefore the output of a single-step simulation in which the assumed thickness of the resist layer was its original 260 nm. The dual up–down topographical peaks near each step-change in stamp relief are fairly well captured by the simulation, although the peaks do appear a little sharper in the simulation results than in the experimentally measured topography.

7.12.4. Investigating the effect of layer thickness and stamp relief

The use of a soft stamp material therefore appears valuable as a way of creating very narrow features from a pattern with much larger features. Some simple simulations were performed to establish what factors determine the characteristic lateral dimension of the small features produced in this way.

Firstly, the relief and stiffness of the stamp were kept constant while the initial thickness of the resist layer was varied. The characteristic lateral dimension of the imprinted groove was in each case approximately two times the initial layer thickness.

Secondly, the relief height of the stamp was varied while the thickness of the resist layer was kept constant. In this series of simulations, the lateral dimension of the imprinted groove did not vary; the *depth* of the groove for a given applied pressure did however reduce with the stamp relief.

7.12.5. Summary

The use of a particularly soft stamp allows features to be imprinted with lateral dimensions that are comparable to the thickness of the imprinted layer, even if the features appearing on the stamp are far larger. This technique could, in fact, be used to produce imprinted patterns with *twice* the resolution available during the fabrication of the stamp: both *edges* of each stamp feature become discrete features in the resist.

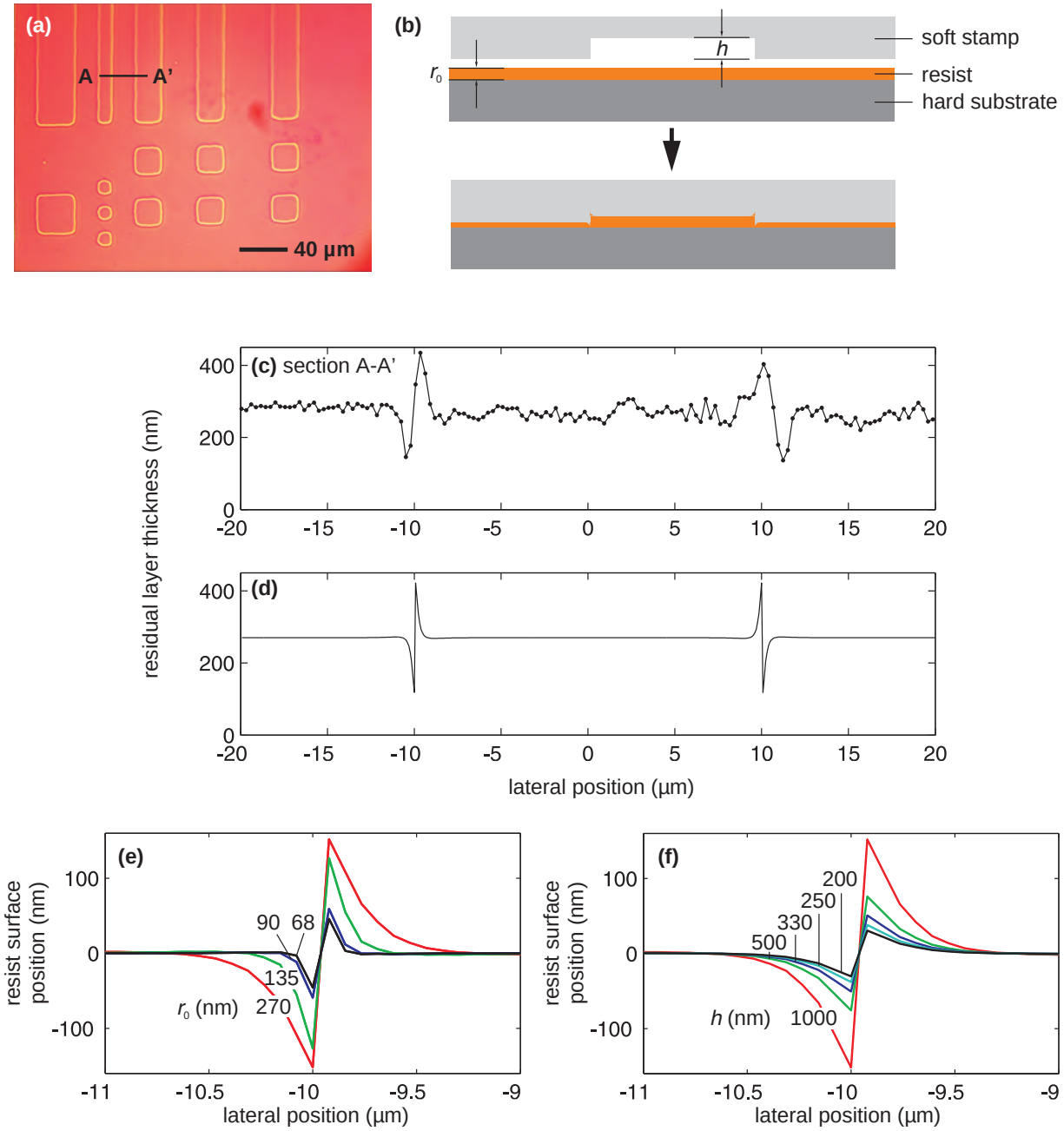

Figure 7.43: Using a soft imprint stamp to produce imprinted features with lateral dimensions much smaller than the features on the stamp. An experimental sample of 270 nm-thick 950k PMMA spun on to Si was imprinted at 160 °C under 10 MPa for 10 mins using a PDMS stamp of ~1 micron relief. An optical micrograph of part of the sample (a) shows that the resist was only imprinted near the edges of each feature. A schematic of the hypothesized stamp deformation mode is shown in (b). An interferometrically-obtained cross section through part of the sample is shown in (c). A corresponding simulated resist topography, assuming a resist viscosity of 2×10^8 Pa.s and a stamp stiffness of 700 kPa, is shown in (d). According to further simulations (e), the characteristic lateral dimension of a trench imprinted in this way is around 1–2 times the spun-on layer thickness. Reducing the relief-height of the stamp in simulations (f) appears not to reduce the lateral dimension of the imprinted feature but merely to reduce the depth of imprinting that is obtained.

7.13. Wafer-scale non-uniformity

The modeling approach so far presented has assumed that the stamp is patterned with an infinite array of identical die, and that there is no *net* transfer of material into or out of each die region. In reality, there may be wafer-scale nonuniformity of residual layer thickness, resulting either from initial waviness or bow of the stamp or the substrate, or from the radial flow of material towards the edges of the stamp.

Describing wafer-scale nonuniformity would require the addition of a new layer to the modeling hierarchy. The stamp might simply rest on top of the wafer to be imprinted [233], or alternatively could be clamped at its edges and held a small distance away from the wafer surface, making contact with the layer to be imprinted only when a hydrostatic pressure is applied to the backside of the stamp and it deforms [57, 239]. Both of these popular configurations would need to be considered when modeling wafer-scale nonuniformity.

7.14. Relaxing the assumption of resist incompressibility

Although an assumption of layer incompressibility is expected to be appropriate in most cases, it is important to consider how the model would change if the layer were in fact compressible.

The formulae of Nogi and Kato [188] were used in the previous chapter to obtain the discrete Fourier transform of the load-response function for a layer having a specified Poisson's ratio and thickness. The d.c. component of the Fourier transform is undefined in Nogi's and Kato's formulae, and since all previous modeling assumed the layer to be incompressible, this component was previously set to zero. If the layer is in fact compressible, we can readily find the appropriate non-zero value for the d.c. component by considering the case in which uniform pressure is applied to a layer of infinite lateral extent. For unit applied pressure, the amount of compression, Δ, of a layer of thickness r is given by:

$$\Delta = \frac{E_1 f_{Poi}(\nu)}{r} \tag{7.62}$$

where

$$f_{Poi}(\nu) = 1 - \frac{2\nu^2(1+\nu)}{1-\nu^2}. \tag{7.63}$$

For incompressible layers, $f_{Poi} = 0$. In all cases, the above relation assumes that the underlying substrate is stiff. The point load-response function of a compressible layer on a stiff substrate can therefore be found by substituting the layer's stiffness and Poisson's ratio into Nogi's and Kato's formulae, setting the d.c. component to zero as before, inverse-transforming the spectrum, and shifting every element of the resulting spatial function in the direction of application of the load by an amount

$$\frac{E_1 f_{Poi}(\nu)}{rMN} \tag{7.64}$$

where MN is the number of elements in matrix describing the function. In other words, this procedure corrects the d.c. component of the point load-response to allow for compressibility.

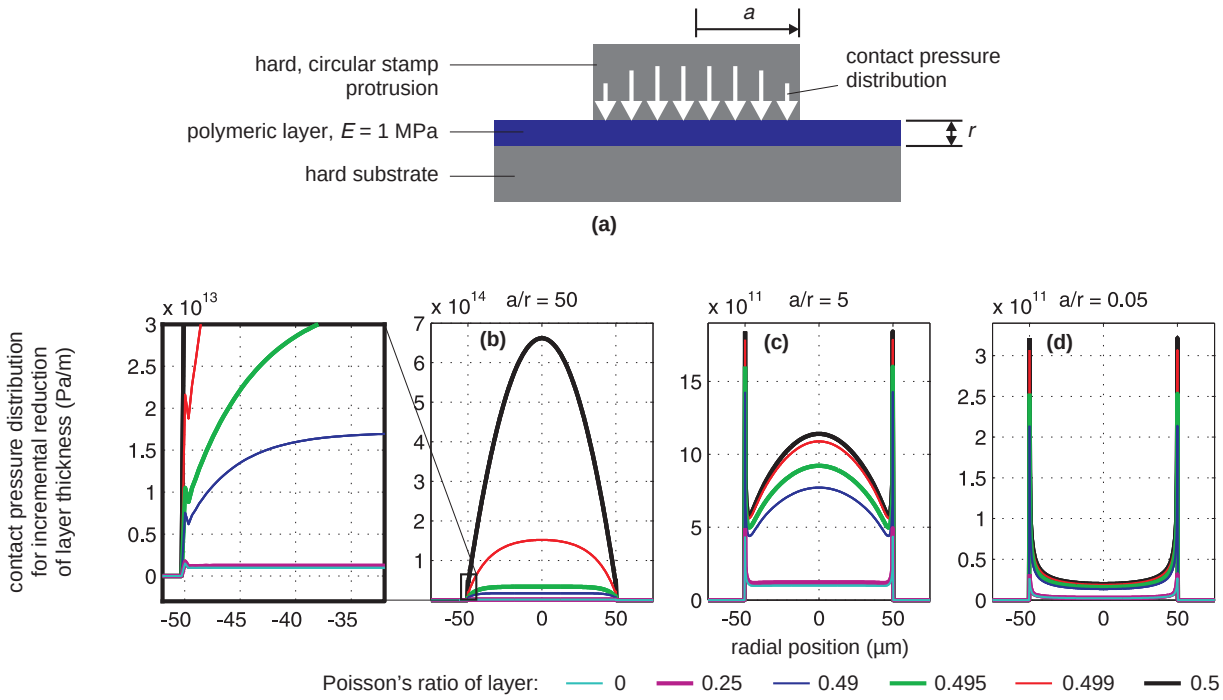

Figure 7.44: Illustration of contact pressure distributions for the imprinting of a circular punch of radius a = 50 μm into layers of varying a/r and varying Poisson's ratio. (a) r = 1 μm; (b) r = 10 μm; (c) r = 1 mm.

In the thin-layer limit, even a tiny amount of layer compressibility has a profound effect on the contact pressure distribution expected. For a Poisson's ratio of zero, the problem is essentially one of uniaxial compression in the contact region, with, as expected, a uniform simulated contact pressure of 10^{12} Pa/m for an incremental compression of a 1 μm layer having a Young's modulus of 1 MPa. What is more striking, though, is that the simulated contact pressure distribution for a Poisson's ratio of 0.499 is so different from that for a perfectly incompressible layer with a Poisson's ratio of 0.5.

As the layer thickness becomes a larger multiple of the diameter of the imprinted feature, the impact of introducing a very small deviation from perfect incompressibility diminishes. In all layer-thickness cases, however, the contact pressure distribution is noticeably flatter and with a lower spatial average by the time Poisson's ratio is reduced to 0.25 or lower.

It therefore appears to be crucially important to know the compressibility of the resist material being used. We do, however, remain comfortable in our assumption of an incompressible resist, because, when processed, resists are usually either liquids or rubbery solids. As we shall see, an incompressible resist model describes well our experimental results and those of some others.

To understand further the effect of layer compressibility, the scaled, differential pressure–compliance, $dp_{g,0}/\rho dr'$, was simulated as a function of r' for an array of parallel lines of infinite extent having ρ = 0.5. The simulation was performed for Poisson's ratio, ν, in the range 0 to 0.5. Figure 7.45 illustrates the marked dependence of $dp_{g,0}/\rho dr'$ upon ν. For an incompressible layer (ν = 0.5), we see the relationship described previously, whereby for thin layers the differential pressure–compliance is inversely proportional to the cube of the layer thickness and for thick layers the differential pressure–compliance is a pattern-dependent constant. At the other extreme, meanwhile, for ν = 0, we see a virtually uniaxial compression of the layer in which the differential pressure–compliance is inversely proportional to the layer thickness alone. For intermediate values of ν, we see behavior that is a combination of the two

extreme cases. For a sufficiently small layer thickness, a layer with finite compressibility will always tend towards an inverse relationship between differential pressure–compliance and layer thickness: the inverse-cube relationship of the incompressible case serves as an upper bound for the differential pressure–compliance.

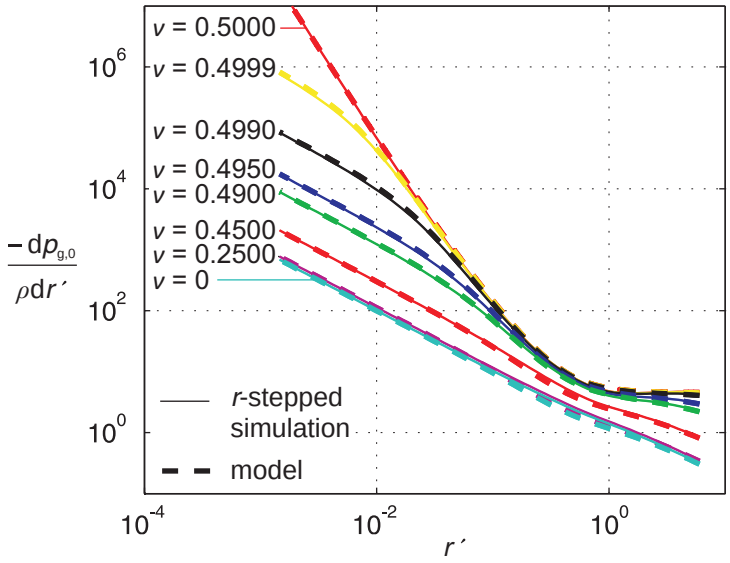

Figure 7.45: Illustration of how the relationship between $\mathrm{d}p_{g,0}/\rho\mathrm{d}r'$ and r' depends on Poisson's ratio of the imprinted layer. The geometry simulated here is an array of parallel lines, with ρ = 0.5.

It appears that it is possible to model the general case of finite-thickness compressible layers by modifying (7.7) as follows:

$$-\frac{\rho\,\mathrm{d}r'}{\mathrm{d}p_{g,0}} = \frac{1}{F_1(r')^{-3} + F_2(r')^{-2} + F_3} + \frac{f_{Poi}(\nu)r'}{1+\frac{1-\rho}{2\rho}\left[\tanh\left(2\log_{10}r'\right)+1\right]}. \tag{7.65}$$

This model is superimposed on Figure 7.45 using heavy dashed lines. Note that (7.65) expresses the *inverse* of the differential pressure–compliance required for unit reduction of thickness of the residual layer. The first term on the right-hand side corresponds to the incompressible-layer model of (7.7), and the second term reflects *compression* of the layer: for a differential increase in applied average pressure, the layer compression is proportional both to f_{Poi} and to r'. The denominator of this second term accounts for the fact that in very thin layers, it is only the material directly beneath the region of stamp–layer contact that is compressed, whereas for layers much thicker than the diameters of imprinted features, virtually the entire bulk of the layer is compressed, approximately uniaxially, with the pattern of the stamp not playing a large part in determining the amount of compression. The $\tanh(2\log_{10}r')$ function captures the transition between the thick- and thin-layer extreme cases.

What this analysis suggests is that introducing even a tiny amount of compressibility into a resist material could help to reduce the pressure–compliance that must be applied in order to obtain a given residual layer thickness. There may be scope to engineer resist materials — for example, by making them nanoporous in some way — that would possess a useful amount of compressibility while still performing their required function as an etch-mask or mechanical component.

These initial simulations also suggest that pattern-dependent variation of the local average of contact pressure during imprint is likely to be less severe for compressible resists. For example, Figure 7.46 shows a set of simulations that are variations of the case discussed in Section 7.7. In all cases, the layer is initially 260 nm thick and has a Newtonian viscosity of 5×10^7 Pa.s; it is imprinted with a silicon stamp under 40 MPa sample-average pressure for two minutes. The only factor changed among cases (a)–(d) of Figure 7.46 is Poisson's ratio of the layer. Simulation case (d), which assumes an incompressible resist, bears the closest resemblance to experimental results; meanwhile, reducing Poisson's ratio even to 0.499 makes the contact pressure distribution far more uniform. The corresponding average residual layer thickness reduces as Poisson's ratio reduces, but the absolute amount of thickness variation does not in fact reduce; in fact, residual layer thickness variation appears to *increase* as a proportion of average residual layer thickness as the layer becomes more compressible.

It appears that the deflections of the *stamp* are governing residual layer thickness variation in this particular simulation example, and making the *layer* compressible cannot, on its own, eliminate these stamp deflections. In any case, there is certainly great scope for further investigation of the relationships between layer compressibility and pattern dependencies.

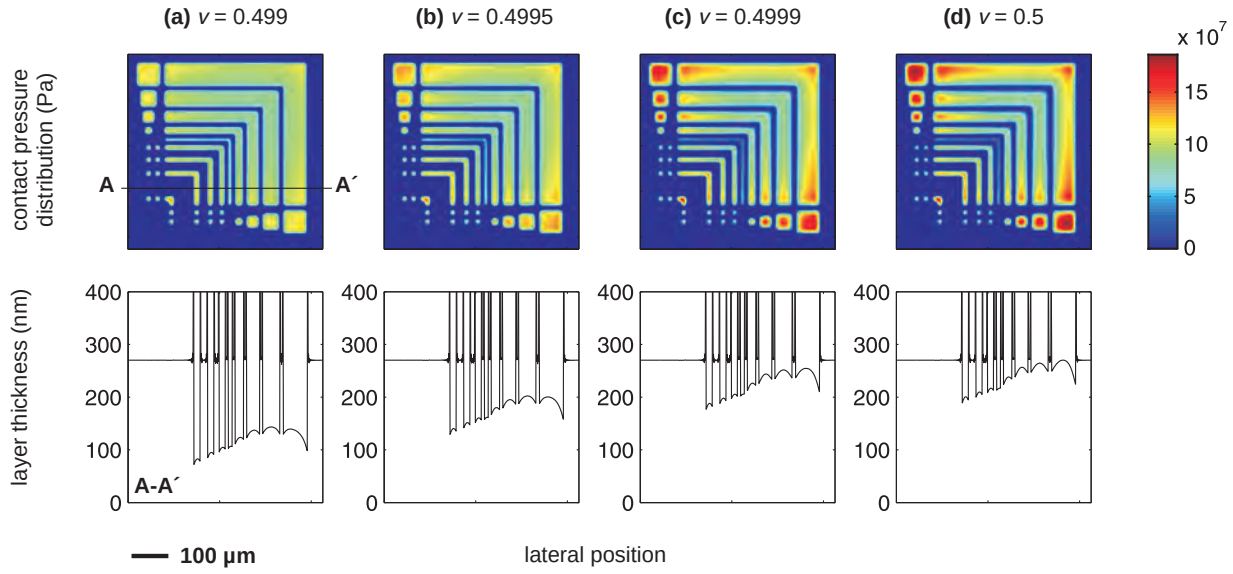

Figure 7.46: How the contact pressure distribution and associated resist topography for the sample of Figure 7.30 changes if Poisson's ratio of the layer is allowed to vary slightly but the elastic moduli of stamp and substrate and the viscosity of the layer remain fixed.

7.15. ‘Design rules’ for thermoplastic NIL

Users of NIL are usually trying to achieve one of two things. Either they want to use the imprinted resist as an etch-mask, or they are trying to pattern a layer that will constitute part of a finished device. An example of the latter aim would be the imprinting of a photonic device into a transparent polymeric layer. Whether the imprinted layer is temporarily or permanently present on the device, nanoimprint users typically seek both complete filling of stamp cavities and a thin and uniform residual layer. Moreover, there is usually a drive to minimize processing time.

7.15.1. What is an acceptable residual layer thickness and uniformity?

A perfect residual layer would usually be one with zero thickness across all imprinted features; yet such an effect is impossible to achieve in practice. Engineers need to establish how thick a residual layer can be tolerated, and how much variation of its thickness is acceptable.

If the imprinted resist is to be used as a mask for a reactive-ion etch, a residual layer prolongs the required etching time. Moreover, a residual layer must not be so thick that the parts of resist that are supposed to be serving as a mask are etched away before the pattern has been fully etched into the underlying material. Engineers therefore need to derive a specification for largest allowable residual layer thickness (RLT) based on the etch-resistance of the imprinted resist, the initial spun-on thickness of the resist, and any constraints on allowable etching time.

RLT *variation*, meanwhile, propagates to the critical dimensions (CDs) of the underlying etched features. Thinner regions of the residual layer will be ‘broken through’ by the etchant earlier than thicker regions. Therefore, material that resides underneath thinner initial residual layers will be exposed to etchants for a longer period, and any parasitic lateral etching of that feature will be more pronounced than in features that originally had thicker residual layers. For the makers of imprint machines, such as Molecular Imprints, it is a priority to characterize the mapping of RLT variation to etched CD variation. It would seem, then, that engineers will typically want to work backwards from the performance specifications of their device, through an understanding of the physics of any etching processes used, to arrive at a specification for the maximum acceptable RLT variation.

Another way of looking at the problem is that etch processes are themselves imperfect: there are usually feature-size, pattern-density, and wafer-scale dependencies of etch-rate. An objective in planning a sophisticated imprint process, then, might be to *compensate* for an imperfect etching process by deliberately varying RLT from die to die or even within a die. Engineers might therefore eventually need imprint simulation tools with the wafer-scale modeling capability alluded to in Section 7.13.

When the imprinted layer is to form a permanent part of a device, meanwhile, residual layers can still have deleterious effects. For example, imprinted polymeric waveguides would leak light into any surrounding residual material.

7.15.2. When are stamp cavities acceptably full with resist?

It is easy to say that stamp cavities should be ‘completely filled’ by an imprint process, but such a specification might be neither necessary nor optimal. For an imprinted etch-mask, what is really required is that the thicker parts of the resist are thick enough to survive the entire etching process. The masking portions do not necessarily need to be uniform in thickness. It can indeed be difficult — and time-consuming — to force a viscoelastic resist material right into the corners of stamp features. What must be avoided, though, are the widely documented ‘capillary bridging’ defects in which resist of a sufficiently low viscosity can arrange itself chaotically within incompletely filled cavities.

If imprinting time can be reduced without sacrificing the effectiveness of the imprinted etch mask, engineers will be keen to know how. On the other hand, complete cavity filling is likely to be very important when the imprinted layer is functional — for example, if it is a waveguide or photonic crystal.

7.15.3. Guidance on feature diameters

Having decided how large an RLT and how much variation of it they can accept, NIL engineers will want to design the stamp and the imprinting process to meet those specifications — usually with as little imprinting time as possible.

It was seen in the analysis of Section 7.4 — and is clear from the Scott equations [213] — that the 'difficulty' of imprinting an array of features into a thin film of resist is proportional to the *square* of the characteristic diameter, a, of stamp protrusions. This relationship assumes that the areal density of protrusions is fixed, and by 'difficulty', we mean the quantity $\mathrm{d}p_g/\mathrm{d}r$. Designers should therefore be aware that the required product of average imprinting pressure and loading duration is likely to scale as the average of the *squares* of stamp protrusion diameters. A sensible design rule would use knowledge of resist properties and imprint machine capabilities to place an upper limit on feature diameters. Designers could be required to insert 'relief' cavities into large protrusions to ease their imprinting.

7.15.4. Guidance on cavity volume density

Around the time when the cavities of a stamp first become completely filled, most material flow will have been local — over lengths of no more than a single feature diameter — and there will not have been time for much long-range transport of resist material over distances of many feature diameters. Assuming an incompressible resist, a good approximation to the residual layer thickness can therefore be obtained using just the initial layer thickness r_0 and the local cavity volume density of the stamp. In Figure 7.35 and Figure 7.36, we see that indeed the thicker residual layers correspond very closely to regions with low cavity volume densities.

Once cavities are filled, there is of course the possibility of longer-range flow of resist material to equalize residual layer thickness among regions of different cavity volume density. Whatever the viscosity of the resist, and whatever the pressure applied to the stamp, the time-scales over which this equalization can occur will be substantially longer than those involved in the initial filling — simply because the length scales for flow are so much longer.

Designers would therefore be well advised to distribute the volumes of cavities as uniformly as possible across the stamp. This aim might be achieved through the introduction of dummy cavities or protrusions. The more uniform the residual layer needs to be, the shorter the lateral length scale over which 'uniformity' of cavity volume density should be enforced. If the relief height, h, of the stamp is constant for all features, this design rule is equivalent to requiring the *areal* density of protrusions, ρ, to be uniform.

7.15.5. Guidance on the uniformity of $F_1 a^2 \rho$

As well as addressing RLT uniformity in cases where cavities are completely filled, it would be valuable to have a design rule for the case where stamp cavities are *not* going to be completely filled. In this situation, the resist layer is 'frozen' when the length-scales of material transport are still comparable to individual feature diameters, and achieving RLT uniformity relies on maintaining uniform *stamp* and *substrate* deflections. In Section 7.4, we derived relationships between $\mathrm{d}p_g/\rho\mathrm{d}r'$ and r', in which, for layers that are thin compared with the feature diameter, a:

$$\frac{\mathrm{d}p_g}{\mathrm{d}r} = F_1 a^2 \rho \cdot \tag{7.66}$$

From this relation, we observe that to keep the local average of stamp–layer contact pressure — and hence stamp/substrate deflections — uniform as r reduces, we require $F_1 a^2 \rho$ to be kept spatially uniform. As material begins to touch the tops of cavities, the validity of this design rule is likely to deteriorate, but it does at least provide some guidance.

7.15.6. Summary of rules

We have therefore outlined three possible design rules: (*i*) an upper limit on a, (*ii*) a requirement to keep ρ spatially uniform, and (*iii*) a requirement to keep $F_1 a^2 \rho$ spatially uniform. Rule (*i*) might in fact be better expressed as an upper limit on $F_1 a^2 \rho$, since sparse arrays of large features can in principle be imprinted as quickly as dense arrays of smaller ones if their values of $F_1 a^2 \rho$ are equal.

Rule (*ii*) is applicable when cavities will be completely filled; Rule (*iii*) should be enforced if cavities will remain incompletely filled. Rule (*ii*) is more constraining than Rule (*iii*); if it proves impossible to keep ρ sufficiently uniform in a design, engineers might consider the additional expense of varying cavity heights so that cavity volume density *can* be kept uniform. Such an approach is demonstrated by Hiroshima [245].

The rule of keeping $F_1 a^2 \rho$ uniform is correct only when the feature diameters are much larger than the layer thickness and a squeezing model of the residual layer is valid; in contrast, the guidance to make ρ (or cavity volume density) uniform holds for all patterns.

These rules are all designed with thermal NIL in mind, where the initial resist layer is usually of uniform thickness. Various other methods could however be used to circumvent the effects of pattern-density or feature-size inhomogeneities: for example, patterning the starting resist layer or varying its thickness. Cheng and Guo photolithographically pattern a starting resist layer relatively coarsely so that finer features can subsequently be introduced via nanoimprint [92]. Many pattern density difficulties are alleviated in step-and-flash imprint lithography, meanwhile, because liquid resist droplets are dispensed on to the wafer in an arrangement that can be tailored to almost any distribution of cavity volumes [246].

7.15.7. Process selection once pattern design is fixed

Once basic pattern design constraints have been satisfied as far as possible, processing parameters need to be selected. In general, the less viscous the resist the smaller the loads that are needed to imprint a given pattern in a reasonable time, and therefore the smaller the elastic deflections of the stamp will be during imprinting. In turn, the smaller RLT variation will be. Engineers could use the simulation tools proposed in this chapter to evaluate RLT variation for various sets of processing parameters.

7.16. Summary and outlook

In this chapter we have presented a set of approaches to simulating thermal nanoimprint lithography. Most of the work has assumed linear viscoelastic resist materials. Firstly a set of approximate functional relationships was obtained between applied pressure history, viscoelastic layer properties, and residual layer thickness, for three regular patterns. Secondly, possible modes of stamp and substrate deflections were analyzed. Thirdly, stamp-/substrate-deflection and layer-deformation models were integrated to produce a 'hierarchical' method for simulating the NIL of complex patterns.

These methods have been demonstrated in use, attempting to representing three sets of experimental results: (*i*) those reported by Kehagias *et al.*, (*ii*) those reported by Pedersen *et al.*, and (*iii*) those obtained at MIT using custom-designed test stamps. In the third case, substantial shear-thinning was observed and a modification of the simulation method was proposed as a way of capturing this non-linear material behavior.

The simulation method is fast to run and the resolution with which results are delivered can be arbitrarily specified. A simulation using a 64 × 64 matrix-representation of a pattern has been successfully completed in less than a minute. Outputs of the model are residual layer thickness, contact pressure distribution, and the proportions of cavity volumes filled.

It has been noted that the use of a particularly soft stamp material has the effect of producing imprinted 'grooves', located at the edges of stamp features and with a width comparable to that of the imprinted layer. This effect can be exploited to create small features in resist from much larger ones on a stamp.

Most of the work has assumed incompressible resist materials and experimental results suggest that this is a reasonable assumption. We have however briefly explored the effect of relaxing this assumption.

Step-and-flash imprint lithography is receiving growing interest and it would be valuable to extend this simulation capability for that process. To do so, two major modifications will be required: firstly, the incorporation of capillary forces, and secondly, the capability to model the squeezing and merging of discrete resist droplets below the stamp.

8. Conclusions

The purpose of this thesis has been to propose simulation methods that can enhance the benefits of using two manufacturing techniques: the micro-embossing of thermoplastic polymers, and nanoimprint lithography. While there has previously been much experimental work to understand and enhance embossing/imprinting processes, there has until now been no truly systematic way of representing and understanding pattern dependencies in either micro-embossing or nanoimprint. This thesis begins to meet that need.

In simulating micro-embossing, engineers need to know whether a stamp pattern they have designed will be faithfully replicated when pressed into a softened thermoplastic under a proposed set of conditions. What is needed is a prediction of whether every cavity on the stamp will be filled with polymer for a given embossing temperature, pressure and loading duration. The simulation method described in this thesis provides such a prediction. The embossed polymer is modeled as a Kelvin-Voigt viscoelastic material, and its behavior is linearized for the strain-rate range commonly encountered in hot embossing. The behavior of the embossed layer is further described using the displacement of its surface in response to a normally applied mechanical impulse in space and in time. We have shown that it is possible to represent the embossed polymer topography at the end of the embossing process by the convolution of this impulse response with the evolving stamp–polymer contact pressure distribution. We have also demonstrated that this topography can be calculated without resorting to a time-stepping simulation.

The simulation method has been calibrated for three widely used thermoplastics: PMMA, PC and a cyclic olefin polymer, Zeonor 1060R. The method has been shown to represent well the experimental data obtained from just above the materials' glass-transition temperatures up to 20–30 K above T_g. The model captures the cavity-penetration depths of the polymeric materials with an r.m.s. error of less than 2 μm for cavity heights ranging up to 20–30 μm. The method has been demonstrated for features whose peak cavity-penetration depths do not exceed their widths; for features with higher penetration-to-width ratios, strain stiffening of the material may become relevant and would present an additional modeling challenge that our linear material representation would not be able to meet on its own. Our continuum material model appears to represent experimental data well for cavities down to five microns in diameter; at much smaller feature-sizes comparable to polymer chain diameters, the model would be expected to break down.

Our material calibration procedure has highlighted some differences in behavior among the three materials tested. For example, PMMA exhibits much more distinct 'rubbery' behavior than the other two materials, such that at embossing temperatures of 130 °C or 140 °C, the loading duration has little influence on an embossed PMMA topography if it is longer than about a minute. We have shown that the practice of embossing a test-pattern into a polymeric material can be a time-efficient way of characterizing its properties. Although the full set of experiments reported in this thesis took about a day to perform for each material, we believe that the procedure could be reduced to around an hour's length by cutting the number of experiments performed and by making the test pattern easier to measure after embossing.

We have argued that our simulation approach produces solutions at least 10^3 times more quickly than could finite-element modeling of an equivalent pattern. Our method does not, of course, capture all the phenomena that a full finite-element simulation could, but our approach does appear to offer the possibility of being used iteratively during the design of devices that are to be hot-embossed.

We have proposed a simple way of abstractly representing feature-rich stamp patterns. The method relies on dividing the pattern into a relatively coarse grid of regions, and characterizing each region as having a particular feature shape, pitch, and areal density. Our simulation approach has successfully been

demonstrated using this abstracted representation. What is now needed is an automated way of abstracting patterns that do *not* fall neatly into a grid of homogenous regions of features. Any pattern abstraction routine must be sufficiently computationally inexpensive; otherwise the benefits of fast simulation could be lost.

In nanoimprint lithography, meanwhile, what is needed from simulation is not simply a prediction of whether stamp cavities will fill with polymer, but also an impression of the uniformity of thickness of the polymer's residual layer. We have proposed a way of simulating nanoimprint that provides both of these required model outputs. In this thesis we have chosen to focus on the kind of nanoimprint in which a uniform layer of thermoplastic polymeric resist is spun on to a hard substrate and then imprinted.

We have described a way of modeling the deflections of stamp and substrate that govern the amount of residual layer nonuniformity. We distinguish between a stamp's *bending* and its local *indentation*, offering insights for the selection of stamp materials and for the engineering of multi-layered stamps.

We have compared the outputs of our nanoimprint simulation approach with experimental data both reported in the literature and obtained at MIT. In the case of one literature report of a PMMA layer imprinted 80 K above T_g [89], our Newtonian resist model captures the measured trends in residual layer thickness, but with discrepancies as large at 15% in the absolute simulated thickness. Meanwhile, a Newtonian resist model was found to be *in*appropriate for representing the results we obtained when imprinting PMMA at only 55 K above T_g. In that case we have observed what appears to be substantial shear-thinning of the PMMA, and we have proposed a way of representing that non-linear material behavior in a modified simulation. This modified simulation approach offers realistic output under certain limited conditions, but remains numerically unstable and requires refinement.

Finally, we have proposed some simple layout 'design rules' that could assist device designers in minimizing residual layer thickness variation. The extent to which patterns can realistically conform to these rules — given the functional design constraints of most applications of imprint — needs further exploration.

The set of techniques described in this thesis forms a basis for a family of process-design and pattern-refinement software tools. In doing so, these modeling approaches could be the key to much broader industrial acceptance of hot micro-embossing and of nanoimprint lithography.

9. Future work

In the course of this thesis certain phenomena have been neglected and certain process variants ignored for the sake of simplicity. Here we explain several ways in which our simulation capabilities could be extended to make them decidedly more useful.

9.1. Improved pattern abstraction methods

The ‘hierarchical’ simulation techniques proposed in this thesis involve dividing a pattern into a coarse square grid of regions and characterizing each region with a particular feature shape, size, and areal density. The abstracted pattern representations shown in this thesis were constructed manually. For the approach to be truly useful to design engineers, the abstraction process needs to be automated.

Certain pattern regions might contain large arrays of two or more interspersed feature shapes or sizes. It would be helpful to have a way of describing such regions with an effective ‘average’ pattern shape, size and areal density.

Some patterns — particularly biomedical micro-/nano-fluidic devices — will not readily lend themselves to abstraction on a coarse square grid. Many real patterns will contain small areas rich in detail surrounded by large regions with almost no features. It will probably be worth investigating whether there are useful, more compact ways of describing such patterns — for example, ‘quad tree’ representations.

In semiconductor design, the transistor-level and lower metal layers are often constructed on a regular grid by synthesizing arrays of ‘cells’ taken from libraries of standard designs. The existing hierarchical approach might work rather well here: the pitch of the coarse grid would be chosen to correspond to the sizes of cells, and each cell would be pre-characterized with a cell-level imprint simulation so that its pressure–residual-layer-thickness behavior was known.

Any algorithms used to analyze and abstract complex patterns will of course need to be sufficiently fast to run that their use does not negate the benefits of fast embossing/imprinting simulation.

9.2. Improved material calibration methods

We suspect that much of the unmodeled sample-to-sample variation encountered during Chapter 2’s material calibration experiments results from our failure to control polymer temperature more tightly than ±1 K. As we attempt to make the calibration procedure more compact by reducing the number of experiments needed, it will become more important to control precisely the temperature of each experiment. Moreover, it is laborious to take measurements from the patchwork-like test-pattern of Chapter 2. A simpler, more compact pattern such as that introduced in Chapter 6 is promising, but could probably be improved upon in future, to incorporate a wider range of feature sizes.

9.3. Step-and-flash imprint modeling

There is a growing school of thought in the semiconductor industry that step-and-flash imprint is a far more promising option than thermal nanoimprint. The use of discrete droplets of low-viscosity resist

appears to make it much more straightforward to mitigate pattern dependencies and to achieve high processing throughput than is possible with the use of a spun-on layer of thermoplastic resist. It will therefore be valuable to extend our simulation methods to deal with SFIL.

9.3.1. Modeling of capillary forces

In current SFIL processes, capillary forces between stamp and resist do much of the work in pulling the stamp down on to the wafer, and they will need to be represented in any realistic simulation of the process.

Even in thermal NIL, there are circumstances under which it would be useful to be able to simulate the effects of surface tension of the imprinted polymer. At higher temperatures and lower molecular weights, chaotically arranged capillary bridges are regularly observed in the literature to form between the polymer layer and the tops of incompletely filled cavities. This observation belies the assumption, made in much thermal NIL simulation work, that surface forces are negligible. It would be helpful to model stamp–polymer contact angle as a function of stamp and polymer properties, and to be able to predict the occurrence of defects such as capillary bridges [247].

9.3.2. Droplet spreading and merging

A key step in current SFIL processing is planning the locations and volumes of liquid resist droplets that will be ink-jet printed on to the substrate before imprinting. As discussed in Chapter 7, gas may become trapped in cavities as droplets are squeezed beneath the stamp and the resist–gas interface of each droplet travels across the pattern. Moreover, gas may become trapped at the locations where droplets coalesce. It would be valuable to have a fast simulation method for predicting locations of trapped gas at the feature scale. To this end, the method proposed in Section 7.11 could be used as part of a time-stepped simulation.

It would also be beneficial to be able to predict gas trapping in *hierarchical* simulations. One could envisage tracking a droplet's edge as it spread out across a matrix of regions, with each region representing many features. The prediction of whether gas is likely to become trapped in a given region might be a function of the local stamp pattern and of the orientation of the pattern relative to the direction of propagation of the fluid front across it.

9.4. Cases where both temperature and pressure change during embossing

Throughout this thesis we have assumed that the elasticity and viscosity of any polymeric layer is constant throughout the loading cycle, being instantaneously increased at the very end of the loading duration to 'freeze' polymer deformation in place. This may not in fact be a realistic representation of many embossing processes, especially those in which cycle time is of the essence and the deformation that occurs during the polymer cooling period constitutes an important part of the polymer's total deformation.

It will be valuable therefore to be able to describe cases where the polymer's elasticity and viscosity change over time while under load. Here we suggest a way in which that could be done. We re-write the convolution integral that gives the embossed topography as:

$$w(x,y,t)=\frac{-\left(1-\nu^2\right)}{\pi}\int_0^t\int_{-\infty}^{\infty}\int_{-\infty}^{\infty}\frac{p(x',y',t')g(t',t)}{\sqrt{(x-x')^2+(y-y')^2}}\,\mathrm{d}x'\mathrm{d}y'\mathrm{d}t' \tag{9.1}$$

where $g(t',t)$ is the amplitude at time t of the response to a mechanical impulse applied at time t'. Expressions for $g(t',t)$ for several material models are proposed in Table 9.1. In this table, $E(t')$ is the polymer's elasticity as a function of time and $\eta_1(t')$ is its viscosity as a function of time.

Table 9.1: Time-varying impulse response functions for three polymer models.

Type of polymer model	$g(t',t)$
Purely elastic	$\frac{\delta(t'-t)}{E(t')}$
Newtonian liquid	$\frac{1}{\eta_1(t')}$
Kelvin-Voigt model	$\frac{1}{\eta_1(t')}\exp\left[-\int_{t'}^{t}\frac{dt''}{\tau(t'')}\right]$ where $\tau(t)=\frac{\eta_1(t)}{E(t)}$

We then define a new type of virtual pressure–compliance integral, $p_v(x, y, t_h)$, for time t_h at the end of the loading duration, as follows:

$$p_v(x,y,t_h)=\int_0^{t_h} p(x,y,t')g(t',t_h)\,dt'. \tag{9.2}$$

The spatial average, $p_{v,0}(t_h)$, of this pressure–compliance integral is then given as a function of the true time-course of the spatial average of applied pressure:

$$p_{v,0}(t_h)=\int_0^{t_h}\frac{1}{D^2}\int_0^D\int_0^D p(x,y,t')dxdy\,g(t',t_h)dt'=\int_0^{t_h} p_0(t')g(t',t_h)\,dt'. \tag{9.3}$$

The spatial average pressure–compliance integral $p_{v,0}$ can be computed numerically and swiftly before the simulation is performed, and the simulation itself is still a simple 'static' one assuming an elastic layer of unit modulus and an average applied pressure $p_{v,0}(t_h)$. The set of equations to be solved in this static simulation is then defined by:

$$w(x,y,t_h)=\frac{-(1-\nu^2)}{\pi}\int_{-\infty}^{\infty}\int_{-\infty}^{\infty}\frac{p_v(x,y,t_h)}{\sqrt{(x-x')^2+(y-y')^2}}dx'dy'. \tag{9.4}$$

We believe that this approach could be applied to simulate the embossing of thermoplastics, provided that the temperature of the polymer is known as a function of time, and that the polymer's elasticity and viscosity are known as functions of temperature. A similar approach could be taken for simulating UV-curing polymers, where the viscosity would increase over time during curing.

9.5. Modeling thermoplastic bonding

In Section 1.4 we discussed the importance of being able to bond micro-patterned thermoplastic layers while controlling the amount of distortion of the patterns at the bonded interface. A need to be able to simulate the amount of this distortion has been identified. That need has not been answered in this thesis, but offers a valuable avenue along which to extend the work. It appears that there are two key phenomena that will need to be considered in a bonding simulation. Firstly is the penetration of slightly softened thermoplastic material into cavities at the interface being bonded, driven by the applied bonding pressure.

Secondly (as described in Section 2.3.8) is the possible viscoelastic ‘recovery’ of any previously hot-embossed topography when exposed to elevated bonding temperatures.

9.6. Modeling roll-to-roll imprint

It has been mentioned throughout this thesis that roll-to-roll embossing and imprinting could have advantages when areas larger than a wafer need to be patterned (*e.g.* [5, 34, 248, 249]). Roll-to-roll imprint could, indeed, have advantages for *any* size of substrate because a roll-to-roll machine does not need to address the difficulties of applying an embossing pressure uniformly across a large contact area, as is the case when using planar stamps.

It is worth considering how our simulation approaches would need to be adapted for roll-to-roll imprint. One possible configuration is that of Figure 9.1a, in which a flexible thermoplastic film is heated with a flame, pressed between a solid patterned roller and a backing roller, and then cooled by a third roller. This is the configuration patented by Ulsh *et al.* [4]. There is a delay between the application of the imprinting load and the cooling of the polymer, during which it is conceivable that some shape recovery could occur. To simulate the behavior of the imprinted pattern, we would need a way of describing the case in which both temperature and applied average pressure change over time. Such a method is proposed above in Section 9.4. For the time being, we assume that the backing roller is compliant enough that the length of the region over which the thermoplastic film is loaded is many times the film thickness, and many times the characteristic diameter of imprinted features. Under these conditions we believe that the roll-to-roll imprinting case can be approximated as a *planar* embossing case in which we imagine the patterned roller being ‘unwrapped’ to form a planar stamp. The spatial average, $p_{v,0}(t_h)$, of the pressure–compliance integral for this approximate planar simulation would be as defined as in (9.3), where t_h would be the time at which cooling occurred, the pressure profile $p_0(t')$ would be that illustrated in Figure 9.1c, and viscosity and elasticity time-courses would be derived from the temperature–time profile $T(t')$ of Figure 9.1b. This approximation assumes that the combination of the polymer film and the backing roller is flexible enough that pattern interactions are relevant over only a small proportion of the contact region.

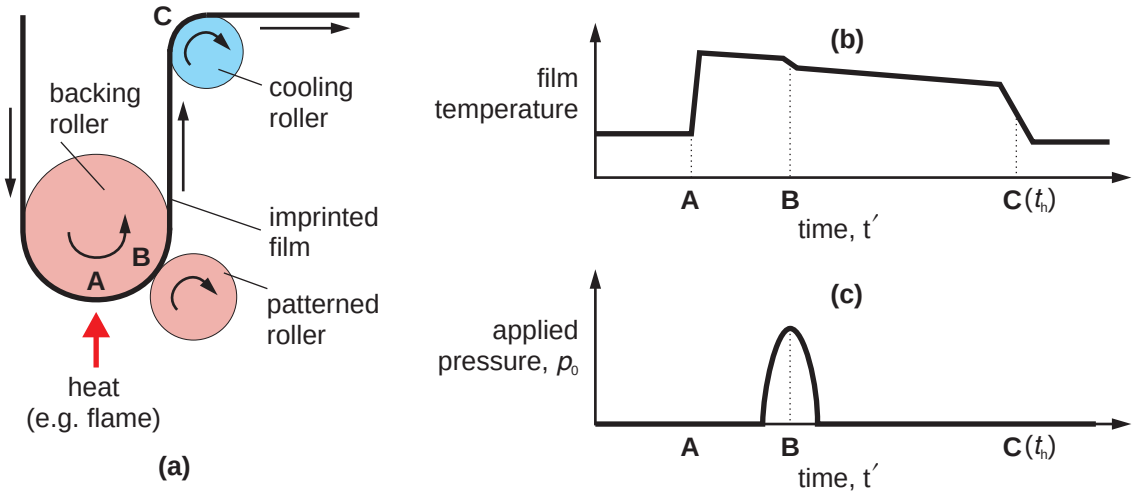

Figure 9.1: A possible roll-to-roll embossing/imprinting setup. (a) Diagram of system, after Ulsh [4]; (b) possible temperature–time profile; (c) possible pressure–time profile.

In cases where the contact region is of a length *comparable* to feature diameters, there may be additional phenomena to model. For example, Yeo *et al.* report a strong orientation dependence when patterning arrays of parallel lines with a roll-to-roll process: when the orientation of the lines is parallel to the direction of motion of the polymeric layer, the depth of penetration of polymer into stamp cavities is substantially smaller than when the trenches are perpendicular to the direction of travel [250]. We suggest that this orientation dependence may result from temperature gradients in the polymer at the scale of individual features. The use of an anisotropic material impulse response could offer a way to represent this behavior.

9.7. Modeling micro-contact printing

There has been wide adoption in recent years of micro-contact printing, in which an elastomeric stamp is used to transfer material to a harder substrate. The material transferred might be absorbed into the stamp before diffusing to form a self-assembled monolayer on desired regions of the hard substrate. Alternatively, the material could assemble as a monolayer on the stamp itself and then be transferred to the substrate directly upon contact. Finally, material could be deposited on to the stamp as a solid film (*e.g.* by sputtering) and then transferred to a substrate that preferentially adheres to the deposited film.

Whatever the details of material transfer, the effectiveness of transfer may depend on the magnitude and uniformity of stamp–substrate contact pressure. We expect that it would be fairly simple to use the elastic point-load response of a stamp to simulate the contact pressure distribution of arbitrary stamp patterns whose relief was small — *i.e.*, where the heights of stamp protrusions were much smaller than their widths. As well as simulating the contact pressure distribution, such an approach would be able to predict elastic stamp deflections and would alert micro-contact printing users to any regions of a pattern where the ‘roof’ of the stamp would make contact with the substrate.

For stamps with features that are taller than they are wide, there are additional deflections that would need to be modeled, including:

- Compression of individual features;
- Possible buckling of individual features;
- Stiction of adjacent features that can flex laterally and are close enough to touch.

Any of the above types of deflections could create defects in contact-printed patterns and it would be desirable to be able to predict their occurrence for arbitrarily patterned stamps. It would also be valuable to be able to compute, for a given pattern, the printing force that would need to be applied to ensure conformal contact of all stamp protrusions with a substrate of a given roughness.

Hui *et al.* [251] and Bietsch *et al.* [252] investigate analytically these modes of stamp failure; incorporating these analyses into a computationally inexpensive micro-contact printing simulator would appear to be fairly low-hanging fruit.

9.8. Modeling demolding forces and the probability of stamp damage

It has been discussed in this thesis that in hot micro-embossing the selection of a temperature–time profile must:

- allow the material to become soft enough to be deformed under a reasonable pressure;
- limit differential thermal contraction of the stamp and the polymer layer, so that excessive lateral clamping forces and consequent damage to the stamp are avoided.

We have presented a way of selecting processing parameters to meet the first of these requirements, but there is not yet a way of quantifying the risk of thermal-contraction damage for a given stamp design. It would be valuable to develop such a simulation capability. We expect that the capability would need to be built at the layer/stamp-scale, since the largest and most potentially damaging differential shrinkages occur at the edges of an embossed region. Any thermal contraction simulation would need to run at a comparable speed to that of the embossing simulation we have already demonstrated, because the design of an optimal embossing process would make use of both types of simulation concurrently.

9.9. Modeling the imprinting of additional materials

There are several additional types of materials whose embossing or imprinting it could be valuable to be able to simulate. In some cases, the functional properties of these materials change when strained, and these changes would most likely need to be modeled.

9.9.1. Semiconducting, conducting, and electroactive polymers

For micro- and nano-fluidic devices to reach greater levels of integration, it will be desirable to incorporate electrodes, actuators, and even semiconductor devices for controlling signals, sensing chemical concentrations, and emitting and sensing light. The use of conducting, semiconducting, and electroactive polymers could be attractive for these purposes, for the same reasons that *non*-functional polymers are valued for building the *bodies* of the devices: they are mechanically tough, often transparent, and can be processed in less energy-intensive ways that can silicon, ceramics, and metals.

It is conceivable that these new polymeric materials could be patterned by imprinting. An understanding of their viscoelastic properties as functions of temperature would certainly be useful. Moreover, it would be helpful to investigate whether the strains induced in a deposited layer by imprinting cause changes — either useful or parasitic — in their functional properties.

9.9.2. Sophisticated shape-memory polymers

It has been demonstrated that certain polymers can be ‘programmed’, through loading, to have two or three possible stable shapes; the material can then be caused to switch between these shapes by changing its temperature [253]. It would be interesting to study whether films of these materials could be programmed with micron-scale patterns by imprinting. An ability to do so might allow systems of valves, for example, to be constructed simply.

9.9.3. Metals and semiconductors

There have been reports of the imprinting of silver and gold nanostructures [254], and of silicon [255]. The nanoindentation properties of the relatively soft semiconducting alloy mercury cadmium telluride have also been studied [256], and it may be possible to pattern such films using nanoimprint.

9.9.4. Carbon nanotube forests

Forests of approximately millimeter-length, vertically-aligned, multi-wall carbon nanotubes are promising for use in microsystems — for example as electrodes or filters. We have already demonstrated the use of micron-scale, room-temperature embossing to transfer topographies to such forests [257]. The nanotube forests appear to deform by buckling beneath regions where contact is made with the stamp. At step-changes in embossed topographical height, defects are often observed whereby compressed regions of the forest appear to have 'torn' away from neighboring regions. Nanotube forests appear to be highly compressible films with a distinct compressive yield stress. Carefully instrumented imprinting experiments could be used to determine more precisely the yielding properties of nanotube forests, perhaps leading to a better understanding of their structure.

9.9.5. Biological tissues

Finally, the simulation methods of this thesis could also be used to model the time-dependent mechanical response of biological tissues — such as skin or intestinal lining. One might imagine the resulting models being used to design haptic computer interfaces or medical implants.

References

[1] D.C. Duffy, J.C. McDonald, O.J.A. Schueller, and G.M. Whitesides, "Rapid Prototyping of Microfluidic Systems in Poly(dimethylsiloxane)," *Analytical Chemistry*, vol. 70, 1998, pp. 4974-4984.

[2] C.K. Huang, "Polymeric nanofeatures of 100 nm using injection moulding for replication," *Journal of Micromechanics and Microengineering*, vol. 17, 2007, pp. 1518-26.

[3] A.V. Larsen, T. Makela, P. Majander, A. Ahopelto, and A. Kristensen, "Roll-to-roll thermal nanoimprinted microfluidic separation devices," in *Proc. Nanoimprint and Nanoprint Technology*, 2008.

[4] M.J. Ulsh, M.A. Strobel, D.F. Serino and J.T. Keller, "Embossed optical polymer films," U.S. Patent 6 096 247, 2000.

[5] H. Tan, A. Gilbertson, and S.Y. Chou, "Roller nanoimprint lithography," *42nd International Conference on Electron, Ion, and Photon Beam Technology and Nanofabrication*, Chicago, IL, 1998, pp. 3926-8.

[6] T. Nielsen, D. Nilsson, F. Bundgaard, P. Shi, P. Szabo, O. Geschke, and A. Kristensen, "Nanoimprint lithography in the cyclic olefin copolymer, Topas®, a highly ultraviolet-transparent and chemically resistant thermoplast," *Journal of Vacuum Science & Technology B (Microelectronics and Nanometer Structures)*, vol. 22, 2004, pp. 1770-5.

[7] J. Han, "Nanofluidics," in *Introduction to Nanoscale Science and Technology (Nanostructure Science and Technology)* M.D. Ventra, S. Evoy and J.E. Hughes Jr., Eds., Springer, 2004, pp. 632 ff.

[8] H. Wang and Y. Wang, "Flow in microchannels with rough walls: flow pattern and pressure drop," *Journal of Micromechanics and Microengineering*, vol. 17, 2007, pp. 586-96.

[9] B.Y. Tay, L. Liu, N.H. Loh, S.B. Tor, Y. Murakoshi, and R. Maeda, "Surface roughness of microstructured component fabricated by µMIM," *Materials Science & Engineering A (Structural Materials: Properties, Microstructure and Processing)*, vol. 396, 2005, pp. 311-19.

[10] L. Lin, Y. Cheng, and C. Chiu, "Comparative study of hot embossed micro structures fabricated by laboratory and commercial environments," *Microsystem Technologies*, vol. 4, 1998, pp. 113-116.

[11] M.B. Esch, S. Kapur, G. Irizarry, and V. Genova, "Influence of master fabrication techniques on the characteristics of embossed microfluidic channels," *Lab on a Chip*, vol. 3, 2003, pp. 121-7.

[12] N. Gadegaard, E. Martines, M.O. Riehle, K. Seunarine, and C.D.W. Wilkinson, "Applications of nano-patterning to tissue engineering," *Microelectronic Engineering*, vol. 83, Jan. 2006, pp. 1577-1581.

[13] P. Mela, A. van den Berg, Y. Fintschenko, E.B. Cummings, B.A. Simmons, and B.J. Kirby, "The zeta potential of cyclo-olefin polymer microchannels and its effects on insulative (electrodeless) dielectrophoresis particle trapping devices," *Electrophoresis*, vol. 26, 2005, pp. 1792-9.

[14] J. Eijkel, "Liquid slip in micro- and nanofluidics: recent research and its possible implications," *Lab on a chip*, vol. 7, Mar. 2007, pp. 299-301.

[15] J.K. Beattie, "The intrinsic charge on hydrophobic microfluidic substrates," *Lab on a chip*, vol. 6, Nov. 2006, pp. 1409-1411.

[16] A. Pozzato, S.D. Zilio, G. Fois, D. Vendramin, G. Mistura, M. Belotti, Y. Chen, and M. Natali, "Superhydrophobic surfaces fabricated by nanoimprint lithography," *Microelectronic Engineering*, vol. 83, Jan. 2006, pp. 884-888.

[17] N. Lee, S. Moon, S. Kang, and S.E. Ahn, "The Effect of Wettability of Nickel Mold Insert on the Surface Quality of Molded Microlenses," *Optical Review*, vol. 10, 2003, pp. 290-294.

[18] Y.C. Jung and B. Bhushan, "Contact angle, adhesion and friction properties of micro-and nanopatterned polymers for superhydrophobicity," *Nanotechnology*, vol. 17, 2006, pp. 4970-4980.

[19] A. Bhattacharyya and C.M. Klapperich, "Thermoplastic Microfluidic Device for On-Chip Purification of Nucleic Acids for Disposable Diagnostics," *Analytical Chemistry*, vol. 78, 2006, pp. 788-792.

[20] N. Vourdas, A. Tserepi, and E. Gogolides, "Nanotextured super-hydrophobic transparent poly(methyl methacrylate) surfaces using high-density plasma processing," *Nanotechnology*, vol. 18, 2007, 125304.

[21] R. Lin and M.A. Burns, "Surface-modified polyolefin microfluidic devices for liquid handling," *Journal of Micromechanics and Microengineering*, vol. 15, 2005, pp. 2156-2162.

[22] A.C. Henry, T.J. Tutt, M. Galloway, Y.Y. Davidson, C.S. McWhorter, S.A. Soper, and R.L. McCarley, "Surface Modification of Poly(methyl methacrylate) Used in the Fabrication of Microanalytical Devices," *Analytical Chemistry*, vol. 72, Nov. 2000, pp. 5331-5337.

[23] T.J. Johnson, D. Ross, M. Gaitan, and L.E. Locascio, "Laser modification of preformed polymer microchannels: Application to reduce band broadening around turns subject to electrokinetic flow," *Analytical Chemistry*, vol. 73, 2001, pp. 3656-3661.

[24] C.M. Klapperich, K. Komvopoulos, and L. Pruitt, "Plasma surface modification of medical-grade ultra-high molecular weight polyethylene for improved tribological properties," *Materials Research Society Symposium - Proceedings*, vol. 550, 1999, pp. 331-336.

[25] V. Piotter, T. Hanemann, R. Ruprecht, and J.E. Haußelt, "Injection molding and related techniques for fabrication of microstructures," *Microsystem Technologies*, vol. 3, 1997, pp. 129-133.

[26] Y. Tian, P. Zhang, G. Liu, and X. Tian, "The lifetime comparison of Ni and Ni-PTFE moulding inserts with high aspect-ratio structure," *Microsystem Technologies*, vol. 11, 2005, pp. 261-264.

[27] J.X. Gao, L.P. Yeo, M.B. Chan-Park, J.M. Miao, Y.H. Yan, J.B. Sun, Y.C. Lam, and C.Y. Yue, "Antistick postpassivation of high-aspect ratio silicon molds fabricated by deep-reactive ion etching," *J Microelectromech Sys*, vol. 15, 2006, pp. 84-93.

[28] M. Beck, M. Graczyk, I. Maximov, E. Sarwe, T.G.I. Ling, and L. Montelius, "Improving Nanoimprint Lithography Stamps for the 10 nm Features," in *Proc. IEEE-NANO*, 2001, pp. 17-22.

[29] P. Mao, "Fabrication and characterization of nanofluidic channels for studying molecular dynamics in confined environments," S.M. thesis, Massachusetts Institute of Technology, Cambridge, MA, 2005.

[30] W. Liao and S.L. Hsu, "A novel liquid thermal polymerization resist for nanoimprint lithography with low shrinkage and high flowability," *Nanotechnology*, vol. 18, 2007, 065303 (5pp).

[31] M.B. Chan-Park, Y.C. Lam, P. Laulia, and S.C. Joshi, "Simulation and investigation of factors affecting high aspect ratio UV embossing," *Langmuir*, vol. 21, 2005, pp. 2000-2007.

[32] J.X. Gao, M.B. Chan-Park, D.Z. Xie, Y.H. Yan, W.X. Zhou, B.K.A. Ngoi, and C.Y. Yue, "UV Embossing of Sub-micrometer Patterns on Biocompatible Polymeric Films Using a Focused Ion Beam Fabricated TiN Mold," *Chemistry of Materials*, vol. 16, Mar. 2004, pp. 956-958.

[33] P. Chu, “Avery Dennison Micro-Nano Replication Capabilities for MEMS and Microfluidics,” *International Conference on MEMS, Nano and Smart Systems*, 2005, p. 27.

[34] S. Seo, T. Kim, and H.H. Lee, “Simple fabrication of nanostructure by continuous rigiflex imprinting,” *Microelectronic Engineering*, vol. 84, Apr. 2007, pp. 567-572.

[35] Y. Mizukami, D. Rajniak, and M. Nishimura, “Integrated micro-electrophoretic chip fabricated using a new stereolithographic process,” *Proceedings of the IEEE Micro Electro Mechanical Systems (MEMS)*, 2000, pp. 751-756.

[36] A. Ostendorf and B.N. Chichkov, “Two-photon polymerization: A new approach to micromachining,” *Photonics Spectra*, vol. 40, 2006, pp. 72-80.

[37] M. Dirckx, H. Taylor and D. Hardt, “High-temperature de-molding for cycle time reduction in hot embossing,” in *Proc. Soc. Plastics Engineers Annual Technical Conf.*, 2007, pp. 2972–2976.

[38] M. Worgull, M. Heckele, and W.K. Schomburg, “Large-scale hot embossing,” *Microsystem Technologies*, vol. 12, 2005, pp. 110-115.

[39] Y. Guo, G. Liu, Y. Xiong, and Y. Tian, “Study of the demolding process—implications for thermal stress, adhesion and friction control,” *Journal of Micromechanics and Microengineering*, vol. 17, 2007, pp. 9-19.

[40] Y. Guo, G. Liu, X. Zhu, and Y. Tian, “Analysis of the demolding forces during hot embossing,” *Microsystem Technologies*, vol. 13, 2007, pp. 411-415.

[41] Y. Chen, J. Tao, X. Zhao, and Z. Cui, “Study of pattern placement error by thermal expansions in nanoimprint lithography,” *Journal of Microlithography, Microfabrication and Microsystems*, vol. 5, 2006, 011002.

[42] H.W. Ro, Y. Ding, H. Lee, D.R. Hines, R.L. Jones, E.K. Lin, A. Karim, W. Wu and C.L. Soles, “The role of stress in nanoimprint lithography,” in *Proc. Int. Soc. Opt. Eng.*: *Emerging Lithographic Technologies X*, 2006, 615116.

[43] T. Leveder, S. Landis, L. Davoust, S. Soulan and N. Chaix, “Demolding strategy to improve the hot embossing throughput,” in *Proc. Int. Soc. Opt. Eng.*, 2007, 65170N.

[44] T. Leveder, S. Landis, L. Davoust, and N. Chaix, “Optimization of demolding temperature for throughput improvement of nanoimprint lithography,” *Microelectronic Engineering*, vol. 84, 2007, pp. 953-957.

[45] D. Yao, P. Nagarajan, L. Li, and A.Y. Yi, “A strategy for rapid thermal cycling of molds in thermoplastic processing,” *Journal of Manufacturing Science and Engineering, Transactions of the ASME*, vol. 128, 2006, pp. 837-843.

[46] Interview with H. Becker, Apr. 2009.

[47] “International Technology Roadmap for Semiconductors.” Internet: http://www.itrs.net, [May 7, 2009].

[48] “Commercialization of nanoimprint lithography.” Internet: http://www.nilcom.org, [Aug. 5, 2007].

[49] “Emerging Nanopatterning Methods.” Internet: http://ec.europa.eu/research/fp6, [Aug. 5, 2007].

[50] C. Sotomayor Torres, S. Zankovych, J. Seekamp, A. Kam, C. Clavijo Cedeno, T. Hoffmann, J. Ahopelto, F. Reuther, K. Pfeiffer, G. Bleidiessel, G. Gruetzner, M. Maximov, and B. Heidari, “Nanoimprint lithography: An alternative nanofabrication approach,” *Materials Science and Engineering C*, vol. 23, 2003, pp. 23-31.

[51] T. Balla, S.M. Spearing, and A. Monk, “An assessment of the process capabilities of nanoimprint lithography,” *Journal of Physics D: Applied Physics*, vol. 41, 2008, 174001.

[52] L. Guo, “Nanoimprint Lithography: Methods and Material Requirements,” *Advanced Materials*, vol. 19, 2007, pp. 495-513.

[53] L.J. Guo, “Recent progress in nanoimprint technology and its applications,” *Journal of Physics D: Applied Physics*, vol. 37, 2004, pp. R123-R141.

[54] G.L.W. Cross, “The production of nanostructures by mechanical forming,” *Journal of Physics D: Applied Physics*, vol. 39, 2006, pp. R363-R386.

[55] H. Schift, “Nanoimprint lithography: An old story in modern times? A review,” *Journal of Vacuum Science & Technology B: Microelectronics and Nanometer Structures*, vol. 26, Mar. 2008, pp. 458-480.

[56] M. Colburn, S.C. Johnson, M. D. Stewart, S. Damle, T.C. Bailey, B. Choi, M. Wedlake, T.B. Michaelson, S.V. Sreenivasan, J.G. Ekerdt and C.G. Willson, “Step and flash imprint lithography: a new approach to high-resolution patterning,” in *Proc. Int. Soc. Opt. Eng.*, vol. 3676, 1999, pp. 379–389.

[57] W. Wu, W.M. Tong, J. Bartman, Y. Chen, R. Walmsley, Z. Yu, Q. Xia, I. Park, C. Picciotto, J. Gao, S. Wang, D. Morecroft, J. Yang, K.K. Berggren, and R.S. Williams, “Sub-10 nm Nanoimprint Lithography by Wafer Bowing,” *Nano Letters*, vol. 8, Nov. 2008, pp. 3865-3869.

[58] S.Y. Chou, P.R. Krauss, and P.J. Renstrom, “Imprint lithography with 25-nanometer resolution,” *Science*, vol. 272, 1996, pp. 85-87.

[59] S. Harrer, J.K.W. Yang, K.K. Berggren, F. Ilievski and C.A. Ross, “Pattern generation by using multi-step room-temperature nanoimprint lithography,” in *Proc. IEEE*-NANO, 2006, pp. 576–579.

[60] S. Matsui, Y. Igaku, H. Ishigaki, J. Fujita, M. Ishida, Y. Ochiai, M. Komuro, and H. Hiroshima, “Room temperature replication in spin on glass by nanoimprint technology,” *The 45th International Conference on Electron, Ion, and Photon Beam Technology and Nanofabrication*, Washington, DC (USA), 2001, pp. 2801-2805.

[61] J.H. Song, H. Huh, S.H. Kim, and H.T. Hahn, “Finite element analysis of room temperature nanoimprint lithography process with rate dependent plasticity,” *Materials Science Forum*, vol. 505-507, 2006, pp. 85-90.

[62] D.-Y. Khang and H. Yoon, “Room-Temperature Imprint Lithography,” *Advanced Materials*, vol. 13, 2001, pp. 749-752.

[63] G.L.W. Cross, B.S. O’Connell, H.O. Ozer, and J.B. Pethica, “Room temperature mechanical thinning and imprinting of solid films,” *Nano Letters*, vol. 7, 2007, pp. 357-362.

[64] D. Yao and P. Nagarajan, “Cold forging method for polymer microfabrication,” *Polymer Engineering and Science*, vol. 44, 2004, pp. 1998-2004.

[65] S. Youn, A. Ueno, M. Takahashi, and R. Maeda, “Microstructuring of SU-8 photoresist by UV-assisted thermal imprinting with non-transparent mold,” *Microelectronic Engineering*, vol. 85, Sep. 2008, pp. 1924-1931.

[66] J.S.M. Behl, “Towards Plastic Electronics: Patterning Semiconducting Polymers by Nanoimprint Lithography,” *Advanced Materials*, vol. 14, 2002, pp. 588-591.

[67] S.H. Ahn and L.J. Guo, “High-Speed Roll-to-Roll Nanoimprint Lithography on Flexible Plastic Substrates,” *Advanced Materials*, vol. 20, 2008, pp. 2044-2049.

[68] “Lab on Foil.” Internet: http://labonfoil.eu, [May 7, 2009].

[69] T. Haatainen, J. Ahopelto, G. Gruetzner, M. Fink, and K. Pfeiffer, “Step stamp imprint lithography using a commercial flip chip bonder,” in *Proc. Emerging Lithographic Technologies IV*, Santa Clara, CA, USA: Society of Photo-Optical Instrumentation Engineers, 2000, pp. 874-880.

[70] H. Scheer, T. Glinsner, M. Wissen, and R. Pelzer, “Nanostructuring of polymers by hot embossing lithography,” Proc. SPIE, vol. 5374, 2004, pp. 203-208.

[71] A. van Oosten, P. Nikolsky, J. Huckabay, R. Goossens, and R. Naber, “Pattern split rules! A feasibility study of rule based pitch decomposition for double patterning,” in *Proc. Photomask Technology 2007*, Monterey, CA, USA: SPIE, 2007, 67301L.

[72] A. Ladenburger, A. Reiser, J. Konle, M. Feneberg, R. Sauer, K. Thonke, F. Yan, and W.A. Goedel, “Regular silicon pillars and dichroic filters produced via particle-imprinted membranes,” *Journal of Applied Physics*, vol. 101, 2007, 34302-1.

[73] E. Schaffer, T. Thurn-Albrecht, T.P. Russell, and U. Steiner, “Electrically induced structure formation and pattern transfer,” *Nature*, vol. 403, 2000, pp. 874-877.

[74] S.H. Lee, P. Kim, H.E. Jeong, and K.Y. Suh, “Electrically induced formation of uncapped, hollow polymeric microstructures,” *Journal of Micromechanics and Microengineering*, vol. 16, 2006, pp. 2292-2297.

[75] S. Pagliara, L. Persano, A. Camposeo, R. Cingolani, and D. Pisignano, “Registration accuracy in multilevel soft lithography,” *Nanotechnology*, vol. 18, 2007, 175302.

[76] H. Ina, K. Kasumi, E. Kawakami, and K. Uda, “Critical issues study of nano-imprint tool for semiconductor volume production,” *Emerging Lithographic Technologies XI*, San Jose, CA, USA: SPIE, 2007, 65170M-8.

[77] A. Borjon, J. Belledent, Y. Trouiller, C. Gardin, C. Couderc, Y. Rody, F. Sundermann, J. Urbani, F. Foussadier, J. Planchot, E. Yesilada, P. Montgomery, B. Willkinson, M. Saied, C. Martinelli, G. Kerrien, L.L. Cam, F. Vautrin, F. Robert, and P. Schiavone, “Analysis of the diffraction pattern for optimal assist feature placement,” *Microelectronic Engineering*, vol. 84, 2007, pp. 741-745.

[78] M. Muhlberger, I. Bergmair, W. Schwinger, M. Gmainer, R. Schoftner, T. Glinsner, C. Hasenfuss, K. Hingerl, M. Vogler, H. Schmidt, and E.B. Kley, “A Moire method for high accuracy alignment in nanoimprint lithography,” *Microelectronic Engineering*, vol. 84, 2007, pp. 925-927.

[79] N. Li, W. Wu, and S.Y. Chou, “Sub-20-nm Alignment in Nanoimprint Lithography Using Moiré Fringe,” *Nano Letters*, vol. 6, Sep. 2006, pp. 2626-2629.

[80] D.L. White and O.R. Wood, “Novel alignment system for imprint lithography,” *44th International Conference on Electron, Ion, and Photon Beam Technology and Nanofabrication*, Rancho Mirage, CA, USA, 2000, pp. 3552-6.

[81] J. Shao, Y. Ding, Y. Tang, H. Liu, B. Lu, and D. Cui, “A novel overlay process for imprint lithography using load release and alignment error pre-compensation method,” *Microelectronic Engineering*, vol. 85, Jan. 2008, pp. 168-174.

[82] H. Schulz, M. Wissen, and H.-C. Scheer, “Local mass transport and its effect on global pattern replication during hot embossing,” *Microelectronic Engineering*, vol. 67-68, Jun. 2003, pp. 657-663.

[83] H.-C. Scheer and H. Schulz, “A contribution to the flow behavior of thin polymer films during hot embossing lithography,” *Microelectronic Engineering*, vol. 56, 2001, pp. 311-332.

[84] H.-C. Scheer, H. Schulz, T. Hoffmann, and C.M. Sotomayor Torres, “Problems of the nanoimprinting technique for nanometer scale pattern definition,” *J. Vac. Sci. Technol. B*, vol. 16, 1998, pp. 3917-3921.

[85] C. Gourgon, C. Perret, G. Micouin, F. Lazzarino, J.H. Tortai, O. Joubert, and J.-.E. Grolier, "Influence of pattern density in nanoimprint lithography," *Journal of Vacuum Science and Technology B: Microelectronics and Nanometer Structures*, vol. 21, 2003, pp. 98-105.

[86] F. Lazzarino, C. Gourgon, P. Schiavone, and C. Perret, "Mold deformation in nanoimprint lithography," *Journal of Vacuum Science and Technology B: Microelectronics and Nanometer Structures*, vol. 22, 2004, pp. 3318-3322.

[87] L.J. Heyderman, H. Schift, C. David, J. Gobrecht, and T. Schweizer, "Flow behaviour of thin polymer films used for hot embossing lithography," *Microelectronic Engineering*, vol. 54, 2000, pp. 229-245.

[88] M. Wissen, H. Schulz, N. Bogdanski, H. Scheer, Y. Hirai, H. Kikuta, G. Ahrens, F. Reuther, and T. Glinsner, "Impact of residual layer uniformity on UV stabilization after embossing," *The 48th International Conference on Electron, Ion, and Photon Beam Technology and Nanofabrication*, San Diego, California (USA): AVS, 2004, pp. 3224-3228.

[89] N. Kehagias, V. Reboud, C.M. Sotomayor Torres, V. Sirotkin, A. Svintsov, and S. Zaitsev, "Residual layer thickness in nanoimprint: experiments and coarse-grain simulation," *Microelectronic Engineering*, vol. 85, 2008, pp. 846-9.

[90] R.H. Pedersen, L.H. Thamdrup, A.V. Larsen, and A. Kristensen, "Quantitative Strategies to Handle Stamp Bending in NIL," in *Proc. Nanoimprint and Nanoprint Technology*, 2008.

[91] N. Kehagias, V. Reboud, G. Chansin, M. Zelsmann, C. Jeppesen, C. Schuster, M. Kubenz, F. Reuther, G. Gruetzner, and C.M. Sotomayor Torres, "Reverse-contact UV nanoimprint lithography for multilayered structure fabrication," *Nanotechnology*, vol. 18, 2007, 175303.

[92] X. Cheng and L.J. Guo, "One-step lithography for various size patterns with a hybrid mask-mold," *Microelectronic Engineering*, vol. 71, May. 2004, pp. 288-293.

[93] K. Okuda, N. Niimi, H. Kawata, and Y. Hirai, "Hybrid nanoimprint for micro-nano mixture structure," *Proc. SPIE*, vol. 6533, 2007, 65330R.

[94] N. Bogdanski, M. Wissen, S. Mollenbeck, and H. Scheer, "Challenges of residual layer minimisation in thermal nanoimprint lithography," *Proc. SPIE*, vol. 6533, 2007, 65330Q.

[95] H. Schift, L.J. Heyderman, M.A.D. Maur, and J. Gobrecht, "Pattern formation in hot embossing of thin polymer films," *Nanotechnology*, vol. 12, 2001, pp. 173-177.

[96] S. Landis, N. Chaix, D. Hermelin, T. Leveder, and C. Gourgon, "Investigation of capillary bridges growth in NIL process," *Microelectronic Engineering*, vol. 84, Jan. 2007, pp. 940-944.

[97] N. Chaix, C. Gourgon, S. Landis, C. Perret, M. Fink, F. Reuther, and D. Mecerreyes, "Influence of the molecular weight and imprint conditions on the formation of capillary bridges in nanoimprint lithography," *Nanotechnology*, vol. 17, 2006, pp. 4082-4087.

[98] Interview with W. Wu of Hewlett-Packard Laboratories, Jan. 2009.

[99] X. Liang, H. Tan, Z. Fu, and S.Y. Chou, "Air bubble formation and dissolution in dispensing nanoimprint lithography," *Nanotechnology*, vol. 18, 2007, 025303.

[100] Interview with Professor R. Bonnecaze, Apr. 2009.

[101] S. Reddy and R.T. Bonnecaze, "Simulation of fluid flow in the step and flash imprint lithography process," *Microelectronic Engineering*, vol. 82, Sep. 2005, pp. 60-70.

[102] M. Colburn, B.J. Choi, S.V. Sreenivasan, R.T. Bonnecaze, and C. Grant Willson, "Ramifications of lubrication theory on imprint lithography," *Microelectronic Engineering*, vol. 75, Sep. 2004, pp. 321-329.

[103] D. Morihara, "Numerical study on bubble trapping in UV nanoimprint lithography," *Proc. Nanoimprint and Nanoprint Technology*, 2008.

[104] S. Reddy, P.R. Schunk, and R.T. Bonnecaze, "Dynamics of low capillary number interfaces moving through sharp features," *Physics of Fluids*, vol. 17, Dec. 2005, pp. 122104-6.

[105] L. Ressier, C. Martin, and J.P. Peyrade, "Atomic force microscopy study of micrometric pattern replica by hot embossing lithography," *Microelectronic Engineering*, vol. 71, May. 2004, pp. 272-276.

[106] N. Bogdanski, M. Wissen, S. Möllenbeck, and H. Scheer, "Structure size dependent recovery of thin polystyrene layers in thermal imprint lithography," *Microelectronic Engineering*, vol. 84, Jan. 2007, pp. 860-863.

[107] G.L.W. Cross, R.M. Langford, B.S. O'Connell, and J.B. Pethica, "The mechanics of nanoimprint forming," *2004 MRS Fall Meeting*, Boston, MA, United States: Materials Research Society, 2004, pp. 15-26.

[108] P.S. Hong and H.H. Lee, "Pattern uniformity control in room-temperature imprint lithography," *Applied Physics Letters*, vol. 83, 2003, pp. 2441-2443.

[109] J. Taniguchi, T. Kawasaki, Y. Tokano, Y. Kogo, I. Miyamoto, M. Komuro, H. Hiroshima, N. Sakai, and K. Tada, "Measurement of Adhesive Force Between Mold and Photocurable Resin in Imprint Technology," *Japanese Journal of Applied Physics*, vol. 41, 2002, pp. 4194-4197.

[110] V. Trabadelo, H. Schift, S. Merino, S. Bellini, and J. Gobrecht, "Measurement of demolding forces in full wafer thermal nanoimprint," *Microelectronic Engineering*, vol. 85, 2008, pp. 907-909.

[111] S. Landis, N. Chaix, C. Gourgon, and T. Leveder, "Quantitative characterizations of a nanopatterned bonded wafer: force determination for nanoimprint lithography stamp removal," *Nanotechnology*, vol. 19, 2008, 125305.

[112] Interview with Professor C.G. Willson, Apr. 2009.

[113] Y.H. Yan, M.B. Chan-Park, W.C. Ching, and C.Y. Yue, "Interaction of anti-adhesive silicone films with UV embossing resin," *Applied Surface Science*, vol. 249, Aug. 2005, pp. 332-339.

[114] M. Beck, M. Graczyk, I. Maximov, E. Sarwe, T.G.I. Ling, M. Keil, and L. Montelius, "Improving stamps for 10 nm level wafer scale nanoimprint lithography," *Microelectronic Engineering*, vol. 61-62, 2002, pp. 441-448.

[115] K. Tsunozaki and Y. Kawaguchi, "Preparation methods and characteristics for fluorinated polymers for mold replication," in *Proc. Micro- and Nano-Engineering*, 2008.

[116] A. Baba, M. Iwamoto, K. Tsubaki, and T. Asano, "Easy Release of Mold in Imprint Lithography Using Ion-Beam-Irradiated Photoresist Surface," *Japanese Journal of Applied Physics*, vol. 41, 2002, pp. 4190-4193.

[117] S. Yoshitake, H. Sunaoshi, K. Yasui, H. Kobayashi, T. Sato, O. Nagarekawa, E. Thompson, G. Schmid, and D.J. Resnick, "The development of full field high resolution imprint templates," *Photomask Technology 2007*, Monterey, CA, USA: SPIE, 2007, 67300E-9.

[118] D.L. Olynick, J.A. Liddle, B.D. Harteneck, S. Cabrini, and I.W. Rangelow, "Nanoscale pattern transfer for templates, NEMS, and nano-optics," *Micromachining Technology for Micro-Optics and Nano-Optics V and Microfabrication Process Technology XII*, San Jose, CA, USA: SPIE, 2007, 64620J-8.

[119] P. Voisin, A. Jouve, M. Zelsmann, C. Gourgon, and J. Boussey, "Template flatness issue for UV curing nanoimprint lithography," *Proc. SPIE*, vol. 6517, 2007, 65172D.

[120] K. Yoshida, K. Kojima, M. Abe, S. Sasaki, M. Kurihara, H. Mohri, and N. Hayashi, "Metrology for templates of UV nano imprint lithography," *Photomask Technology 2007*, Monterey, CA, USA: SPIE, 2007, 67305O-8.

[121] T. DiBiase, M. Ahamdian, and I. Malik, "Comprehensive defect analysis methodology for nano imprint lithography," *Microelectronic Engineering*, vol. 84, Jan. 2007, pp. 989-993.

[122] J. Perez, K. Selinidis, S. Johnson, B. Fletcher, F. Xu, J. Maltabes, I. McMackin, D. Resnick, and S.V. Sreenivasan, "A study of imprint-specific defects in the step and flash imprint lithography process," *Proc. SPIE*, vol. 6517, 2007, 65170L.

[123] H.S. Park, H.H. Shin, M.Y. Sung, W.B. Choi, S.W. Choi, and S.Y. Park, "Novel process to improve defect problems for thermal nanoimprint lithography," *IEEE Transactions on Semiconductor Manufacturing*, vol. 20, 2007, pp. 13-19.

[124] W.J. Dauksher, N.V. Le, K.A. Gehoski, E.S. Ainley, K.J. Nordquist, and N. Joshi, "An electrical defectivity characterization of wafers imprinted with step and flash imprint lithography," *Proc. SPIE*, vol. 6517, 2007, 651714.

[125] K. Selenidis, J. Maltabes, I. McMackin, J. Perez, W. Martin, D.J. Resnick, and S.V. Sreenivasan, "Defect reduction progress in step and flash imprint lithography," *Photomask Technology 2007*, Monterey, CA, USA: SPIE, 2007, 67300F-12.

[126] K. Byeon, E. Hong, S. Hong, S. Hwang, C. Hong, and H. Lee, "Imprinting process for a large area pattern transferring on light-emitting diodes structure to improve light extraction," in *Proc. Nanoimprint and Nanoprint Technology*, 2008.

[127] S.H. Kim, K. Lee, J. Kim, M. Kwon, and S. Park, "Fabrication of photonic crystal structures on light emitting diodes by nanoimprint lithography," *Nanotechnology*, vol. 18, 2007, 055306.

[128] C. Jones, D. Lentz, G. Doyle, M. Miller, M. Ganapathisubramanian, X. Lu, D. Resnick, and D.L. LaBrake, "Manufacturing implications for photonic crystal patterning using imprint lithography," *Proc. SPIE*, vol. 6486, 2007, 64860Q.

[129] C.M. Bruinink, M. Burresi, M.J. de Boer, F.B. Segerink, H.V. Jansen, E. Berenschot, D.N. Reinhoudt, J. Huskens, and L. Kuipers, "Nanoimprint Lithography for Nanophotonics in Silicon," *Nano Letters*, vol. 8, 2008, pp. 2872-2877.

[130] M. Belotti, J. Torres, E. Roy, A. Pepin, Y. Chen, D. Gerace, L.C. Andreani, and M. Galli, "Replication of photonic crystals by soft ultraviolet-nanoimprint lithography," *Journal of Applied Physics*, vol. 99, Jan. 2006, 024309.

[131] D. Psaltis, S.R. Quake, and C. Yang, "Developing optofluidic technology through the fusion of microfluidics and optics," *Nature*, vol. 442, Jul. 2006, pp. 381-386.

[132] G. Emiliyanov, J.B. Jensen, O. Bang, P.E. Hoiby, L.H. Pedersen, E.M. Kjr, and L. Lindvold, "Localized biosensing with Topas microstructured polymer optical fiber," *Optics Letters*, vol. 32, 2007, pp. 460-462.

[133] A. Tuteja, W. Choi, G.H. McKinley, R.E. Cohen, and M.F. Rubner, "Design parameters for superhydrophobicity and superoleophobicity," *MRS Bulletin*, vol. 33, 2008, pp. 752-758.

[134] W. Wu, Z. Yu, S. Wang, R.S. Williams, Y. Liu, C. Sun, X. Zhang, E. Kim, Y.R. Shen, and N.X. Fang, "Midinfrared metamaterials fabricated by nanoimprint lithography," *Applied Physics Letters*, vol. 90, 2007, 63107-1.

[135] Z. Yu, W. Wu, L. Chen, and S.Y. Chou, "Fabrication of large area 100 nm pitch grating by spatial frequency doubling and nanoimprint lithography for subwavelength optical applications," *45th*

International Conference on Electron, Ion and Photon Beam Technology and Nanofabrication, Washington, DC, 2001, pp. 2816-19.

[136] L. Chen, J.J. Wang, F. Walters, X. Deng, M. Buonanno, S. Tai, and X. Liu, "58 nm half-pitch plastic wire-grid polarizer by nanoimprint lithography," *J. Vac. Sci. Technol. B*, vol. 25, 2007, pp. 2654-2657.

[137] I. Puscasu, G. Boreman, R.C. Tiberio, D. Spencer, and R.R. Krchnavek, "Comparison of infrared frequency selective surfaces fabricated by direct-write electron-beam and bilayer nanoimprint lithographies," *Journal of Vacuum Science and Technology B: Microelectronics and Nanometer Structures*, vol. 18, 2000, pp. 3578-3581.

[138] "NanoOpto.com : Technology." Internet: http://www.nanoopto.com, [May 7, 2009].

[139] M. Nakajima, T. Yoshikawa, K. Sogo, and Y. Hirai, "Fabrication of multi-layered nano-channels by reversal imprint lithography," *Microelectronic Engineering*, vol. 83, Sep. 2006, pp. 876-879.

[140] N. Gadegaard, E. Martines, M. Riehle, K. Seunarine, and C. Wilkinson, "Applications of nano-patterning to tissue engineering," *Microelectronic Engineering*, vol. 83, Sep. 2006, pp. 1577-1581.

[141] V.N. Truskett and M.P.C. Watts, "Trends in imprint lithography for biological applications," *Trends in biotechnology*, vol. 24, 2006, pp. 312-317.

[142] H. Schift, S. Bellini, U. Pieles, and J. Gobrecht, "Sustained polymer membranes fabricated by nanoimprint lithography," *Journal of Microlithography, Microfabrication, and Microsystems*, vol. 5, Jan. 2006, 011010-5.

[143] D.J. Resnick, M. Miller, G. Schmid, C. Brooks, N. Khusnatsinov, D. LaBrake, and S. Sreenivasan, "Patterned media using step and flash imprint lithography," in *Proc. Nanoimprint and Nanoprint Technology*, 2008.

[144] M.C.R. Heijna, J. Loffler, B.B. Van Aken, W.J. Soppe, H. Borg, and P.P.G.J.M. Peeters, "Nanoimprint lithography of light trapping patterns in sol-gel coatings for thin film silicon solar cells," *Photonics for Solar Energy Systems II*, Strasbourg, France: SPIE, 2008, 70020C-7.

[145] D. Cheyns, K. Vasseur, C. Rolin, J. Genoe, J. Poortmans, and P. Heremans, "Nanoimprinted semiconducting polymer films with 50 nm features and their application to organic heterojunction solar cells," *Nanotechnology*, vol. 19, 2008, 424016.

[146] M. Aryal, F. Buyukserin, K. Mielczarek, X. Zhao, J. Gao, A. Zakhidov, and W. Hu, "Imprinted large-scale high density polymer nanopillars for organic solar cells," *J. Vac. Sci. Technol. B*, vol. 26, 2008, pp. 2562-2566.

[147] M. Kim, J. Kim, J.C. Cho, M. Shtein, L.J. Guo, and J. Kim, "Flexible conjugated polymer photovoltaic cells with controlled heterojunctions fabricated using nanoimprint lithography," *Applied Physics Letters*, vol. 90, Mar. 2007, 123113-3.

[148] C. Ting, M. Huang, H. Tsai, C. Chou, and C. Fu, "Low cost fabrication of the large-area anti-reflection films from polymer by nanoimprint/hot-embossing technology," *Nanotechnology*, vol. 19, 2008, 205301.

[149] M. Kang, M. Kim, J. Kim, and L.J. Guo, "Organic Solar Cells Using Nanoimprinted Transparent Metal Electrodes," *Advanced Materials*, vol. 20, 2008, pp. 4408-4413.

[150] J.S. Gwag, M. Oh-e, M. Yoneya, H. Yokoyama, H. Satou, and S. Itami, "Advanced nanoimprint lithography using a graded functional imprinting material tailored for liquid crystal alignment," *Journal of Applied Physics*, vol. 102, 2007, 063501-5.

[151] Y. Yi, M. Nakata, A.R. Martin, and N.A. Clark, "Alignment of liquid crystals by topographically patterned polymer films prepared by nanoimprint lithography," *Applied Physics Letters*, vol. 90, Apr. 2007, 163510-3.

[152] J. Bae, J. Chang, K. Kim, B. Kim, and S. Lim, "Large area UV nanoimprint lithography for TFT-LCD devices," in *Proc. Nanoimprint and Nanoprint Technology*, 2008.

[153] A. Baba, M. Hizukuri, M. Iwamoto, and T. Asano, "Fabrication of Carbon-Based Field Emitters Using Stamp Technology," *Japanese Journal of Applied Physics*, vol. 38, 1999, pp. 7203-7207.

[154] L.H. Thamdrup, A. Klukowska, and A. Kristensen, "Stretching DNA in polymer nanochannels fabricated by thermal imprint in PMMA," *Nanotechnology*, vol. 19, 2008, 125301.

[155] B. Bilenberg, M. Hansen, D. Johansen, V. Ozkapici, C. Jeppesen, P. Szabo, I.M. Obieta, O. Arroyo, J.O. Tegenfeldt, and A. Kristensen, "Topas-based lab-on-a-chip microsystems fabricated by thermal nanoimprint lithography," *J. Vac. Sci. Technol. B*, vol. 23, 2005, pp. 2944-2949.

[156] F. Patolsky, G. Zheng, and C.M. Lieber, "Nanowire-based biosensors," *Analytical Chemistry*, vol. 78, 2006, pp. 4260-4269.

[157] N. Chen, C. Liao, H.J. Chen, and F. Huang, "GHz band surface acoustic wave filter fabrication by UV nanoimprint," in *Proc. Nanoimprint and Nanoprint Technology*, 2008.

[158] H. Jung, H. Choi, J. Yoon, H. Hwang, and G. Jung, "Resistance random access memory fabricated by nanoimprint lithography," in *Proc. Nanoimprint and Nanoprint Technology*, 2008.

[159] K. Selinidis, E. Thompson, G. Schmid, J. Maltabes, I. McMackin, N. Stacey, S. Sreenivasan, and D.J. Resnick, "Imprint Mask Infrastructure for the 32 nm Node and Beyond," in *Proc. Nanoimprint and Nanoprint Technology*, 2008.

[160] D. Shepard, "Topolithography and its Application to the Manufacture of 3D Diode-based Memories," in *Proc. IEEE International Solid-State Circuits Conference*, 2003.

[161] S. Youn, A. Ueno, M. Takahashi, and R. Maeda, "Microstructuring of Dual Damascene Opening by Hot Embossing Combined with Etch-Back Process," *Japanese Journal of Applied Physics*, vol. 47, 2008, pp. 5189-5196.

[162] C.G. Willson, "Multilayer Structures by Step and Flash Imprint Lithography," in *Proc. Micro- and Nano-Engineering*, 2008.

[163] W. Jen, F. Palmieri, B. Chao, M. Lin, J. Hao, J. Owens, K. Sotoodeh, R. Cheung, and C.G. Willson, "Multilevel step and flash imprint lithography for direct patterning of dielectrics," *Proc. SPIE*, vol. 6517, 2007, 65170K.

[164] E. Lausecker, Y. Huang, S. Wagner, and J.C. Sturm, "Self-Aligned Multilevel Molds for top-Grate FET Fabrication using Imprint Lithography," in *Proc. Nanoimprint and Nanoprint Technology*, 2008.

[165] H.D. Rowland, W.P. King, A.C. Sun, and P.R. Schunk, "Impact of polymer film thickness and cavity size on polymer flow during embossing: Toward process design rules for nanoimprint lithography," *Journal of Micromechanics and Microengineering*, vol. 15, 2005, pp. 2414-2425.

[166] H.D. Rowland and W.P. King, "Polymer deformation and filling modes during microembossing," *Journal of Micromechanics and Microengineering*, vol. 14, 2004, pp. 1625-1632.

[167] Y. Juang, L.J. Lee, and K.W. Koelling, "Hot embossing in microfabrication. Part II: Rheological characterization and process analysis," *Polymer Engineering and Science*, vol. 42, 2002, pp. 551-566.

[168] Y. Juang, L.J. Lee, and K.W. Koelling, "Hot embossing in microfabrication. Part I: Experimental," *Polymer Engineering and Science*, vol. 42, 2002, pp. 539-550.

[169] J. Jeong, Y. Choi, Y. Shin, J. Lee, K. Park, E. Lee, and S. Lee, "Flow behavior at the embossing stage of nanoimprint lithography," *Fibers and Polymers*, vol. 3, 2002, pp. 113-119.

[170] D. Yao, V.L. Virupaksha, and B. Kim, "Study on squeezing flow during nonisothermal embossing of polymer microstructures," *Polymer Engineering and Science*, vol. 45, 2005, pp. 652-660.

[171] D.A. Mendels, "Multi-scale modelling of nano-imprint lithography," *Proc. SPIE*, vol. 6151, 615113.

[172] H.D. Rowland, W.P. King, A.C. Sun, and P.R. Schunk, "Simulations of nonuniform embossing: The effect of asymmetric neighbor cavities on polymer flow during nanoimprint lithography," *J. Vac. Sci. Technol. B*, vol. 23, 2005, pp. 2958-2962.

[173] H. Takagi, M. Takahashi, R. Maeda, Y. Onishi, Y. Iriye, T. Iwasaki, and Y. Hirai, "Analysis of time dependent polymer deformation based on a viscoelastic model in thermal imprint process," *Microelectronic Engineering*, vol. 85, 2008, pp. 902-906.

[174] Y. Hirai, T. Konishi, T. Yoshikawa, and S. Yoshida, "Simulation and experimental study of polymer deformation in nanoimprint lithography," *Journal of Vacuum Science and Technology B: Microelectronics and Nanometer Structures*, vol. 22, 2004, pp. 3288-3293.

[175] Y. Hirai, Y. Onishi, T. Tanabe, M. Shibata, T. Iwasaki, and Y. Iriye, "Pressure and resist thickness dependency of resist time evolutions profiles in nanoimprint lithography," *Microelectronic Engineering*, vol. 85, 2008, pp. 842-5.

[176] H.-C. Scheer, N. Bogdanski, M. Wissen, T. Konishi, and Y. Hirai, "Polymer time constants during low temperature nanoimprint lithography," *Journal of Vacuum Science and Technology B: Microelectronics and Nanometer Structures*, vol. 23, 2005, pp. 2963-2966.

[177] W. Young, "Analysis of the nanoimprint lithography with a viscous model," *Microelectronic Engineering*, vol. 77, 2005, pp. 405-411.

[178] H. Hocheng and C.C. Nien, "Numerical analysis of effects of mold features and contact friction on cavity filling in the nanoimprinting process," *Journal of Microlithography, Microfabrication, and Microsystems*, vol. 5, 2006, 011004-1-7.

[179] M. Worgull, M. Heckele, J.F. Hetu, and K.K. Kabanemi, "Modeling and optimization of the hot embossing process for micro- and nanocomponent fabrication," *Journal of Microlithography, Microfabrication, and Microsystems*, vol. 5, Mar. 2006, 011005.

[180] C. Lin, R. Chen, and C. Hung, "The characterisation and finite-element analysis of a polymer under hot pressing," *International Journal of Advanced Manufacturing Technology*, vol. 20, 2002, pp. 230-235.

[181] E.M. Arruda, M.C. Boyce, and R. Jayachandran, "Effects of strain rate, temperature and thermomechanical coupling on the finite strain deformation of glassy polymers," *Mechanics of Materials*, vol. 19, 1995, pp. 193-212.

[182] N.M. Ames, "A thermo-mechanical finite deformation theory of plasticity for amorphous polymers: application to micro-hot-embossing of poly(methyl methacrylate)," Ph.D. dissertation, Massachusetts Institute of Technology, Cambridge, MA, 2007.

[183] V. Sirotkin, A. Svintsov, S. Zaitsev, and H. Schift, "Viscous flow simulation in nanoimprint using coarse-grain method," *Microelectronic Engineering*, vol. 83, 2006, pp. 880-883.

[184] S. Zaitsev, V. Sirotkin, A. Svintsov, and H. Schift, "Coarse-grain method for modeling of stamp and substrate deformation in nanoimprint," *Microelectronic Engineering*, vol. 84, 2007, pp. 868-71.

[185] V. Sirotkin, A. Svintsov, S. Zaitsev, and H. Schift, "Coarse-grain simulation of viscous flow and stamp deformation in nanoimprint," *Journal of Vacuum Science and Technology B: Microelectronics and Nanometer Structures*, vol. 25, 2007, pp. 2379-2383.

[186] N. Kehagias, V. Reboud, C.M. Sotomayor Torres, V. Sirotkin, A. Svintsov, and S. Zaitsev, "The IMPRINT software: quantitative predictions of the residual resist thickness in nanoimprint," *20th International Microprocesses and Nanotechnology Conference*, Kyoto, Japan: IEEE, 2007, pp. 404-5.

[187] V. Sirotkin, A. Svintsov, H. Schift, and S. Zaitsev, "Coarse-grain method for modeling of stamp and substrate deformation in nanoimprint," *Microelectronic Engineering*, vol. 84, Jan. 2007, pp. 868-871.

[188] T. Nogi and T. Kato, "Influence of a hard surface layer on the limit of elastic contact - Part I: Analysis using a real surface model," *Journal of Tribology, Transactions of the ASME*, vol. 119, 1997, pp. 493-500.

[189] K.L. Johnson, *Contact Mechanics*, Cambridge: Cambridge University Press, 1985.

[190] F. Wang and L.M. Keer, "Numerical simulation for three dimensional elastic-plastic contact with hardening behavior," *Journal of Tribology*, vol. 127, 2005, pp. 494-502.

[191] W. Peng and B. Bhushan, "A numerical three-dimensional model for the contact of layered elastic/plastic solids with rough surfaces by a variational principle," *Journal of Tribology*, vol. 123, 2001, pp. 330-342.

[192] S. Cai and B. Bhushan, "A numerical three-dimensional contact model for rough, multilayered elastic/plastic solid surfaces," *Wear*, vol. 259, 2005, pp. 1408-1423.

[193] I.A. Polonsky and L.M. Keer, "A numerical method for solving rough contact problems based on the multi-level multi-summation and conjugate gradient techniques," *Wear*, vol. 231, 1999, pp. 206-19.

[194] I.A. Polonsky and L.M. Keer, "Fast methods for solving rough contact problems: a comparative study," *Journal of Tribology*, vol. 122, 2000, pp. 36-41.

[195] K.F. Lei, W.J. Li, and Y. Yam, "Effects of contact-stress on hot-embossed PMMA microchannel wall profile," *Microsystem Tecnologies*, vol. 11, 2005, pp. 353-357.

[196] H. Taylor, Y.C. Lam, and D. Boning, "A computationally simple method for simulating the micro-embossing of thermoplastic layers," *Journal of Micromechanics and Microengineering*, vol. 19, 2009, 075007.

[197] E. Lee and J. Radok, "The contact problem for viscoelastic bodies," *American Society of Mechanical Engineers — Transactions — Journal of Applied Mechanics Series E*, vol. 27, 1960, pp. 438-444.

[198] X. Xie, "Physical Understanding and Modeling of Chemical Mechanical Planarization in Dielectric Materials," Ph.D. dissertation, Massachusetts Institute of Technology, Cambridge, MA, 2007.

[199] "MatLab Documentation." Internet: http://www.mathworks.com, [May 7, 2009].

[200] M.L. Williams, R.F. Landel, and J.D. Ferry, "The temperature dependence of relaxation mechanisms in amorphous polymers and other glass-forming liquids," *Journal of the American Chemical Society*, vol. 77, 1955, pp. 3701-3707.

[201] M.E. Dirckx, "Design of a fast cycle time hot micro-embossing machine," S.M. thesis, Massachusetts Institute of Technology, Cambridge, MA, 2005.

[202] N.M. Ames, V. Srivastava, S.A. Chester, and L. Anand, "A thermo-mechanically coupled theory for large deformations of amorphous polymers. Part II: Applications," *International Journal of Plasticity*, vol. 25, Aug. 2009, pp. 1495-1539.

[203] N.G. McCrum, C.P. Buckley, and C.B. Bucknall, *Principles of polymer engineering*, Oxford: Oxford University Press, 1997.

[204] D. Yao and B. Kim, "Simulation of the filling process in micro channels for polymeric materials," *Journal of Micromechanics and Microengineering*, vol. 12, 2002, pp. 604-610.

[205] H. Taylor, D. Boning, C. Iliescu, and B. Chen, "Computationally efficient modelling of pattern dependencies in the micro-embossing of thermoplastic polymers," *Microelectronic Engineering*, vol. 85, 2008, pp. 1453-6.

[206] C.S. Burrus, T.W. Parks, and J.F. Potts, *DFT/FFT and convolution algorithms: theory and implementation*, New York: Wiley, 1984.

[207] "Abaqus User's Manual." Internet: http://www.simulia.com, [May 7, 2009].

[208] D. Henann, Personal communication, 2008.

[209] R.B. Heywood, *Photoelasticity for Designers*, Oxford: Pergamon Press, 1969.

[210] A. Ajovalasit, S. Barone, and G. Petrucci, "Towards RGB photoelasticity: Full-field automated photoelasticity in white light," *Experimental Mechanics*, vol. 35, 1995, pp. 193-200.

[211] S. Shirouzu, H. Shikuma, N. Senda, M. Yoshida, S. Sakamoto, K. Shigematsu, T. Nakagawa, and S. Tagami, "Stress-Optical Coefficients in Polycarbonates," *Japanese Journal of Applied Physics*, vol. 29, 1990, pp. 898-901.

[212] T.C. O'Sullivan and R.B. King, "Sliding contact stress field due to a spherical indenter on a layered elastic half-space," *Journal of Tribology*, vol. 110, 1988, pp. 235-40.

[213] R. Byron Bird, *Dynamics of polymeric liquids*, New York: Wiley, 1987.

[214] C. Iliescu, F.E.H. Tay, and J. Wei, "Low stress PECVD-SiNx layers at high deposition rates using high power and high frequency for MEMS applications," *Journal of Micromechanics and Microengineering*, vol. 16, 2006, pp. 869-74.

[215] H. Schift, "Nanorheology," in *Alternative Lithography*, C. Sotomayor Torres, Ed., Kluwer, 2003.

[216] H. Schulz, M. Wissen, N. Bogdanski, H.-C. Scheer, K. Mattes, and C. Friedrich, "Impact of molecular weight of polymers and shear rate effects for nanoimprint lithography," *Microelectronic Engineering*, vol. 83, Feb. 2006, pp. 259-280.

[217] H.-C. Scheer, N. Bogdanski, S. Möllenbeck, M. Wissen, K. Zimmer, and J. Zajadacz, "Fingerprint stamp for evaluation of polymer flow time constants in thermal nanoimprint," *Microelectronic Engineering*, vol. 84, Jan. 2007, pp. 949-952.

[218] N. Bogdanski, M. Wissen, S. Möllenbeck, and H.-C. Scheer, "Polymers below the critical molecular weight for thermal imprint lithography," *Microelectronic Engineering*, vol. 85, 2008, pp. 825-829.

[219] H.-C. Scheer, N. Bogdanski, M. Wissen, and S. Möllenbeck, "Imprintability of polymers for thermal nanoimprint," *Microelectronic Engineering*, vol. 85, 2008, pp. 890-896.

[220] T. Leveder, S. Landis, L. Davoust, and N. Chaix, "Flow property measurements for nanoimprint simulation," *Microelectronic Engineering*, vol. 84, Jan. 2007, pp. 928-931.

[221] H.J. Patrick, T.A. Germer, Y. Ding, H.W. Ro, L.J. Richter, and C.L. Soles, "Scatterometry for in situ measurement of pattern reflow in nanoimprinted polymers," *Appl. Phys. Lett.*, vol. 93, Dec. 2008, 233105.

[222] R.L. Jones, C.L. Soles, E.K. Lin, W. Hu, R.M. Reano, S.W. Pang, S.J. Weigand, D.T. Keane, and J.P. Quintana, "Pattern fidelity in nanoimprinted films using critical dimension small angle x-ray scattering," *Journal of Microlithography, Microfabrication, and Microsystems*, vol. 5, Mar. 2006, 013001.

[223] R.L. Jones, T. Hu, C.L. Soles, E.K. Lin, R.M. Reano, S.W. Pang, and D.M. Casa, "Real-Time Shape Evolution of Nanoimprinted Polymer Structures during Thermal Annealing," *Nano Letters*, vol. 6, Jul. 2006, pp. 1723-1728.

[224] E. Buck, K. Petersen, M. Hund, G. Krausch, and D. Johannsmann, "Decay Kinetics of Nanoscale Corrugation Gratings on Polymer Surface: Evidence for Polymer Flow below the Glass Temperature," *Macromolecules*, vol. 37, 2004, pp. 8647-8652.

[225] "MicroResist Technology." Internet: http://www.microresist.de, [May 7, 2009].

[226] I.G. Romero, F. Reuther, M. Fink, and G. Gruetzner, "Rheological Characterisation and Tuning of Polymers for Nanoimprint Lithography," in *Proc. Nanoimprint and Nanoprint Technology*, 2008.

[227] D. Lyebyedyev, H. Schulz, H.-C. Scheer, and K. Pfeiffer, "Characterisation of new thermosetting polymer materials for nanoimprint lithography," *Materials Science and Engineering C*, vol. 15, 2001, pp. 241-243.

[228] T. Hoffmann, "Viscoelastic properties of polymers," in *Alternative Lithography*, C. Sotomayor Torres, Ed., Kluwer, 2003.

[229] C.D. Han, *Rheology and Processing of Polymeric Materials*, Oxford: Oxford University Press, 2007.

[230] J.K. Lee and C.D. Han, "Evolution of polymer blend morphology during compounding in an internal mixer," *Polymer*, vol. 40, Nov. 1999, pp. 6277-6296.

[231] M.V. Chukalina, V. Sirotkin, A. Svintsov, and S.I. Zaitsev, "Polymer Chain Effects in Nanoimprinting," *Proc. Trends in Nanotechnology*, 2004.

[232] M.V. Chukalina, V.N. Matveev, V.V. Sirotkin, A.A. Svintsov, and S.I. Zaitsev, "Deformation and viscouse [*sic*] flow in nano-imprinting," *Proceedings of the 8th International Symposium Nanostructures: Physics and Technology*, St. Petersburg, Russian Federation: Ioffe Institute, 2000, pp. 121-124.

[233] H. Gao, H. Tan, W. Zhang, K. Morton, and S.Y. Chou, "Air Cushion Press for Excellent Uniformity, High Yield, and Fast Nanoimprint Across a 100 mm Field," *Nano Letters*, vol. 6, Sep. 2006, pp. 2438-2441.

[234] K. Deguchi, N. Takeuchi, and A. Shimizu, "Evaluation of pressure uniformity using a pressure-sensitive film and calculation of wafer distortions caused by mold press in imprint lithography," *Japanese Journal of Applied Physics, Part 1: Regular Papers and Short Notes and Review Papers*, vol. 41, 2002, pp. 4178-4181.

[235] S. Timoshenko, *Theory of Plates and Shells*, New York: McGraw-Hill, 1959.

[236] J.N. Reddy, *Theory and Analysis of Elastic Plates and Shells*, Boca Raton, Fla: CRC, 2007.

[237] D. Suh, S. Choi, and H.H. Lee, "Rigiflex lithography for nanostructure transfer," *Advanced Materials*, vol. 17, 2005, pp. 1554-1560.

[238] G. McClelland, C. Rettner, M. Hart, K. Carter, M. Sanchez, M. Best, and B. Terris, "Contact mechanics of a flexible imprinter for photocured nanoimprint lithography," *Tribology Letters*, vol. 19, 2005, pp. 59-63.

[239] R.H. Pedersen, O. Hansen, and A. Kristensen, "A compact system for large-area thermal nanoimprint lithography using smart stamps," *Journal of Micromechanics and Microengineering*, vol. 18, 2008, 055018.

[240] H. Hocheng and W.H. Hsu, "Effect of Back Mold Grooves on Improving Uniformity in Nanoimprint Lithography," *Japanese Journal of Applied Physics*, vol. 46, 2007, pp. 6370-6372.

[241] T. Nielsen, A. Kristensen, and O. Hansen, "Flexible Nano-Imprint Stamp," US Patent application 11/574,645, 2005.

[242] M. Colburn, A. Grot, B.J. Choi, M. Amistoso, T. Bailey, S.V. Sreenivasan, J.G. Ekerdt, and C.G. Willson, "Patterning nonflat substrates with a low pressure, room temperature, imprint lithography process," *Journal of Vacuum Science and Technology B: Microelectronics and Nanometer Structures*, vol. 19, 2001, pp. 2162-2172.

[243] I. Bergmair, M. Mühlberger, M. Gusenbauer, R. Schöftner, and K. Hingerl, "Equalising stamp and substrate deformations in solid parallel-plate UV-based nanoimprint lithography," *Microelectronic Engineering*, vol. 85, 2008, pp. 822-824.

[244] "MicroResist Technology: Products, Applications." Internet: http://www.microresist.de, [May 7, 2009].

[245] H. Hiroshima, "Nanoimprint with thin and uniform residual layer for various pattern densities," in *Proc. Micro- and Nano-Engineering*, 2008.

[246] "Molecular Imprints, Inc." Internet: http://www.molecularimprints.com, [May 7, 2009].

[247] N. Bogdanski, S. Mollenbeck, and H. Scheer, "Contact angles in thermal imprint," in *Proc. Nanoimprint and Nanoprint Technology*, 2008.

[248] T. Huang, J. Ciou, P. Huang, K. Hsieh, and S. Yang, "Fast fabrication of integrated surface-relief and particle-diffusing plastic diffuser by use of a hybrid extrusion roller embossing process," *Optics Express*, vol. 16, 2008, pp. 440-447.

[249] J. Lee, S. Park, K. Choi, and G. Kim, "Nano-scale patterning using the roll typed UV-nanoimprint lithography tool," *Microelectronic Engineering*, vol. 85, 2008, pp. 861-865.

[250] L.P. Yeo, S.H. Ng, Z. Wang, Z. Wang, and N.F.D. Rooij, "Micro-fabrication of polymeric devices using hot roller embossing," *Microelectronic Engineering*, vol. 86, Jun. 2009, pp. 933-936.

[251] C.Y. Hui, A. Jagota, Y.Y. Lin, and E.J. Kramer, "Constraints on Microcontact Printing Imposed by Stamp Deformation," *Langmuir*, vol. 18, 2002, pp. 1394-1407.

[252] A. Bietsch and B. Michel, "Conformal contact and pattern stability of stamps used for soft lithography," *Journal of Applied Physics*, vol. 88, Oct. 2000, pp. 4310-4318.

[253] I. Bellin, S. Kelch, R. Langer, and A. Lendlein, "Polymeric triple-shape materials," *Proceedings of the National Academy of Sciences*, vol. 103, Nov. 2006, pp. 18043-18047.

[254] S. Buzzi, F. Robin, V. Callegari, and J.F. Löffler, "Metal direct nanoimprinting for photonics," *Microelectronic Engineering*, vol. 85, Feb. 2008, pp. 419-424.

[255] S.Y. Chou, C. Keimel, and J. Gu, “Ultrafast and direct imprint of nanostructures in silicon,” *Nature*, vol. 417, 2002, pp. 835-837.

[256] M. Martyniuk, R. Sewell, C. Musca, J. Dell, and L. Faraone, “Determination of HgCdTe elasto-plastic properties using nanoindentation,” *Journal of Electronic Materials*, vol. 35, 2006, pp. 1197-1205.

[257] A.J. Hart, H.K. Taylor, and A.H. Slocum, “2D and 3D growth of carbon nanotubes on substrates, from nanometre to millimetre scales,” *International Journal of Nanomanufacturing*, vol. 1, 2007, pp. 701-709.

[258] **“**Visible Light Spectrum.” Internet: http://www.efg2.com/Lab/ScienceAndEngineering/Spectra.htm, [May 7, 2009].

Appendix A: Supplementary plots of bulk embossing data

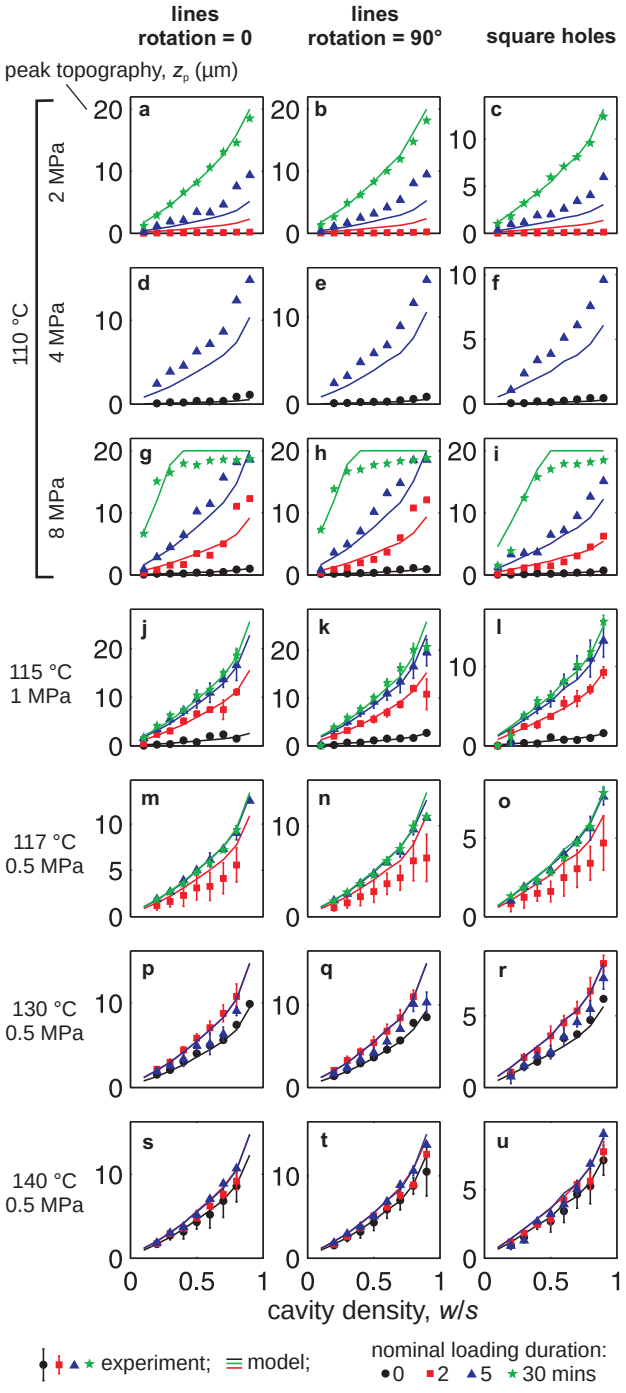

Figure A.1: Cavity penetration depths, z_p, for PMMA as a function of cavity opening density, *w*/*s*, and nominal loading duration, for 50-μm-pitch cavities. For temperatures of 115 °C and above, two samples were processed at each set of conditions; in these cases the mean value of z_p is plotted and error bars represent the ranges of the results.

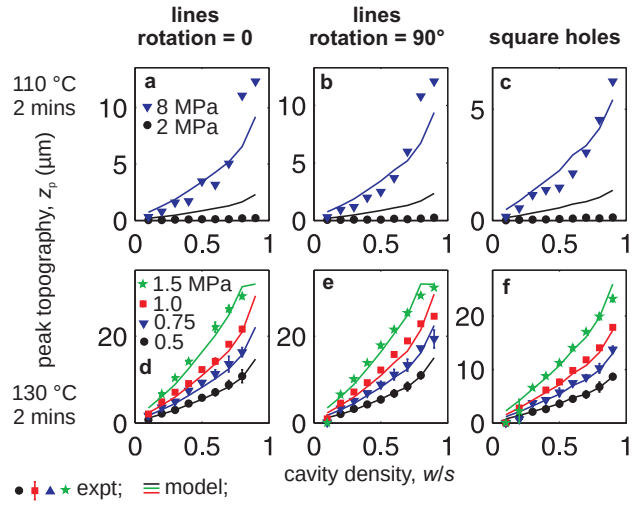

Figure A.2: Cavity penetration depths, z_p, for PMMA as a function of cavity opening density, *w/s*, and sample-average pressure, for 50-μm-pitch cavities and 2-minute nominal loading durations. For temperatures of 115 °C and above, two samples were processed at each set of conditions; in these cases the mean value of z_p is plotted and error bars represent the ranges of the results.

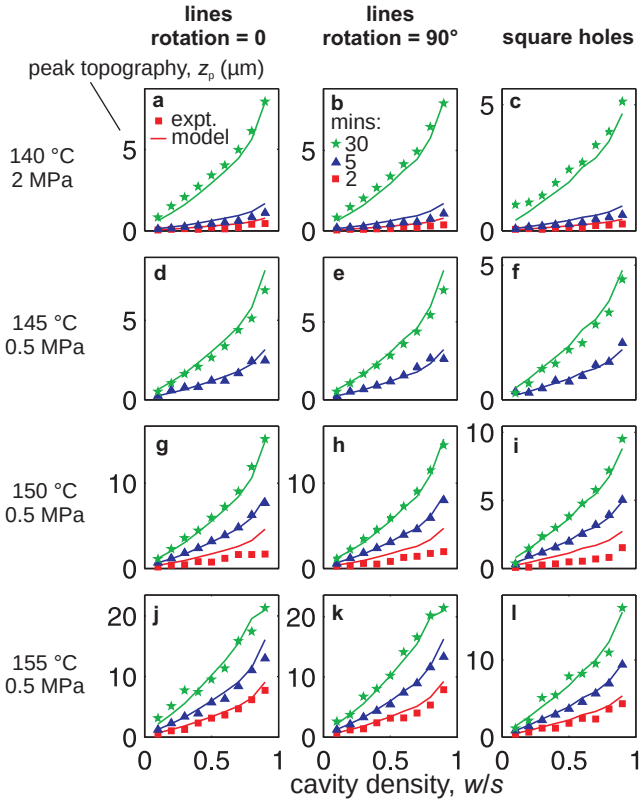

Figure A.3: Cavity penetration depths, z_p, for PC as a function of cavity opening density, *w/s*, and nominal loading duration, for 50-μm-pitch cavities.

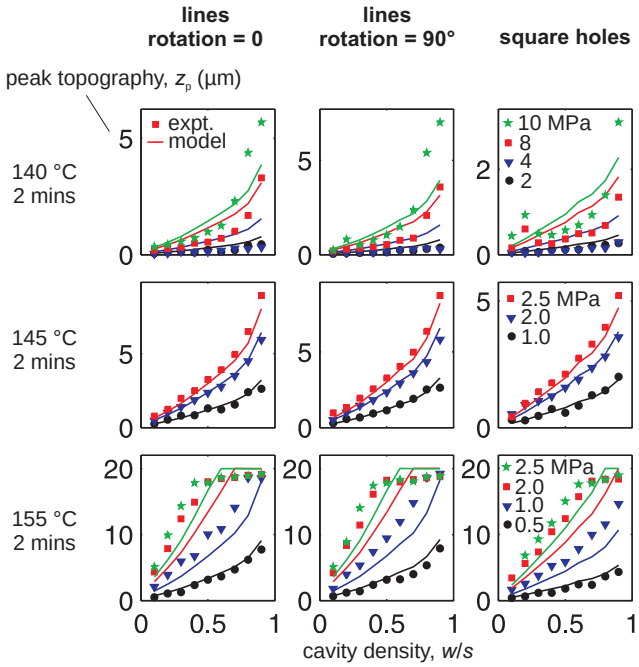

Figure A.4: Cavity penetration depths, z_p, for PC as a function of cavity opening density, *w/s*, and sample-average pressure, for 50-μm-pitch cavities and 2-minute nominal loading durations.

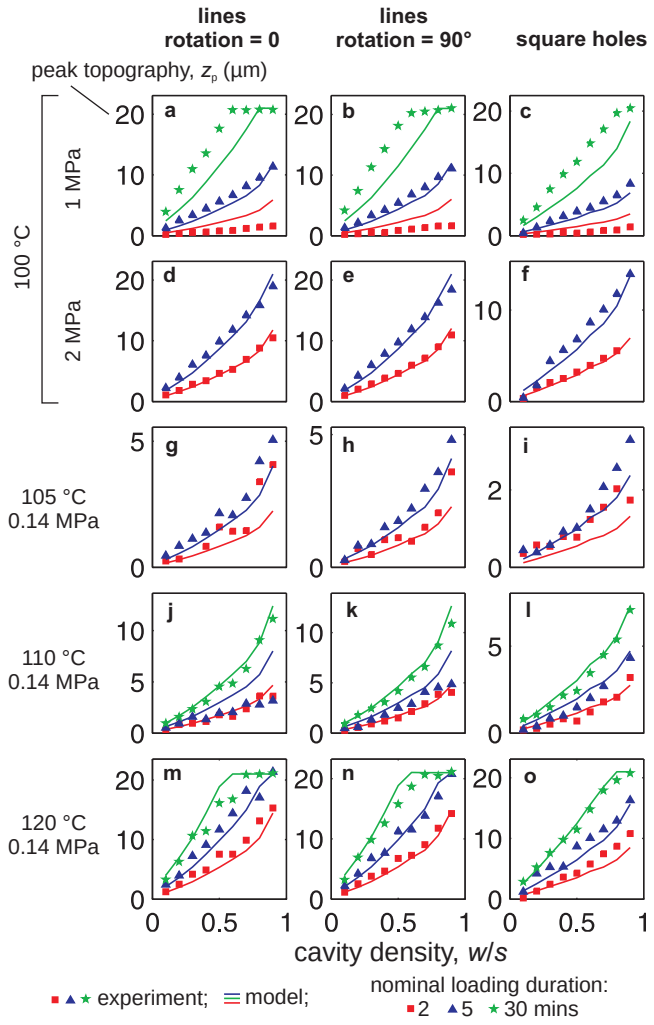

Figure A.5: Cavity penetration depths, z_p, for Zeonor 1060R as a function of cavity opening density, *w/s*, and nominal loading duration, for 50-μm-pitch cavities.

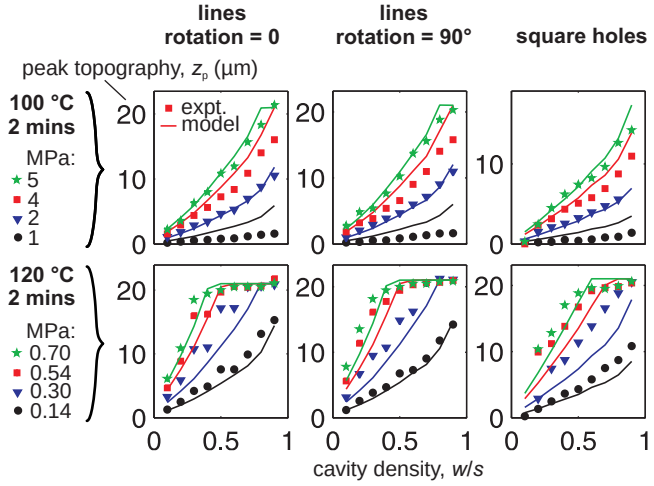

Figure A.6: Cavity penetration depths, z_p, for Zeonor 1060R as a function of cavity opening density, *w/s*, and sample-average pressure, for 50-μm-pitch cavities and 2-minute nominal loading durations.

Appendix B: Simulating optical interference images from imprinted resist layers

For several of the experiments presented in this thesis, optical micrographs of nanoimprinted patterns are shown. With knowledge of the refractive index of the imprinted layer, the thickness of the polymer layer can be estimated from the colors of the micrograph.

The situation is as shown in cross-section in Figure B.1: white light from the optical microscope is incident, approximately normally, on the imprinted surface of the polymer film. A proportion of the light reflects from the surface of the polymer, and some reflects from the polymer–silicon interface. Because the refractive index of the polymer layer (in the range 1.3–1.7 for most polymers) lies between those of air (~1) and silicon (~3.5), there is not expected to be a phase-change accompanying either of these reflections.

When the illustrated path of a component of the light inside the polymer has a length, $2r$, equal to an integer multiple of its wavelength inside the polymer, λ_p, constructive interference occurs between the light reflected from the upper and lower surfaces of the polymer layer, and that wavelength dominates in the optical micrograph. For visible light and for the values of r encountered in the experiments described in this thesis, the cases where $\lambda_p = 2r$, $\lambda_p = r$ and $\lambda_p = 2r/3$ may be relevant. Multiple-reflection paths in the polymer film are possible, but not relevant for the film thicknesses considered in this thesis. This approach further assumes that the coherence length of the illumination is longer than the path of light in the film.

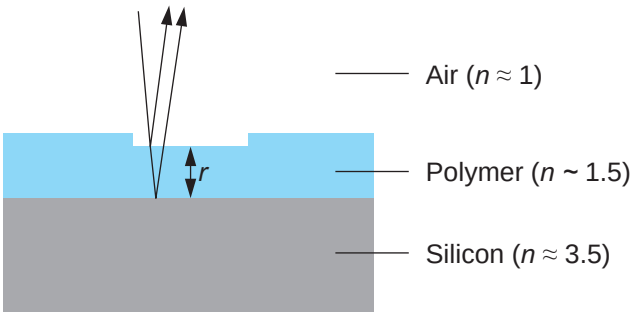

Figure B.1: Reflection of light in an imprinted film showing refractive indices, *n*, of the regions.

With this understanding it is possible to map the polymer layer thicknesses predicted by a mechanical simulation to the dominant visible wavelengths in a simulation of an optical micrograph. Comparison of experimentation with simulation could be assisted by such a mapping.

The wavelengths in free space, λ_0, of the constructively interfering light that would be in the visible spectrum for the experiments shown in this thesis are given by:

$$\lambda_0 = \lambda_p n = \begin{cases} 2rn/3 \\ rn \\ 2rn \end{cases} \tag{B.1}$$

where n is the refractive index of the polymer layer. These free-space wavelengths can be mapped to the RGB color space, and therefore plotted as simulated images, using the widely-employed relation illustrated in Figure B.2 [258]. Outside the free-space wavelength range 350–830 nm, nothing is assumed to be visible.

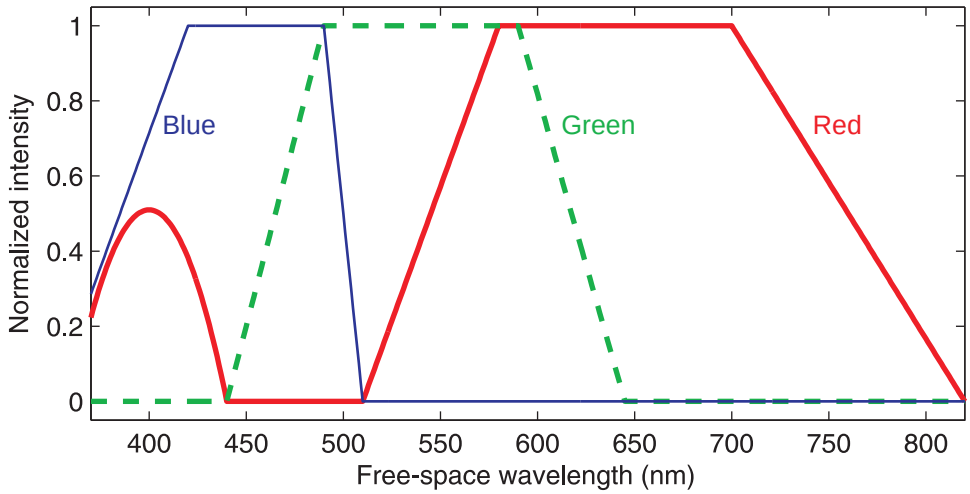

Figure B.2: The chosen mapping of free-space wavelength to RGB values.

Assuming a polymer refractive index of 1.5, this analysis is expected to be valid for light visible in the spectrum 350–820 nm and for polymer layer thicknesses between 117 nm and 466 nm. To estimate the value of r for thinner layers, the possibility of multiple-reflection modes would need to be considered. For thicker layers, path lengths equal to larger multiples of the wavelength would need to be considered — assuming the coherence length of the illumination were long enough.

In the optical simulations actually shown in this thesis, the plotted RGB intensities were found by adding the intensities associated with only the wavelength sets $\lambda_0 = rn$ and $\lambda_0 = 2rn$; including the wavelength set $\lambda_0 = 2rn/3$ was found not to improve the simulations of optical micrographs taken from known film profiles [90]. It is possible that for optical path differences equal to three or more wavelengths, the coherence of the light source used was insufficient to provide interference.